ELECTROCHEMICAL REDUCTION OF CARBON DIOXIDE ON COPPER ELECTRODES

A thesis submitted in partial fulfilment of the requirements for the

Degree

of Doctor of Philosophy in Chemical and Process Engineering

in the University of Canterbury

by C.F.C. Lim

University of Canterbury

2017

Acknowledgements

This work was carried out at the Department of Chemical and Process Engineering (CAPE), University of Canterbury, New Zealand from February 2013 to July 2017, and was financially supported by the Marsden Fund Council from government funding, managed by the Royal Society of New Zealand.

The completion of this thesis would not have been possible without the continuous support and encouragement from several people, whom I wish to acknowledge here.

To my supervisor, Dr Aaron Marshall, thank you for the past 4.5 years, throughout which your generous support, patience and guidance has led this project so far despite the initial challenges and difficulties of the work. I am very thankful for the two publications that we have accomplished together with Professor David Harrington.

To all technical staff at CAPE, thank you for not withholding your assistance, experience and expertise in relations to laboratory work. Without you, the department cannot function. Special thanks go to Stephen Hood, Stephen Beuzenberg, Leigh Richardson, Graham Mitchell, Glenn Wilson, Tim Moore and Michael Sandridge. Your assistance down to the smallest of things makes working in the laboratory a whole lot easier.

To technical staff outside of CAPE, specifically Rob McGregor at Chemistry and Mike Flaws at Mechanical Engineering, thank you for contributing to this work by sharing your unique expertise and experience.

To all my colleagues, past and present, thank you for making my time in and out of CAPE a memorable one.

Finally, to my Father in Heaven, and to my family, I could never have done this without your unconditional love. This is for you.

Yours sincerely,

Calvin Fung Chye Lim

'No problem can be solved by the same kind of thinking that created it'

– Albert Einstein

'If I have seen further, it is by standing on the shoulders of giants'

– Isaac Newton

'

Summary

Global warming, climate change and over-dependence on non-renewable fossil fuels demand long-term solutions to reduce CO_2 emissions and develop alternative and renewable fuels. The electrochemical reduction of CO_2 is part of the ambitious, but certainly not impossible, "carbon neutral cycle", which incorporates CO_2 as the unlimited carbon source for the production of high density fuels, and renewable energy as the driving force behind the process.

The majority of this work focusses on various aspects of electrochemical CO_2 reduction on polycrystalline Cu electrodes, although preliminary work was also performed on a number of Au_9/TiO_2 modified Cu electrodes. Initially, the general behaviour of the electrode potential and CO_2 reduction activity over long periods of galvanostatic electrolysis was investigated, along with the effects of current density and electrolyte concentration. Overall, the results obtained are consistent with those in the literature, and cover important observations including the major reduction products on Cu electrodes, their pH and potential dependence, and the widely reported deactivation of CO_2 reduction.

Following reports in the literature regarding the deactivation of CO_2 reduction, attempts were made to prolong the CO_2 reduction activity using periodic cyclic voltammetry and potentiostatic steps throughout extended periods of galvanostatic CO_2 reduction. However, contrary to previous literature, it is demonstrated that temporarily interrupting galvanostatic CO_2 reduction with short periods at potentials between −0.5 and −0.1 V vs Ag|AgCl suppresses the formation of CH_4, CO and C_2H_4. It is proposed that the suppression is caused by the partial removal or oxidation of adsorbed CO_2 reduction intermediates, the absence of which allowed the Cu surface to be more active for the hydrogen evolution reaction. Unexpectedly, when brief potentiostatic steps were conducted at more negative potentials (−1.2 V vs Ag|AgCl), the CO_2 reduction selectivity switched from CH_4 to CO, and was maintained for at least 2 hours. This change in selectivity is proposed to be caused by an increase in the surface coverage of CO_{ads} (at the expense of H_{ads}) during the brief −1.2 V steps, which then enabled the Cu cathode to switch between multiple steady-state surface coverages when the cathodic current is re-applied.

The observation of the sensitivity of CO_2 reduction on cell hydrodynamics prompted a systematic investigation into the effects of mass transfer on CO_2 reduction using a polycrystalline Cu rotating cylinder electrode. When the mass transfer rate increases (by increasing the rotation rate), the current efficiencies toward CO_2 reduction products decreased while that for the HER increased. Additionally, the selectivity of CO_2 reduction was observed to change, with CO becoming favoured over CH_4 with increasing mass transfer rates. These observations are in contrast to the widely reported effects of pH and CO_2 concentration, the values of which can be indirectly controlled by varying the rotation rate. Instead, the results are more consistent with the enhanced mass transfer of dissolved CO away from the electrode surface, which decreases the surface coverage of CO_{ads}, preventing the further reduction of CO_{ads} to hydrocarbons and changing the selectivity from CH_4 to CO. This particular work highlights the importance of cell hydrodynamics, and the need to consider these effects when comparing results between different experimental configurations or designing electrochemical cells and cathodes for industrial applications.

Following the strategy of developing novel electrocatalysts with a level of surface heterogeneity, the catalytic ability of TiO_2/Cu and Au_9/TiO_2/Cu electrodes prepared through spin-coating of commercial

TiO_2 (P25) and chemically synthesised Au_9/TiO_2 nanoparticles onto polished Cu substrates were investigated. It was determined that as the TiO_2 loading increases, the electrode potential during constant current electrolysis tend to become more positive, pointing toward an enhancement in the electrochemical activity of the electrode. The increase in electrode potential is further observed when Au_9 nanoparticles are introduced into the TiO_2/Cu electrocatalyst. However, the enhancement in electrochemical activity is found to be largely in favour toward the HER rather than CO_2 reduction. Nevertheless, despite the very low overpotentials at the modified Cu electrodes, surprising amounts of CO are still produced with current efficiencies generally comparable to that of the Cu controls and Ti electrodes at similar current densities but at much higher overpotentials. This suggests a form of synergy at the active sites of the Au_9/TiO_2/Cu interfaces which may have lowered the CO adsorption strength, hence allowing similar amounts of CO to be produced at much lower overpotentials.

Deputy Vice-Chancellor's Office
Postgraduate Office

UNIVERSITY OF CANTERBURY
Te Whare Wānanga o Waitaha
CHRISTCHURCH NEW ZEALAND

Co-Authorship Form

This form is to accompany the submission of any thesis that contains research reported in co-authored work that has been published, accepted for publication, or submitted for publication. A copy of this form should be included for each co-authored work that is included in the thesis. Completed forms should be included at the front (after the thesis abstract) of each copy of the thesis submitted for examination and library deposit.

Please indicate the chapter/section/pages of this thesis that are extracted from co-authored work and provide details of the publication or submission from which the extract comes:

Chapter 5, section 5.3.1, pp 60-63
Chapter 6, pp 73-86

C.F.C. Lim*, et al.*, Altering the selectivity of galvanostatic CO_2 reduction on Cu cathodes by periodic cyclic voltammetry and potentiostatic steps, Electrochimica Acta, 222 (2016) 133-140.

Please detail the nature and extent (%) of contribution by the candidate:

The candidate is the first author of the journal paper and wrote most of the text.

Certification by Co-authors:

If there is more than one co-author then a single co-author can sign on behalf of all.

The undersigned certifies that:

- The above statement correctly reflects the nature and extent of the PhD candidate's contribution to this co-authored work.
- In cases where the candidate was the lead author of the co-authored work he or she wrote the text.

Name: *Aaron Marshall*
Signature: 

Date: *29/7/2017*

Deputy Vice-Chancellor's Office
Postgraduate Office

UNIVERSITY OF CANTERBURY
Te Whare Wānanga o Waitaha
CHRISTCHURCH NEW ZEALAND

Co-Authorship Form

This form is to accompany the submission of any thesis that contains research reported in co-authored work that has been published, accepted for publication, or submitted for publication. A copy of this form should be included for each co-authored work that is included in the thesis. Completed forms should be included at the front (after the thesis abstract) of each copy of the thesis submitted for examination and library deposit.

Please indicate the chapter/section/pages of this thesis that are extracted from co-authored work and provide details of the publication or submission from which the extract comes:

Chapter 2, section 2.3.6, pp 22-23
Chapter 7, pp 89-100

C.F.C. Lim, *et al.*, Effects of mass transfer on the electrocatalytic CO_2 reduction on Cu, Electrochimica Acta, 238 (2017) 56-63.

Please detail the nature and extent (%) of contribution by the candidate:

The candidate is the first author of the journal paper and wrote most of the text.

Certification by Co-authors:

If there is more than one co-author then a single co-author can sign on behalf of all.

The undersigned certifies that:

- The above statement correctly reflects the nature and extent of the PhD candidate's contribution to this co-authored work.
- In cases where the candidate was the lead author of the co-authored work he or she wrote the text.

Name: *Aaron Marshall*
Signature: 

Date: *29/7/2017*

Table of Contents

1 Introduction

1.1 The Carbon Neutral Cycle

Renewable energy is currently one of the world's major topics of research. This is mainly due to the need to lessen society's dependence on fossil fuels which are quickly dwindling and also the urgency to mitigate greenhouse gas emissions. The excessive usage of carbon-containing fossil fuels and their products both in the industry and the transportation sector has led to the uncontrolled release of carbon dioxide (CO_2) into the atmosphere, significantly contributing to global warming and climate change [1]. The realisation of the detrimental consequences this has on the world's environment has led to the development of various alternative and renewable carbon-neutral energy sources such as solar, wind, hydroelectricity, biomass, geothermal and nuclear power in the effort to implement them as a replacement to fossil fuels.

While some renewable energies are already successfully implemented on large scales such as nuclear power and hydroelectricity, certain sources like solar and wind power are highly intermittent and thus are not able to respond to energy demands consistently in both time and space [2]. To overcome this problem, any surplus energy from renewable sources can be converted into a form that is storable and portable so that it can be used whenever and wherever the demand is present, much like the fossil based fuels used today [1, 3].

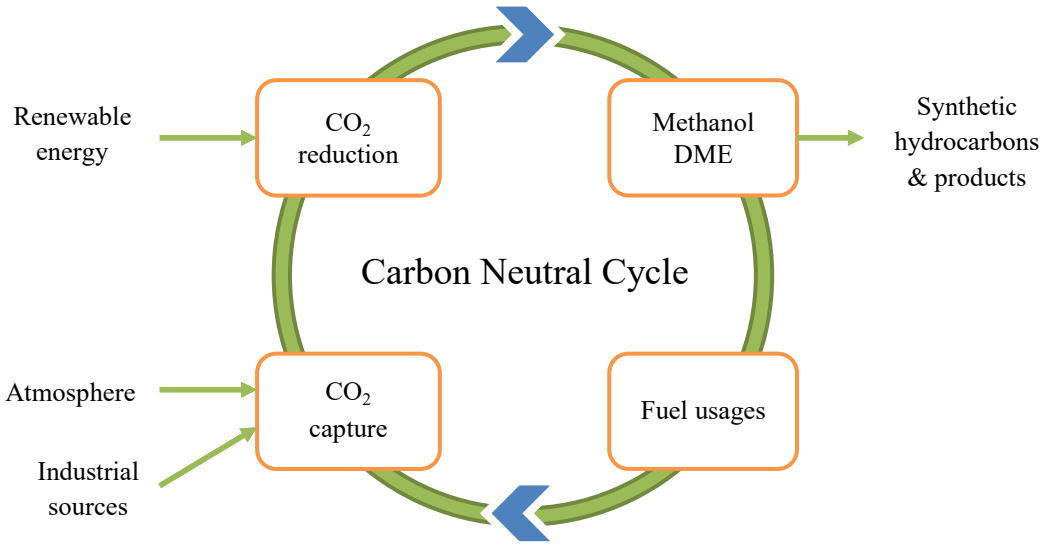

Figure 1.1: The "carbon neutral cycle", adapted from [1]. In this illustration, the reduction of CO_2 captured from various sources is powered by renewable energy to produce methanol and dimethyl-ether, which can be used to produce carbon neutral fuels, synthetic hydrocarbons and their varied products.

One of the ways to store surplus energy from renewable sources is to convert them into chemical energy through the "chemical recycling of carbon dioxide" or the "carbon neutral cycle" [1, 3-7] as illustrated in Figure 1.1. This idea proposes the capture of CO_2 from natural and industrial sources, daily human activities or even the atmosphere itself, and the subsequent reductive conversion to high energy density fuels, using renewable energy sources as the driving force behind the process. In other words, research aims to mimic nature's own photosynthetic CO_2 cycle, i.e. *"artificial photosynthesis"* [2, 4], so that instead of introducing new CO_2 into the atmosphere through the combustion of carbon-based fossil fuels, existing CO_2 is used as the inexhaustible carbon source to produce carbon-neutral

renewable fuels. From the renewable fuels produced such as methanol and dimethyl-ether, various other synthetic hydrocarbons can also be made [1]. What is attractive about the chemical recycling of CO_2 is that it essentially allows the continued use of carbon-based fuels in an environmentally renewable and carbon-neutral manner, and in many ways, with minor modifications, also allows the continued use of current technologies and infrastructure designed for fossil fuels [1, 3-5].

If implemented successfully, the "carbon neutral cycle" will significantly facilitate the mitigation of CO_2 emission and remedy global warming and climate change. More importantly, it will provide a permanent alternative to fossil fuels through the recycling of CO_2 as the unlimited carbon source to produce renewable, sustainable and carbon-neutral fuels and synthetic hydrocarbons that can be derived from them.

1.2 Electrochemical CO_2 reduction

CO_2 reduction methods can be broadly classified into four major categories: thermochemical, biochemical, photochemical and electrochemical reduction. Thermochemical methods to reduce CO_2 have been in existence for several decades. A well-known example is the conversion of CO_2 and H_2 to methanol under a catalyst generally composed of $Cu/ZnO/AlO_3$, which is arguably similar to the current industrial method of producing methanol from syngas [1, 8-11]. This conversion process requires temperatures and pressures around 220−330 °C and 50−100 atm respectively [10, 11]. At lower pressures, CO_2 and H_2 can also be converted into hydrocarbons using Fischer-Tropsch type catalysts, however similar elevated temperatures are still required [12, 13]. As expected, due to their immoderate operating conditions, thermochemical methods are highly energy intensive, and hence in current times it is still most conveniently and efficiently driven by fossil fuels. Biochemical methods generally employ autotrophic organisms and specific enzymes to capture CO_2 and catalyse its reduction to complex molecules [14, 15] while photochemical methods aim to directly mimic natural photosynthesis by utilising light harvesting materials and photo/electrocatalysts to coincidentally split water and reduce CO_2 under irradiation from sunlight [16-19]. Generally, research on both biochemical and photochemical methods strive to directly utilise sunlight as the unlimited energy source to convert CO_2 to high energy density fuels at ambient conditions. The downside of this goal is that it neglects the availability of many other types of renewable energy sources.

Electrochemical methods on the other hand aim to utilise renewable electrical energy, which can be sourced from a wide range of renewable energies, to drive the CO_2 conversion process at ambient conditions under a well suited electrocatalyst [4, 20]. Hence, electrochemical methods are not limited to just one or two renewable energy sources, but because most renewable energy sources today are harnessed in the form of electrical energy, electrochemical methods can easily be adapted and coupled to almost all forms of renewable energy. This makes electrochemical methods very attractive as potential enabling technologies for CO_2 utilisation. As with many novel methods of CO_2 reduction, the electrochemical reduction of CO_2 however is still fraught with challenges that need to be overcome before being economically viable. Some of the main challenges are described below.

A prospective example of CO_2 utilisation through electrochemical CO_2 reduction is the direct production of methanol as described by reactions 4 and 8 in Table 1.1, which is simply the reverse of the methanol combustion reaction. Methanol is highly desirable in the research of CO_2 recycling and energy storage due to its high energy density, suitability as a substitute fuel for internal combustion engines, and convenience as a starting material for producing synthetic hydrocarbons and chemicals [1, 3]. Thermodynamically, the minimum energy requirement to produce methanol from CO_2 is not very different to that for water electrolysis, i.e. E^0_{cell} = 1.21 V (20 mV less than that for water

electrolysis). However, despite the low thermodynamic requirement, the cathodic reaction to produce methanol or any other CO_2 reduction product is kinetically hindered by large activation barriers amounting to overpotentials of at least 1 V or more [21-24], causing the process to be energetically inefficient. This is mainly due to the large amount of energy required to activate the naturally stable CO_2 molecule. It has been widely proposed that the activation of CO_2 proceeds through the single electron reduction of CO_2 to the $CO_2^{\bullet-}$ radical anion intermediate from which subsequent reduction takes place [4, 21, 25-28]. The standard potential for the formation of this radical anion is very negative, i.e. −1.9 V vs SHE [29-31]. In addition to CO_2 activation, the need for multiple concerted proton-electron transfer steps which would have their own respective associated activation energies will also introduce further overpotentials, especially for the production of more complex products beyond CO. Hence, due to these kinetic challenges, the thermodynamic potentials given in Table 1.1 can generally be misleading*. It is the role of electrocatalysts to overcome these overpotentials and improve the energy efficiency of the process. Well-designed electrocatalysts decreases the activation barriers by stabilising adsorbed intermediates, enabling alternative reaction pathways with lower barriers and by providing adjacent reaction sites which facilitate the reaction between adsorbed intermediates.

Table 1.1: Thermodynamic potentials of various half reactions involving CO_2 reduction in aqueous solutions at pH 0 or 7, 25 °C, and unit activity for other reactants and products.

		E (V vs SHE)[a]	
Cathode:		pH 0	pH 7[b]
(1)	$2H^+ + 2e^- \leftrightarrow H_2$	0	−0.41
(2)	$CO_2 + 2H^+ + 2e^- \leftrightarrow HCOOH$	−0.17	−0.58
(3)	$CO_2 + 2H^+ + 2e^- \leftrightarrow CO + H_2O$	−0.10	−0.52
(4)	$CO_2 + 6H^+ + 6e^- \leftrightarrow CH_3OH + H_2O$	0.02	−0.40
(5)	$CO_2 + 8H^+ + 8e^- \leftrightarrow CH_4 + 2H_2O$	0.17	−0.25
(6)	$2CO_2 + 12H^+ + 12e^- \leftrightarrow C_2H_4 + 4H_2O$	0.08	−0.34
(7)	$2CO_2 + 14H^+ + 14e^- \leftrightarrow C_2H_6 + 4H_2O$	0.14	−0.27
Anode:			
(8)	$6H_2O \leftrightarrow 12H^+ + 12e^- + 3O_2$	1.23	0.81

[a]Thermodynamic potentials are calculated using the change in Gibbs free energy and the relation $G^0 = -nFE^0$. The pH dependence of the potentials is described by the Nernst equation. See Appendix 1 for calculations.

[b]The majority of works on the electrochemical reduction of CO_2 in aqueous solutions are conducted in the neutral to acidic region due to the $CO_2/HCO_3^-/CO_3^{2-}$ equilibria when the electrolyte is saturated with CO_2.

Another major challenge to overcome is the product selectivity of the reaction. The electrochemical reduction of CO_2 in aqueous electrolytes leads to a myriad of products not limited to those presented in Table 1.1. One study had even revealed 16 possible CO_2 reduction products, 11 of which are oxygenated C_2 and C_3 hydrocarbons [32]. In addition, because the electrochemical reduction of CO_2 occurs at potentials on par or more negative than water electrolysis, there exists a competition between the electrochemical reduction of CO_2 and the hydrogen evolution reaction. Therefore H_2 is also a main product of the reaction in aqueous solutions, which may or may not be an advantage depending on the intended application† [1, 25]. In general, the product distribution is primarily a strong function of the electrocatalyst (metals, oxides, alloys etc.) and electrolyte used (aqueous or non-aqueous). Secondarily, operating conditions such as electrode potential or current density,

* For example, according to reaction 5, the formation of CH_4 is thermodynamically more favourable than CO and $HCOO^-$ although the production of CH_4 requires 8 multiple concerted proton-electron steps to form while CO and $HCOO^-$ only requires 2. In actuality, the onset potential for CH_4 production is significantly more negative than that of CO and $HCOO^-$.

† The production of H_2 from the electrochemical reduction of CO_2 can be advantageous when the aim is to produce syngas ($CO + H_2$) from which long-chain hydrocarbons can be produced through a secondary Fischer-Tropsch process [1].

electrolyte and reactant concentrations, pH, temperature and pressure, and various other factors such as the purity of the electrode and electrolyte, and the degree of mixing used in the electrochemical cell (mass transfer effects) have also demonstrated significant influence on the product selectivity. The majority of these factors are described in chapter 2. To improve the reaction selectivity, much research is still needed to determine suitable electrocatalysts and electrolyte combinations (electrolyte can serve as a co-catalyst), as well as optimal operating conditions that will facilitate the synthesis of a desired product(s).

Although it is clear that many challenges still remain before the electrochemical reduction of CO_2 can be commercially implemented, significant advances in electrocatalysis and fuel cell design are already paving the way to make the process a reality. In particular, well-designed electrochemical cells that overcome mass transfer limitations, facilitate reactant/products concentration and separation, and allow optimisation of operating temperatures such as gas diffusion electrodes and solid oxide cells are already present in the market. As research progresses to design an electrocatalytic system that improves the energy efficiency and product selectivity, while adapting existing technologies to improve the commercial viability of the process, it is only a matter of time that the electrochemical reduction of CO_2 will revolutionise green energy technologies.

1.3 Thesis focus and outline

The literature surrounding the electrochemical reduction of CO_2 is rather varied in its scope to say the least [25, 33-37]. At large however, the research work can be broadly classified into two groups based on the type of catalytic system used. The first group is one where molecular catalysts such as transition-metal complexes are used as electrocatalysts, and are usually operated in a homogeneous phase, although a heterogeneous set-up is possible by immobilising or depositing the electrocatalysts onto an electrode surface [38-40]. The second group, which is more common, is the use of heterogeneous bulk electrodes placed in contact with an electrolyte to give an electrode/electrolyte boundary where the reaction occurs. Since the nature of the electrolyte, i.e. aqueous or non-aqueous, strongly influences the reaction mechanism and product distribution, research work can further be classified based on whether aqueous or non-aqueous solvents are used. For this thesis, the research scope is focussed on the heterogeneous electrochemical CO_2 reduction on bulk electrodes in aqueous solutions. Hence, throughout the thesis, "the electrochemical reduction of CO_2", "CO_2 reduction" and other variations of the phrase refer to the said scope unless otherwise stated.

Since the 1985 pioneering discovery by Hori et al. that Cu metal electrodes could further reduce CO_2 past $HCOO^-$ and CO to CH_4, C_2H_4 and possibly other hydrocarbons [41-43] with relatively higher current efficiencies than other metals, research on the electrochemical reduction of CO_2 has gained significant momentum. Not long after, many researchers have concluded that Cu, a relatively cheap metal, has a unique capability to catalyse CO_2 reduction to hydrocarbons, whereas other transition metals mainly produce CO, $HCOO^-$ or H_2. To date, a considerable portion of the literature has been devoted to demonstrate and investigate how and why Cu is unique, and to design and characterise novel Cu-based electrocatalysts in order to incorporate the unique catalytic ability of Cu for CO_2 reduction. However, from our perspective, it seems that as more work is being contributed to the literature, more differing opinions, inconsistencies, irreproducibility and at times direct contradictions in results and conclusions are found. Evidently, this makes understanding and reviewing the literature significantly more difficult as more novel and complex work are being contributed. To support this observation, a number of recently published works have emphasised the high sensitivity of the reaction selectivity to commonplace factors that are easily overlooked such as electrolyte concentration, buffer strength and stirring (mass transfer), temperature and pressure, interfacial pH

and CO_2 concentration etc. These works stressed that not all improvements (or otherwise) in results can always be attributed to the intrinsic catalytic property of the electrocatalysts investigated. In fact one should always carefully consider other non-catalytic related factors, some of which may contribute a significant level of impact on the results. Clearly, because experimental methods between research groups often differ and standardisation of procedures generally does not exist in the context of electrochemical CO_2 reduction, it is perceivable why large variations in results and conclusions are present in the literature. Therefore, as our understanding of the effects of these factors increases, it is important that researchers factor them in during the design of experiments and analysis of results, not limiting to ongoing and future work, but also for all published work in the literature.

In accordance with works that highlighted the importance of non-catalytic factors, a significant portion of this thesis also presents findings that lead to corroborating conclusions. Much of the work in this thesis is centred on polycrystalline Cu, which is relatively simple to prepare and generally goes against the mainstream focus of discovering new and efficient electrocatalysts for the electrochemical reduction of CO_2. The experimental method used for the work is also well established and relatively basic. However, in spite of the simplicity of the system, several new findings were discovered, and our understanding of the electrochemical reduction of CO_2 on Cu electrodes is further improved.

The contents of the thesis chapters are briefly described below. Note that chapters 6 and 7 are works which we have published elsewhere, and therefore we present them here in their entirety and in their original journal structure; hence, the reader may encounter some material within these two chapters that has already been covered elsewhere in the thesis. Chapter 8 is a short chapter detailing some preliminary work that due to time constraints was not pursued further. The appendices provide additional material that supplement the overall thesis and are appropriately referenced to within the thesis chapters.

- Chapter 2 presents a literature review on the electrochemical reduction of CO_2 focusing mainly on Cu metal. Topics most relevant to the scope of the thesis are selected. A brief overview on some Cu-based electrodes is also given.
- Chapter 3 gives an overview of the experimental set-up and methods used for the work done in this thesis.
- Chapter 4 presents a mathematical model adapted from Gupta et al. [44] to model time-dependent changes in chemical species concentrations during the electrochemical reduction process.
- Chapter 5 presents results on galvanostatic electrochemical CO_2 reduction on polycrystalline Cu and discusses the effects of current density and electrolyte concentration.
- Chapter 6 describes how the use of periodic cyclic voltammetry and potentiostatic steps can alter reaction selectivity during galvanostatic electrochemical CO_2 reduction. This chapter has been published in Electrochimica Acta.
- Chapter 7 presents results on galvanostatic electrochemical CO_2 reduction on a polycrystalline Cu rotating cylinder electrode and shows how mass transfer can have a significant impact on the reaction selectivity. This chapter has been published in Electrochimica Acta.
- Chapter 8 is a short chapter summarising preliminary results of the electrochemical CO_2 reduction on polycrystalline Cu supported Au_9/TiO_2 electrodes.

2 Literature Review

2.1 Introduction

The literature review is written with the aim to provide the reader with various important results and discussions on the electrochemical reduction of CO_2 on Cu metal. A short discussion on some Cu-based electrodes is also presented. Despite the fact that much of the defining work on Cu metal electrodes was performed a while ago (since the 1980s), relevant research on Cu and Cu-based electrodes is still being carried out today. Hence, the literature review is presented using a mixture of old and recent work to discuss the relevant topics chosen for the thesis. Several important and recommended reviews on the subject of electrochemical CO_2 reduction are [22, 25, 45-49].

2.2 Classification of metal electrodes for CO_2 reduction

Most of the systematic experimental studies to characterise the catalytic ability of various metal electrodes for the electrochemical reduction of CO_2 were carried out in the 1980s [41, 50, 51]. Notably, Azuma et al. [51] investigated the reaction on 32 different metal electrodes, which included most of the transition metals. By observing the product distribution obtained on various metal electrodes at ambient conditions, the metals can generally be classified into four groups (Table 2.1).

The first group (e.g. Pb, Hg, In, Sn, Cd, Tl, Bi) produces formate (or formic acid) as the main CO_2 reduction product, usually with high current efficiencies. These metals are commonly known for their high hydrogen overvoltage and hence are choice electrodes in early electrochemical CO_2 reduction studies, given that the hydrogen evolution reaction (HER) competes with CO_2 reduction in aqueous solutions. Because formate ($HCOO^-$) is the main product, it is clear that the breaking of the first C−O bond of the $CO_2^{\bullet-}$ radical is not favoured. Instead the radical anion is protonated (or hydrogenated by H_{ads}) at the carbon atom, giving $HCOO^-$ as the main product. These metals also have negligible CO adsorption properties, indicating that the formation of CO_{ads} from $CO_2^{\bullet-}$ radical is not favoured.

In contrast to the first group, the second group (e.g. Au, Ag, Zn, Pd, Ga) produces mainly gaseous CO as the main CO_2 reduction product. These metals have intermediate hydrogen overvoltage and weak CO adsorption properties. As $CO_{(g)}$ is the main product, the breaking of the first C−O bond of the $CO_2^{\bullet-}$ radical occurs favourably on these metals. However due to the weak adsorption of CO, further reduction of CO_{ads} is prevented and hence the CO_{ads} is released as $CO_{(g)}$.

The third group, which is unique to Cu metal only, can further reduce CO_{ads} to CH_4 and C_2H_4 with relatively high current efficiencies, and other higher ordered products in smaller quantities. Cu metal also has intermediate hydrogen overvoltage but unlike the metals from group 2, Cu adsorbs CO with intermediate strength at ambient conditions. It is this intermediate adsorption of CO that many researchers agree gives Cu the ability to stabilise CO_{ads} "just right", as per the Sabatier principle [52], for the further reduction of CO_{ads} to hydrocarbons [48, 53-55].

The fourth group (e.g. Pt, Ni, Fe, Ti) consists of metals that do not reduce CO_2 readily and produce mainly H_2. These metals are well-known for their low hydrogen overvoltage and are widely studied for applications in water electrolysis. These metals also have strong CO adsorption properties, which can lead to electrode poisoning by blocking of active sites by CO_{ads}. Hence, in CO_2 reduction applications, the formation of a tightly adsorbed CO_{ads} monolayer on the electrode surface prevents both the release of CO_{ads} as $CO_{(g)}$ and the further reduction of CO_{ads} to hydrocarbons, leading to H_2 as the only principle product in aqueous solutions.

Table 2.1: Classification of metal electrodes for the electrochemical reduction of CO_2 in aqueous solutions based on product distribution [22, 25, 47, 48, 56].

Group	Electrode metal(s)	Main product(s)	Properties
1	Pb, Hg, In, Sn, Cd, Tl, Bi	$HCOO^-$	• High hydrogen overvoltage • Negligible CO adsorption strength • $CO_2^{\bullet-}$ either free in solution or weakly adsorbed through oxygen coordination • "$HCOO^-$ formation" metal
2	Au, Ag, Zn, Pd, Ga	CO, H_2	• Intermediate hydrogen overvoltage • Weak CO adsorption strength • $CO_2^{\bullet-}$ adsorbed likely through carbon coordination • "CO formation" metal
3	Cu	CH_4, C_2H_4, CO, $HCOO^-$, H_2	• Intermediate hydrogen overvoltage • Intermediate CO adsorption strength • $CO_2^{\bullet-}$ adsorbed likely through carbon coordination • "CO formation" metal
4	Pt, Ni, Fe, Ti	H_2	• Low hydrogen overvoltage • High CO adsorption strength • $CO_2^{\bullet-}$ adsorbed likely through carbon coordination • "CO formation" metal

In Hori's work [22, 48, 56], the 4 groups above are more broadly classified into either "$HCOO^-$ formation" or "CO formation" metals. Metals in group 1 are "$HCOO^-$ formation" while those from groups 2 to 4 are "CO formation". This classification, as implied by the group names, is based on the tendency of the metal to stabilise the $CO_2^{\bullet-}$ radical and form either $HCOO^-$ or CO_{ads}, i.e. the "CO selectivity" [56], with the subsequent proton-electron transfer step (Figure 2.1). For "$HCOO^-$ formation" metals, it is suggested that the $CO_2^{\bullet-}$ radical is not readily adsorbed and is present in the electrolyte solution close to the electrode surface [28]. The $CO_2^{\bullet-}$ radical existing in this manner is nucleophilic at the C atom due to the high density of unpaired electrons localised on the C atom [57]. Hence, the $CO_2^{\bullet-}$ radical is favourably protonated at the C atom to form $HCOO^{\bullet}$, which is then reduced to $HCOO^-$ through an electron transfer. On the other hand, for "CO formation" metals, the $CO_2^{\bullet-}$ radical is thought to adsorb on the electrode surface through C-coordination, i.e. adsorb through the C atom. In this case, the stabilised $CO_2^{\bullet-}$ radical on the metal surface has an increased electron density at the O atoms [58]. This promotes protonation at one of the O atoms to form the carboxyl intermediate ($COOH_{ads}$), which is subsequently reduced to CO_{ads} through an electron transfer. The suggestion of the adsorption and stabilisation of the $CO_2^{\bullet-}$ radical on "CO formation" metals but not on "$HCOO^-$ formation" ones is consistent with the overall observation that CO_2 reduction usually occurs at lower overpotentials on "CO formation" metals, e.g. formation of $CO_{(g)}$ on Au electrodes [59], which is likely due to the stabilisation of the high energy $CO_2^{\bullet-}$ radical on "CO formation" metals [56].

In contrast to Hori, Gattrell et al. [47] in their review suggest that the formation of CO_{ads} or $HCOO^-$ from the reduction of the $CO_2^{\bullet-}$ radical is rather a matter of the way the $CO_2^{\bullet-}$ radical is coordinated on the electrode surface. For metals producing mainly $HCOO^-$, the mechanism to form $HCOO^-$ is favoured by the $CO_2^{\bullet-}$ radical being adsorbed with O-coordination, as this allows the C atom to be more accessible to H^+ from the electrolyte. In a similar fashion, the mechanism to form CO_{ads} is favoured by adsorption with the C-coordination, as this allows the O atoms to be more easily protonated.

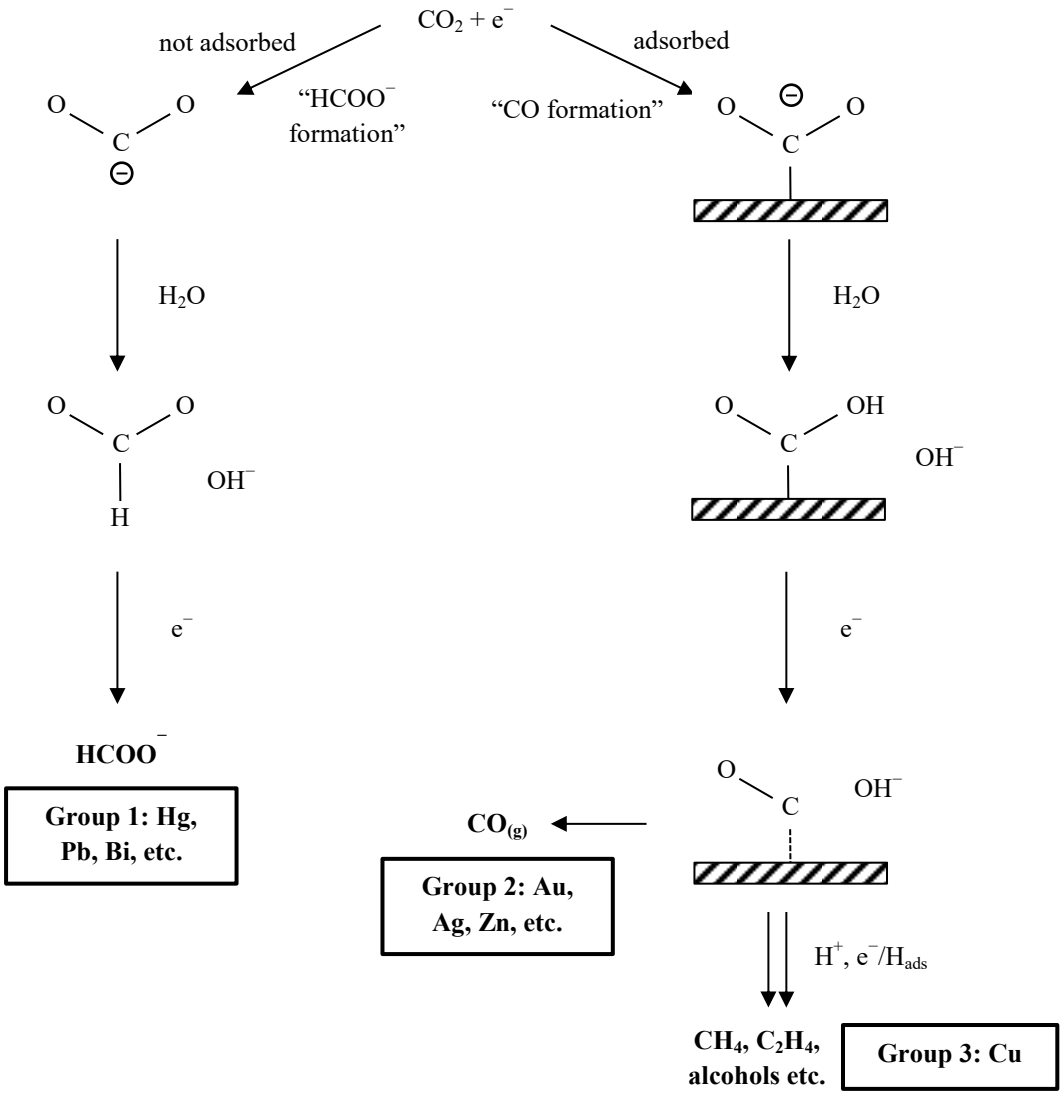

Figure 2.1: Overall mechanism and classification of metal electrodes for the electrochemical reduction of CO_2 based on product distribution. Adapted from [22, 25].

It is worth emphasising that the classification of metal electrodes presented above for the electrochemical reduction of CO_2 in aqueous solutions is largely based on the product distribution observed at ambient or near ambient conditions. There are instances where the product distribution is shown to be strongly dependent on temperature and pressure, even for group 4 metals that hardly give any CO_2 reduction products at ambient conditions. For example, at 30 atm CO_2 pressure, Ni was shown to be able to reduce CO_2 to CO and HCOOH, both at approximately 30% faradaic efficiency (total CO_2 reduction efficiency of 60%) at −1.4 V vs SHE [60]. However, at 1 atm, only H_2 is produced at −1.5 V vs SHE [56]. In fact, it has been emphasised before that hydrocarbons can actually be produced on all metal surfaces, although the rates differ significantly between them when comparing at similar reaction conditions [50, 55].

2.3 CO_2 reduction on Cu metal

As revealed in the previous section, Cu metal has a unique ability to reduce CO_2 to higher products beyond CO with relatively high current efficiencies at ambient conditions. This discovery is accredited to Hori [41-43] and has been confirmed by many other workers since [23, 51, 61-66]. In this section, a range of important parameters that affect the performance of Cu metal is presented and discussed.

2.3.1 Electrode potential

The thermodynamic potentials for various CO_2 reduction reactions are given in Table 1.1. Although the thermodynamic potentials are not very negative, observable CO_2 electro-reduction rates on Cu metal usually occur at overpotentials greater than 1 V [21-24].

The dependence of reaction rates and product selectivity on the electrode potential has been investigated in various early works [23, 45, 65, 67], the results of which have been utilised by many subsequent investigations on Cu electrodes as a standard reference. The reliability of the results of these early investigations is verified by many recent works which show comparable dependence on the electrode potential [32, 68-74]. Part of the reason for the high reproducibility of the results between various research groups is that the potential dependence data is usually obtained using relatively short potentiostatic electrolysis lasting between 30 min to 1 hour per measurement. This allows the true catalytic ability of the electrode to be captured before the effects of various changes to the electrode surface such as crystal reorientation and poisoning become evident.

Figure 2.2 presents a typical example of the dependence of the product selectivity on the electrode potential that is widely referred to by many researchers. At more positive potentials (−0.8 to −1.0 V vs SHE), i.e. low overpotentials, the main CO_2 reduction products are CO and $HCOO^-$, consistent with the fact that the formation of CO and $HCOO^-$ only require 2 e^- per molecule. Additionally, high selectivity to H_2 is also prevalent at low overpotentials, given that CO_2 reduction usually requires a larger overpotential than HER on Cu metal. As the overpotential increases, the selectivity to CO and $HCOO^-$ increases while that to H_2 decreases. Further increase in the overpotential leads to the introduction of C_2H_4 at −1.1 V vs SHE followed by CH_4 at −1.2 V vs SHE, both of which continue to increase with overpotential up to −1.5 V vs SHE. While the selectivity to C_2H_4 and CH_4 continues to rise with overpotential, the selectivity to CO and $HCOO^-$, jointly with H_2, concurrently declines. In other works that investigate electrode potentials more negative than −1.5 V vs SHE (Figure 2.3), it was shown that the H_2 selectivity will eventually begin to increase after passing through a minimum, which happens in concurrence with an overall decline in all CO_2 reduction products [32, 65]. This is frequently attributed to limitations in mass transport of dissolved CO_2 (0.034 M at 25 °C and 1 atm pressure in aqueous solutions [75]) to the electrode surface, allowing HER to be the sole dominant reaction at much higher overpotentials. In some instances, for example in the work by Kuhl et al. [32], CH_4 production was shown to increase together with H_2 at high overpotentials while all other CO_2 reduction products decreased. This was attributed to the increased favourability of proton-electron transfers to adsorbed CO_2 reduction intermediates over C−C coupling between them (which is a required step for the formation of C_2H_4 and other C_{2+} products), due to an increase in H_{ads} coverage which promotes the HER and at the same time decreases the probability of CO_2 reduction intermediates being adsorbed in adjacent reaction sites for C−C bond formation.

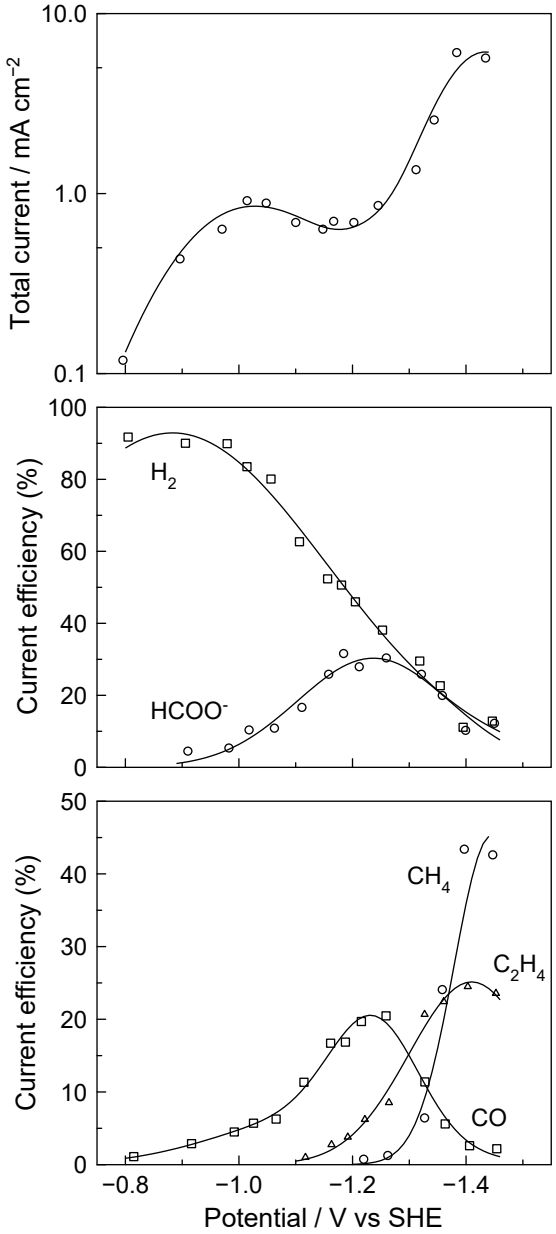

Figure 2.2: Current efficiencies of CO_2 reduction products with the Cu electrode potential in 0.1 M $KHCO_3$ as reported by Hori et al. [67]. Lines are to guide the eye.

The potential dependence of the product selectivity has provided some insights into the CO_2 reduction mechanism on Cu metal. The first observation pertains to the decline in CO and $HCOO^-$ selectivity with increasing overpotentials, which occurs in parallel with the increase in hydrocarbon selectivity. This suggests that coordinated CO and $HCOO^-$ on the electrode surface could be precursors or intermediates in the electro-reduction of CO_2 to hydrocarbons. To investigate this, the electrochemical reduction of CO [23, 63, 64, 67, 76, 77] and $HCOO^-$ [67, 78] were separately performed in conditions comparable to that of electrochemical CO_2 reduction. It was quickly determined that CO as a starting reactant is reduced to hydrocarbons with a similar product distribution to CO_2 reduction, but $HCOO^-$ on the other hand is not readily reduced on Cu metal. These findings, along with strong spectroscopic evidence of the presence of CO_{ads} during CO_2 reduction [54, 79-82], show that CO must first be formed from CO_2 in order for hydrocarbons to be produced, and that $HCOO^-$ is a "dead-end" product. The second observation pertains to the fact that the onset of C_2H_4 always occurs at a lower

overpotential than CH_4. Because C_2H_4 contains 2 carbon atoms, the formation of C_2H_4 will eventually require a reaction step between two C-containing intermediates, e.g. CO_{ads}, COH_{ads} etc., while the formation of CH_4 would only involve one. Hence, it would seem logical that the formation of CH_4 and C_2H_4 follow separate pathways with the local rate determining step (RDS) for C_2H_4 occurring at less negative potentials compared to that for CH_4. Indeed, it is frequently suggested with supporting results that the local RDS for C_2H_4 is a pH-independent electron mediated dimerization step between two C-containing intermediates, likely CO_{ads}, while the local RDS step for CH_4 is the pH-dependent proton-electron transfer to either CHO_{ads} or COH_{ads} [47, 83].

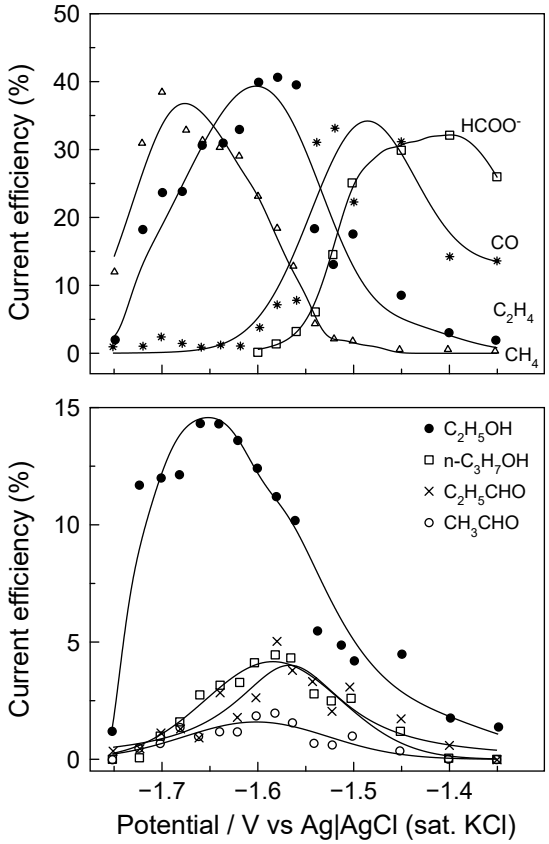

Figure 2.3: Current efficiencies of CO_2 reduction products with the Cu electrode potential in 0.1 M $KHCO_3$ as reported by Noda et al. [65]. Lines are to guide the eye.

Based on the results of the investigations on electrode potential dependence, the most common products of aqueous electrochemical CO_2 reduction on Cu metal are H_2, $HCOO^-$, CO, CH_4 and C_2H_4, with the sum of the current efficiencies of these products usually attaining close to unity. Hence, these products are generally known to be typical for aqueous CO_2 reduction studies, the majority of which would focus their analysis and discussion within this set of products. Some works however have also reported the production of ethanol with appreciable efficiencies, e.g. about 10% current efficiency [32, 65], and other C_2 and C_3 oxygenates with low efficiencies (1% and less) that shares a similar potential dependency as C_2H_4 [32]. Interestingly, methanol and C_2H_6 are quite often not produced on Cu metal, leading to various mechanistic ideas that attempt to reconcile the absence of methanol and C_2H_6 with the occurrence of C_2H_4 and various C_2 and C_3 oxygenates. A short discussion on the reaction mechanism of CO_2 electro-reduction on Cu metal is presented in section 2.3.7.

2.3.2 Electrolyte parameters

Investigations into the electrochemical reduction of CO_2 have extensively explored a wide range of different electrolyte systems, which in general can be classified as either using aqueous or non-aqueous solvents. The type of solvent used, i.e. aqueous or non-aqueous, can profoundly influence the reaction mechanism and product distribution, to the point that CO_2 reduction in either type of electrolyte solvent should really be considered as different systems.

Non-aqueous solvents have been extensively investigated for CO_2 reduction mainly due to the much higher CO_2 solubility achievable in non-aqueous media than in water. Hence, mass transport limitations can be alleviated. In addition, using non-aqueous solvents can suppress the competing HER due to the limited presence of water. The lack of water also permits CO_2 reduction to be studied at temperatures below 0 °C. In relation to the study of reaction mechanisms, non-aqueous solvents are arguably preferred due to the ability to accurately regulate the concentration of water [22, 48]. Common examples of non-aqueous solvents investigated for CO_2 reduction are propylene carbonate, acetonitrile, dimethylformamide (DMF), dimethylsulfoxide (DMSO) and methanol. In these non-aqueous media, with the exception of methanol [84-89] given that methanol is a protic solvent, common CO_2 reduction products on various electrodes including Cu are CO, oxalic acid and formic acid [48]. Oxalic acid (or oxalate) is prevalent in non-aqueous electrolytes, and is due to the lack of water which promotes the dimerization of $CO_2^{\bullet-}$ to $(COO)_2^-$ over the formation of formate (Figure 2.1). Relatedly, CO is formed, not by reaction with water but through an oxygen-carbon coupling mechanism between $CO_2^{\bullet-}$ and CO_2, forming CO and CO_3^{2-} [90-92]. As expected, the product distribution is found to be highly sensitive to the presence of water, which when introduced to the non-aqueous electrolyte increased the production of formic acid over oxalic acid and CO [90, 93], and partly reduced oxalic acid to glycolic and glyoxylic acid [91]. In addition to the non-aqueous electrolytes mentioned above, ionic liquids, e.g. EMIM-BF_4, are also gaining significant attention [94, 95]. These electrolytes generally promote CO_2 reduction by lowering the energy of the $CO_2^{\bullet-}$ intermediate, likely by complexation [94]. One major challenge of utilising non-aqueous systems for CO_2 reduction is the cost, given that non-aqueous solvents are certainly more expensive than water itself; however, these solvents are not consumed during the reaction and hence are recyclable [25].

Aqueous-based electrolytes on the other hand are much cheaper, accessible and easy to prepare. Hence, despite the relatively poor CO_2 solubility, aqueous electrolytes are still widely used by many research groups. The most commonly used aqueous electrolyte is bicarbonate, specifically $KHCO_3$. It is interesting that the reason for this choice is never explicitly explained, other than the fact that it was regularly used by early researchers [23, 41, 50, 62, 64, 65] and is now followed by many others to this day. A more convincing reason would be the common use of caustic KOH as an absorbent for CO_2 in its capture and concentration [6, 20, 96, 97], after which the KOH ultimately becomes $KHCO_3$ through the $CO_2/HCO_3^-/CO_3^{2-}$ equilibria. Hence, performing CO_2 reduction directly on a CO_2 saturated $KHCO_3$ solution would seem logical for future CO_2 capture, concentration and reduction technologies. Because HCO_3^- and CO_3^{2-} species will certainly exist in CO_2 saturated aqueous solutions, another possible reason for using $KHCO_3$ is to simplify the electrolyte system by limiting any anionic effects to HCO_3^- and CO_3^{2-} species, since it is possible that additional anions such as halides [73, 98, 99], sulphides [100] and sulphates [101] can influence results by adsorption on the electrode surface.

Other types of electrolytes occasionally used are phosphate buffers, e.g. KH_2PO_4 + K_2HPO_4, halides, e.g. KCl, and sulphates, e.g. K_2SO_4. By comparison, these electrolytes have shown to give distinct product selectivities on Cu electrodes. At similar electrolyte concentrations (0.1 M) and reaction

conditions (−5 mA cm^{-2}, 19 °C), Hori et al. [43, 67] showed that in KCl and K_2SO_4, C_2H_4 and alcohols are much more selective than CH_4 (C_2H_4/CH_4 ratio of 4.2 and 3.7 respectively), while H_2 production is significantly suppressed (Table 2.2). In $KHCO_3$, C_2H_4 and CH_4 are equally selective (ratio 1.02), but the selectivity to alcohols is significantly lower. In phosphate buffer (0.1 M K_2HPO_4), CH_4 is much more selective than C_2H_4 (ratio 0.11), however H_2 is found to be predominant (72.4%). Notice as well that the electrode potential required for the specified current is about 200 mV more positive in 0.1 M K_2HPO_4. These observations in the phosphate buffer are further accentuated when a higher concentration (0.5 M K_2HPO_4) is used. Aside from possible anion interactions with the Cu surface, e.g. anion adsorption, the differences in reaction selectivities presented in Table 2.2 are largely attributed to the indirect influence of the electrolyte's buffer capacity, which is also dictated by the type of anion and its concentration.

Table 2.2: Current efficiencies of CO_2 reduction products on a Cu electrode in various solutions at −5 mA cm^{-2}. Data obtained from Hori et al. [67].

Electrolyte	Conc. / M	pH	Potential V vs SHE	Current efficiency (%)							
				CH_4	C_2H_4	alcohols	CO	$HCOO^-$	H_2	Total	C_2H_4/ CH_4
$KHCO_3$	0.1	6.8	−1.41	29.4	30.1	9.9	2.0	9.7	10.9	92.0	1.02
KCl	0.1	5.9	−1.44	11.5	47.8	25.5	2.5	6.6	5.9	99.8	4.16
K_2SO_4	0.1	5.8	−1.40	12.3	46.0	22.2	2.1	8.1	8.7	99.4	3.74
K_2HPO_4	0.1	6.5	−1.23	17.0	1.8	0.7	1.3	5.3	72.4	98.5	0.11
	0.5	7.0	−1.17	6.6	1.0	0.6	1.0	4.2	83.3	96.7	0.15

Because the reduction reactions (both CO_2 reduction and H_2 evolution) in aqueous solutions produce OH^- (or consumes H^+), the interfacial pH at the electrode surface will almost always be higher than the bulk solution pH due to concentration gradients developing over time. Although dissolved CO_2 reacts with OH^- to form HCO_3^-, this reaction is relatively slow (rate constant, $k = 7.7 \times 10^3$ M^{-1} s^{-1} [33]), therefore the interfacial pH is usually considered to not be in equilibrium. In electrolytes with buffering abilities such as phosphate buffers and $KHCO_3$, the rise in interfacial pH is thought to be less extreme compared to those without, such as KCl and K_2SO_4. Between phosphate buffers and $KHCO_3$ at similar concentrations, phosphate buffers generally have a stronger buffer capacity compared to $KHCO_3$ at the neutral pH range where most CO_2 reduction work is performed since the pK_a of $H_2PO_4^-$ (pK_a 7.21) is closer to 7 than the pK_a of HCO_3^- (pK_a 10.33) [102]. Hence, it can be shown (by numerical modelling for example [44]) that the interfacial pH at the electrode surface is highest in non-buffering electrolytes (0.1 M KCl and 0.1 M K_2SO_4), followed by 0.1 M $KHCO_3$, and 0.1 M phosphate buffers at similar reaction conditions. Since the buffer capacity increases with concentration, the interfacial pH in the more concentrated 0.5 M phosphate buffer would be the lowest. As the reaction selectivity is strongly influenced by pH, where a lower pH would generally increase the selectivity towards H_2 and CH_4 due to a higher availability of H^+/H_{ads} [74, 103, 104] and also the pH-dependence of the CH_4 formation pathway [83], the observed differences in reaction selectivity between the various electrolytes can largely be explained by the rise in interfacial pH dictated by the electrolytes' buffer capacities, which is a function of the anion and its concentration. Interestingly, the effects of the rise in interfacial pH during CO_2 reduction are frequently overlooked by many researchers. Since the reaction selectivity is strongly sensitive to pH, this may have occasionally led to erroneous analysis whereby observed changes in reaction selectivities have been incorrectly attributed to other factors under investigation. Although the importance of the interfacial pH during CO_2 reduction had already been highlighted by Hori's various papers and reviews [22, 48, 67], it is only recently that the effects of interfacial pH are being re-emphasised again by a number of works [74, 104-107].

Although the majority of works have chosen K^+ based salts as the electrolyte, the choice of the cation has also been demonstrated to greatly influence the product selectivity of CO_2 reduction on Cu electrodes [108, 109]. In Table 2.3, the selectivity to C_2H_4 and alcohols generally increases while that to H_2 and CH_4 decreases with cation size (the cation size increases from $Li^+ < Na^+ < K^+ < Cs^+$ [102]). The influence of the cation is also clearly shown by the increasing C_2H_4/CH_4 ratio and electrode potential (toward more positive potentials) with cation size at similar current densities.

Table 2.3: Current efficiencies of CO_2 reduction products on a Cu electrode in various 0.1 M bicarbonate solutions of different cationic species at −5 mA cm^{-2}. Data obtained from Hori et al. [108].

Electrolyte	Potential / V vs SHE	Current efficiency (%)								
		CH_4	C_2H_4	alcohols	CO	$HCOO^-$	H_2	Total CO_2 red.	Total	C_2H_4/CH_4
$LiHCO_3$	−1.45	32.2	5.2	1.6	*tr.*	4.7	60.5	43.7	104.2	0.16
$NaHCO_3$	−1.45	55.1	12.9	4.8	1.0	7.0	25.1	80.8	105.9	0.23
$KHCO_3$	−1.39	32.0	30.3	12.5	0.5	8.3	14.5	83.6	98.1	0.95
$CsHCO_3$	−1.38	16.3	30.5	11.6	2.4	15.8	24.4	76.6	101.0	1.87

In general, the observed effects of the cations are thought to be derived from the propensity of the cations for specific adsorption on the electrode surface, which is largely dictated by their hydration powers. In this case, Li^+ being the smallest cation amongst the four is more easily hydrated compared to Cs^+, which is the largest [110]. Because small cations are easily hydrated, the surrounding water molecules prevent them from being specifically adsorbed on the electrode surface. Larger cations on the other hand have a higher propensity to be adsorbed due to their lower hydration powers [108]. The adsorption of larger cations is thought to cause the potential at the outer Helmholtz plane (OHP) to become more positive, which decreases the concentration of H^+ at the OHP [108]. Specifically adsorbed cations, being positive in charge, would also repel H^+ away from the cathode surface. Hence, due to the reduced supply of H^+/H_{ads} at the electrode surface when larger cations are specifically adsorbed, the selectivity to H_2 and CH_4 will decrease as expected. In contrast, smaller cations which do not adsorb on the electrode surface do not impede the supply of H^+/H_{ads}. In fact, the water molecules surrounding smaller cations may actually increase the supply of H^+ to the electrode surface. This could explain the high selectivity to H_2 in $LiHCO_3$ compared to the other bicarbonate electrolytes (Table 2.3). The specific adsorption of cations is also thought to stabilise anions through ion-pairing on the electrode surface [111]. In the case of CO_2 reduction, adsorbed cations could stabilise the $CO_2^{\bullet-}$ anion intermediate, thereby facilitating improved CO_2 reduction rates and efficiencies [112]. This is supported by the increasing total current efficiency toward CO_2 reduction, which is coupled with the decreasing overpotentials at similar current densities (−5 mA cm^{-2}) with cation size from Li^+ to K^+ (Table 2.3). The supposed enhancements in overall CO_2 reduction with increasing cation size however is not strong between K^+ and Cs^+, in fact it seems that the presence of Cs^+ decreased the overall selectivity toward CO_2 reduction. This observation is consistent with that of Kyriacou and Anagnostopoulos [109], who suggested that the greater adsorption propensity of Cs^+ may have reduced available reaction sites for CO_2 reduction and hence the overall CO_2 reduction activity. Similar effects of cations have also been observed during CO_2 reduction on Hg [113, 114], and more recently on Ag electrodes [112].

Based on these observations, it is possible to reason out why K^+ based salts, in particular $KHCO_3$, are commonly employed as electrolytes for aqueous CO_2 reduction on Cu electrodes.

2.3.3 *pH and CO_2 concentration*

Not surprisingly, the pH is an important parameter in the electrochemical reduction of CO_2 since H^+/H_{ads} are required reactants for CO_2 reduction to hydrocarbons (Table 1.1). Because the reduction of CO_2 on Cu electrodes produces a wide range of products, various reaction pathways leading to these products exist within the overall reaction mechanism. Some of these pathways are strongly dependent on the pH, especially when the local RDS of a particular pathway involves H^+/H_{ads}.

As revealed in section 2.3.2 (regarding the effects of the rise in interfacial pH), the most common effect of the pH is seen in the change in reaction selectivity from H_2 and CH_4 to C_2H_4 and alcohols with increasing pH. While the enhancement of the HER at lower pH can be adequately explained by the increase in H^+/H_{ads} available at the electrode surface, the preference for CH_4 at lower pH and that for C_2H_4 and alcohols at higher pH is not as straightforward, since the formation of each of these products must involve a number of hydrogenation steps along its pathway. The strong correlation between the change in selectivity from CH_4 to C_2H_4 and the increase in pH was first documented in Hori's various works [22, 43, 48, 67, 77]. It was found that the formation rate of CH_4 is dependent on both the electrode potential and pH, while that for C_2H_4 and ethanol depended only on the electrode potential [115]. Another observation made but not given much attention at the time of discovery is that the onset potential of C_2H_4 formation is always consistently more positive than that of CH_4 [65, 67, 77]. In addition, it was also shown that the Tafel slope or transfer coefficient for the formation of CH_4 is usually different to that for C_2H_4 [23, 45, 115].

To explain these observations, it was generally speculated that the formation of C_2H_4 must follow a separate pathway to the formation of CH_4, and that the C_2H_4 pathway is independent of pH, while the CH_4 pathway is pH dependent, i.e. involves H^+, in or before the local RDS [115]. These conjectures were recently investigated with more rigour by Koper's group using online electrochemical mass spectrometry (OLEMS)* [83, 103]. In short, by combining important results by Hori et al. with their own analysis, they have strongly suggested that the local RDS on the C_2H_4 pathway is the formation of a CO dimer from two CO molecules where the electron transfer is uncoupled from H^+ transfer (hence pH independent), and that the local RDS on the CH_4 pathway is the breaking of the C−O bond in the formyl intermediate, CHO_{ads}, which involves concerted proton-electron transfers (hence pH dependent). Another interesting observation made by Koper's group that is not presently explained by their proposed reaction mechanism is that at very high pH (pH 13), the formation of both H_2 and CH_4 unexpectedly shifted to lower overpotentials [103, 118]. Additionally, they observed that the shifts in overpotentials for H_2 and CH_4 formation seem to mirror each other with changes in pH, suggesting some form of relationship between them that is currently unexplained. The decrease in overpotentials for H_2 formation at very high pH can generally be explained by a shift in the mechanism from proton discharge (which is pH dependent) to water discharge (which is pH independent), and this shift is suggested to occur around pH 11−12 [47, 119]. Hence, it may also be possible that a similar shift in the CH_4 formation mechanism occurs at very high pH.

Due to the relatively low CO_2 solubility in aqueous solutions, the CO_2 reduction rate is usually limited by the diffusion of CO_2 to the electrode surface at high current densities. To overcome mass transport

* Unlike long-term electrolysis at a specified potential or current density, the tip-based sampling technique of OLEMS allows the online detection of volatile reaction intermediates and products through mass spectrometry as they are being formed when the electrode potential is varied [116]. This is advantageous for CO reduction studies, where gaseous products are difficult to measure using conventional chromatography techniques due to the low CO reduction currents caused by the poor solubility of CO (1/40 of that of CO_2 [117]). A disadvantage of this technique is that a faradaic balance cannot be calculated since the detection of products is measured as ion currents, which are usually normalized for comparison between measurements.

limitations, the concentration of CO_2 in aqueous electrolytes can be increased by lowering the temperature or by increasing the pressure of CO_2. The solubility of CO_2 in water improves with decreasing temperatures; hence, several researchers have performed CO_2 reduction at low temperatures* down to −4 °C [23, 42, 50, 51, 120, 121]. In general, lowering the operating temperature has shown to improve the overall current efficiencies of CO_2 reduction on various metal

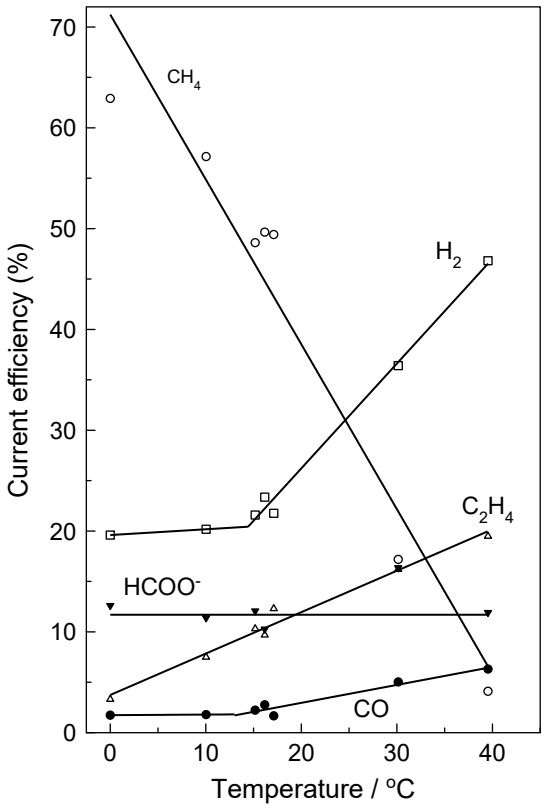

Figure 2.4: Temperature dependence of the current efficiencies of CO_2 reduction products on Cu as reported by Hori et al [42]. Experiments were conducted at −5 mA cm^{-2} and in 0.5 M $KHCO_3$. The electrode potential ranged from −1.39 V vs SHE at 0 °C to −1.33 V vs SHE at 40 °C. Lines are to guide the eye.

electrodes. Even on metals such as Ni and Ti that predominantly produce H_2 at room temperatures, CO, CH_4 and HCOOH were found to be produced at 0−2 °C with appreciable efficiencies [50, 51]. The overall improvement in CO_2 reduction selectivity with decreasing temperatures is generally attributed to the higher CO_2 concentrations available at lower temperatures. On Cu electrodes, Hori et al. [42] have shown that the current efficiency of CH_4 improves remarkably with decreasing temperatures, while that of H_2, C_2H_4 and CO decreases (Figure 2.4). The current efficiency of $HCOO^-$ on the other hand was not sensitive to temperature. The increase and decrease in CH_4 and H_2 selectivity respectively with decreasing temperature is consistent with the findings of other workers [23, 51, 120]. Despite the overall CO_2 reduction selectivity improving with decreasing temperatures, it was found by Kaneco et al. [120] that the partial current density toward CO_2 reduction actually remained steady between −4 and 15 °C at a constant potential of −2.0 V vs Ag|AgCl (sat. KCl). The partial current density toward H_2 production on the contrary clearly decreased with decreasing temperatures. Likewise, Kim et al. [23] observed that the CH_4 formation rate at 0 °C is about half of

* The concentration of CO_2 in water at 1 atm CO_2 pressure is 0.034 M at 25 °C, which almost doubles to 0.078 M at 0 °C [75]. The freezing temperatures of the electrolyte solutions are lower than 0 °C due to the presence of dissolved salts.

that at 22 °C, but the current efficiencies are twice larger at 0 °C. Hence, the improved selectivity toward CO_2 reduction is not due to an enhancement in CO_2 reduction rates, but most likely due to a suppression of the HER at low temperatures. The HER suppression is probably caused by an increase in surface coverage of CO_{ads}, which is known to inhibit the HER by blocking active reaction sites [80, 122, 123], due to the higher concentration of CO_2 at low temperatures. The inhibition of HER at low temperatures is consistent with the decrease in electrode potential from −1.33 V vs SHE at 40 °C to −1.39 V vs SHE at 0 °C at the same current density of −5 mA cm^{-2} (Figure 2.4). The increase in overpotentials with decreasing temperatures could also be due to the need for thermal activation for certain CO_2 reduction reactions, as it had been suggested for Ni electrodes [121].

The concentration of CO_2 in aqueous electrolytes can also be increased by raising the CO_2 pressure in accordance to Henry's law [75]. In the laboratory, high pressures (often less than 100 atm) for CO_2 reduction are usually achieved by using high pressure autoclaves [25]. By comparison, high pressure CO_2 reduction has been demonstrated to produce some of the highest current densities for CO_2 reduction; for example, 523 mA cm^{-2} at 30 atm on Cu wire electrodes [124]. Even higher current densities for CO_2 reduction can be obtained when gas diffusion electrodes (GDE) are used alongside elevated pressures, as has been shown for Ag-GDE (3.05 A cm^{-2} at 30 atm) [125]. In general, increasing the CO_2 pressure has consistently been shown to increase the CO_2 reduction current efficiency and reaction rates for various electrodes, the reason for which is unanimously explained by the higher CO_2 concentration and therefore increased CO_2 mass transport rates to the electrode surface [60, 104, 121, 124, 126-128]. In a relatable manner to CO_2 reduction at low temperatures, metal electrodes that do not readily reduce CO_2 at ambient pressures have also been shown to reduce CO_2 with moderate efficiencies [60, 121, 128]. In addition to the improvement in overall CO_2 reduction rates and efficiency, it was found that the product distribution between various CO_2 reduction products can also vary with CO_2 pressure. On Cu electrodes, Hara et al. [124] have shown that the main reduction products changed from H_2 to hydrocarbons (CH_4, C_2H_4, C_2H_6 and ethanol) and then to HCOOH and CO as the CO_2 pressure increased from 1 to 60 atm at a constant current density of 163 mA cm^{-2}. For all measurements, the electrode potential did not vary significantly between them (−1.60 V vs Ag|AgCl (sat. KCl)), hence the observed change in product selectivity cannot be an effect of a change in electrode potential. Instead, because it is clear that the total CO_2 reduction current efficiency increased while that for H_2 decreased with increasing CO_2 pressure, the authors suggested that the change in product selectivity is related to the suppression of the HER by the enhancement of CO_2 reduction, which increased the surface coverage of CO_{ads}. With the increase in CO_{ads} coverage and suppression of HER, the surface coverage of H_{ads} decreases. Because the production of hydrocarbons requires H^+/H_{ads}, a decrease in available H_{ads} will limit reduction of CO_2 to CO and HCOOH only despite the higher CO_2 concentration at increased CO_2 pressures. Kas et al. [104] have also observed a change in product selectivity with increasing CO_2 pressure in CO_2 reduction on Cu nanoparticles. From 1 to 9 atm at −1.8 V vs Ag|AgCl (3 M KCl), they observed a change in selectivity from CH_4 to C_2H_4, while CO production gradually increased. Similarly, the authors attributed the change in selectivity to an increase in CO_{ads} coverage, which promoted the production of C_2H_4 over CH_4 by increasing the rate of C−C coupling between CO_{ads}. The suggestion that the CO_{ads} coverage increased with CO_2 pressure was validated by an observed increase in CO production with CO_2 pressure at −1.1 V vs Ag|AgCl (3 M KCl), where the current efficiency for CO significantly increased from 20% to 70% at 1 and 9 atm respectively. Since high conversion rates are important for any practical CO_2 reduction reactors, it is quite feasible that high pressure systems will be used for industrial electrochemical CO_2 reduction applications in the future.

2.3.4 *Electrode crystalline structure*

The relationship between the electrode surface structure and the electrochemical activity is fundamentally important in understanding the reaction mechanism of an electrochemical process. The structural sensitivity of CO_2 reduction on Cu electrodes was first reported by Frese [45] who observed that the CH_4 formation rate is highest on the (111)* surface, followed by (110) and (100), after performing CO_2 reduction on Cu single crystal electrodes in 0.5 M $KHCO_3$ at various potentials. The preference for CH_4 on (111) surfaces is explained in terms of the relative binding strength of CO, where CO is most weakly bound on (111) compared to (110) and (100); hence, the lower binding energy of CO promotes favourable thermodynamics and activation energy in the RDS, which was presumed to be the electrochemical splitting of CO_{ads}.

The investigation into the effects of crystal orientations of Cu was further pursued by Hori's group [82, 129-131]. Their studies essentially focussed on the (111), (110) and (100) basal planes with the introduction of steps of varying densities. The different Cu single crystal orientations investigated by Hori are [n(100) × (111)], [n(100) × (110)], [n(111) × (100)], [n(111) × (111)] and [n(110) × (100)]†, and CO_2 reduction was performed on these electrodes in 0.1 M $KHCO_3$ at −5 mA cm^{-2}. In summary, Hori's results showed that CH_4 is predominantly formed over C_2H_4 on (111) surfaces, which is consistent with the findings by Frese [45] and recent results by Christophe et al. [132]. In addition to that, C_2H_4 is found to be favoured over CH_4 on (100) surfaces. The preference for C_2H_4 over CH_4 on (100) surfaces is further amplified by the introduction of either (111) or (100) steps into the (100) basal plane up to n = 6 to 4. As the selectivity of C_2H_4 improved with the introduction of steps, the formation of other C_{2+} products, i.e. ethanol, allyl alcohol, *n*-propanol, acetaldehyde and propionaldehyde, also generally improved. However, a further increase in the step density for n less than 4 reversed the C_2H_4 over CH_4 selectivity, where CH_4 becomes more selective than C_2H_4 at n = 2. The electrode potential generally did not vary much and remained within −1.3 to −1.4 V vs SHE with the introduction of steps, although the data does suggest that the electrode potential becomes slightly less negative as the C_2H_4 selectivity increases. It is clear however that the electrode potential is significantly lower on the (100) surface, i.e. −1.39 V vs SHE, compared to (111), i.e. −1.52 V vs SHE, for the specified current density of −5 mA cm^{-2}. Another interesting observation by Hori's group is the increased formation of acetaldehyde, ethanol and acetic acid (total C_{2+} current efficiency of 66%) at the expense of CH_4 (6.9%) on (110) surfaces, which is the crystal orientation obtained by introducing (111) steps at n = 2 into the (111) basal plane, i.e. [2(111) × (111)]. The high selectivity toward C_{2+} products over CH_4 on (110) surfaces is reversed with the introduction of (100) steps into the (110) basal plane.

Some of the major findings by Hori's group, specifically on the apparent selectivity for C_2H_4 on (100) surfaces, were further expounded by Koper's group through the OLEMS technique [103, 118, 133]. By studying both CO_2 and CO reduction‡ on (100) and (111) surfaces at various solution pH, they uncovered strong evidence that C_2H_4 is formed on (100) at relatively low overpotentials, and that this unique pathway to C_2H_4 on (100) is independent of the solution pH. C_2H_4 was also formed on (111) surfaces; however the onset potentials in this case are more negative and comparable to that for CH_4 formation, and are shown to be dependent on the solution pH. Hence, based on their observations, the

* The lattice structure of Cu is face-centred-cubic (FCC).

† [n(110) × (100)] means that the electrode surface consist of n atomic rows of (110) terrace and one atomic height of (100) step.

‡ Performing CO reduction instead of CO_2 reduction allows the investigation into a wider range of pH values due to the absence of the $CO_2/HCO_3^-/CO_3^{2-}$ equilibria in aqueous systems [134]. Usually, the results from CO reduction studies can acceptably be made equivalent to that for CO_2 reduction since it has already been well established that CO is a major intermediate in the electrochemical reduction of CO_2 to hydrocarbons and oxygenates.

authors concluded that there must be two distinct pathways to C_2H_4: the first pathway, which is dependent on the pH, involves a common intermediate (the authors suggest that this is likely to be CHO_{ads}) with the formation of CH_4 and occurs at both (111) and (100) surfaces at high overpotentials; the second pathway, which is independent on the pH, occurs exclusively on (100) surfaces at lower overpotentials, presumably through the formation of an adsorbed CO dimer. The mechanism of the second pathway has recently been investigated by theoretical simulations using density functional theory (DFT) calculations, and the results provide overall support for the pathway's existence and exclusivity on the (100) surface [135-138].

Investigations into the structure-sensitivity of CO_2 reduction on Cu electrodes have demonstrated how the surface crystal orientation strongly influences the product selectivity. To some extent, this provides some explanation on why results between research groups can occasionally differ drastically. For example, in preparing electrodeposited Cu electrodes, Frese [45] suggested that the electrodeposition current density or overpotential influences the crystal orientation of the Cu electrodeposits. At low overpotentials, the (111) surface is favourable, followed by (100) and (110) with increasing overpotentials. Given that a large number of works prepared Cu electrodes through electrodeposition, the parameters of which could vary significantly between research groups, it is not surprising if the large variation in results are due to a structural effect of the electrodeposited Cu. High purity polycrystalline Cu electrodes are also commonly used and the various types of pre-treatment procedures between research groups could result in an electrode surface that may not be comparable in terms of the surface structure. Hori's group [131] has documented the difficulty of obtaining reproducible results on the (110) surface, which they attributed to problems relating to surface pre-treatment steps, i.e. electropolishing, ultra-sonication and rinsing solutions, that could inadvertently change the structure and crystal orientation of the surface. Another important observation recently made by Kim et al. [139-141] regarding the use of polycrystalline Cu is that the electrode surface can undergo slow surface reconstruction under cathodic conditions normally applied for CO_2 reduction. Using electrochemical scanning tunnelling microscopy, it was observed that a polycrystalline Cu electrode held at −0.9 V vs SHE in 0.1 M KOH underwent stepwise surface reconstruction from polycrystalline to (111) within 30 min, and then to (100) after a further 30 min [140]. On the (100) surface, it has also been reported that a hydrogen-induced reconstruction of the surface, forming (011) oriented stripe-like structures occurs in acidic media, and that the reconstructed surface showed a concomitant increase in the HER rate [142]. Given the strong influence the crystal orientation has on the product selectivity of CO_2 reduction, such structural changes during the reaction need to be carefully considered and appropriately attributed.

2.3.5 Deactivation of CO_2 reduction

A recurring issue reported by many workers on the electrochemical reduction of CO_2 is the deactivation of the CO_2 reduction reaction, where the overall CO_2 reduction rate and selectivity declines with time in favour of the HER. This loss in CO_2 reduction activity is not unique to Cu electrodes, and has also been observed for other widely studied metal electrodes such as Au [143] and Ag [144, 145]. The time-scale over which the deactivation occurs varies significantly between reports, from as short as 10 mins [66, 146] to a gradual deactivation over several hours [104, 147]. The fact that the activity loss takes place over such a varied time-scale suggests that the deactivation process can occur through a number of ways, although much of the mechanism for this loss in activity remains debatable and poorly understood.

One possible explanation for the observed decrease in CO_2 reduction activity and coincidental increase in H_2 evolution on polycrystalline Cu electrodes is the restructuring of crystal orientation to

the (100) and (011) surfaces, which have been demonstrated to be active surfaces for the HER [142, 148]. Although transient changes in surface structure could partly explain the promotion of the HER, the observed deactivation in CO_2 reduction activity is often quite severe and too swift to be attributed to structural effects. Hence, it is commonly proposed that the electrode surface is poisoned during the reaction, either by the accumulation of CO_2 reduction products and intermediates, which is essentially inevitable, or by the electrodeposition of trace metallic impurities present in the electrolyte solution, which can generally be prevented by pre-treating the electrolyte. Electrode poisoning could also be caused by the deposition of organic impurities from the water or CO_2 gas used [83, 149] or by a cathodically formed oxide/hydroxide species [150], although these poisoning species are less commonly reported.

The poisoning by accumulation of CO_2 reduction products and intermediates is strongly supported by many workers due to the frequently reported observation, by spectroscopy such as XPS [64, 151], AES [63, 64], Raman spectroscopy [152], and EDS [147, 153, 154], of graphitic and amorphous carbon on the electrode surface after electrolysis. It was presumed that carbon must have formed during CO_2 reduction both as a product and an intermediate species to hydrocarbons. In addition to carbon, which does not dissolve into the solution, some suggests that the poisoning species can also be a soluble CO_2 reduction intermediate which can be adsorbed on the electrode surface by equilibrium [155]. The poisoning by CO_2 reduction products and intermediates, especially carbon, is further supported by the observation that carbon electrodes are generally inert towards CO_2 reduction [51, 156-158].

The poisoning by electrodeposition of trace metallic impurities is strongly supported by Hori's group [149]. Based on their work, they suggested that Fe^{2+} and Zn^{2+} impurity ions present even in trace amounts in the electrolyte solution can drastically inhibit the CO_2 reduction activity in favour of H_2 evolution when electrodeposited under the cathodic conditions applied. The suggestion of Fe and Zn as the principal poisoning species was based on the equilibrium redox potential of the metals, which was deemed comparable to the potential of two anodic peaks observed in post-CO_2 reduction stripping cyclic voltammetry (CV) when underpotential deposition was taken into account. The poisoning capability of electrodeposited Fe and Zn was further demonstrated when the deactivation of CO_2 reduction was reproduced by the deliberate addition of small quantities (0.1 μM) of $FeSO_4$ and $ZnSO_4$ salts into a newly pre-treated electrolyte solution through pre-electrolysis, which they had shown to give prolonged CO_2 reduction activity when used. Because of the detrimental effect these metallic impurities have on CO_2 reduction activity, Hori has advocated strongly the importance of electrolyte purification by pre-electrolysis[*], an electrolyte pre-treatment step that has been adopted by many workers since. The case for the electrodeposition of metallic impurities as the principle mode of deactivation is further supported by Wuttig et al. [159] who recently provided, in addition to stripping CVs, spectroscopic (XPS) evidence of Zn and Pb on the Cu surface after CO_2 reduction. The occurrence of these electrodeposited metal impurities is found to be coincident with the loss of CO_2 reduction activity and selectivity in favour of H_2 evolution. However, in contrast to Hori, pre-electrolysis was found to be ineffective in their work, as is also found by several others [146, 160-162]. Instead, the metallic ions were found to be effectively removed by ion complexation either in-situ by the addition of ethylenediaminetetraacetic acid (EDTA) into the electrolyte solution or ex-situ by pre-treating the solution using solid-supported iminodiacetate resins (Chelex).

[*] Pre-electrolysis is performed by essentially scavenging the solution cathodically with a sacrificial electrode. In Hori's work [149], the electrolyte was pre-electrolysed using a Pt black cathode (20 mm × 30 mm) at −25 μA cm^{-2} for at least 16 hours under Ar atmosphere and mildly stirred conditions.

While the deactivation of CO_2 reduction can be reduced by electrolyte pre-treatment methods, several works have shown that the CO_2 reduction activity can also be revived or extended by performing periodic anodic pulses, steps or stripping CVs during electrolysis [149, 151, 153, 155, 160, 163]. It is believed that these anodic treatment steps oxidise and strip away adsorbed poisoning species from the electrode surface, thus reactivating the electrode for CO_2 reduction. However, by bringing the electrode into anodic conditions, the product selectivity can also change significantly due to structural alterations, e.g. by repetitive oxide formation and reduction [71, 143, 160, 164-166], and variation in surface coverages of adsorbed species such as CO_{ads} and H_{ads} [147, 167], depending on how anodic the potentials are during these treatments. Therefore, researchers need to be aware of these changes when attempting to prolong CO_2 reduction activity through periodic anodic treatments.

Although the principal mode of the deactivation of CO_2 reduction activity remains strongly debated between researchers, it is important to remember that electrode poisoning can occur through a variety of ways and that the dominant poisoning mechanism in one system may not always be similar to that in another system.

2.3.6 Mass transfer effects

While the reaction selectivity of CO_2 reduction is primarily a function of the electrocatalysts' intrinsic properties, process conditions such as temperature, CO_2 pressure and electrolyte concentration also exert significant influence on the reaction selectivity of CO_2 reduction on Cu electrodes, as per discussions in the preceding sections. Therefore, it has been emphasised that differences in reaction selectivity cannot always be exclusively attributed to differences in intrinsic catalytic behaviour [49, 104, 107], and researchers need to carefully consider and appropriately attribute the contribution of process conditions to their results.

In addition to the above-mentioned factors, another interesting observation is that the selectivity can also change by simply agitating the electrolyte [23, 124, 168]. Clearly, stirring or agitating the electrolyte improves mass transfer to and from the electrode surface due to a decrease in the diffusion layer thickness. Hence, in relation to the local pH and CO_2 concentration, a higher stirring rate shifts the interfacial pH closer to that in the bulk, and increases the flux of dissolved CO_2 to the electrode [44]. Due to the sensitivity of CO_2 reduction on pH and CO_2 concentration as discussed in section 2.3.3, it is not surprising that mass transfer effects can greatly influence the reaction selectivity. Indeed, it has been observed that an increased selectivity for CO production is usually seen when the electrolyte is stirred, compared to one that is stagnant [23, 124].

It is well known that adsorbed CO is a major intermediate for CO_2 reduction [24, 54, 64, 81], and uniquely for Cu electrodes, CO is adsorbed with moderate strength [53, 54, 76] which in accordance to the Sabatier principle, facilitates its further reduction to hydrocarbons. The fact that CO binds neither too strongly nor too weakly on Cu suggests that the surface coverage of CO exists in equilibrium with dissolved CO in the diffusion layer [54]. This explains the observation of early potentiometric [80] and voltammetry [67] experiments, where CO was suggested to desorb easily when the electrolyte was stirred or purged with an inert gas to remove dissolved CO. Hence, in addition to local pH and CO_2 concentration, a significant change in CO surface coverage can also be caused by stirring the electrolyte due to mass transfer of dissolved CO away from the vicinity of the electrode surface. With decreased CO surface coverage, hydrocarbon production will decrease, explaining the observed enhanced selectivity towards CO for stirred electrolytes.

The sensitivity of the reaction selectivity on electrolyte stirring poses a challenge in comparing results in the literature as the hydrodynamics will undoubtedly vary between different cell configurations and

research groups. Therefore, it was suggested that the level of stirring be quantified [44] so that the effects of mass transfer on CO_2 reduction can be determined. Unfortunately, reports on this subject in the literature are very limited; therefore, chapter 7 of this thesis presents work that extensively investigates the effects of mass transfer on CO_2 reduction using a Cu rotating cylinder electrode.

2.3.7 Reaction mechanism

The reaction mechanism by which CO_2 is reduced on Cu electrodes is an area of intense debate. Despite extensive research, both experimental and theoretical, many aspects of the mechanism still remain largely uncertain. This is understandable as proposing a conclusive mechanism that accounts for every observed product of CO_2 reduction is challenging. The high complexity of the reaction was demonstrated recently by Kuhl et al., who reported 16 different reduction products on Cu, 11 of which are C_2 and C_3 oxygenates [32]. Nevertheless, a number of detailed mechanistic pathways have been proposed for the formation of notable CO_2 reduction products, specifically $HCOO^-$, CO, CH_4 and C_2H_4. The formation pathways of the many other products observed by Kuhl et al. remain largely unexplored, though it is worth emphasising that they occurred in very small quantities and were only detectable by NMR spectroscopy [32].

As discussed in section 2.2, the formation of CO or $HCOO^-$ largely depends on the adsorption and coordination of the $CO_2^{\bullet-}$ radical on the electrode surface (Figure 2.1). Briefly, $HCOO^-$ is suggested to form when the $CO_2^{\bullet-}$ radical is not readily adsorbed or weakly adsorbed through O-coordination. Due to the C atom being nucleophilic in this manner, proton transfer to the C atom is promoted. This is followed by an electron transfer leading to $HCOO^-$ formation. On the other hand, CO is said to form when the $CO_2^{\bullet-}$ radical is adsorbed through C-coordination, which stabilises the $CO_2^{\bullet-}$ radical and promotes protonation at one of the O atoms to form the carboxyl intermediate ($COOH_{ads}$). This intermediate is subsequently reduced through de-hydroxylation to CO_{ads}, which can either be desorbed as gaseous CO, or further reduced to hydrocarbons or oxygenates. Electrochemical reduction of formate or formic acid has shown that $HCOO^-$ cannot be reduced to other products, and therefore is considered to be a "dead-end" product [67, 78]. CO, on the other hand, is widely accepted as the major precursor or intermediate through which hydrocarbons and oxygenates are formed.

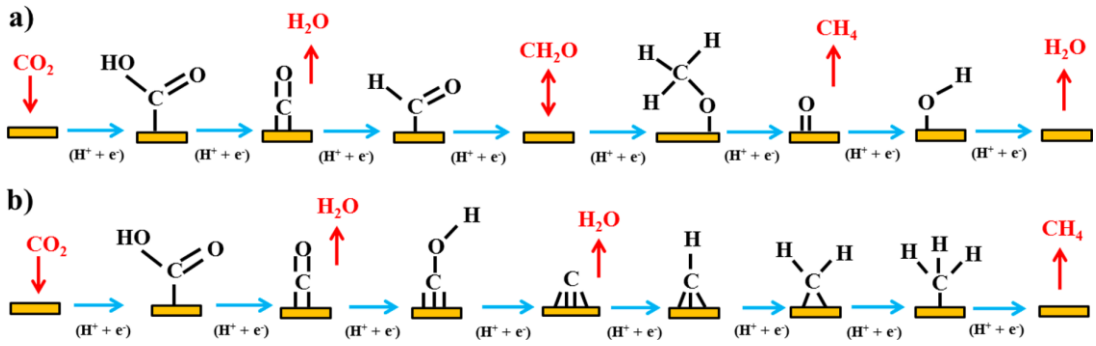

Figure 2.5: Reaction mechanism for the reduction of CO_2 to CH_4 proposed by (a) Peterson et al. [24] based on a thermodynamic DFT analysis, and by (b) Nie et al. [169, 170] based on a combined thermodynamic and kinetic DFT analysis. The two mechanisms differ from CO_{ads} onwards, where the mechanism by Peterson et al. suggests the formation of (a) CHO_{ads}, while the mechanism by Nie et al. suggests the formation of (b) COH_{ads}. Reprinted with permission from [49]. Copyright 2015 American Chemical Society.

Generally, early mechanistic studies have considered surface carbene ($CH_{2,ads}$), formed from the reduction of CO_{ads}, to be the key intermediate toward the formation of both CH_4 and C_2H_4 [64, 66, 67,

115, 155]. From $CH_{2,ads}$, CH_4 is formed through two proton-electron transfers, while C_2H_4 is formed through dimerization of two $CH_{2,ads}$ species. Hori et al. [115] have also suggested an alternative pathway, where a CO-insertion type mechanism to $CH_{2,ads}$ forms CH_2-CO_{ads}, which is then reduced to C_2H_4 and alcohols. However, the first theoretical DFT study of CO_2 reduction on Cu electrodes, conducted by Peterson et al. [24], disclosed a mechanism that is in contrast to these early works. Using a computational hydrogen electrode (CHE) model, the most thermodynamically favoured pathway to CH_4 on a (211) surface was elucidated. Based on their simulations, CO_{ads} is first reduced to the formyl intermediate (CHO_{ads}), after which subsequent proton-electron transfer steps to the C-atom leads to CH_2O_{ads}, CH_3O_{ads} (methoxy) and finally CH_4, leaving the leftover O_{ads} to be reduced to H_2O (Figure 2.5a). The proposal for the formation of methoxy in the reaction pathway to CH_4 raises an important question as to why methanol is very seldom observed in the electrochemical reduction of CO_2 on Cu electrodes, since in gas-phase methanol synthesis, Cu-based catalysts ($Cu/ZnO/Al_2O_3$) are also used, and methanol is also suggested to form through the methoxy intermediate [10, 171]. Peterson et al. explained this by stating the fact that the electrochemical proton transfer step to the methoxy intermediate to form CH_4 is not possible in gas-phase synthesis. In electrochemistry, H^+ in the electrolyte solution are available to react with the methyl (CH_3) end of methoxy to form CH_4, and thermodynamically, this was shown to be more favourable than the proton transfer to the oxygen end, which gives methanol. In gas phase reactions, the hydrogen source will most likely come from co-adsorbed H_{ads}, which would have easier access to the oxygen end of methoxy, hence promoting methanol formation. However, the suggestion that CH_4 forms through methoxy contradicts experimental observations by Schouten et al. [83] on the electrochemical reduction of formaldehyde (CH_2O) and methoxide[*] (CH_3O^-) on Cu. They observed that the reduction of formaldehyde essentially produced methanol and very little CH_4, while no reduction activity was observed for the reduction of methoxide. Hence, instead of the successive hydrogenation of CHO_{ads} without breaking the C−O bond, i.e. forming the methoxy intermediate, the authors suggested that the C−O bond in the CHO_{ads} intermediate must be broken early to form carbene ($CH_{2,ads}$), which is then reduced to CH_4. Nevertheless, Peterson argued that the reduction of formaldehyde could have increased the concentration of OH_{ads} spectator species, which can shift the thermodynamically favoured product from CH_4 to methanol due to a weakening of the oxygen binding strength of methoxy to the Cu surface, as determined by their DFT simulations of CO_2 reduction on Cu surfaces with oxygen-based species [172]. However, no arguments were presented for the lack of reduction activity of methoxide.

An alternative reaction mechanism for the reduction of CO to CH_4 which is generally more consistent with various experimental observations is one that is suggested by Nie et al. [169, 170]. By including kinetic barriers of elementary steps in their DFT analysis on (111) surfaces, they proposed that the reduction of CO to CH_4 should occur through the hydroxymethylidyne (COH_{ads}) intermediate, and not CHO_{ads} (Figure 2.5b). The formation of COH_{ads} from CO_{ads} was also suggested by Hori et al. [115]. From COH_{ads}, the C−O bond is broken to form surface carbon, onto which subsequent proton-electron transfer steps lead to the formation of surface carbene ($CH_{2,ads}$), which will then be reduced to CH_4 through further proton-electron transfers, and C_2H_4 through non-electrochemical dimerization. Determination of kinetic barriers in their analysis also revealed that the CHO_{ads} pathway will solely form methanol rather than methane due to highly prohibitive kinetics toward CH_4 formation (selectivity ratio of 6×10^{17} for methanol over CH_4). Hence, it appears that the reaction pathway through COH_{ads} is consistent with experimental observations that CH_4 is always preferred over methanol from CO_2 (or CO) reduction, and that methanol (not CH_4) is predominantly produced from formaldehyde reduction on Cu. In addition, the COH_{ads} pathway is also consistent with the widely

[*] Methanol (CH_3OH) is deprotonated to methoxide (CH_3O^-) in a solution of high pH.

reported deactivation of CO_2 reduction activity by graphitic carbon, which has been observed after CO_2 reduction through various surface-sensitive techniques as discussed in section 2.3.5. Furthermore, the formation of surface carbon as a poisoning intermediate within the pathway to CH_4 is consistent with the observation by Kas et al. [104] who reported significant deactivation when CH_4, and not C_2H_4, is the dominant product.

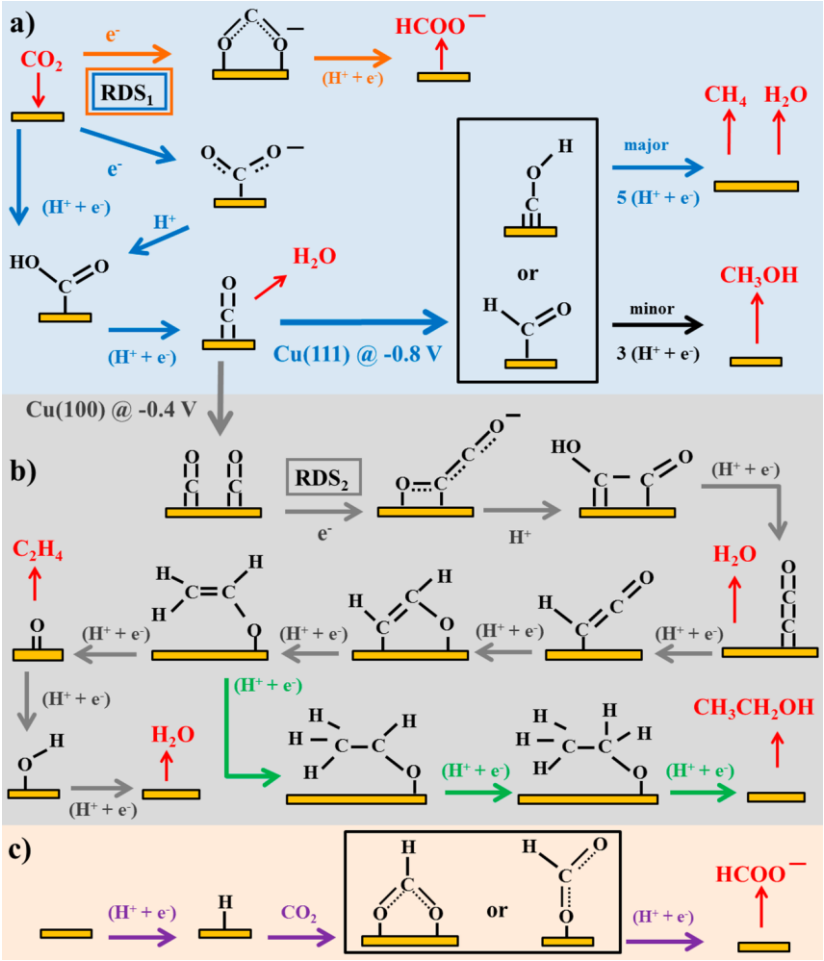

Figure 2.6: Possible reaction pathways suggested by Koper's group [49] for the reduction of CO_2 to (a) $HCOO^-$, CO, CH_4 and methanol, along the C_1 pathway; (b) C_2H_4 and ethanol, along the C_2 pathway; and (c) $HCOO^-$, through a CO_2 insertion step into a metal−H bond. Potentials are reported against the RHE scale and RDS indicates rate-determining steps. Reprinted with permission from [49]. Copyright 2015 American Chemical Society.

While the reduction of CO_{ads} to either CHO_{ads} or COH_{ads} and their respective pathways that follow mainly describe the mechanism toward CH_4 formation, they do not expound on the formation of C_2H_4 very well, aside from the suggested dimerization of surface carbene ($CH_{2,ads}$) species, which presumably only occurs at much higher overpotentials. In fact, experimental observations have consistently shown that C_2H_4 is formed preferentially at lower overpotentials without any simultaneous formation of CH_4, and that the formation of C_2H_4 is independent of pH as opposed to CH_4, which showed a strong pH dependency (see sections 2.3.1 and 2.3.3). These observations were further discovered to be structure-sensitive and occur exclusively on the (100) surface of Cu, while on both (100) and (111) surfaces, CH_4 and C_2H_4 are formed simultaneously at high overpotentials (see section 2.3.4). Therefore, by taking into account these important experimental observations which suggests the existence of structure-sensitive and pH dependent pathways, Koper's group recently [49]

proposed a comprehensive mechanism, schematically illustrated in Figure 2.6, for the reduction of CO_2 on Cu electrodes. In this mechanism, an additional pathway to C_2H_4 (C_2 pathway) which occurs exclusively on the (100) surface through a CO dimerization step is introduced (Figure 2.6b). The CO dimerization step, which they suggest is the local RDS in this pathway, is mediated only by electron transfer, forming an adsorbed $C_2O_2^-$ intermediate. Proton transfer only occurs after the formation of $(C_2O_2^-)_{ads}$. This decoupling of proton-electron transfer, where only electron transfer occurs in the local RDS, explains the lack of pH dependence of C_2H_4 formation in this pathway. The formation of CH_4 (C_1 pathway, Figure 2.6a) essentially follows the pathways suggested in the preceding discussion (Figure 2.5), where the CO_{ads} intermediate is reduced to either CHO_{ads} or COH_{ads} and further on to CH_4 (or methanol). Although not illustrated in Figure 2.6, the authors also suggest that the formation of C_2H_4 can occur through dimerization of C_1 intermediates along the CH_4 pathway at higher current densities or overpotentials, and takes place on both (100) and (111) surfaces.

Despite the complexity of the reaction, investigation into the mechanism of CO_2 reduction is an important area of research and must be further pursued in order to design more efficient and selective electrocatalysts for CO_2 reduction.

2.4 CO_2 reduction on Cu-derived electrodes

Cu metal, although unique in comparison to other metals in terms of its CO_2 reduction ability, i.e. able to reduce CO_2 to more than just CO and $HCOO^-$, does so inefficiently (with high overpotentials) and with poor selectivity. Hence, much effort has gone into designing and characterising novel Cu-based electrocatalysts which retain the unique catalytic ability of Cu and at the same time synergistically improve the efficiency and selectivity of the CO_2 reduction reaction.

One approach is the design of bimetallic catalysts or Cu alloys. Generally, alloying Cu with another metal has shown to significantly reduce the overpotentials for the formation CO_2 reduction products [173-176]. For two-electron-transfer products like CO and HCOO−, the shift in onset potentials can sometimes go as close as their equilibrium potential [175, 176]. Although most Cu alloys do not show significant improvements in product selectivity toward hydrocarbons (CH_4 and C_2H_4), certain alloys are able to generate products that cannot be made by the individual metals separately in detectable amounts [175-177]. For example, Watanabe et al. [175, 176] showed that Cu−Cd and Cu−Ni alloys are able to produce methanol up to approximately 5 and 10% current efficiencies respectively at low overpotentials, while these metals in their individual pure form produce methanol only in negligible amounts [48]. These improvements in catalytic ability are generally thought to be brought about by synergistic effects between adjacent sites of the different metals in the alloy, where the stabilisation and adsorption of intermediates and reactants can be made favourable for selective and efficient CO_2 reduction [176, 178, 179].

Another approach to improve the performance of Cu involves the application of Cu oxides. Unlike Cu metal, Cu oxide surfaces have been demonstrated to produce significant amounts of methanol from CO_2 reduction [180-183]. The oxidised Cu surfaces investigated were prepared through various methods, most commonly through thermal air oxidation, anodisation, and electrodeposition. Amongst these methods, Le et al. [182, 183] discovered that the methanol yield (43 μmol cm^{-2} h^{-1}) and current efficiencies (38%) is highest on electrodeposited Cu(I) oxide films. They suggested that Cu(I) active sites may play a critical role in the selectivity toward methanol by stabilising key intermediates like methoxy and by acting as hydrogen donor sites that promote the reduction of methoxy to methanol. The experimentally observed selectivity toward methanol on Cu oxide surfaces is recently explained by theoretical DFT simulations, where the preference toward methanol over CH_4 (from the methoxy

intermediate) on oxidised Cu surfaces is due to the weakening of the oxygen binding strength of methoxy to the electrode surface [172]. Despite the apparent selectivity toward methanol, an obvious problem with using Cu oxide surfaces is their poor stability in the cathodic conditions of CO_2 reduction, during which the Cu oxides are completely reduced to Cu metal. Although there are several arguments which claim that a small amount of Cu oxide can persists [45, 69, 160, 180, 184, 185] or even form [45] during CO_2 reduction (possibly due to Cu_2O being a semiconductor), methanol production is generally not observed after the majority of the Cu oxide has been reduced to metallic Cu.

While Cu oxides have the ability to catalyse the production of methanol, the Cu metal surfaces derived from the reduction of intentionally oxidised Cu also present unprecedented catalytic activity. These surfaces, which are currently gaining widespread attention, are usually composed of highly catalytic Cu nano-sized structures, and hence are usually referred to as "oxide-derived Cu nanoparticles". Synthesis of the oxide-derived Cu has been achieved through various methods, which include thermal oxidation and subsequent reduction either electrochemically or thermally under H_2 [186-190], chemical [191-193] or electrochemical deposition [69, 70, 104, 185, 194] of Cu oxide followed by electrochemical reduction, oxidation-reduction potential cycling [68, 72, 134, 195, 196], anodisation [197-199] and anodic pulsing [152, 165, 166]. When used for CO_2 reduction, these surfaces are usually reported to significantly lower the onset potentials of CO_2 reduction, enhance the selectivity toward C_2 products (C_2H_4, ethanol, acetate) over CH_4, enhance CO and HCOOH formation at low overpotentials, and delay the deactivation of CO_2 reduction. The origins of these remarkable improvements in energy efficiency, selectivity and stability compared to polycrystalline Cu electrodes are still under debate between research groups, especially when certain oxide-derived Cu surfaces are observed to be more active in some ways than others [200]. Furthermore, a distinction is made between oxide-derived Cu nanoparticles and those that are commercially available, indicating that the particle size effect of nanoparticles may not be the sole contributor [187, 201, 202]. Nevertheless, the improvements are often attributed to the surface morphology of the oxide-derived Cu surface, which in comparison to a smooth polycrystalline surface, would generally contain a much higher density of under-coordinated sites, steps, edges, defects and grain boundaries. The enhanced selectivity toward C_2 products over CH_4 is largely claimed to be due to a high number of (100) facets, although some works also emphasised on the significant contribution of interfacial pH effects toward enhancing C_2 products on roughened surfaces [104, 194, 196]. Additionally, there are some who suggest that residual oxide sites are actually responsible for the observed catalytic activity [69, 185], although the majority would disagree and claim that most, if not all, of the oxide precursor is completely reduced to metallic Cu. In any case, oxide-derived Cu surfaces are highly catalytic for CO_2 reduction. Due to the simplicity of the surface modification, these electrodes hold great potential and deserve on-going investigation and development.

Ultimately, an efficient and selective electrocatalyst for the reduction of CO_2 will require a degree of surface heterogeneity where multiple adjacent active sites are available to facilitate the stabilisation and reaction between different adsorbed reaction intermediates. This requirement can be achieved through supported metal nanoparticles, where the interfaces between metal nanoparticles and their support material synergistically serve as highly active sites. Notably, metal nanoparticles can be supported on conductive oxide phases, demonstrating high catalytic activity in various electrocatalytic processes [203-206]. For the electrochemical reduction of CO_2, oxide supported Cu nanoparticles such as Cu/ZnO [207] and Cu/TiO_2 [45] have been studied as electrocatalyst. An increase in alcohol yields of at least an order of magnitude compared to polycrystalline Cu is observed on these electrodes, and is generally attributed to synergistic effects at the interface between Cu and the oxide

phase which lowered the reaction barriers for the hydrogenation of CO_{ads} [207]. A more recent example which demonstrates the high potential of the synergy between different adjacent active sites is the efficient reduction of CO_2 to ethanol on Cu nanoparticles supported on nitrogen-doped graphene [208]. Current efficiencies of ethanol as high as 63% (at −1.2 V vs RHE) were observed on this electrode, whereby the apparent selectivity to ethanol (but not C_2H_4 and C_2H_6) is suggested to be facilitated by a novel synergistic mechanism between Cu nanoparticles and the nanostructured N-doped graphene support. It is likely that the future of electrocatalyst design and development will focus on the potential synergy between various catalytic materials, while incorporating the highly catalytic properties of nanostructures, to design efficient and selective electrocatalysts for CO_2 reduction through novel reaction mechanisms.

2.5 Thesis research contribution

The research presented in this thesis contributes to the literature of the electrochemical reduction of CO_2 in several aspects.

The first contribution relates to the effects of applying anodic treatments during CO_2 reduction. Anodic treatments, typically in the form of periodic anodic pulses and potential cycling, are usually applied to prolong the activity of CO_2 reduction by stripping away adsorbed poisons on the electrode surface. In some cases, the reaction selectivity can also be altered significantly, as discussed in section 2.3.5. However, our attempts to prolong the activity of CO_2 reduction had brought some unexpected results that are contrary to previous literature. Instead of prolonging CO_2 reduction, we found that our short anodic interruptions significantly suppressed the formation of CO_2 reduction products and promoted the HER. Additionally, we observed a previously unreported drastic change in reaction selectivity from CH_4 to CO, which can be maintained for prolonged periods of time, when short potentiostatic interruptions at −1.2 V were applied. These findings are explained and discussed in chapter 6, which has been published in Electrochimica Acta.

The second contribution relates to the effects of mass transfer during CO_2 reduction, as introduced in section 2.3.6. Given that most work on the electrochemical reduction of CO_2 is performed using heterogeneous electrocatalysts, the effects of mass transport of reactants and products may very well have a significant impact on the overall CO_2 reduction reaction. Additionally, since the hydrodynamics will undoubtedly vary between different cell configurations and research groups, the important effects of mass transfer need to be understood and appropriately identified. However, reports on this subject in the literature are very limited. Therefore, by using a Cu rotating cylinder electrode for which fundamental hydrodynamics allowing the prediction of mass transfer have been previously developed, we have extensively investigated the effects of mass transfer on CO_2 reduction. We have also adapted the mathematical model by Gupta et al. [44] in our work to aid in the estimation of interfacial concentrations of species during CO_2 reduction. From the Cu rotating cylinder electrode results and estimations by adapting Gupta's model, we discuss our findings on the effects of mass transfer in chapter 7. This work has also been published in Electrochimica Acta.

Other contributions relate to the characterisation of the CO_2 reduction activity of polycrystalline Cu supported Au_9/TiO_2 nanoparticles. This preliminary work, presented in chapter 8, is in line with the overall strategy in developing novel electrocatalysts with a level of surface heterogeneity which aims to investigate the potential synergy between various catalytic materials.

3 Experimental Methods

3.1 Introduction

This chapter details the experimental aspects of CO_2 reduction performed in this thesis. The overall experimental set-up, materials and their preparation, measurements and analysis are presented. In addition, a brief discussion of some of the experimental challenges faced throughout this work is given. Certain experimental procedures that are specific to a particular chapter are presented within that chapter itself.

3.2 Electrochemical cell set-up

Two types of electrochemical cell set-up were used for this work. The first set-up is designed for the use of planar disc electrodes (Figure 3.1), while the second set-up is designed for rotating cylinder electrodes (RCE) (Figure 3.2). Both cells are custom-made from borosilicate glass and are conventional H-type with two compartments.

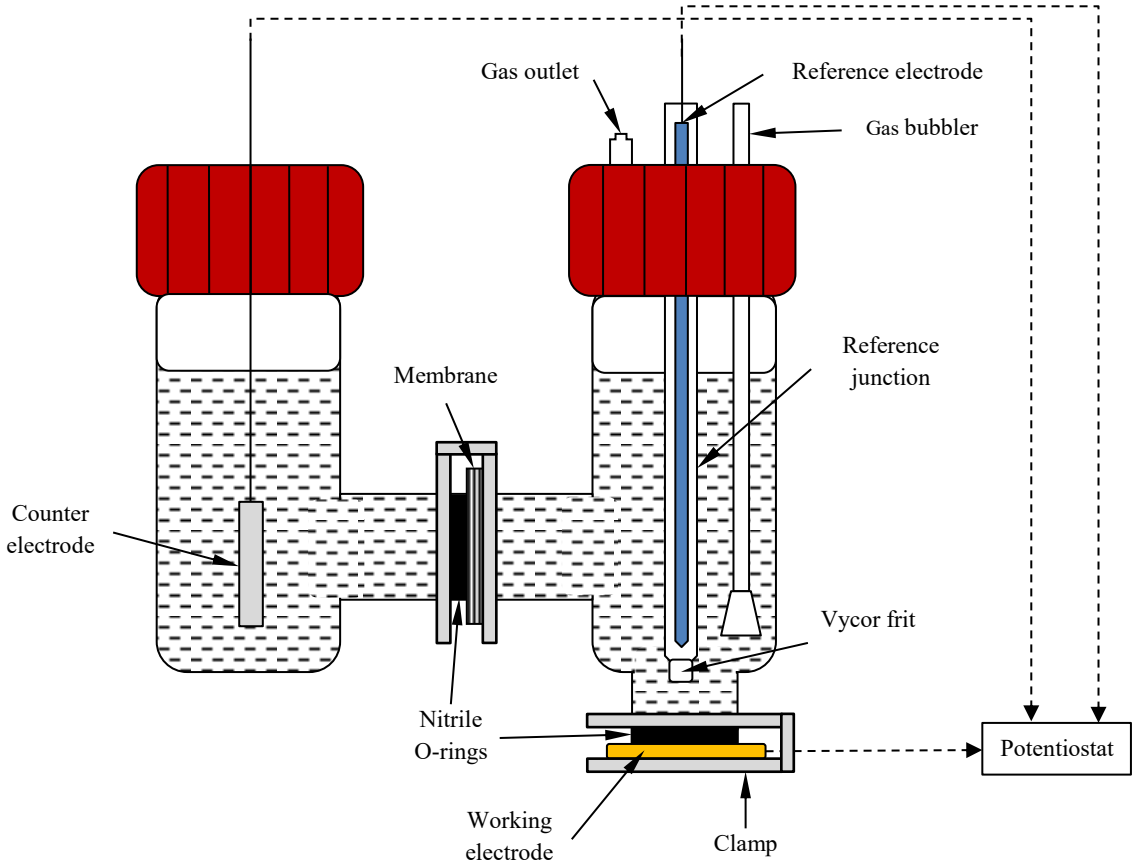

Figure 3.1: Schematic of the electrochemical cell designed for planar disc electrodes.

For the planar disc electrode set-up (Figure 3.1), the working electrode is secured under the catholyte chamber, which has a bottom opening, with a nitrile O-ring and a clamp. A Cu board connected to an electrical wire and placed under the working electrode serves as the conducting element to the potentiostat. The circular geometric area of the electrode surface exposed to the electrolyte is 3.14 cm^2 (2.0 cm diameter). A membrane sheet separates the catholyte chamber from the anolyte, also secured in place with a nitrile O-ring and a clamp at the H-junction. The cap of the catholyte chamber permits

the placement of a glass gas bubbler, which disperses gas bubbles through a glass frit, and a glass reference electrode junction with a Vycor frit at the bottom. A reference junction is used to prevent contamination from the reference electrode, for example by leakage of Cl^- from a Ag|AgCl electrode. A gas outlet is also positioned at the cap to allow gas effluents to be collected for measurements and analysis. To ensure that air contamination in the gas effluent is eliminated, the catholyte chamber cap is designed to be gas tight with a series of nitrile O-rings which secures the interfaces between the cap and the gas outlet, reference junction, gas bubbler and the catholyte chamber itself. The nitrile O-rings and clamps which secures the working electrode and the membrane are also effective in preventing leaks and air contamination. The anolyte chamber on the other hand does not need to be gas tight and a counter electrode is positioned in the chamber as normal. Both catholyte and anolyte chambers can each hold an approximate electrolyte volume of 40 ml, although only 30 to 35 ml is usually used in the catholyte to prevent spill over into the gas outlet. Some researchers prefer the use of small electrolyte volumes, e.g. 8 ml [32], to increase the concentration of liquid products in the electrolyte to improve detection and analysis.

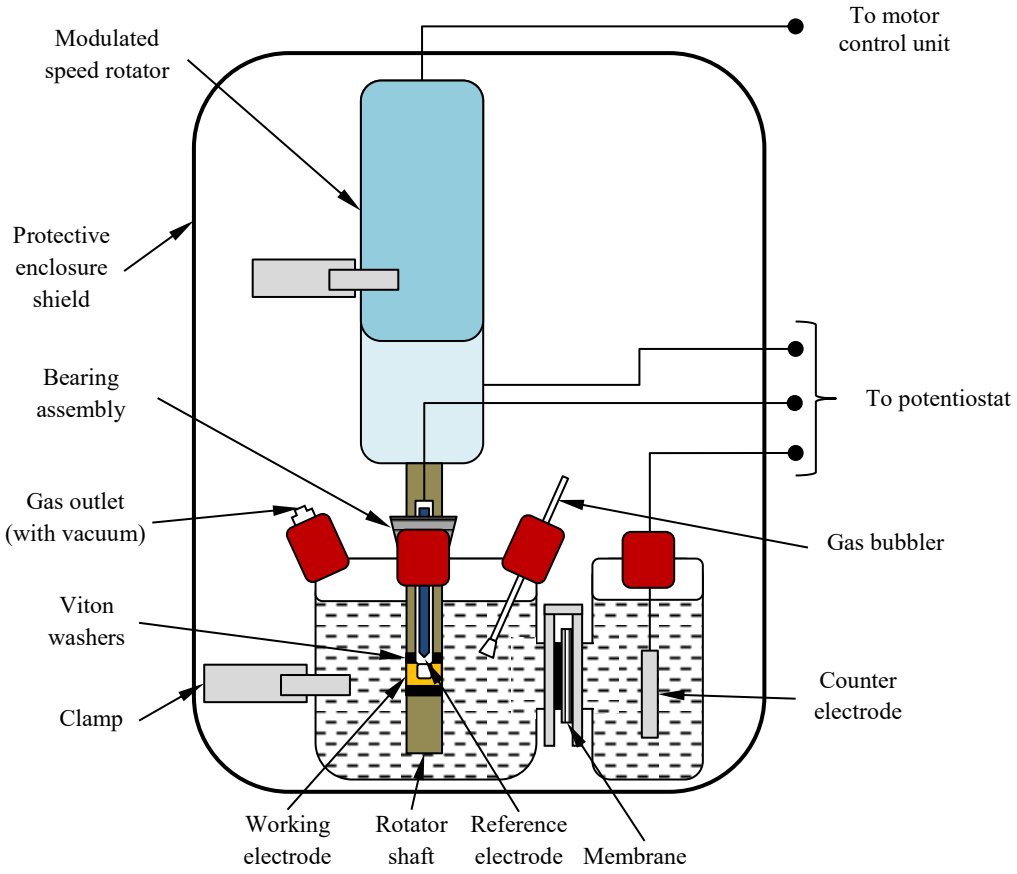

Figure 3.2: Schematic of the electrochemical cell designed for rotating cylinder electrodes (RCE).

The electrochemical cell set-up for the RCE is generally similar in principle to that of the planar disc electrode, however physical differences exists to suit the purpose of electrode rotation. Instead of a single cap, the gas outlet, reference electrode junction, and gas bubbler are introduced into the catholyte chamber through individual side ports. The working electrode is an annular cylinder with an outer exposed geometric area of 3 cm^2 (1.5 cm outer diameter, 0.64 cm height), secured on a polyetheretherketone (PEEK) rotator shaft with Viton washers. The working electrode is electrically

coupled to the shaft and then to the rotator brushes present in the modulated speed rotator, from which electrical connections to the potentiostat can be made. The rotator shaft is positioned at the centre of the catholyte chamber, which can hold approximately 400 ml of electrolyte, and is secured in place by a bearing assembly designed to precisely fit the rotator shaft. Because the bearing assembly is not designed to be gas tight, a vacuum is used to draw the gas effluent from the chamber at a rate that is approximately half of that of the flow rate of the inflow gas through the gas bubbler. This ensures that contamination by air from outside the cell is minimised. All equipment relating to the rotator is obtained from Pine Research Instrumentation.

3.3 Materials and their preparation

Polycrystalline Cu metal, purity 99.99% sourced from Advent Research Materials Ltd, is the electrode material used in the majority of the work in this thesis. Originally in the form of a rod, the Cu metal is mechanically machined into planar discs (2.5 cm diameter, 4 mm thickness) and annular cylinders (1.5 cm outer diameter, 0.64 cm height). In our work, the Cu electrode is prepared by mechanical polishing using silicon carbide papers (down to P2000 grade) followed by alumina slurries (1.0, 0.3 and 0.05 μm) until a mirror finish is obtained on the relevant surface for electrochemical measurements (Figure 3.3). The mechanically polished electrode is subsequently ultra-sonicated and rinsed for degreasing with isopropanol and 18.2 MΩ cm deionised (DI) water, and used without further treatment.

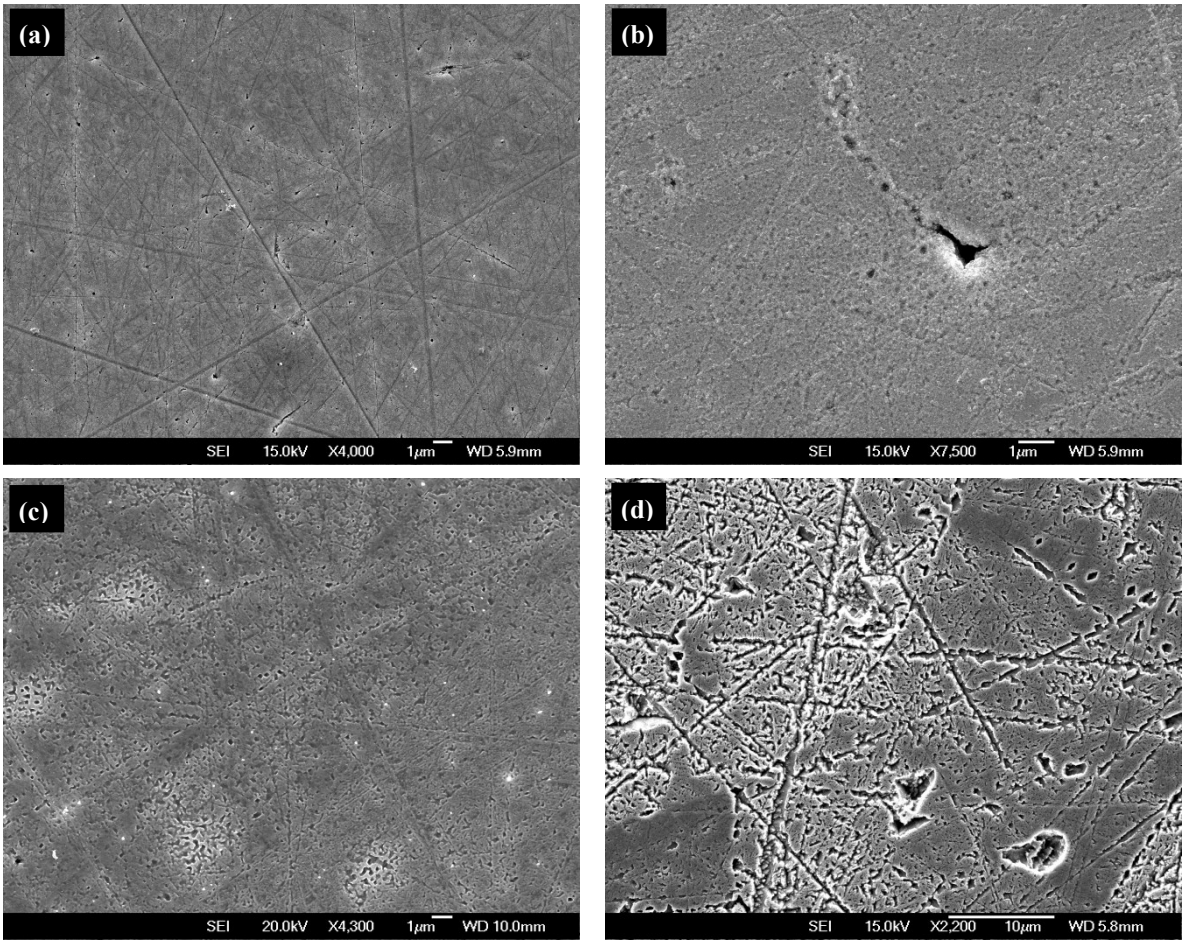

Figure 3.3: SEM images of polycrystalline Cu after (a) mechanical polishing to a mirror finish, (b) oxidation of (a) in air at 200 °C for 1 hour, (c) subsequent acid wash of (b) in 10 v/v% HCl for approximately 30 s, and (d) acid wash of (a) in 10 v/v% HCl for 6.5 hours.

In the literature, the majority of the CO_2 reduction studies on Cu metal have included electropolishing (usually in concentrated phosphoric acid) as a pre-treatment step after mechanical polishing. Electropolishing, when performed in the diffusion limited regime, removes surface irregularities, stressed layers and contaminants, resulting in an overall smoother surface that is free of impurities [47], and generally aids in improving the reproducibility of results [160]. However, after performing several CO_2 reduction experiments on Cu electrodes with and without electropolishing, we did not observe any significant differences in results and reproducibility between them. Although electropolishing is widely used for pre-treatment as per the standard procedure used in the seminal works of Hori [67], we highlight a few works on CO_2 reduction that have omitted electropolishing [73, 74, 123, 132, 209], or have shown that electropolishing does not significantly improve results [23, 210].

Due to the strong affinity of Cu toward oxygen, a native oxide layer is present when the electrode is exposed to air. Hence, some have additionally applied acid washes (commonly with HCl and HNO_3) to the Cu electrode, often with the intention to remove the oxide layer [23, 41, 45, 51, 146, 160], given that the catalytic properties of Cu oxides are different from that of Cu metal. However, it seems that performing the additional acid washes can cause more variation in results rather than improvements in reproducibility [23, 45, 146]. Furthermore, our attempts to remove an intentionally grown oxide layer from mechanically polished Cu electrodes through acid washes in 10% HCl have caused significant roughening of the surface (Figure 3.3). Hence, to avoid further complications and variations in results, we have also chosen to omit acid washes. Nevertheless, we believe that any pre-existing surface oxide would have been thoroughly removed by the various stages in mechanical polishing needed to achieve a mirror finish, although we acknowledge that electropolishing would also do the same, arguably better. However, regardless of whether electropolishing was performed or not, the Cu electrodes will still be unavoidably exposed to air before the start of CO_2 reduction, hence a thin layer of surface oxide would still form. Given the instability of Cu oxides under CO_2 reduction conditions, and the fact that the thickness of the oxide layer formed during the short time between polishing and the start of CO_2 reduction is small, it is very likely that the oxide layer is rapidly reduced to Cu metal during CO_2 reduction.

The CO_2 gas (99.995% purity, Laser Grade) is sourced from BOC Ltd. Some works, like those of Hori [67], have included additional steps to further purify the CO_2 gas, e.g. passing through a washing bottle containing H_2CrO_4 + H_2SO_4 acid and through an activated Cu column, since the CO_2 gas may contain impurities that can cause the deactivation of the Cu electrode [83]. Other workers have also taken steps to humidify the CO_2 gas with water to minimize the evaporation of volatile liquid products [32]. Although it is probably beneficial to humidify and further improve the purity of the CO_2 gas, we rationalized that the inclusion of additional items into the experimental set-up could increase the potential for undetected contamination. Since the CO_2 gas is already of high purity with known concentrations of existing impurities as provided by the manufacturer, i.e. we know with confidence the composition of the CO_2 gas entering the system, we have decided to use the CO_2 gas as provided without further treatments. For certain experiments where a CO_2-free atmosphere is desired, Ar gas (99.999% purity, Zero Grade, BOC Ltd) is used instead, also without further treatments.

The electrolyte used for all CO_2 reduction work in this thesis is $KHCO_3$ sourced from Sigma Aldrich (99.7%, ACS reagent). The electrolyte solution is prepared by using 18.2 MΩ cm DI water to make a 1 M stock solution which is pre-electrolysed for at least 48 hours at −1.1 V vs Ag|AgCl (sat. KCl) using Pt wires. After pre-electrolysis, the 1 M $KHCO_3$ stock solution is diluted to the required working concentration, which is usually 0.2 M. For CO_2 reduction experiments, the electrolyte solution prepared is saturated with the CO_2 gas for at least 1 hour, after which the pH reaches the

equilibrium value (pH 7 for CO_2 saturated 0.2 M $KHCO_3$). Pre-electrolysis of the electrolyte solution is adopted by most workers following the recommendation of Hori's group [149] who had strongly advocated for its practice to remove trace metal impurities, namely Fe and Zn. They suggest that metal impurities, even in trace amounts, will be electrodeposited on the Cu surface during CO_2 reduction and hence cause its deactivation. However, the effectiveness of pre-electrolysis in preventing the deactivation of CO_2 reduction is debatable in the literature [146, 160-162], with some suggesting that a more effective method, i.e. metal ion chelation [159], be used to remove the metal impurities. In our work, we also observed little difference in CO_2 reduction activity between solutions that were pre-electrolysed and those that were not. To determine the effectiveness of our pre-electrolysis procedure in removing metal impurities, we have measured the concentrations of Fe, Zn and Pb using ICP-MS before and after pre-electrolysis (Table 3.1). Even without pre-electrolysis, the concentration of Fe and Pb is 10 and 100 times below the manufacturer's specifications respectively. Furthermore, the concentration of Zn is almost always below the detection limit of ICP-MS. Based on the ICP-MS measurements (Table 3.1) of pre-electrolysed samples, the effectiveness of our pre-electrolysis procedure is questionable. Although it may seem that a longer pre-electrolysis time of 65 hours removed more Fe compared to pre-electrolysis for 48 hours, the concentration of Fe after 48 hours of pre-electrolysis was found to be contradictorily higher than the samples not pre-electrolysed. Moreover, the concentration of Pb does not seem to be correlated meaningfully with pre-electrolysis time, though we do recognise that the concentration of Pb is much lower than Fe. Because our samples were high in salt content, dilution of the samples by at least an order magnitude (from 1 M to 0.08 M) was required for ICP-MS analysis. Despite having diluted the samples, the analysis still reported relatively low recoveries (about 60%). Hence, we emphasise that the accuracy of the ICP-MS analysis may have been compromised due to the need for sample dilution. Regardless, for most of our work, we have opted to use solutions that were pre-electrolysed for at least 48 hours, in-line with the suggestion by Hori to minimise the deactivation of CO_2 reduction by metal impurities.

Table 3.1: Concentration of trace Fe, Zn and Pb impurities, as measured using ICP-MS, in 1 M $KHCO_3$ before and after pre-electrolysis at −1.1 V vs Ag\|AgCl (sat. KCl) using Pt wires.

Pre-treatment of 1 M $KHCO_3$	Concentration (ppb)		
	Fe	Zn	Pb
Not pre-electrolysed	13.9	0.2	1.1
	11.4	< *d.l.*[a]	0.4
After pre-electrolysis for 48 hours	22.4	< *d.l.*	0.3
	15.5	< *d.l.*	0.2
After pre-electrolysis for 65 hours	7.6	< *d.l.*	0.6
	9.4	< *d.l.*	0.7
Manufacturer's specification (maximum concentration)	*100*	–	*100*

[a] *d.l.: detection limit.*

The membrane used to separate the catholyte from the anolyte is a commercial Nafion 115 cation exchange membrane, and is prepared in accordance to established procedures in the literature [211-213]. Briefly, we prepared the Nafion membranes using the following procedure: Step 1, the membranes are soaked in DI water for 10 mins; step 2, treated in 3% H_2O_2 solution heated to the boiling point to oxidise organic impurities; step 3, rinsed in DI water to remove traces of H_2O_2; step 4, soaked in hot (about 80 °C) H_2SO_4 to remove metallic impurities; step 5, rinsed with DI water again to remove traces of H_2SO_4; step 6, stored in 0.1 M KOH for 1 hour to exchange H^+ with K^+; and finally step 7, stored in pre-electrolysed 0.2 M $KHCO_3$. Because the membranes are prepared in the K^+ form, and that the concentration of K^+ is many orders of magnitude larger than that of H^+ at the pH

values used in our work, K^+ is selectively transferred through the membrane (from anolyte to catholyte) as the principal charge carrier. This selective transport of K^+ to the catholyte during electrolysis is significant, the effects of which (see section 3.6) become more pronounced for long-term electrolysis and small catholyte volumes. Despite these effects, cation exchange is still chosen over anion exchange to prevent the transport of $HCOO^-$, which is a major product of CO_2 reduction, to the anolyte to be re-oxidised, the occurrence of which can affect charge balance calculations.

For all electrolysis experiments, a self-made Ag|AgCl (sat. KCl) electrode was used as the reference (see Appendix 2) while Pt foil was used as the counter electrode.

3.4 Electrochemical measurements

All electrochemical measurements were conducted using a GAMRY Reference 3000 potentiostat and performed at ambient temperature and pressure. Cyclic voltammetry, electrochemical impedance spectroscopy, chronoamperometry (constant potential) and chronopotentiometry (constant current) were the measurements most frequently made.

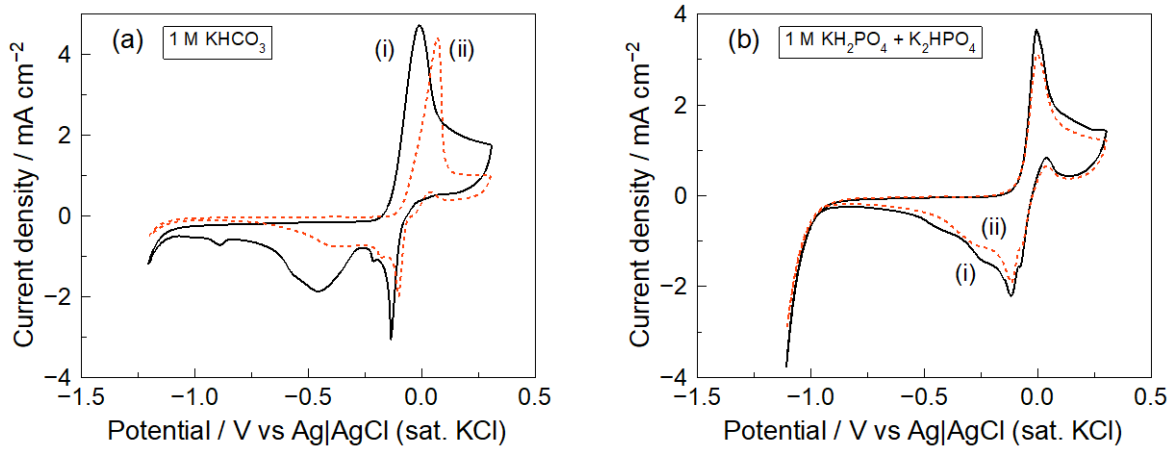

Figure 3.4: Cyclic voltammetry of mechanically polished Cu surfaces in (a)(i) Ar purged 1 M $KHCO_3$ (pH 8.3) with no solution agitation, (a)(ii) CO_2 saturated 1 M $KHCO_3$ (pH 7.5) with continuous CO_2 bubbling at 20 ml min^{-1}, (b)(i) Ar purged 1 M KH_2PO_4 + K_2HPO_4 (pH 6.1) with continuous Ar bubbling at 20 ml min^{-1}, and (b)(ii) CO_2 saturated 1 M KH_2PO_4 + K_2HPO_4 (pH 6.1) with continuous CO_2 bubbling at 20 ml min^{-1}. Potential range −1.2 V to +0.3 V, speed 50 mV s^{-1}.

Cyclic voltammetry (CV) is an electroanalytical technique which measures the current when the electrode potential is cycled between two potential limits at a certain rate. This method is widely used for the study of redox behaviour [214], the characterisation of which we have performed on the surface of mechanically polished polycrystalline Cu as an initial experiment. The CV measurements were obtained between −1.2 V and +0.3 V vs Ag|AgCl (sat. KCl) in 1 M $KHCO_3$ (not pre-electrolysed), either purged beforehand with Ar gas or saturated continuously by CO_2 bubbling (Figure 3.4a). The oxidation and reduction peaks of Cu and Cu oxides respectively are clearly exhibited in the CV measurements, and are consistent with many CV measurements of Cu available in the literature [215, 216]. With regards to the presence of CO_2 in the electrolyte, the redox currents of Cu and Cu oxides in the CV measurements are probably too large to allow any notable electro-activity by dissolved CO_2 to be recorded. Instead, the dissimilarity between the two CV measurements, namely the shift in peak potentials and the difference in peak sizes, are respectively caused by the decrease in solution pH and agitation of the electrolyte due to CO_2 bubbling. The observed shift in peak potentials can be described by the pH dependence of the equilibrium potential of Cu oxidation to

Cu_2O, reaction (3.1), as given by Pourbaix [217]. The pH difference of 0.8 units between CO_2 saturated and Ar purged 1 M $KHCO_3$ gives a difference in potential of 0.0591 × 0.8 = 47 mV, which

$$2Cu + H_2O \leftrightarrow Cu_2O + 2H^+ + 2e^- \qquad E_{eq}\ (V\ vs\ SHE) = 0.471 - 0.0591pH \qquad R(3.1)$$

is in overall consistent with the magnitude of the observed shift in peak potentials. The decrease in peak sizes in the case where CO_2 is bubbled through the electrolyte can be partly explained by the increase in solution agitation, which enhances the transport of soluble Cu species, e.g. $Cu(OH)_x$ and $CuCO_3$ formed at oxidising potentials [215, 216], away from the electrode surface, preventing their further oxidation to solid Cu_2O and CuO, and their reduction back to Cu metal. The differences in the CV measurements are shown to reconcile when both CO_2-free and CO_2 saturated measurements were repeated in 1 M phosphate buffer solutions at pH 6.1 with similar hydrodynamics, where the electrolyte was either bubbled with CO_2 or Ar gas at similar flow rates (Figure 3.4b). Once more, the electro-activity of CO_2 is also not evident in the CV measurements in the phosphate buffer electrolyte, although the onset of the HER is 150 mV more positive than in the $KHCO_3$ case, consistent with results that show a higher selectivity toward HER in phosphate buffer compared to $KHCO_3$ electrolytes (see section 2.3.2).

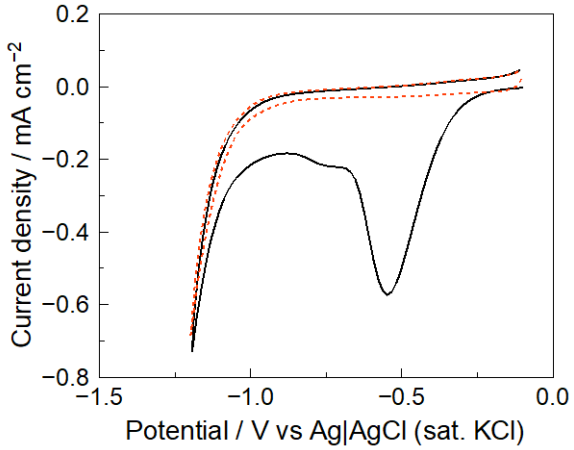

Figure 3.5: Cyclic voltammograms (100 mV s^{-1}) of a newly polished Cu in 0.2 M $KHCO_3$ which show the successful reduction of Cu oxides. (——), first cycle; (– – –), subsequent cycles.

Because Cu oxides and oxide-derived Cu possess different catalytic abilities than polished Cu surfaces, we have specifically chosen to avoid potentials where Cu oxide can form in all electrochemical measurements prior and during CO_2 reduction. Based on the CV measurements presented in Figure 3.4, oxidising potentials above −0.1 V vs Ag|AgCl (sat. KCl) were avoided at neutral pH. The open circuit potential (OCP) of newly polished Cu in 0.2 M $KHCO_3$ is usually −0.1 V vs Ag|AgCl (sat. KCl) and below, hence a CV between −0.1 V and −1.2 V at 100 mV s^- is usually performed before the start of CO_2 reduction to confirm the complete reduction of surface oxides formed by exposure to air after mechanical polishing (Figure 3.5). Typically, during the first cycle from −0.1 to −1.2 V, two reduction peaks at −0.55 V and −0.75 V corresponding to reduction of Cu(II) to Cu(I), and Cu(I) to Cu(0) respectively are observed. During the subsequent cycles these reduction peaks are absent which indicates that the oxide layer formed after polishing is easily reduced, and thus it is unlikely that during CO_2 reduction (which typically occurs at −1.5 to −1.8 V in our experiments), any oxide will be present. Cyclic voltammetry was also used more frequently in our work presented in chapter 6, where we document the effects of periodic CV interruptions during constant current CO_2 reduction.

Electrochemical impedance spectroscopy (EIS) is an electroanalytical technique that essentially applies an alternating potential or current perturbation signal (typically in a sinusoidal waveform) to the cell and measures the resulting current or potential response over a wide range of frequencies [218]. The applications of EIS are numerous, but one of its basic uses is the measurement of the solution resistance between the working and reference electrodes, which must be taken into account when determining the potential of the working electrode. For a certain electrode area and electrolyte type, the solution resistance generally depends on the electrolyte concentration and the distance between the working and reference electrodes. The solution resistance also depends on the operating temperature, where a small increase in the cell temperature during electrolysis at high current densities can slightly decrease the solution resistance (due to increase in solution conductivity with temperature) [32]. Hence, in our long-term (over 10 hours) electrolysis work, we regularly measure (every 15 minutes) the solution resistance to account for the selective transport of K^+ through the Nafion membrane to the catholyte (from the anolyte), which decreases the solution resistance with time, and also because our electrochemical cells are not temperature controlled. The EIS measurements to obtain the solution resistance were performed over a frequency range of 100 kHz to 10 Hz, with a 5 mV rms (root mean squared) AC potential signal superimposed on top of an applied DC potential (potentiostatic EIS) or an applied DC current (hybrid EIS[*]), for constant potential and constant current electrolysis respectively. By analysing the EIS spectra based on the equivalent circuit of a simplified Randles cell[†] (Figure 3.6), the solution resistance is obtained by reading the real impedance value at high frequencies where the imaginary impedance value is zero (Figure 3.7). With the solution resistance (R_s) known, the measured electrode potential can then be corrected using Ohm's law ($E_{corrected} = E_{measured} - i_{total}R_s$, where i_{total} is the total current).

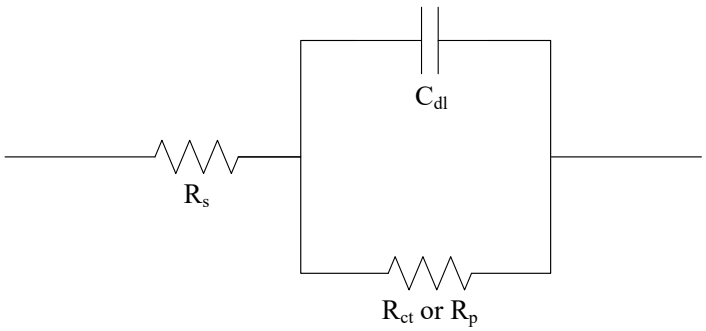

Figure 3.6: Equivalent circuit of a simplified Randles cell, which consists of the solution resistance (R_s) in series with the parallel combination of the double layer capacitor (C_{dl}) and the charge transfer (R_{ct}) or polarisation (R_p) resistance. At high frequencies, the imaginary component of the impedance, which is solely attributed to C_{dl}, becomes zero as it offers no impedance. Hence, the current only consists of charging current and the only impedance it encounters is the solution resistance.

Aside from the electrolyte concentration, a major factor determining the solution resistance is the placement of the reference junction. Usually, the distance between the working and reference electrodes is made as small as practically possible so that the solution resistance can be minimised to avoid instrument complications during potentiostatic control, e.g. potentiostat stability during positive-feedback compensation. However, our attempts to bring the reference junction as close as

[*] Instead of applying a fixed AC current signal (galvanostatic EIS), hybrid EIS adjusts the magnitude of the AC current such that a nearly constant AC potential level, as specified by the user, is obtained. Hybrid EIS was chosen over galvanostatic EIS as the data acquired was less noisy.

[†] The equivalent circuit of the simplified Randles cell is that of the Randles cell where the Warburg impedance, which describes a kind of resistance to mass transfer, is not important [218]. The Randles equivalent circuit is one of the simplest and most common, and is often the starting point for other more complex models.

possible to the electrode surface, in particular for the cell set-up for planar disc electrodes (Figure 3.1), have introduced into the EIS spectra at high frequencies a large inductance like feature (Figure 3.7b), which becomes increasingly prominent as the distance decreases. We currently do not have a clear explanation for this inductance like feature, though we suggests that it might be related to the non-uniformity of the current distribution, or perhaps the cell geometry which forces a less than ideal current flow path. As the effects of this inductance like feature on our experimental results are uncertain, we have chosen instead to minimise this feature by maintaining an appropriate distance between the working and reference electrodes without significantly increasing the solution resistance. This is determined to be approximately 55 Ω for a 0.2 M $KHCO_3$ solution at the chosen distance (approximately 25 mm) for the planar disc electrode set-up. In contrast, the inductance like feature is quite minimal for the RCE set-up (Figures 3.2 and 3.7c), and the solution resistance can be minimised to 4 Ω for a 0.2 M $KHCO_3$ solution at a distance of about 10 mm.

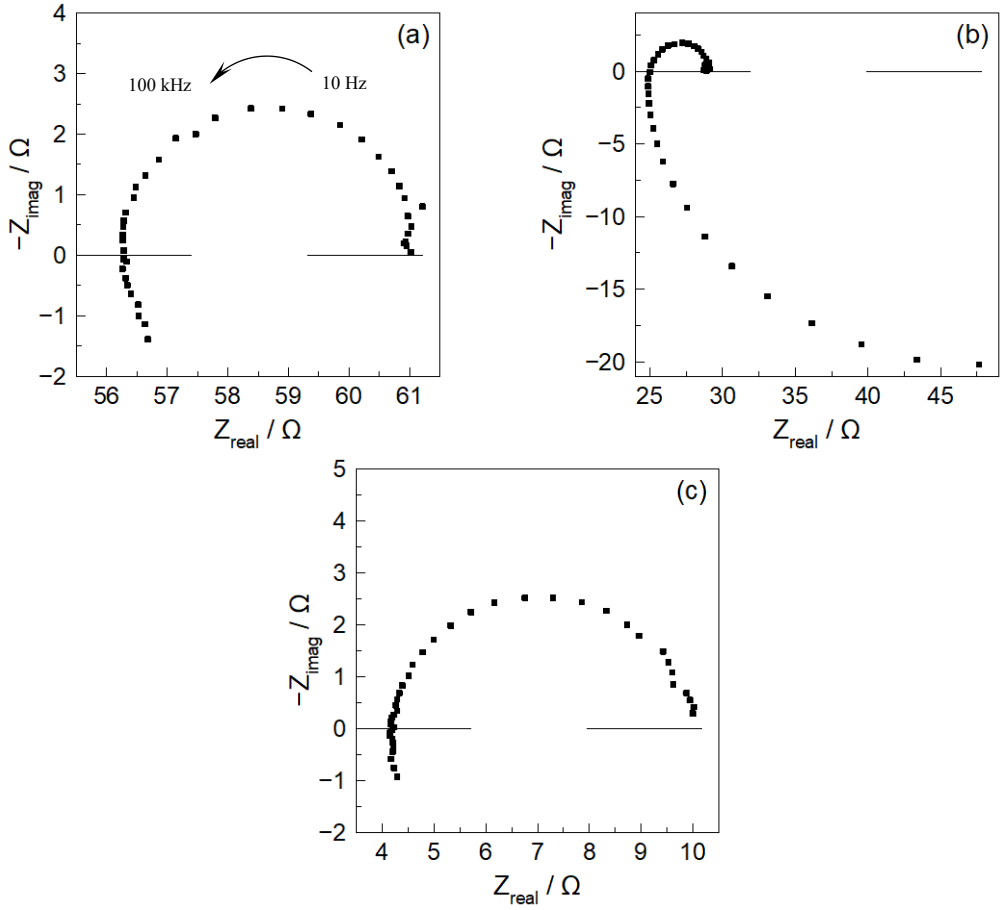

Figure 3.7: Nyquist plots of the initial hybrid EIS measurements of constant current (−5 mA cm^{-2}) CO_2 reduction on polished Cu in pre-electrolysed 0.2 M $KHCO_3$ with a distance between working and reference electrodes of approximately (a) 25 mm, and (b) 15 mm using the planar disc electrode set-up, and (c) 10 mm using the RCE set-up. The solution resistance is obtained by reading the real impedance value (x-axis) at high frequencies where the imaginary impedance value (y-axis) is zero. An inductor like feature in the EIS spectra becomes increasing prominent when the distance between working and reference electrodes becomes smaller (compare (a) and (b)). EIS parameters: 100 kHz to 10 Hz, 5 mV rms superimposed on −5 mA cm^{-2}.

Electrolysis was performed either using chronoamperometry (constant potential) or chronopotentiometry (constant current). However, due to the large solution resistances for the planar disc electrode set-up, constant potential experiments have been difficult to execute even with positive

feedback compensation, as the remaining uncompensated resistance along with transient changes in the current density are large enough to cause a significant variation in the electrode potential. In addition, because the catholyte volume used in the planar disc electrode set-up is relatively small (30 to 35 ml) and that transient changes in the current density during potentiostatic control is generally unpredictable, the changes in solution resistance with time caused by the flux of K^+ ions into the catholyte are substantial but yet cannot be estimated in advance. This complicates positive feedback compensation when constant potential electrolysis is in progress, since the potentiostat can generally only compensate about 75% of the solution resistance without introducing instabilities during measurements. Hence, all reported electrolysis experiments using the planar disc electrode set-up were performed under constant current. While we acknowledge that constant potential measurements are usually preferred for fundamental studies since the reaction rate and product distribution are always potential dependent, we also recognise that the potential dependence of CO_2 reduction on Cu electrodes has already been widely studied and therefore well-known (see section 2.3.1); hence the effects on reaction selectivity by changes in electrode potential during constant current measurements can be appropriately attributed with confidence. The difficulties in potentiostatic control described above are generally not encountered when using the RCE set-up since the solution resistance is much smaller and the catholyte volume is large enough to buffer the effects of K^+ transport. However, in the case of our work presented in chapter 7 where the RCE was used to study the effects of mass transfer on CO_2 reduction, constant current is still preferred over constant potential measurements, as varying current densities during constant potential reduction can cause significant variation in interfacial pH [44]. Because the reaction selectivity is known to be strongly dependent on pH (see section 2.3.3), a varying interfacial pH within an experiment may complicate the interpretation of results where the effects of mass transfer are of main interest. Hence, to prevent this complication, we have opted for constant current measurements, through which the interfacial pH can be controlled majorly by mass transport.

In our work, a general sequence of electrochemical measurements for a standard long-term CO_2 reduction experiment can be summarised as below:

1. OCP measurement
2. Potentiostatic EIS at OCP to measure solution resistance before electrolysis
3. Cyclic voltammetry (between −0.1 to −1.2 V vs Ag|AgCl (sat. KCl)) to show the reduction of oxides
4. Sequence loop (15 minutes each loop)
    a. Hybrid or potentiostatic EIS at specified current or potential
    b. Chronopotentiometry or chronoamperometry
5. Cyclic voltammetry (between −1.2 to −0.1 V vs Ag|AgCl (sat. KCl)) to show stripping of adsorbed species
6. Potentiostatic EIS at OCP to measure solution resistance after electrolysis
7. OCP measurement

3.5 CO_2 reduction product analysis

In most cases, the products of CO_2 reduction are measured by conventional chromatography methods. Other more sensitive methods such as nuclear magnetic resonance (NMR) [32] and online electrochemical mass spectrometry (OLEMS) [83] have also been used, although a disadvantage of mass spectrometry is the inability to calculate current efficiencies. For our work, product detection and analysis is mainly done using gas chromatography (GC) and high pressure liquid chromatography (HPLC), for gaseous and liquid products respectively. GC measurements were performed during

electrolysis at 15 minute intervals, i.e. online GC measurement, while HPLC measurements for liquid products in the catholyte were only performed post-electrolysis.

The gas chromatograph used for gaseous products analysis is a SRI 8610C Gas Chromatograph (Multi-Gas #3 configuration) equipped with a haysep-D column with TCD and FID detectors[*]. The FID detector is coupled to a "methaniser" which converts CO and CO_2 to CH_4 through a nickel powdered catalyst supplied with H_2 before detection. The GC is calibrated to detect and quantify H_2, CO, CH_4, C_2H_4 and C_2H_6. CO_2 is not calibrated for our application since it is the reactant gas which makes up most of the gas effluent to the GC; hence it appears on the chromatogram (at its proper retention time) as a large broad peak which exceeds the detectors' maximum limit under the sensitivity levels used for the detection of reduction products, which are relatively much less concentrated in the gas effluent. The detection limits of the GC are approximately 100 ppm for H_2 and 10 ppm for CO_2 reduction products, which equates to current efficiencies[†] of approximately 1% for H_2, 0.1% for CO_2 reduction products at −15.71 mA total current (−5 mA cm^{-2} on a polished planar Cu disc electrode) and 10 ml min^{-1} total gas effluent. The typical uncertainties associated to the calculated current efficiencies for an example GC measurement are given in Table 3.2. The uncertainty of the current efficiency of C_2H_6 is the highest amongst the rest as its measured concentration is usually very low and hence significantly far from the concentration range used for calibration. H_2 and CH_4 on the other hand have lower uncertainties as their measured concentrations are usually within or close to the calibrated range. Because C_2H_6 is very seldom observed during CO_2 reduction on polished Cu (see section 2.3.1), it is usually omitted from the estimation of the uncertainty of the total gaseous current efficiency.

Table 3.2: Current efficiencies of gaseous products and their associated uncertainties for an example GC measurement during CO_2 reduction on a polished planar Cu disc electrode. 0.2 M $KHCO_3$, −5 mA cm^{-2}, 20 ml min^{-1} CO_2 flow.

Gaseous product	Current efficiency (%)	Uncertainty[a] (±%)
H_2	43.8	0.6
CO	1.6	1.5
CH_4	36.1	0.9
C_2H_4	0.7	1.7
C_2H_6	0.1	6.7
Total:	82.3	2.5[b]

[a]Contributions to uncertainties from ALICAT mass flow controllers and GC calibration.

[b]Estimated using the error propagation method. C_2H_6 was omitted as it is very seldom observed for CO_2 reduction on polished Cu.

The HPLC used for liquid products analysis is a HP 1100 series HPLC equipped with a SUPELCOGEL™ C-610H column with a diode array (UV/Vis) and a refractive index detector. The HPLC is calibrated to detect and quantify formic acid, acetic acid and methanol. Formic acid is almost always detected from CO_2 reduction experiments since it is one of the major soluble products, but acetic acid and methanol on the other hand are scarce on polished Cu electrodes. The detection limit

[*] The thermal conductivity detector (TCD) is a universal detector that operates based on the difference in thermal conductivity of gases. It is highly sensitive to H_2 when Ar gas is used as the carrier gas, hence the TCD is mainly used to detect and quantify H_2 in our application. The flame ionisation detector (FID) operates based on the ionisation of analyte compounds using a H_2 flame and is highly sensitive to compounds with C−H bonds. Hence it is mainly used for detection and quantification of CO_2 reduction products. H_2 and air are not detected on the FID.

[†] The current efficiency, defined as the percentage of the total current going towards the formation of a certain product, is calculated based on the number of moles of electrons required to reduce CO_2 to that product. From the GC measurements, the volumetric production rate of a certain product is converted to a molar basis assuming the ideal gas law. The Faraday constant (96485 C per mol e^-) is then used to convert from moles to coulombs.

of formic acid for our HPLC method is 0.1 mM, which equates to an overall current efficiency of approximately 0.1% after 10 hours of CO_2 reduction at −15.71 mA in 35 ml of electrolyte. Table 3.3 lists the typical uncertainty for the overall current efficiency of formic acid, the value of which is used alongside those from Table 3.2 to estimate the unaccounted current efficiency and its associated uncertainty over a single measurement period (typically 15 minutes) assuming that the formation rate of formic acid is constant over the whole electrolysis period.

Table 3.3: Estimation of the unaccounted current efficiency in a single measurement period (typically 15 minutes) assuming that the rate of formic acid production is constant over the electrolysis period.

	Current efficiency (%)	Uncertainty (±%)
Total gaseous *(from Table 3.2)*	82.3	2.5
Overall formic acid[a] *(assume constant)*	8.0	2.8
Total *(gaseous + formic acid)*	90.3	3.8[b]
Unaccounted:	*100 − 90.3* = 9.7	3.8

[a]After 10 hours of CO_2 reduction on polished planar Cu disc electrode. 0.2 M $KHCO_3$, −5 mA cm^{-2}.
[b]Estimated using the error propagation method.

As revealed in Table 3.3, the total unaccounted current efficiency cannot be fully attributed to measurement uncertainties from mass flow rates and GC + HPLC calibrations, which suggests other sources of uncertainties, e.g. use of ideal gas law estimation when calculating current efficiencies, or the presence of other products not detected by our GC + HPLC method. Another contribution to the unaccounted current efficiency that is especially significant for the first few GC measurements is the dilution of the gas effluent by the volume between the headspace of the electrochemical cell and the GC. By approximating this volume as a CSTR (see Appendix 3), steady-state conditions can only be achieved after more than 15 minutes for a 50 ml volume, which is approximately the headspace volume of the RCE set-up. Hence, the dilution effect of the product gas on the total current efficiency is more prominent in the RCE set-up, in contrast to the planar disc electrode set-up where the headspace is much smaller, i.e. approximately 10 ml which requires more than 5 minutes to reach steady-state. Nevertheless, as our electrolysis experiments are 10 hours long, the dilution effect is usually limited to only the first two or three data points, i.e. within the first hour of electrolysis. Current efficiencies can also be underestimated due to saturation of the catholyte with the product gases formed during electrolysis; however, we point out that the partial pressure of the products gases in question are relatively much lower compared to CO_2 in the gas effluent, and that their solubilities are also significantly lower (by 10 times or more compared to that of CO_2) [102, 117].

More details on GC parameters, calibration and uncertainty analysis are given in Appendix 4, while similar information for HPLC is given in Appendix 5.

3.6 Experimental challenges

Throughout the course of this work, several experimental challenges were encountered. Some of the more notable ones are described in this section.

One of the experimental challenges encountered relates to the mechanical polishing of Cu to produce a mirror finish. As described in section 3.3, Cu electrodes are mechanically polished to a mirror finish using silicon carbide (SiC) papers and alumina slurries. Occasionally, however, polishing with SiC papers have inadvertently caused the transfer of SiC particles onto the Cu surface. The SiC particles (confirmed by EDS) are shown by SEM to be firmly embedded onto the Cu surface (Figure 3.8), and our efforts to remove them by ultra-sonication have been unsuccessful. Based on our results, the influence of these embedded SiC particles and the mechanisms by which they affect CO_2 reduction is

inconclusive. Briefly, in the phosphate buffer electrolyte, CO_2 reduction performed on Cu surfaces embedded with SiC particles has consistently shown significant suppression of CO_2 reduction activity compared to a SiC-free surface at similar potentials. However, when performed in the $KHCO_3$ electrolyte, a SiC-embedded surface has occasionally produced high CO_2 reduction activity similar to that observed on a SiC-free surface. These results possibly suggest a complex mechanism that involves an interaction between the SiC particles and adsorbed anions. Nevertheless, to avoid using Cu surfaces with large amounts of SiC-embedded particles in our experiments, all Cu electrodes after polishing with SiC papers were first observed with the naked eye or under an optical microscope. With the naked eye, if the amount of embedded SiC particles is high, the electrode surface will usually appear "cloudy" instead of a pristine mirror finish. Even if a mirror finish is obtained, the polished electrode is further observed under the SEM to verify that the amount of embedded SiC particles is minimal.

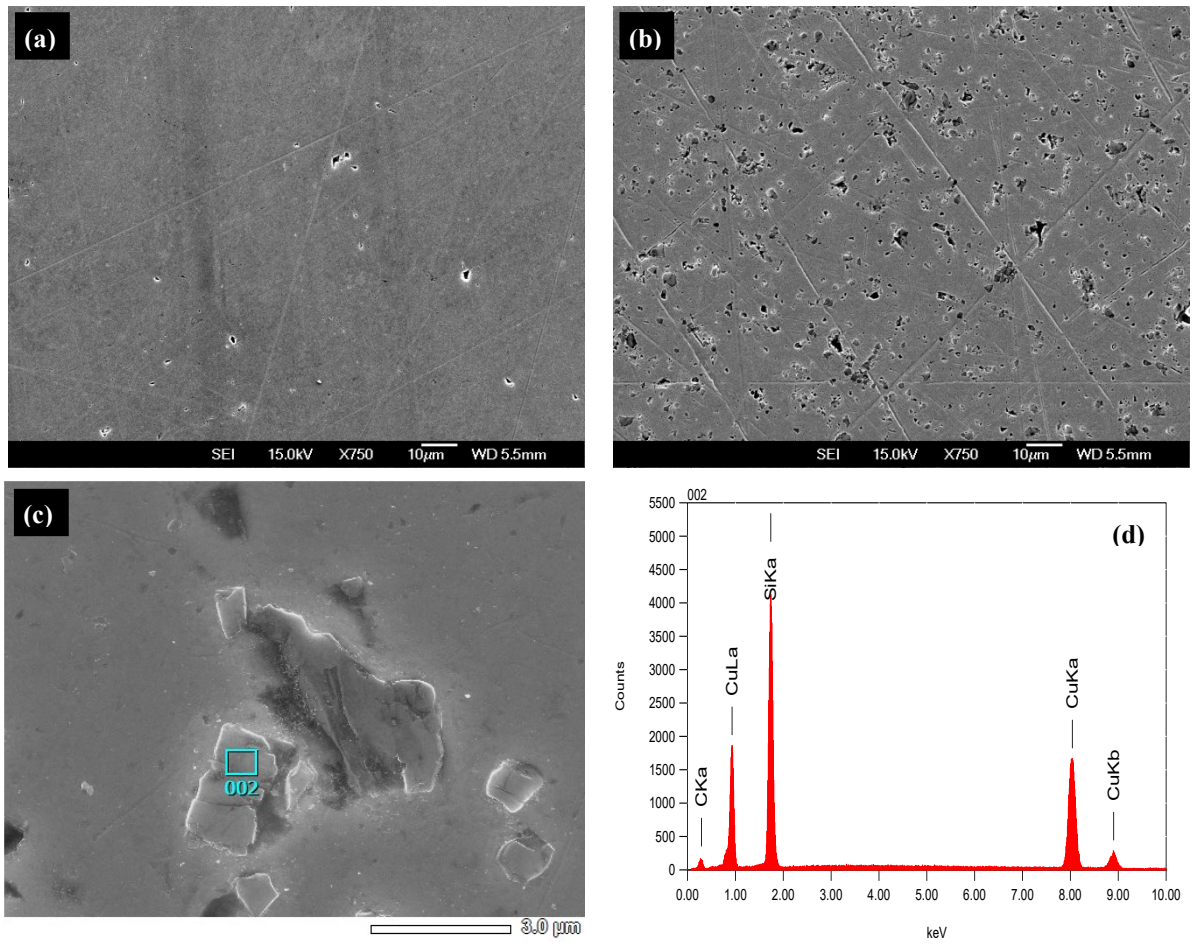

Figure 3.8: SEM images of polycrystalline Cu after mechanical polishing (a) without and (b) with embedded SiC particles. EDS analysis, (c) and (d), shows that the embedded particles are SiC.

Another notable experimental difficulty pertains to the execution of potentiostatic electrolysis using the planar disc electrode set-up. The difficulties are generally caused by large solution resistances due to the need to place the reference junction at a further position to minimise the inductance like feature in the EIS spectra (Figure 3.7), the effects of which are currently unknown, and the relatively small electrolyte volume (30 to 35 ml) which augments the rate of decrease of the solution resistance with electrolysis time due to the selective transport of K^+ to the catholyte through the cation exchange membrane (Figure 3.9). Large solution resistances are generally not ideal for potentiostatic

electrolysis since any remaining uncompensated resistance, if significant enough, can cause considerable fluctuations in the corrected working potential when the current density varies, which almost always occurs for CO_2 reduction on Cu electrodes due to transient changes such as surface oxide reduction, restructuring of crystal orientation and electrode poisoning. The variation in working potential would probably be less if the current density were small; however larger current densities are usually preferred for bulk CO_2 reduction electrolysis to enable easier product detection and analysis. The unpredictable variation in current density also poses a problem in positive feedback compensation when constant potential electrolysis is in progress, since the rate of decrease of the solution resistance, which depends on the flux of K^+ and hence the current density (Figure 3.9b), cannot be estimated in advance to ensure compensation of not more than 75% of the solution resistance, above which instrument instabilities can occur. Due to these complications, all reported electrolysis experiments using the planar disc electrode set-up were performed under constant current, and any effects on reaction selectivity by changes in electrode potential during constant current measurements were appropriately attributed using existing results in the literature.

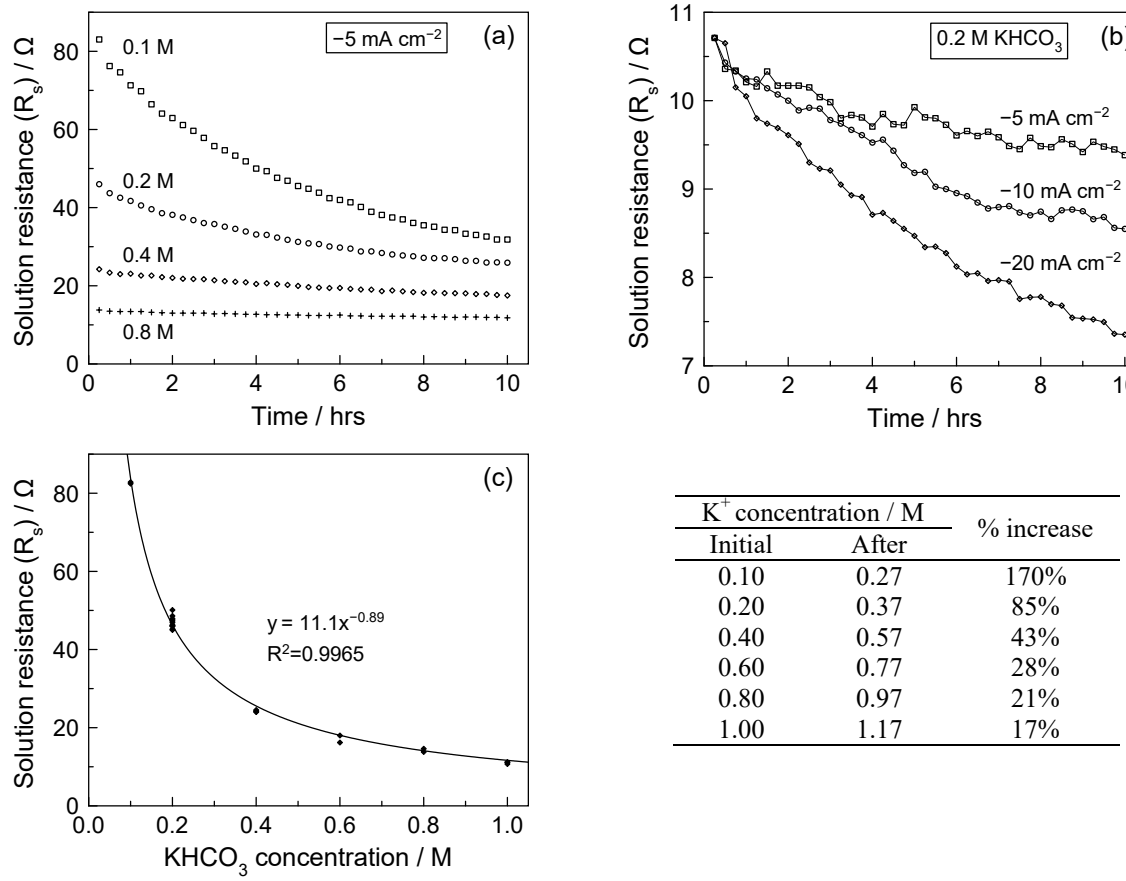

K^+ concentration / M		% increase
Initial	After	
0.10	0.27	170%
0.20	0.37	85%
0.40	0.57	43%
0.60	0.77	28%
0.80	0.97	21%
1.00	1.17	17%

Figure 3.9: Changes in measured solution resistance with electrolysis time as a function of (a) initial $KHCO_3$ concentration at −5 mA cm^{-2} (total current −15.71 mA), and (b) current density for 0.2 M $KHCO_3$. Connecting lines are to guide the eye. (c) Relationship between measured solution resistance and $KHCO_3$ concentration before the start of electrolysis. Inset table shows calculated K^+ concentration in the catholyte after 10 hours of electrolysis at −15.71 mA assuming K^+ to be the principal charge carrier.

The selective transfer of K^+ to the catholyte also introduces other complications, one of which is the gradual change in concentrations of species involved in the $CO_2/HCO_3^-/CO_3^{2-}$ equilibria. This change is effectively an increase in the concentration of $KHCO_3$, and hence the buffer capacity of the bulk electrolyte with time, and poses an additional factor that needs to be accounted for during the

interpretation of results since the product distribution of CO_2 reduction has been shown to be strongly dependent on the buffer capacity of the electrolyte (see section 2.3.2). The increase in K^+ concentration could also influence CO_2 reduction through the cationic effect, where the adsorption of large cations such as K^+ have been suggested to affect product selectivity (see section 2.3.2), and through a modest decrease in the solubility of CO_2 with increasing salt content due to the "salting-out" effect* [75, 220, 221], which can introduce further mass transport limitations. These complications may or may not have a significant impact on experimental results, but nevertheless, their contribution should not be so quickly dismissed and be correctly attributed when appropriate.

* At 25 °C and 1 atm CO_2 pressure, the equilibrium concentration of CO_2 is 33 mM in a solution of 0.2 M ionic strength, and 28 mM at 1.0 M ionic strength. Values were calculated using an empirical equation provided by Wigley and Plummer [219].

4 Mathematical Model for CO_2 Reduction

4.1 Introduction

This chapter details the derivation and development of a mathematical model for CO_2 reduction that aims to estimate the interfacial concentrations of species at the electrode surface. As the conditions near the electrode surface, mainly the pH and CO_2 concentration, are oftentimes quite different from the bulk solution during typical current densities of CO_2 reduction, it is important that the interfacial conditions be estimated so that their effects can be correctly attributed. The model presented here is largely based on the model initially developed by Gupta et al. [44] but with several added improvements; however for completeness sake, the entire model which includes most of the original by Gupta et al. is presented here in its entirety. The major differences between the model presented here and that of Gupta et al. are:

(i) The inclusion of differential equations to account for changes in the bulk electrolyte due to electrode reactions and the selective transfer of K^+ from the anolyte to the catholyte, both of which can affect interfacial concentrations through changes in CO_2 solubility, CO_2 equilibria and pH of the bulk electrolyte. The simulated bulk concentrations with time are hence used as the boundary condition at the interface between the bulk electrolyte and the diffusion boundary layer, instead of a fixed boundary condition as used by Gupta et al..
(ii) The current efficiency values which define the boundary condition at the electrode surface are updated with time using values measured during electrolysis, instead of fixed specified current efficiency values as used by Gupta et al..
(iii) The inclusion of ionic strength and activity coefficients in the calculations using the Davies equation [75].

The derivation of the model is presented in sections 4.2 and 4.3, where section 4.2 details how changes in the concentrations of species in the bulk electrolyte during electrolysis are simulated, while section 4.3 presents a finite difference model (largely adapted from Gupta et al.) that is used to estimate the interfacial concentrations. Section 4.4 gives some examples on using the model to estimate interfacial concentrations during CO_2 reduction. The model is not without its limitations and assumptions, the more important ones of which are generally the neglect of water dissociation kinetics, i.e. the assumption that the water dissociation reaction is always at equilibrium, and the neglect of electro-osmosis effects across the membrane.

4.2 Bulk electrolyte model

This section presents a model that was developed to simulate changes in the bulk electrolyte during CO_2 reduction electrolysis. Consider the catholyte of an electrochemical cell undergoing CO_2 reduction electrolysis such as one depicted in Figure 4.1. Within the boundaries of the catholyte, there are generally four processes that are of importance:

(i) The continuous saturation of the catholyte with CO_2 through gas bubbling at a constant flow rate.
(ii) The selective transfer of K^+ into the catholyte from the anolyte through the Nafion membrane.
(iii) The electrochemical reactions which consume CO_2, H_2O and/or H^+, and generate OH^- and electrolysis products (H_2, CO, CH_4, $HCOO^-$ etc.).
(iv) CO_2 equilibria reactions (see Appendix 6).

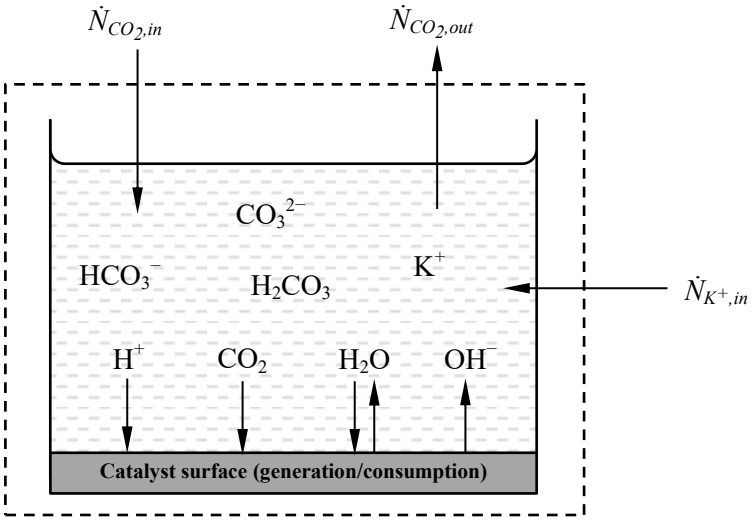

Figure 4.1: Mass flows, generation and consumption of species to/from and within the catholyte of an electrochemical cell undergoing CO_2 reduction electrolysis. The mass balances on electrolysis products, H_2CO_3 and H_2O are not included in the model.

Because most of the major products of CO_2 reduction are uncharged and their solubilities are much lower than that of CO_2 (generally about 10 times lower), it is assumed that their interactions with each other and with other species in the electrolyte are negligible; hence, the generation and mass outflow rates of electrolysis products are assumed equal and therefore not included in the model. For simplicity, the interaction of $HCOO^-$ with other species is also assumed to be relatively minor since its concentration in the catholyte after electrolysis is usually only about 0.01 M. On the other hand, important interactions between species occur through CO_2 equilibria and water ionisation, as given by reactions (4.1) to (4.3). In the alkaline form, CO_2 equilibria can be written as reactions (4.4) and (4.5), which are more dominant in cases where the interfacial pH is alkaline due to the use of low buffer capacity electrolytes [44]. The rate constants for reactions (4.4) and (4.5) are given in Table 4.1.

$$CO_2 + H_2O \leftrightarrow H_2CO_3 \leftrightarrow H^+ + HCO_3^- \quad \text{R(4.1)}$$

$$HCO_3^- \leftrightarrow H^+ + CO_3^{2-} \quad \text{R(4.2)}$$

$$H_2O \leftrightarrow H^+ + OH^- \quad \text{R(4.3)}$$

$$CO_2 + OH^- \overset{k1}{\leftrightarrow} HCO_3^- \quad \text{R(4.4)}$$

$$HCO_3^- + OH^- \overset{k2}{\leftrightarrow} CO_3^{2-} + H_2O \quad \text{R(4.5)}$$

Table 4.1: Rate constants for CO_2 equilibria reactions (4.4) and (4.5) at 25 °C [33, 44].

Reaction	Forward rate constant / M^{-1} s^{-1}	Reverse rate constant[a] / s^{-1}
(4.4)	$k_{1f} = 5.93 \times 10^3$	$k_{1r} = 1.28 \times 10^{-4}$
(4.5)	$k_{2f} = 1 \times 10^8$	$k_{2r} = 1.16 \times 10^4$

[a]The reverse rate constants used in this model are slightly different from that used by Gupta et al.. The values given here are more consistent with the equilibrium constants of the reactions.

By specifying the catholyte as the control volume (Figure 4.1) and incorporating the four major processes mentioned above, mass balances for CO_2, HCO_3^-, CO_3^{2-}, OH^- and K^+ are derived. Due to

its negligible concentration, H_2CO_3 is not included in the model[*]. H_2O is also not included since its concentration does not change significantly after electrolysis[†]. Because water dissociation is assumed to always be in equilibrium, the concentration of H^+ (and hence the pH) is calculated from that of OH^- using the equilibrium constant of reaction (4.3) through $pH = -\log K_w + \log \gamma_{OH^-} + \log [OH^-]$, where K_w is the water dissociation constant and γ_{OH^-} is the activity coefficient of OH^-; hence the mass balance for H^+ is not derived. Assuming perfect mixing and a constant volume, V for the catholyte, the mass balances for CO_2, HCO_3^-, CO_3^{2-}, OH^- and K^+ are derived and given as equations (4.1) to (4.5), which form into a system of ordinary differential equations (ODE).

$$\text{Accumulation} = \text{Flow in} - \text{Flow out} + \text{Generation} - \text{Consumption}$$

$$\frac{d[CO_2]}{dt} = \left(\frac{\dot{N}_{CO_2,in} - \dot{N}_{CO_2,out}}{V}\right) - k_{1f}[CO_2][OH^-] + k_{1r}[HCO_3^-] - CO_{2,con} \quad \text{E(4.1)}$$

$$\frac{d[HCO_3^-]}{dt} = k_{1f}[CO_2][OH^-] - k_{1r}[HCO_3^-] - k_{2f}[HCO_3^-][OH^-] + k_{2r}[CO_3^{2-}] \quad \text{E(4.2)}$$

$$\frac{d[CO_3^{2-}]}{dt} = k_{2f}[HCO_3^-][OH^-] - k_{2r}[CO_3^{2-}] \quad \text{E(4.3)}$$

$$\frac{d[OH^-]}{dt} = -k_{1f}[CO_2][OH^-] + k_{1r}[HCO_3^-] - k_{2f}[HCO_3^-][OH^-] + k_{2r}[CO_3^{2-}] + OH^-_{gen} \quad \text{E(4.4)}$$

$$\frac{d[K^+]}{dt} = \frac{\dot{N}_{K^+,in}}{V} \quad \text{E(4.5)}$$

The first term on the right hand side of equation (4.1) can be expressed as equation (4.6), which accounts for the gas-liquid transfer of CO_2 into the catholyte and was derived based on the two-film theory assuming that the resistance to mass transfer is mainly at the liquid-side film (Appendix 8). The value of A, which is the total gas-liquid interfacial area, is experimentally difficult to estimate because CO_2 is introduced into the catholyte via vigorous gas bubbling. However, since A and V are constants, they can be grouped together with the mass transfer coefficient to form a single constant, i.e. $\beta = K_M A/V$, which we can provide an estimation for as explained later. With $[CO_2]$ being the instantaneous CO_2 concentration, the concentration difference ($[CO_2]_{eq} - [CO_2]$) serves as the driving force for CO_2 transfer into the catholyte.

$$\frac{\dot{N}_{CO_2,in} - \dot{N}_{CO_2,out}}{V} = \frac{K_M A}{V}\left([CO_2]_{eq} - [CO_2]\right) = \beta\left([CO_2]_{eq} - [CO_2]\right) \quad \text{E(4.6)}$$

where			
	K_M	Overall mass transfer coefficient	m s^{-1}
	A	Total gas-liquid interfacial area	m^2
	$[CO_2]_{eq}$	$[CO_2]$ at equilibrium with gas phase CO_2	M

The rate of CO_2 consumption by electrochemical reduction, $CO_{2,con}$ is expressed as equation (4.7) in

[*] The concentration of H_2CO_3 is only about 10^{-3} that of CO_2 as the hydration of CO_2 to H_2CO_3 is much slower compared to the subsequent ionisation of H_2CO_3; Since H_2CO_3 is uncharged and has no particular significance in the acid-base equilibria, it is usually grouped with the relatively more concentrated dissolved CO_2 as $[CO_2]_{total} = [H_2CO_3] + [CO_2]$. For simplicity, we will just use $[CO_2]$ to refer to $[H_2CO_3] + [CO_2]$.

[†] After electrolysis at −15 mA for 10 hours, assuming 100% current efficiency toward H_2 production, the amount of H_2O consumed is only 0.05 ml.

terms of the total current and the current efficiencies of CO_2 reduction products. Similarly, the OH^- generation term, OH^-_{gen}, is expressed as equation (4.8), which includes hydrogen evolution in addition to the CO_2 reduction reactions. Note the stoichiometric coefficients (see Table 1.1) used to relate moles e^- with moles CO_2 and moles OH^- in equations (4.7) and (4.8) respectively. The rate of transfer of K^+ into the catholyte is expressed in terms of the total current as equation (4.9). All remaining terms in the mass balance equations are rate terms based on CO_2 equilibria, i.e. reactions (4.4) and (4.5).

$$CO_{2,con} = \frac{|i_{total}|}{VF}\left(\frac{CE_{HCOO^-}}{n_{HCOO^-}} + \frac{CE_{CO}}{n_{CO}} + \frac{CE_{CH_4}}{n_{CH_4}} + 2\frac{CE_{C_2H_4}}{n_{C_2H_4}} + 2\frac{CE_{C_2H_6}}{n_{C_2H_6}}\right) \quad \text{E(4.7)}$$

$$OH^-_{gen} = \frac{|i_{total}|}{VF}\left(\frac{CE_{HCOO^-}}{n_{HCOO^-}} + 2\frac{CE_{CO}}{n_{CO}} + 8\frac{CE_{CH_4}}{n_{CH_4}} + 12\frac{CE_{C_2H_4}}{n_{C_2H_4}} + 14\frac{CE_{C_2H_6}}{n_{C_2H_6}} + 2\frac{CE_{H_2}}{n_{H_2}}\right) \quad \text{E(4.8)}$$

$$\dot{N}_{K^+,in} = \frac{|i_{total}|}{F} \quad \text{E(4.9)}$$

where			
	i_{total}	Total cathodic current	mA
	F	Faraday constant	96485 C per mol e^-
	CE_j	Current efficiency for species j	[-]
	n_j	Number of moles e^- to form 1 mole of species j	[-]

Hence, with the initial concentrations of CO_2, HCO_3^-, CO_3^{2-}, OH^- and K^+, along with measured and calculated values for the various parameters required in equations (4.6) to (4.9), the system of ODEs, i.e. equations (4.1) to (4.5) can be readily solved. In our case, the equations were solved in MATLAB (see Appendix 9).

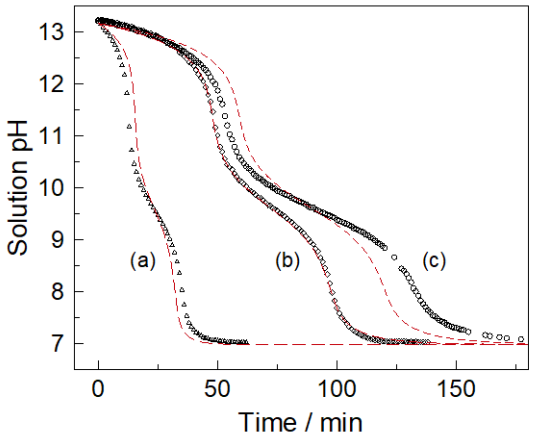

Figure 4.2: Change in pH of a 0.2 M KOH solution undergoing CO_2 saturation through CO_2 bubbling (1 atm pressure) in (a) the planar disc electrode cell (30 ml solution, 10 ml min^{-1} CO_2), (b) a typical volumetric cylinder (400 ml solution, 20 ml min^{-1}) and (c) the rotating cylinder electrode cell (400 ml solution, 20ml min^{-1}). The bulk electrolyte model (dashed line) is fitted to the experimentally measured pH with time using a β value of (a) 3.25×10^{-3}, (b) 1.05×10^{-3}, and (c) 0.85×10^{-3}.

Regarding β, obtaining a directly calculated value based on the two-film model, or any other gas-liquid transfer model in fact, is difficult since the liquid film thickness and the total gas-liquid interfacial area cannot be readily measured. Instead, an estimate of the value for β is obtained by

fitting the model to the measured change in pH with time of a KOH solution bubbled with a constant flow rate of CO_2 (1 atm pressure) without any electrolysis current (Figure 4.2)*. As β is likely a function of the electrochemical cell's hydrodynamic conditions, the model is fitted to both the planar disc electrode and the rotating cylinder electrode (RCE) set-up at the CO_2 flow rates typically used for each cell, i.e. 10 ml min^{-1} and 20 ml min^{-1} respectively. The initial conditions in this case only involve the concentrations of K^+ and OH^-, which are both equal to the concentration of KOH used. Since there is no electrolysis current, equations (4.7) to (4.9) equals zero. Overall, the model fits the experimental data with reasonable accuracy (Figure 4.2) and the estimated β values are 3.25×10^{-3} and 0.85×10^{-3} for the planar disc electrode and RCE set-up respectively (at their respective CO_2 flow rates). Interestingly, the model fit is much more accurate for the case where the CO_2 saturation of KOH was performed in a measuring cylinder. The deviation of the model observed for the electrochemical cells could possibly be due to certain effects of the cell geometry on the homogeneity of the solution during CO_2 saturation.

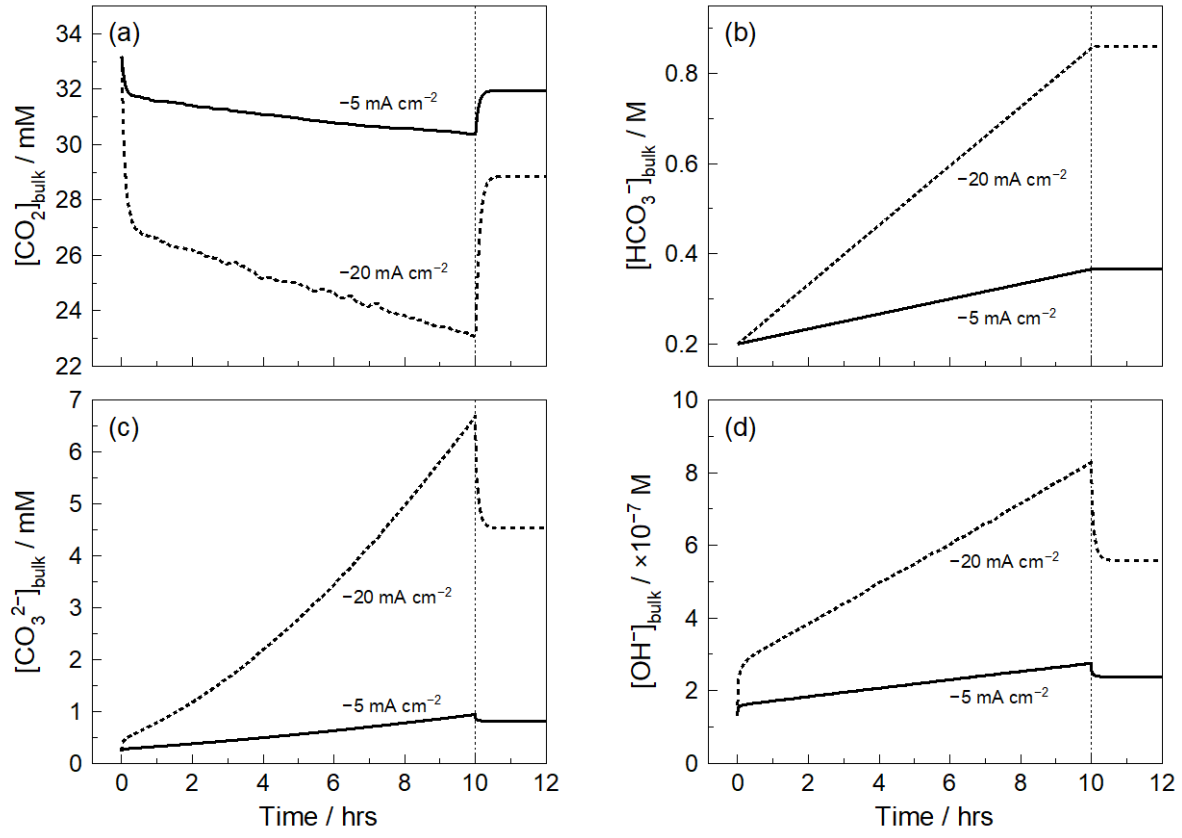

Figure 4.3: Change in concentrations of (a) CO_2, (b) HCO_3^-, (c) CO_3^{2-} and (d) OH^- in the bulk electrolyte (35 ml of CO_2 saturated 0.2 M $KHCO_3$) with time during CO_2 reduction on a polished Cu planar disc at -5 mA cm^{-2} (solid line) and -20 mA cm^{-2} (dashed line) for 10 hours. The model simulation continues for an additional 2 hours after the end of electrolysis, where the bulk electrolyte concentrations tend back to equilibrium. The electrode geometrical area is 3.14 cm^2.

Using the estimated β values, the change with time of the bulk electrolyte during electrolysis can be simulated, the results of which for a typical CO_2 reduction experiment on polished Cu are given in Figures 4.3 and 4.4 for the planar disc electrode and the RCE respectively.

* Saturating a KOH solution with CO_2 will eventually result in a CO_2 saturated $KHCO_3$ solution when equilibrium is achieved.

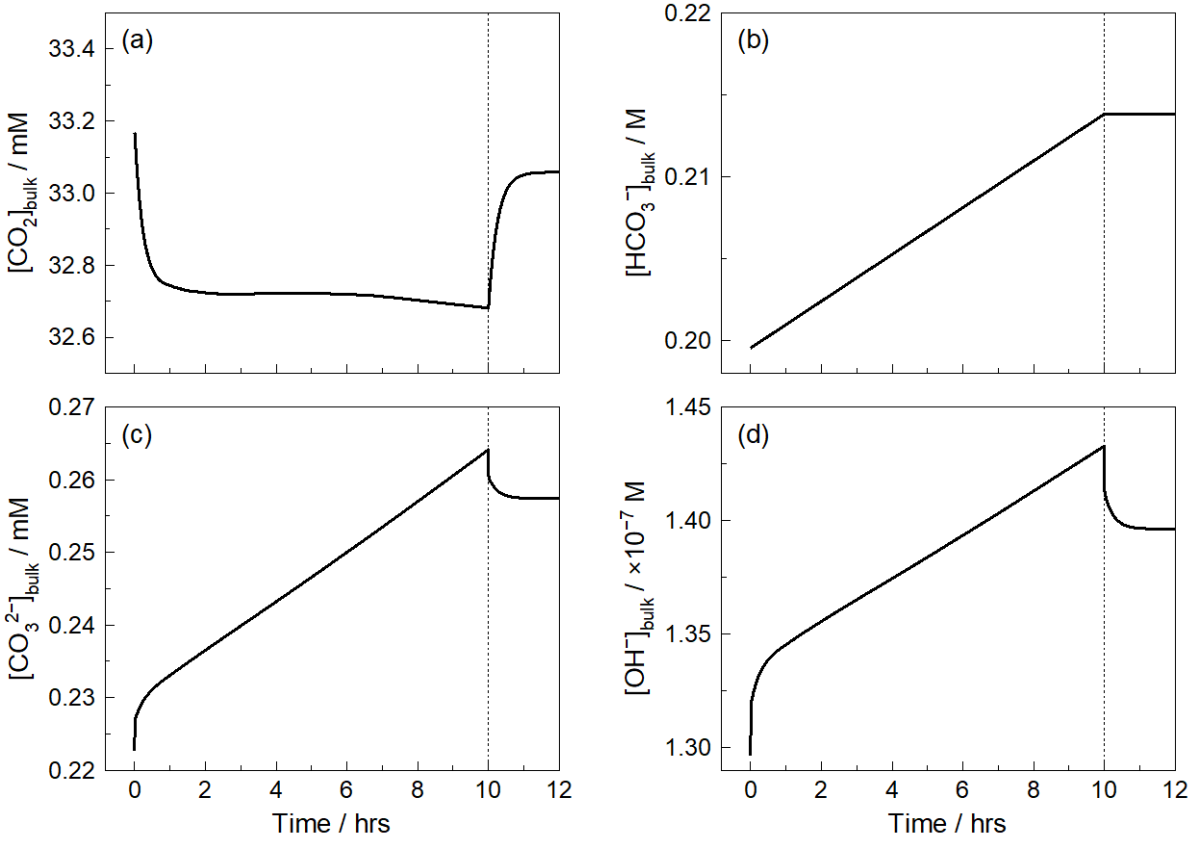

Figure 4.4: Change in concentrations of (a) CO_2, (b) HCO_3^-, (c) CO_3^{2-} and (d) OH^- in the bulk electrolyte (400 ml of CO_2 saturated 0.2 M $KHCO_3$) with time during CO_2 reduction on a polished Cu RCE at −5 mA cm^{-2} for 10 hours. The model simulation continues for an additional 2 hours after the end of electrolysis, where the bulk electrolyte concentrations tend back to equilibrium. The electrode geometrical area is 3.0 cm^2 (1.5 cm outer diameter, 0.64 cm height) and the rotation rate is 10 rpm.

From the model simulation results, it is shown that the concentrations of species in the bulk electrolyte are generally not in equilibrium during electrolysis, and is clearly more pronounced at higher current densities and smaller electrolyte volumes. This is likely due to the accumulation of OH^- (produced from the electrode reactions), the consumption of which by CO_2 through buffering is relatively slow (5.93×10^3; reaction (4.4)). The non-equilibrium condition of the bulk electrolyte throughout electrolysis is further supported by measurements of the bulk pH with time, where the bulk pH is also shown to be consistently above the equilibrium value (Figure 4.5). After electrolysis, where the current is zero, the model shows the bulk electrolyte concentrations and pH tending back to equilibrium (with 1 atm CO_2 pressure).

In the original model by Gupta et al. [44], the concentrations of species in the bulk electrolyte are assumed to be constant and at equilibrium, and were used as the boundary condition at the interface between the bulk electrolyte and the diffusion boundary layer. However, it is clear that the bulk electrolyte's composition is not constant and neither is it at equilibrium throughout electrolysis, especially for high current densities and small electrolyte volumes. Hence, in our model, the simulated transient bulk concentrations were used as the boundary condition instead.

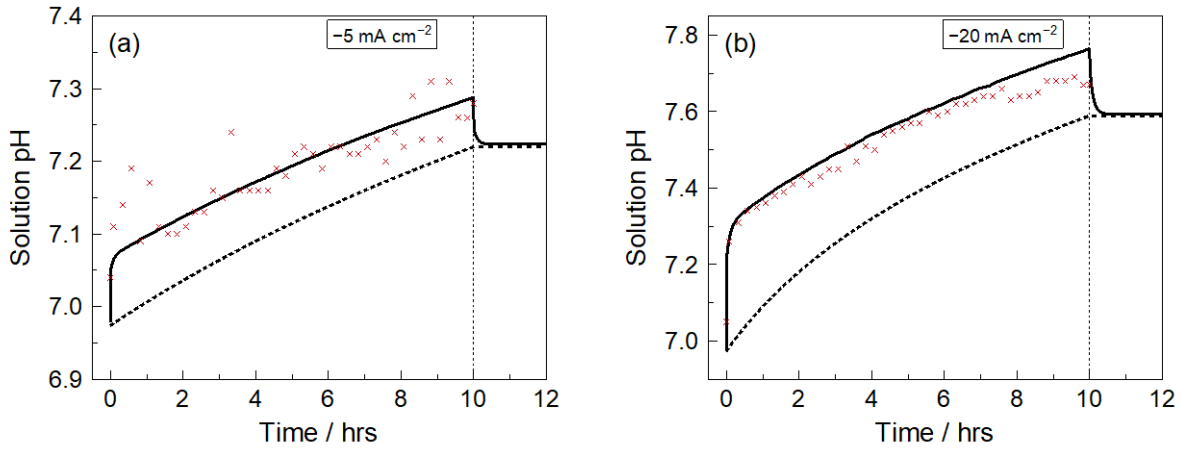

Figure 4.5: Change in bulk pH with time during CO_2 reduction on a polished Cu planar disc at (a) −5 mA cm^2 and (b) −20 mA cm^2 for 10 hours. The pH measurements (×) are overlaid with the model simulations (solid line). During electrolysis, the bulk pH is shown to be consistently higher than the equilibrium pH (dashed line).

4.3 Finite difference model

This section presents a finite difference model developed to estimate interfacial concentrations at the electrode surface during CO_2 reduction electrolysis, and is mainly adapted from the original model by Gupta et al. [44].

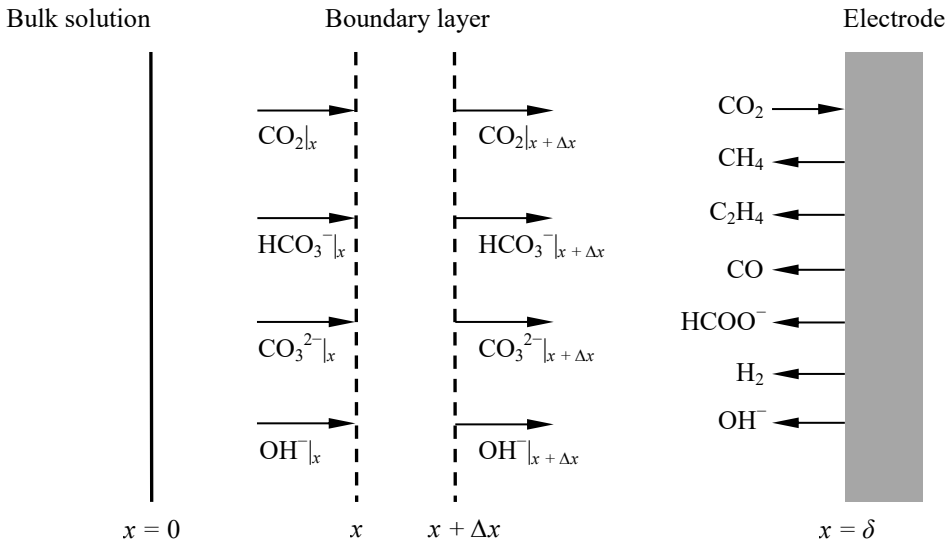

Figure 4.6: Illustration of the diffusion boundary layer between the bulk solution and the electrode surface, adapted from [44].

Consider the diffusion boundary layer between the bulk solution and the electrode surface as illustrated in Figure 4.6. Within this boundary layer, film theory is assumed to be applicable where velocity gradients and convective effects are assumed negligible. Hence, within the strip of solution with volume ΔV, cross-sectional area A, and thickness Δx as depicted in Figure 4.6, a general mass balance for a species φ written as equation (4.14) can be derived by invoking Fick's first law, where N_φ and D_φ are the molar quantity and diffusion coefficient of species φ respectively.

$$\text{Accumulation} = \text{Flow in} - \text{Flow out} + \text{Generation} - \text{Consumption}$$

$$\frac{\delta N_\varphi}{\delta t} = -D_\varphi A \left.\frac{\delta[\varphi]}{\delta x}\right|_x - \left(-D_\varphi A \left.\frac{\delta[\varphi]}{\delta x}\right|_{x+\Delta x}\right) + \text{Generation} - \text{Consumption} \quad \text{E(4.10)}$$

$$\frac{\delta N_\varphi}{\delta t} = D_\varphi A \left(\left.\frac{\delta[\varphi]}{\delta x}\right|_{x+\Delta x} - \left.\frac{\delta[\varphi]}{\delta x}\right|_x\right) + \text{Generation} - \text{Consumption} \quad \text{E(4.11)}$$

$$\left(\frac{1}{\Delta V}\right)\frac{\delta N_\varphi}{\delta t} = \frac{D_\varphi}{\Delta x}\left(\left.\frac{\delta[\varphi]}{\delta x}\right|_{x+\Delta x} - \left.\frac{\delta[\varphi]}{\delta x}\right|_x\right) + \text{Generation} - \text{Consumption} \quad \text{E(4.12)}$$

$$\frac{\delta[\varphi]}{\delta t} = D_\varphi \frac{\left(\left.\frac{\delta[\varphi]}{\delta x}\right|_{x+\Delta x} - \left.\frac{\delta[\varphi]}{\delta x}\right|_x\right)}{\Delta x} + \text{Generation} - \text{Consumption} \quad \text{E(4.13)}$$

By taking the limit of $\Delta x \to 0$,

$$\frac{\delta[\varphi]}{\delta t} = D_\varphi \frac{\delta^2[\varphi]}{\delta x^2} + \text{Generation} - \text{Consumption} \quad \text{E(4.14)}$$

The generation and consumption terms for a certain species within the solution volume ΔV is derived from the equilibrium reactions between the various species existing in the solution volume, i.e. reactions (4.4) and (4.5). Hence, using the rate constants given in Table 4.1, the mass balances for CO_2, HCO_3^-, CO_3^{2-} and OH^- can be written as equations (4.15) to (4.18), forming a set of partial differential equations (PDEs).

$$\frac{\delta[CO_2]}{\delta t} = D_{CO_2}\frac{\delta^2[CO_2]}{\delta x^2} - k_{1f}[CO_2][OH^-] + k_{1r}[HCO_3^-] \quad \text{E(4.15)}$$

$$\frac{\delta[HCO_3^-]}{\delta t} = D_{HCO_3^-}\frac{\delta^2[HCO_3^-]}{\delta x^2} + k_{1f}[CO_2][OH^-] - k_{1r}[HCO_3^-] - k_{2f}[HCO_3^-][OH^-] + k_{2r}[CO_3^{2-}] \quad \text{E(4.16)}$$

$$\frac{\delta[CO_3^{2-}]}{\delta t} = D_{CO_3^{2-}}\frac{\delta^2[CO_3^{2-}]}{\delta x^2} + k_{2f}[HCO_3^-][OH^-] - k_{2r}[CO_3^{2-}] \quad \text{E(4.17)}$$

$$\frac{\delta[OH^-]}{\delta t} = D_{OH^-}\frac{\delta^2[OH^-]}{\delta x^2} - k_{1f}[CO_2][OH^-] + k_{1r}[HCO_3^-] - k_{2f}[HCO_3^-][OH^-] + k_{2r}[CO_3^{2-}] \quad \text{E(4.18)}$$

Note that the mass balances for H_2CO_3, H_2O and H^+ are not considered in the finite difference model for the same reasons expounded in section 4.2. For K^+, its concentration is assumed to be uniform throughout the bulk solution and the diffusion boundary layer; hence a mass balance on K^+ over the strip of solution is unnecessary. On the other hand, concentration gradients do exists for dissolved electrolysis products which transfer away from the electrode surface after their formation. However, because most of the major electrolysis products on Cu electrodes ($HCOO^-$ being the main exception) are gaseous at the ambient operating conditions employed, the modelling of mass transfer of dissolved products is additionally complicated by gas-liquid transfer through gas bubbles and its accompanying kinetics. Since the electrolysis products have no direct involvement in the CO_2 equilibria reactions, it

is sufficient that their mass transfer away from the electrode surface be understood qualitatively so that the model can be simplified. The diffusion coefficients for the various species at infinite dilution and 25 °C are listed in Table 4.2. These values, following the model by Gupta et al., are corrected for the effects of viscosity, μ at various electrolyte concentrations (Table 4.3) using the Stokes-Einstein's equation, where $D\mu/T$ = constant at T = 298 K.

Table 4.2: Diffusion coefficients for CO_2, HCO_3^-, CO_3^{2-} and OH^- at infinite dilution and 25 °C [102].

Species	D^0 / m^2 s^{-1}
CO_2	1.91×10^{-9}
HCO_3^-	1.19×10^{-9}
CO_3^{2-}	9.23×10^{-10}
OH^-	5.27×10^{-9}

At x = 0, i.e. the interface between the bulk electrolyte and the diffusion boundary layer, the concentrations of species are equal to that of the bulk solution, written as equations (4.19) to (4.22). These equations form the boundary conditions at x = 0, and their time dependent values are obtained through simulation of the bulk electrolyte concentrations with electrolysis time using the bulk electrolyte model presented in the previous section.

$$[CO_2]_{x=0} = [CO_2]_{bulk} \quad \text{E(4.19)}$$

$$[HCO_3^-]_{x=0} = [HCO_3^-]_{bulk} \quad \text{E(4.20)}$$

$$[CO_3^{2-}]_{x=0} = [CO_3^{2-}]_{bulk} \quad \text{E(4.21)}$$

$$[OH^-]_{x=0} = [OH^-]_{bulk} \quad \text{E(4.22)}$$

At $x = \delta$, i.e. at the electrode surface, the boundary conditions relate to the consumption of CO_2 and generation of OH^- due to the electrode reactions, written as equations (4.23) to (4.26), where $CO_{2,con}$ and OH^-_{gen} are the molar consumption and generation rate per unit catholyte volume of CO_2 and OH^- as expressed in equations (4.7) and (4.8) respectively. Note that V is the total volume of the catholyte and A is the electrode geometrical area in equations (4.23) and (4.26). At t = 0, i.e. the initial conditions before the start of electrolysis, the concentrations of all species are simply their equilibrium values at the particular electrolyte concentration and CO_2 partial pressure. A list of equilibrium values calculated using the CO_2 equilibria equations (see Appendix 6) at various $KHCO_3$ concentrations and at 25 °C and 1 atm CO_2 pressure is given in Table 4.3.

$$D_{CO_2} \frac{\delta[CO_2]}{\delta x}\bigg|_{x=\delta} = -CO_{2,con}\left(\frac{V}{A}\right) \quad \text{E(4.23)}$$

$$D_{HCO_3^-} \frac{\delta[HCO_3^-]}{\delta x}\bigg|_{x=\delta} = 0 \quad \text{E(4.24)}$$

$$D_{CO_3^{2-}} \frac{\delta[CO_3^{2-}]}{\delta x}\bigg|_{x=\delta} = 0 \quad \text{E(4.25)}$$

$$D_{OH^-} \frac{\delta[OH^-]}{\delta x}\bigg|_{x=\delta} = OH^-_{gen}\left(\frac{V}{A}\right) \quad \text{E(4.26)}$$

Table 4.3: Equilibrium and viscosity values for CO_2 saturated $KHCO_3$ solutions at various concentrations at 25 °C and 1 atm CO_2 pressure (note: correction was made for the effects of ionic strength using the Davies equation for charged species, and the empirical equation by Wigley and Plummer for CO_2; see Appendix 6).

$[KHCO_3]$ / M	$[CO_2]_{eq}$ / M	$[HCO_3^-]_{eq}$ / M	$[CO_3^{-2}]_{eq}$ / M	$[OH^-]_{eq}$ / M	pH	μ / mPa s[a]
0.05	3.44×10^{-2}	5.00×10^{-2}	1.12×10^{-5}	3.25×10^{-8}	6.42	1.009
0.1	3.40×10^{-2}	9.99×10^{-2}	4.99×10^{-5}	6.49×10^{-8}	6.70	1.015
0.2	3.32×10^{-2}	2.00×10^{-1}	2.23×10^{-4}	1.30×10^{-7}	6.97	1.027
0.5	3.10×10^{-2}	4.97×10^{-1}	1.53×10^{-3}	3.23×10^{-7}	7.35	1.067
1	2.81×10^{-2}	9.88×10^{-1}	5.86×10^{-3}	6.42×10^{-7}	7.65	1.145

[a]Viscosity values were obtained from [44].

The thickness of the diffusion boundary layer, δ is generally a function of the hydrodynamics at the vicinity of the electrode surface. For a rotating cylinder electrode (RCE), a theoretical derivation by Gabe and Robinson [222, 223] of the mass transfer equation for turbulent flow* reveals the following dimensionless correlation given as equation (4.27), where *St*, *Re* and *Sc* are the dimensionless Stanton, Reynolds and Schmidt numbers respectively, and Φ is a constant which depends on the electrode cell geometry and roughness effects.

$$St = \Phi\left(Re^{-\frac{1}{3}}\right)\left(Sc^{-\frac{2}{3}}\right) \qquad \text{E(4.27)}$$

By substituting the dimensionless numbers in equation (4.27) with their respective constitutive parameters, i.e. $St = D/(\delta u)$, $Re = du\rho/\mu$ and $Sc = \mu/(\rho D)$, equation (4.28) for the diffusion boundary layer thickness can be obtained, where d is the RCE outer diameter, u is the peripheral velocity and ρ is the liquid density.

$$\delta = \frac{1}{\Phi}\left[\frac{D\mu d}{\rho u^2}\right]^{\frac{1}{3}} \qquad \text{E(4.28)}$$

The theoretical analysis by Gabe and Robinson agrees well with prior experimental investigations by Eisenberg et al. [225], who empirically deduced a mass transfer correlation for a smooth surface RCE, written as equation (4.29) that is currently widely accepted for RCE applications.

$$St = 0.0791(Re^{-0.3})(Sc^{-0.644}) \qquad \text{E(4.29)}$$

Hence, experimentally, the constant Φ is determined to be 0.0791, and the index exponents for *Re* and *Sc* are −0.3 and −0.644 respectively. Expressing equation (4.29) in terms of the mass transfer coefficient (k_L) and physical parameters relating to the RCE and electrolyte solution gives the more commonly used form of the RCE mass transfer correlation, written as equation (4.30).

$$k_L = 0.0791 d^{-0.3}\left(\frac{\mu}{\rho}\right)^{-0.344} D^{0.644} u^{0.7} \qquad \text{E(4.30)}$$

As $k_L = D/\delta$, the diffusion boundary layer thickness can be expressed as equation (4.31).

$$\delta = 12.64\left(\frac{D^{0.356}\mu^{0.344}d^{0.3}}{\rho^{0.344}u^{0.7}}\right) \qquad \text{E(4.31)}$$

* For all but the lowest rotation rates, the flow surrounding the RCE is turbulent. Generally, the transition from laminar to turbulent flow occurs at a *Re* value between 50 and 200 [224]. For a 1.5 cm outer diameter cylinder, a *Re* number of 200 corresponds to a rotation rate of about 15 rpm in water at ambient conditions.

Using equation (4.31), the calculated diffusion boundary layer thickness for a 1.5 cm RCE at various rotation rates in 0.2 M $KHCO_3$ at 25 °C is listed in Table 4.4. Generally, for stationary electrodes with no defined hydrodynamics, it is regarded that the diffusion layer thickness is limited to a value of about 500 μm [226]. However, as revealed in Table 4.4, the calculated thickness at very low rotation rates exceeds this limit, i.e. 700 μm at 10 rpm, which is quite unlikely considering the fact that gas bubbles are evolved at the electrode surface during electrolysis which will undoubtedly introduce some turbulence that reduces the overall effective thickness of the diffusion layer. Hence, to better reflect the actual hydrodynamic conditions at the electrode surface during electrolysis, the diffusion layer thickness at rotation rates below 160 rpm was adjusted through scaling so that the maximum layer thickness is limited to only 200 μm at 10 rpm.

Table 4.4: Diffusion boundary layer thickness as calculated using equation (4.31) for a 1.5 cm RCE at various rotation rates in 0.2 M $KHCO_3$ at 25 °C.

Rotation rate (rpm)	*Re*	Diffusion layer thickness (δ) / μm[a]	
		As calculated	Adjusted[b]
10	115	707	*202*
20	229	435	*187*
40	459	268	*165*
80	918	165	*135*
160	1835	101	101
320	3671	62	62
640	7342	38	38
1280	14683	24	24
2560	29366	15	15

[a]An average of the diffusion layer thickness values calculated using the diffusion coefficients of CO_2, HCO_3^-, CO_3^{2-} and OH^- was taken.
[b]Adjusted values by scaling are printed in *italics*.

With the initial and boundary conditions adequately specified and defined, the set of PDEs, i.e. equations (4.15) to (4.18) can be readily solved in MATLAB (see Appendix 10). Some examples of the model simulation of interfacial concentrations during CO_2 reduction electrolysis are presented in section 4.4.

4.4 Estimation of interfacial concentrations

From the finite difference model developed in the previous section, it can be shown that the interfacial concentrations at the electrode surface are strongly dependent on the bulk concentrations, thickness of the diffusion layer, and the electrode reaction rates. Experimentally, these relate to the buffer capacity of the $KHCO_3$ electrolyte (i.e. $KHCO_3$ concentration), the hydrodynamics of the cell (e.g. stirring rate), and the current density of the electrode reactions. To illustrate, Figure 4.7 present model estimations of the interfacial pH and its dependence on these parameters, assuming equilibrium bulk concentrations and typical current efficiency values of CO_2 reduction. From the model estimations, it is clear that the electrode surface conditions are usually quite different from that of the bulk solution at typically reported experimental conditions. For example, in terms of the interfacial pH, an increase by as much as 2 pH units is possible in 0.2 M $KHCO_3$ at −5 mA cm^{-2} for a diffusion layer thickness of 100 μm. The difference between interfacial and bulk pH decreases with increasing $KHCO_3$ concentration due to the increased buffer capacity of the electrolyte. Additionally, the pH increase also becomes lesser at smaller diffusion layer thicknesses, which represents better mass transport rates such as those caused by a higher degree of mixing, and at lower current densities due to slower consumption and generation rates of CO_2 (which also acts as a buffer) and OH^- respectively. Since the product distribution of CO_2 reduction has been shown to be highly sensitive to pH and CO_2

concentration (see section 2.3.3), the model simulation results shown in Figure 4.7 emphasises the importance of estimating interfacial concentrations at the electrode surface during electrolysis and correctly attributing their effects on observed experimental findings.

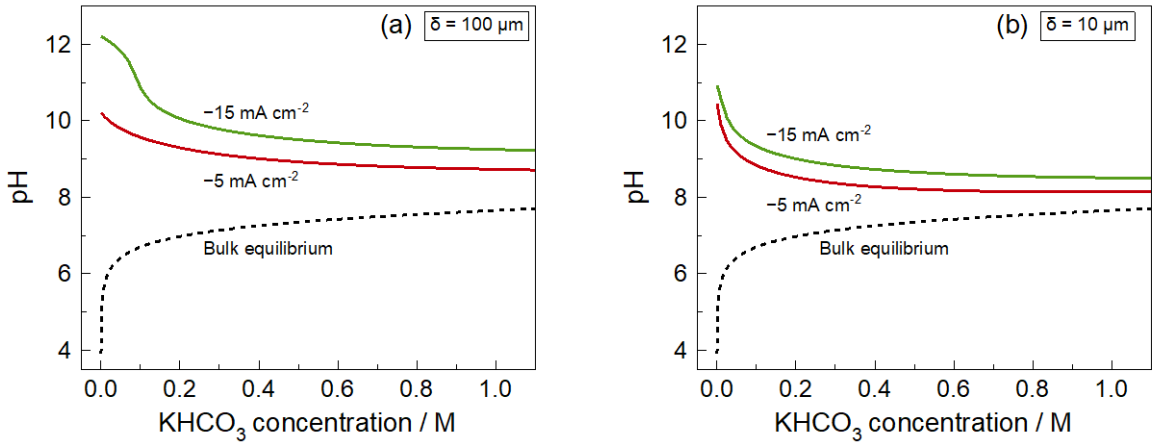

Figure 4.7: Estimation of interfacial pH with $KHCO_3$ concentration at −5 mA cm^2 and −15 mA cm^2 using the finite difference model assuming a diffusion boundary layer thickness of (a) 100 μm, and (b) 10 μm. In both cases, the bulk electrolyte was assumed to be in equilibrium, and current efficiency values (%) of 25, 5, 19.5, 0.5, 10 and 40 were specified for CH_4, CO, C_2H_4, C_2H_6. H_2 and $HCOO^-$ respectively.

Figures 4.9 and 4.10 present estimated interfacial concentrations of actual CO_2 reduction experiments on polished Cu planar disc and RCE respectively, which respectively coincides with the current efficiency plots shown in Figures 4.8a and 4.8b. Note that the discrete steps shown in the plots are due to the boundary conditions of the model being updated every 15 minutes, which is the time interval between discrete GC measurements as shown in Figure 4.8. The plots can be made more continuous if more GC measurements are made per unit time. As shown by the model results, the conditions at the electrode surface are predicted to be quite different from the bulk during CO_2 reduction electrolysis. Of particular interest in most cases is the increase and decrease in interfacial pH and CO_2 concentration respectively due to their strong influence on reaction selectivity. Straightforwardly, the interfacial pH is predicted by the model to always be higher than the bulk solution due to the production of OH^- and its kinetically limited consumption by buffering reactions, i.e. reactions (4.4) and (4.5). [CO_2] on the other hand is always lower than the bulk due to its consumption by electrode reactions and the increase in interfacial pH, which promotes reaction (4.5). [HCO_3^-] and [CO_3^{2-}] are always lower and higher than the bulk respectively, which is consistent with the rise in interfacial pH. With electrolysis time, [HCO_3^-] gradually increases due to the steady influx of K^+ to the catholyte, and is more pronounced for the Cu planar disc electrode case (Figure 4.9) where a smaller electrolyte volume (35 ml) was used, compared to the RCE case (400 ml) (Figure 4.10). The influx of K^+ effectively increases the electrolyte concentration and aside from the increase in [HCO_3^-], is also reflected by the gradual decrease in interfacial pH with time due to the gradual increase in buffer strength of the electrolyte. It is interesting that the current efficiency plots shown in Figures 4.8a and 4.8b are notably different from each other, despite the fact that the Cu electrodes used for both the planar disc and RCE originate from the same source. Hence, it is possible that certain differences in the geometry of the electrode and electrochemical cell between the two set-ups, e.g. electrolyte volume and stirring effects, be the cause of the disparity. For example, based on the estimated interfacial concentrations, a possible reason for the lower overall current efficiency toward CH_4 in the RCE case is the lower interfacial CO_2 concentration (Figure 4.10b) compared to the Cu planar disc case (Figure 4.9b), which is likely due to differences in stirring effects. Additionally, the faster

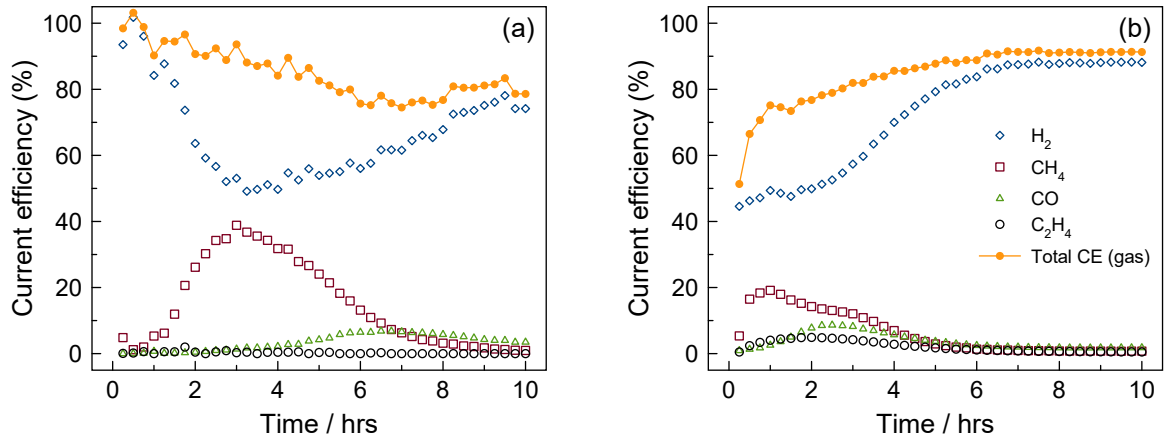

Figure 4.8: Current efficiencies with time of CO_2 reduction on a polished Cu (a) planar disc and (b) RCE (10 rpm) in 0.2 M $KHCO_3$ at −5 mA cm^{-2} for 10 hours. The electrode geometrical area is 3.14 and 3.0 cm^2, while the electrolyte volume is 35 and 400 ml for the polished Cu planar disc and RCE respectively. The major liquid product detected is formic acid, with a total current efficiency of 11.3% and 9.1% for the Cu planar disc and RCE respectively.

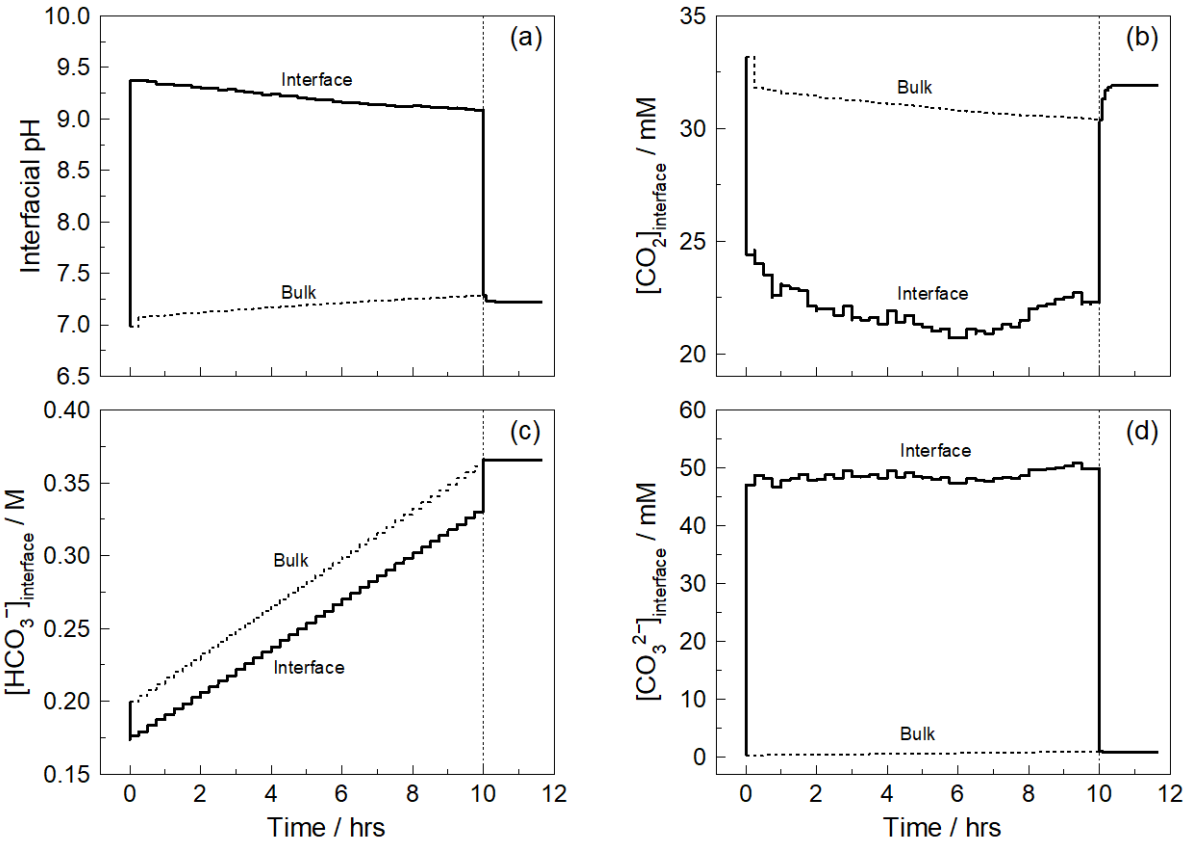

Figure 4.9: Estimated interfacial (a) pH and concentrations of (b) CO_2, (c) HCO_3^- and (d) CO_3^{2-} with time during CO_2 reduction on a polished Cu planar disc in 0.2 M $KHCO_3$ (35 ml) at −5 mA cm^{-2}. The diffusion boundary layer thickness is assumed to be 100 µm. The model simulation continues for an additional 2 hours after the end of electrolysis, where the interfacial pH and concentrations tend back to the bulk values (dashed line). The corresponding current efficiencies with time are given in Figure 4.8a.

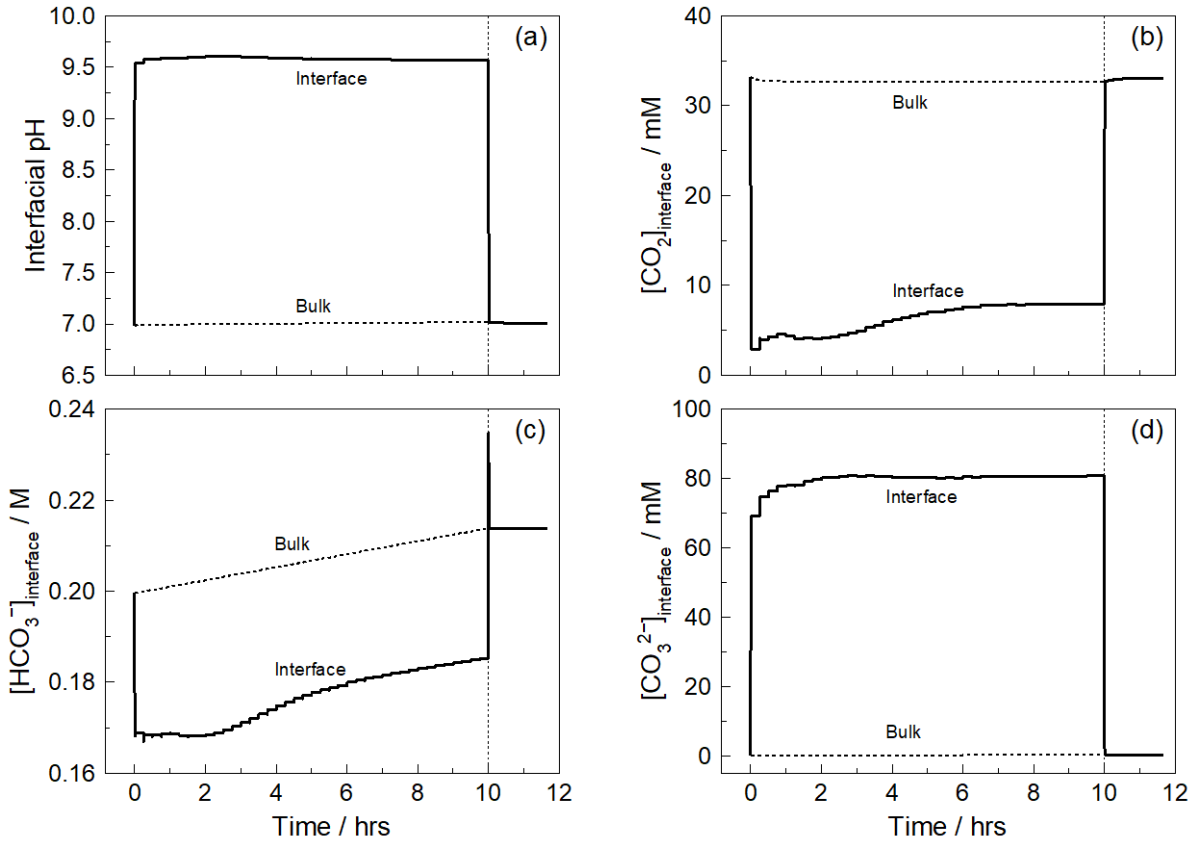

Figure 4.10: Estimated interfacial (a) pH and concentrations of (b) CO_2, (c) HCO_3^- and (d) CO_3^{2-} with time during CO_2 reduction on a polished Cu RCE in 0.2 M $KHCO_3$ (400 ml) at −5 mA cm^{-2}. The rotation rate is 10 rpm which corresponds to a diffusion boundary layer thickness of 200 µm. The model simulation continues for an additional 2 hours after the end of electrolysis, where the interfacial pH and concentrations tend back to the bulk values (dashed line). The corresponding current efficiencies with time are given in Figure 4.8b.

deactivation of the overall CO_2 reduction activity observed in the RCE case could be due to a larger extent of poisoning by solution impurities since a larger electrolyte volume was used.

4.5 Conclusions

In summary, a mathematical model for CO_2 reduction that aims to estimate the interfacial concentrations of species at the electrode surface was developed. Using experimentally determined current efficiencies of CO_2 reduction and simulated bulk concentrations with electrolysis time, the model has shown that the conditions near the electrode surface are oftentimes quite different from the bulk solution during typical current densities of CO_2 reduction. This emphasises the importance of estimating the interfacial conditions so that their effects can be correctly attributed. This is done extensively in the work presented chapter 7, where the model was applied to aid in the study of the effects of mass transfer on CO_2 reduction using the RCE.

5 Galvanostatic CO_2 Reduction on Polycrystalline Cu

5.1 Introduction

This chapter presents results pertaining to galvanostatic CO_2 reduction on polycrystalline Cu that were largely obtained during the early stages of research for this thesis. These experiments were conducted mainly to validate our experimental method by reproducing certain core results of CO_2 reduction on Cu metal found in the literature. Herein, we discuss the general behaviour of the electrode potential and CO_2 reduction activity over long periods of galvanostatic electrolysis at polycrystalline Cu, and also the effects of current density and electrolyte concentration.

5.2 Experimental

The experimental method for the work presented in this chapter has already been covered extensively in chapter 3. However for the benefit of the reader, it is briefly summarised below.

The working electrode is polycrystalline 99.99% Cu (Advent Research Materials Ltd) either in the form of a planar disc or a rotating cylinder electrode (RCE) with an exposed geometrical area of 3.14 cm^2 and 3.0 cm^2 respectively. The preparation of the electrode consists of mechanical polishing to a mirror finish using silicon carbide paper and alumina slurries (down to 0.05 μm), and subsequent rinsing and ultra-sonication with isopropanol and 18.2 MΩ cm deionised water.

A conventional two compartment H-type cell separated by a Nafion 115 cation exchange membrane was used along with a Ag|AgCl (sat. KCl) reference electrode and a Pt foil counter electrode. All potentials are reported against the Ag|AgCl reference electrode unless specifically stated. The electrolyte is $KHCO_3$ (99.7% ACS reagent, Sigma Aldrich), which was first prepared with deionised water into a 1 M stock solution and pre-electrolysed for 48 hours to remove any trace metallic impurities which may poison the Cu cathode (see section 3.3). The required electrolyte was then obtained by further dilution with deionised water and saturation with high purity 99.995% CO_2 prior to electrolysis. The electrolyte volume used is 30 and 400 ml for the Cu planar disc and RCE respectively, as per their respective electrochemical cell design.

During the CO_2 reduction experiments, the catholyte was continuously bubbled with the high purity CO_2 at 10 or 20 ml min^{-1} (Alicat mass flow controller) for the Cu planar disc and RCE respectively. The outlet gas from the electrochemical cell was fed into a gas chromatograph (SRI Instruments, methanizer FID and TCD detectors, haysep-D column) to quantify the H_2, CO, CH_4, C_2H_4 and C_2H_6 produced from the CO_2 reduction process. The liquid reduction products (formic acid, acetic acid and methanol) were measured post-electrolysis using HPLC equipped with a SUPELCOGEL^{TM} C-610H column.

All electrochemical experiments were performed at room temperature and pressure, and controlled using a GAMRY Reference 3000 potentiostat. Throughout each experiment, the solution resistance was measured every 15 minutes using electrochemical impedance spectroscopy (EIS) at the specified current density (with 5 mV rms amplitude, 100 kHz to 10 Hz) and all potential measurements were corrected post experiment. It is critical to regularly measure the solution resistance as during long-term CO_2 reduction, the transport of K^+ through the Nafion membrane (from anode to cathode) alters the solution resistance over time. Note that we also prefer galvanostatic over potentiostatic CO_2 reduction due to these changes in solution resistance, and effects of interfacial pH which are much more challenging to control during potentiostatic CO_2 reduction (see section 3.6).

5.3 Results and discussion

5.3.1 Galvanostatic CO_2 reduction

Several constant current CO_2 reduction electrolyses at −5 mA cm^{-2} in 0.2 M $KHCO_3$ for 10 hours were conducted on the Cu planar disc electrode. A current density of −5 mA cm^{-2} was chosen since that value was often used in most of the seminal works by Hori [48, 67], and the electrolyses were conducted for at least 10 hours in order to capture as much time-dependent information as possible, in contrast to many early works where electrolyses were performed for only 2 hours or less. The resulting current efficiencies and potential with time are summarised in Figure 5.1, while a representative of the estimated interfacial concentrations has been given previously (Figure 4.7). From Figure 5.1a, it is interesting to note that the CO_2 reduction activity lasted throughout the 10 hours, which is in contrast to many works that reported significant deactivation within 1 to 2 hours in $KHCO_3$ electrolytes [64, 66, 146, 149, 153, 160]. As found by others, the major gas products formed were H_2, CH_4, CO and C_2H_4, with only trace amounts of C_2H_6 detected. The major liquid product formed was formic acid and typically corresponded to a current efficiency of <10%, with only trace amounts of acetic acid detected and no methanol. By performing an overall charge balance, the total unaccounted charge was normally <5%.

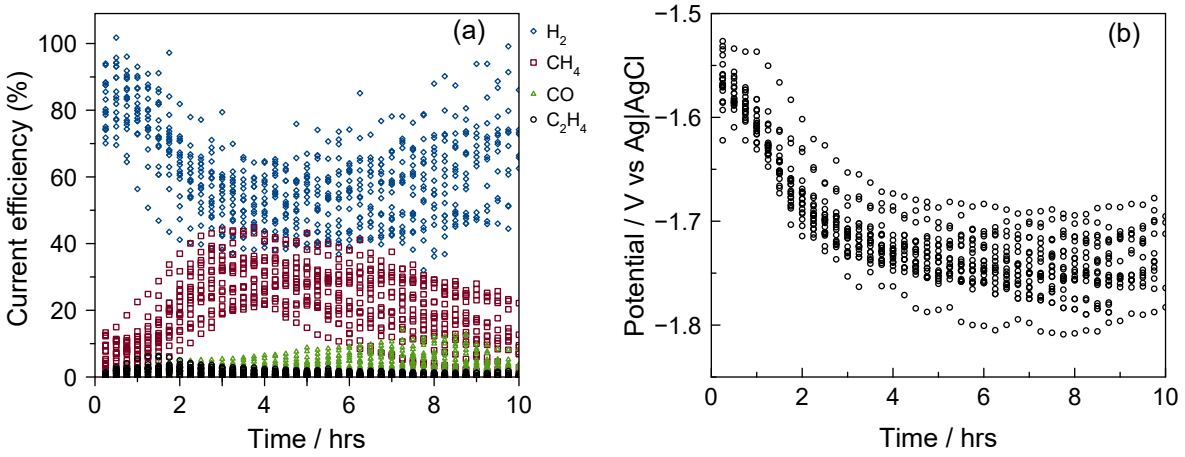

Figure 5.1: (a) Current efficiencies and (b) potential with time for galvanostatic CO_2 reduction on polished Cu planar disc in 0.2 M $KHCO_3$ at −5 mA cm^{-2}. Data from seventeen separate experiments are shown. Legend for (a): H_2 (diamonds), CH_4 (squares), CO (triangles), C_2H_4 (circles).

The activation and then deactivation of the CO_2 reduction reaction on our Cu cathodes (Figure 5.1) is explained as follows. At the start of the CO_2 reduction period, the clean Cu cathode favours the H_2 evolution reaction (HER) over CO_2 reduction. During the first 3 hours, poisoning of the HER occurs by the slow accumulation of CO_2 reduction products, which decreases the available sites for HER and thus the potential becomes more negative to maintain the specified current. We believe this poison is most likely graphite or amorphous carbon which can form through the reduction of adsorbed CO_2 reduction intermediates (see section 2.3.5). As the potential decreases, it traverses through the onset potential for CH_4 and C_2H_4 production, which many have reported to be in the vicinity of −1.5 to −1.7 V [23, 45, 66, 67, 160] for process conditions comparable to ours, and thus the current efficiency for CH_4, CO and C_2H_4 increases at the expense of H_2. As the accumulation of the poisoning carbon continues, the availability of clean Cu sites capable of hydrogenating adsorbed CO to CH_4 and C_2H_4 decrease and thus the selectivity towards CH_4 and C_2H_4 decreases. This results in the current efficiency for CH_4 and C_2H_4 reaching a maximum at 3-5 hours and 1-2 hours respectively. After this, the current efficiency for both CH_4 and C_2H_4 continue to decrease and the current efficiency for CO

and H_2 both increase. The fact that the maximum current efficiency for C_2H_4 occurs at a different time to CH_4 is not surprising given that C_2H_4 formation follows a different pathway to CH_4 formation, but still relies on the hydrogenation of adsorbed CO (see section 2.3.7). While the slow poisoning of the Cu sites by carbon continues to occur, the remaining Cu sites (and possibly the carbon sites [127]) continue to reduce CO_2 to CO and thus the current efficiency for CO production increases with time throughout the whole electrolysis duration (essentially at the expense of CH_4 and C_2H_4). In these constant current electrolysis experiments the maximum current efficiency for CO formation is normally below 10%. Based on the preceding explanation of the activation and subsequent deactivation of the Cu cathode for CH_4 and C_2H_4 formation, we suggest that the hydrogenation of adsorbed CO must follow a Langmuir-Hinshelwood mechanism (i.e. hydrogenation via H_{ads}). In other words, the formation of CH_4 and C_2H_4 decreases because the availability of neighbouring reaction sites which support adjacent CO_{ads} and H_{ads} decrease, whereas if the mechanism followed a Eley-Rideal mechanism, one would expect no increase in CO evolution as any adsorbed CO could be still hydrogenated via H^+.

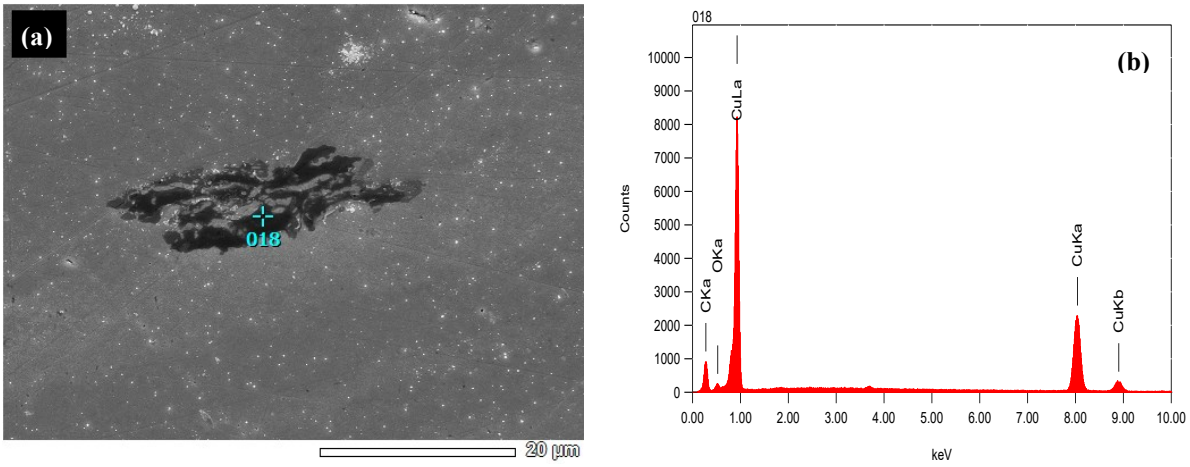

Figure 5.2: Thin carbon deposits observed through (a) SEM and (b) EDS analysis on a polycrystalline Cu electrode after CO_2 reduction at −10 mA cm^{-2} for 10 hours in 0.2 M $KHCO_3$.

While the initial activation period for CO_2 reduction is not normally observed in the literature, Cu cathodes are always found to deactivate during continuous CO_2 reduction (see section 2.3.5). The majority of reports suggest that this deactivation is caused by the poisoning by some intermediates or products (especially graphitic carbon) formed during CO_2 reduction. In our work, examination of our Cu cathodes after long-periods of CO_2 reduction by SEM revealed the formation of thin carbon deposits (Figure 5.2a), with EDS analysis only detecting Cu, C and O (Figure 5.2b). Others have proposed that the deactivation of Cu cathodes is caused by the electrodeposition of trace metallic impurities (Fe^{2+} and Zn^{2+}) present in the electrolyte, and hence advocate that pre-electrolysis of electrolyte solution is of paramount importance [149]. While this mechanism provides a simple explanation, others have tested this hypothesis and found no metallic impurities using surface sensitive techniques [153, 160] and in the work reported here we have used pre-electrolysis to avoid such issues. Terunuma et al. [163] has argued that this deactivation is not consistent with poisoning and instead suggested that the gradual reduction of Cu_2O to metallic Cu, which reduces adjacent Cu_2O and Cu sites, is the reason for the observed increase in current efficiency for CO and H_2 production and decrease in current efficiency for CH_4 and C_2H_4. We suggest that this mechanism seems unlikely in our work as the Cu_2O is shown to be easily reduced in the cyclic voltammetry measurements conducted prior to the galvanostatic CO_2 reduction (Figure 3.5).

As many have shown that morphology can influence the selectivity of CO_2 reduction [107, 194, 195, 227], the fact that polycrystalline Cu cathodes can undergo crystal re-orientation under strong cathodic conditions (see section 2.3.4) could be an alternative explanation for both the activation and subsequent deactivation of Cu for CO_2 reduction. However in our case we found no evidence (by SEM) that the Cu itself changes morphology as a result of CO_2 reduction. We also note that while it is reported that polycrystalline Cu grains are first transformed into the (111) then (100) surface [140], prior literature suggests that CH_4 is favoured on (111) surfaces, while C_2H_4 is favoured on (100) surfaces. Thus if our Cu cathode first transformed into the (111) then (100) surface we would expect to see an increase in C_2H_4 formation with time as the (100) surface develops. But in our experiments we find that the current efficiency for C_2H_4 reaches a maximum before the maximum in current efficiency for CH_4 and thus an explanation based on crystal re-orientation reported by [140] seems unlikely.

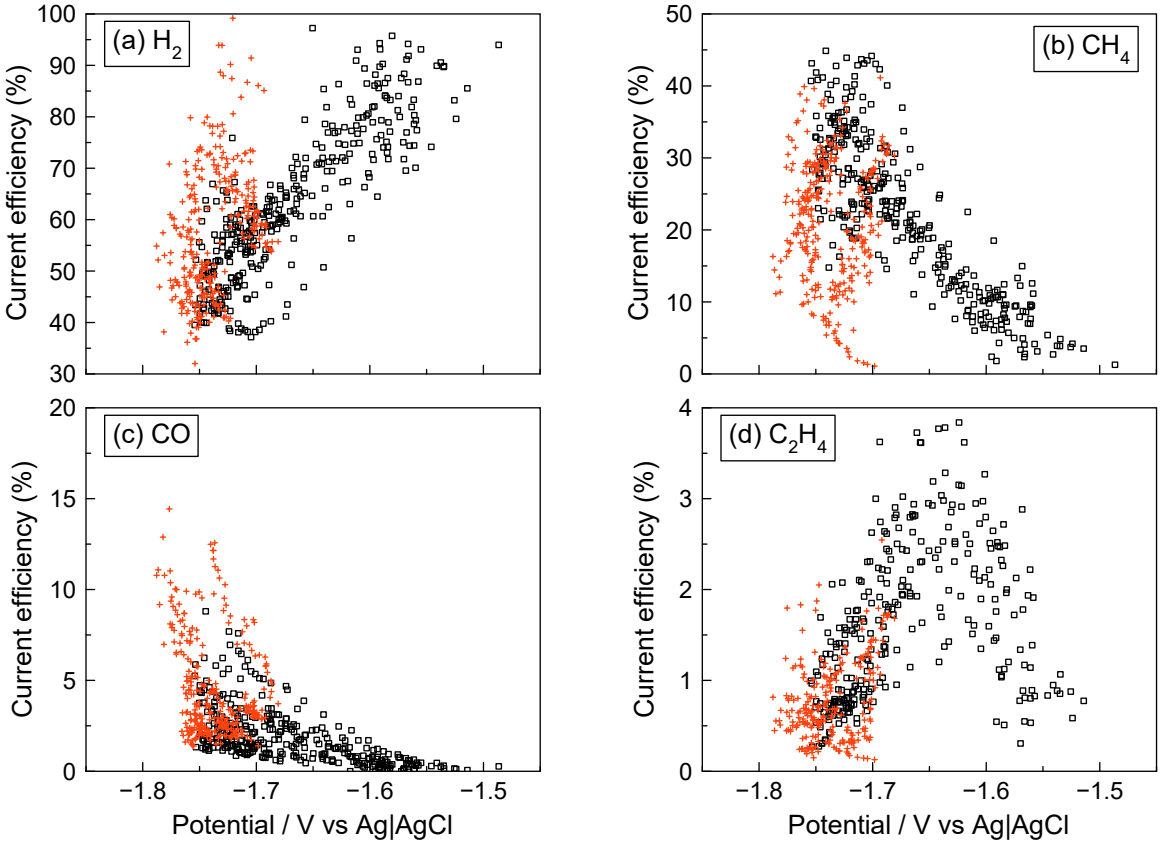

Figure 5.3: Current efficiency of (a) H_2, (b) CH_4, (c) CO and (d) C_2H_4 with potential for galvanostatic CO_2 reduction on polished Cu planar disc using data from Figure 5.1 (galvanostatic at −5 mA cm^{-2} in 0.2 M $KHCO_3$). (□) represents data within the first 5 hours of electrolysis, while (+) represent the last 5 hours.

From the current efficiency data presented in Figure 5.1a, where the electrode potential varied between −1.5 V to slightly less cathodic than −1.8 V (Figure 5.1b), the potential dependence of the current efficiencies of H_2, CH_4, CO and C_2H_4 can be extracted (Figure 5.3). From −1.5 to −1.7 V, as the potential becomes more cathodic, the current efficiency for H_2 decreases while that of the CO_2 reduction products increases. C_2H_4 reaches an optimum at approximately −1.65 V, while CH_4 and CO continue to increase with decreasing potentials up to −1.7 V and −1.8 V respectively. This trend is generally consistent with various reports on potential dependence of CO_2 reduction on Cu electrodes (see section 2.3.1). The observation that CH_4 and C_2H_4 do not share similar trends also suggests different reaction pathways for C_2H_4 and CH_4, which likely begins with adsorbed CO as the last

common intermediate (see section 2.3.7). From −1.7 to −1.8 V however, H_2 and CH_4 deviate from the regularly observed trends, where a switch in their selectivity is observed. As highlighted in Figure 5.3, this generally occurred during the second half of the electrolysis (last 5 hours), and is likely due to gradual poisoning of the electrode, by graphitic carbon for example, that slowly changed the surface of the electrode to one that prefers the HER over CH_4 production.

Despite the reproducibility of the trends explained above, a large spread, e.g. about ±25% for H_2 and CH_4, in the current efficiency of the products is observed (Figure 5.1a). While we have been unable to identify the underlying cause for these variations, it does highlight the apparent sensitivity of the electrochemical CO_2 reduction reaction. The large spread in current efficiency is mirrored by the large spread in potential of the electrode (Figure 5.1b), i.e. the current efficiency for CO_2 reduction is lower when the potential is less negative.

5.3.2 Effects of current density

From the constant current −5 mA cm^{-2} data presented in the previous section, the potential dependence of the current efficiencies between −1.5 and −1.8 V can be shown (Figure 5.3). In order to reveal the dependence of the current efficiencies over an extended potential range, CO_2 reduction on the Cu planar disc was conducted at various current densities between –0.5 to −50 mA cm^{-2}. Under this current density range, the electrode potential varied between −1.2 to −1.85 V. The resulting potential with time and current efficiencies are summarised in Figures 5.4 and 5.5 respectively, while the estimated interfacial concentrations are given in Figure 5.6.

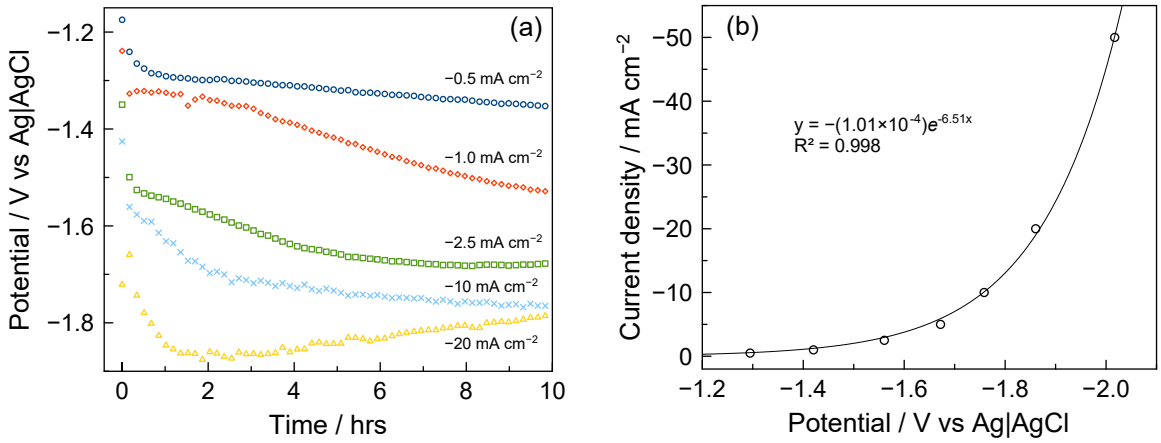

Figure 5.4: (a) Potential with time over 10 hours of galvanostatic CO_2 reduction on polished Cu planar disc in 0.2 M $KHCO_3$ at various current densities (−5 and −50 mA cm^{-2} not shown). By taking the average of the potential with time data before the onset of the deactivation of CO_2 reduction, the exponential relationship between current density and electrode potential given in (b) is obtained.

Generally, the behaviour of the electrode potential and CO_2 reduction activity with time described earlier in section 5.3.1 applies across all current densities studied. However, with increasing current densities, the deactivation of CO_2 reduction activity occurs more rapidly, presumably due to faster formation or deposition of poisoning species, e.g. graphitic carbon or metal impurities, at higher current densities (Figures 5.4a and 5.5). Additionally, due to a higher rate of OH^- production (or H^+ consumption) and K^+ transfer into the catholyte at higher current densities, the difference between bulk and interfacial conditions and their changes with time become more prominent, which can introduce other effects on CO_2 reduction due to changes in electrolyte parameters such as interfacial CO_2 concentration and pH (see Figure 5.6 and section 2.3.2). For example, the interfacial CO_2

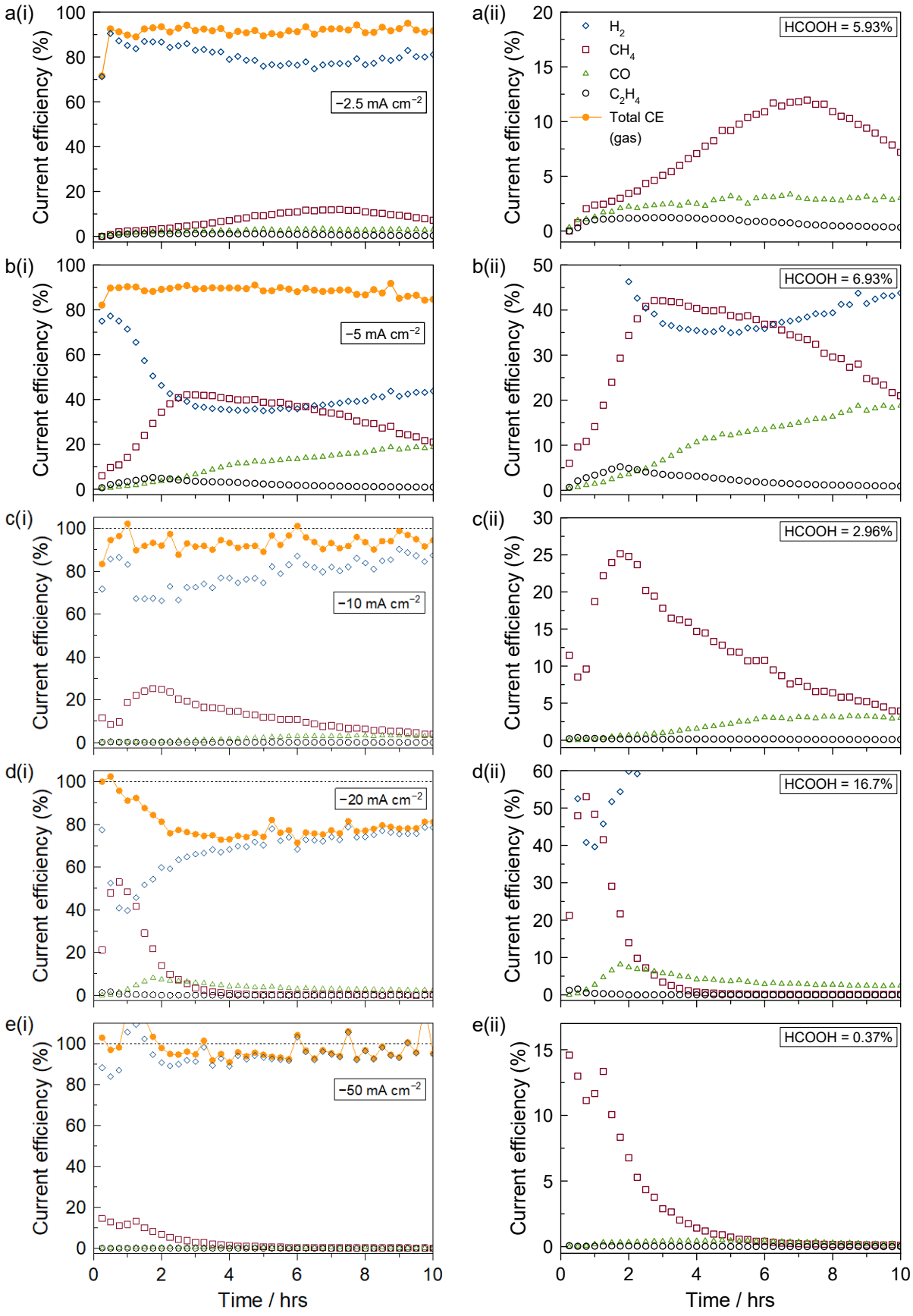

Figure 5.5: Current efficiencies with time for galvanostatic CO_2 reduction on polished Cu planar disc in 0.2 M $KHCO_3$ at various current densities. Data for −0.5 and −1.0 mA cm^{-2} not shown. Figures on the right side column (ii) are enlargements of the figures on the left side column (i).

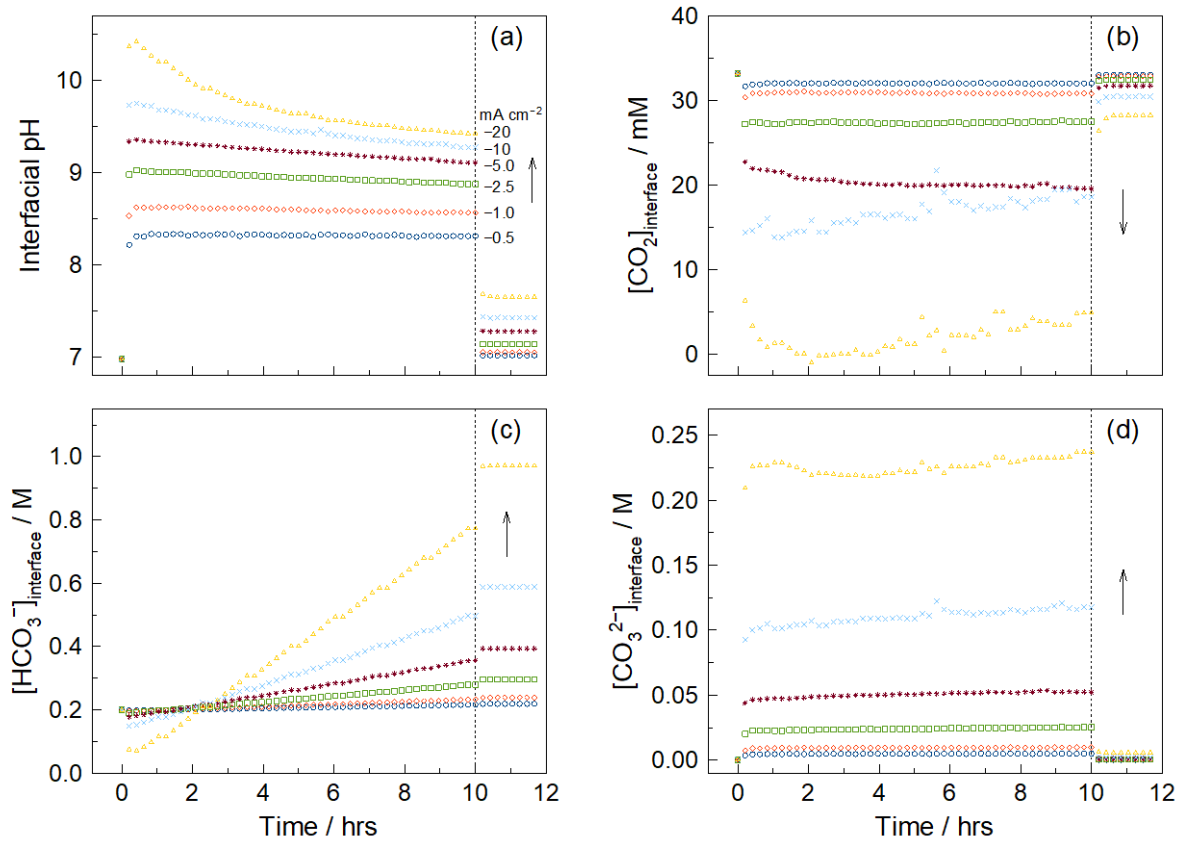

Figure 5.6: Estimated interfacial (a) pH and concentrations of (b) CO_2, (c) HCO_3^- and (d) CO_3^{2-} with time for galvanostatic CO_2 reduction on polished Cu planar disc in 0.2 M $KHCO_3$ (30 ml) at various current densities. The diffusion boundary layer thickness is assumed to be 100 µm. The model simulation continues for an additional 2 hours after the end of electrolysis, where the interfacial pH and concentrations tend back to the bulk values. The inset arrow indicates increasing current densities in the order annotated in (a).

concentration at −50 mA cm^{-2} is estimated to be <5 mM throughout the electrolysis, i.e. about 6 times lower than the bulk concentration (Figure 5.6b), suggesting a higher consumption of CO_2 at the electrode surface. However, a quick estimation of the partial current going toward CO_2 reduction reveal that the interfacial CO_2 concentration cannot merely be a factor of CO_2 consumption by electrode reactions. Instead, the significant rise in interfacial pH at high current densities (Figure 5.6a) promotes CO_2 to act as a buffering agent, where it reacts with OH^- to form HCO_3^- (reaction 4.4). Hence, despite having a larger overpotential suitable for CO_2 reduction, the consumption of CO_2 due to the rise in interfacial pH at high current densities can introduce further mass transfer limitations to CO_2 reduction activity. Notice that the interfacial pH generally decreases with electrolysis time, and the rate of decrease becomes faster with increasing current densities. This is mainly due to the increase in interfacial HCO_3^- concentration with time caused by the transport of K^+ flux into the catholyte (Figure 5.6c), which improves the buffering capacity of the electrolyte through the consumption of OH^- by HCO_3^- (reaction 4.5).

In a similar way to that used in the previous section, the potential dependence of the current efficiencies based on the data from various current densities (Figures 5.4a and 5.5) was extracted (Figure 5.7). As the CO_2 reduction activity was influenced to various degrees by electrode poisoning and changes in electrolyte parameters at different current densities, the data points before and after the onset of observable deactivation were distinctly marked to reflect this. For this data set, the electrode

potential ranged between −1.2 to −1.85 V, i.e. extended to more positive potentials compared to Figure 5.3. By comparison, the trends of the potential dependence of the current efficiencies between −1.5 and −1.8 V presented in both Figures 5.3 and 5.7 are consistent with each other. Above −1.5 V, H_2 is predominant (>80%), but CO is still produced at <2% up to its onset potential of approximately −1.3 V. CH_4 and C_2H_4 on the other hand are only produced with minute efficiencies (<0.3%) above −1.5 V. This is consistent with the onset potentials for CH_4 and C_2H_4 production, which many have reported to be in the vicinity of −1.5 to −1.7 V [23, 45, 66, 67, 160] for process conditions comparable to ours.

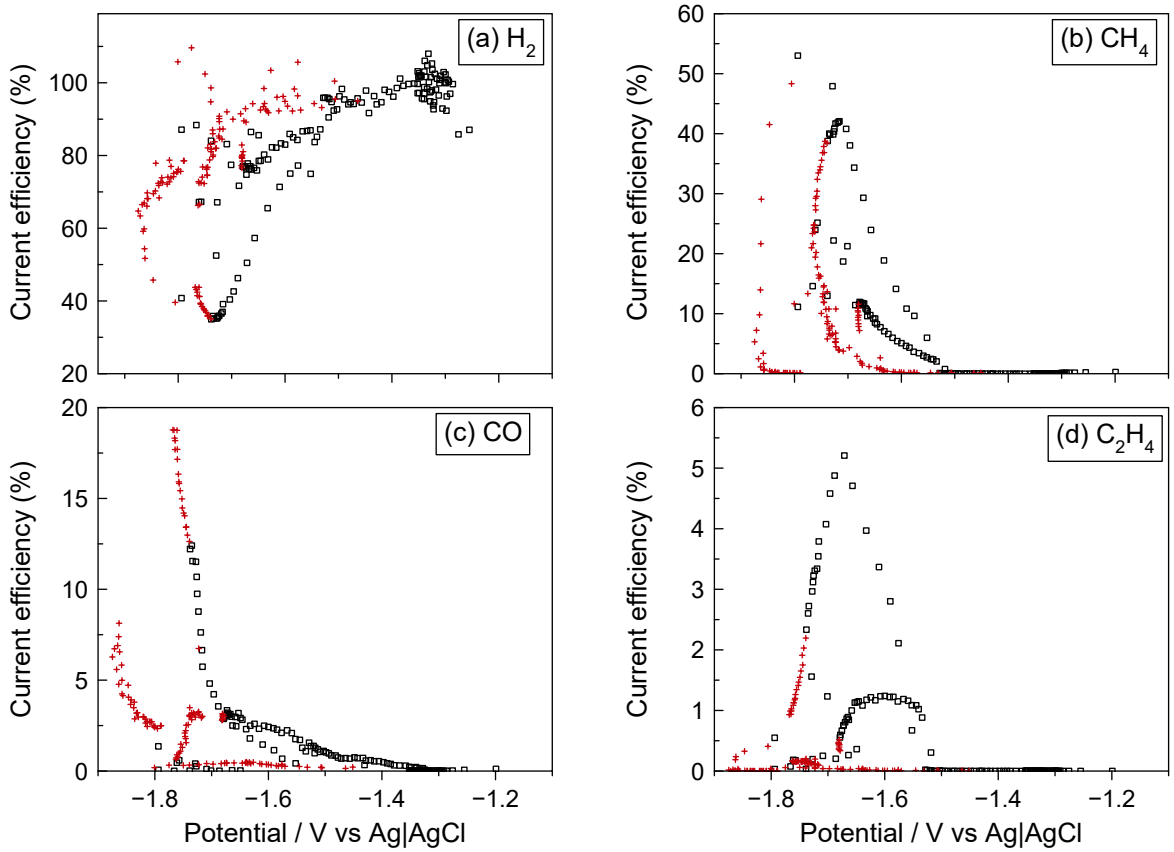

Figure 5.7: Current efficiency of (a) H_2, (b) CH_4, (c) CO and (d) C_2H_4 with potential for galvanostatic CO_2 reduction on polished Cu planar disc using data from Figure 5.5 (galvanostatic at various current densities in 0.2 M $KHCO_3$). (□) represents data before the onset of deactivation of CO_2 reduction activity, while (+) represents data after the onset of deactivation.

5.3.3 Effects of electrolyte concentration

The concentration of the electrolyte is an important, yet often overlooked, parameter that must be considered in the study of CO_2 reduction, given its strong influence on the reaction activity and selectivity as demonstrated by the early works of Hori et al. [67] and re-emphasised by a number of recent works [74, 104]. Generally, the major effects of the electrolyte concentration on CO_2 reduction are largely attributed to the electrolyte buffering strength, which clearly increases with increasing concentration for buffering electrolytes such as $KHCO_3$, although other concentration related factors such as CO_2 solubility and cationic effects may also influence the reaction (see section 2.3.2).

In summary, for electrolytes with no buffering strength (such as KCl) or buffering electrolytes at low concentrations, i.e. low buffering strength, the interfacial conditions at the electrode surface can be drastically different from the bulk electrolyte [44]. In particular, since the reduction reactions produce

OH^- (or consume H^+), the interfacial pH can greatly increase near the electrode surface due to concentration gradients developing over time. On the contrary, at higher concentrations, the increased buffering capacity of the electrolyte is able to limit the rise in interfacial pH so that it is closer to that of the bulk electrolyte. Hence, given the strong dependence of the reaction selectivity on pH, the effects of pH can be translated and observed through varying the concentration of buffered electrolytes. In general, the most commonly reported effect of the pH is seen in the change in reaction selectivity from H_2 and CH_4 to C_2H_4 and alcohols with increasing pH (see section 2.3.3 for a more in-depth discussion on the effects of pH).

Experimentally speaking, obtaining CO_2 reduction data at various electrolyte concentrations is straightforward; however, due to the selective transport of K^+ across the Nafion 115 membrane in our system, the electrolyte concentration gradually increases with time, the extent of which is more pronounced for smaller electrolyte volumes over long-term electrolysis at a certain current density. Since the electrolyte concentration is the parameter under study, it is desirable that its value remains adequately stable throughout electrolysis, so that its effects can be clearly observed between experiments at various concentrations. To achieve this, CO_2 reduction at various $KHCO_3$ concentrations (between 0.05 and 0.8 M) was performed using the Cu RCE instead (at 50 rpm), where the electrolyte volume is 13 times larger, i.e. 400 ml, than that of the planar disc set-up (which is 30 ml). The experiments were conducted at −5 mA cm^{-2} for 10 hours each. The resulting potential with time and current efficiencies are summarised in Figures 5.8 and 5.9 respectively, while the estimated interfacial concentrations are given in Figure 5.10. The total current efficiency (over 10 hours of electrolysis) of reduction products with $KHCO_3$ concentration is given in Figure 5.11.

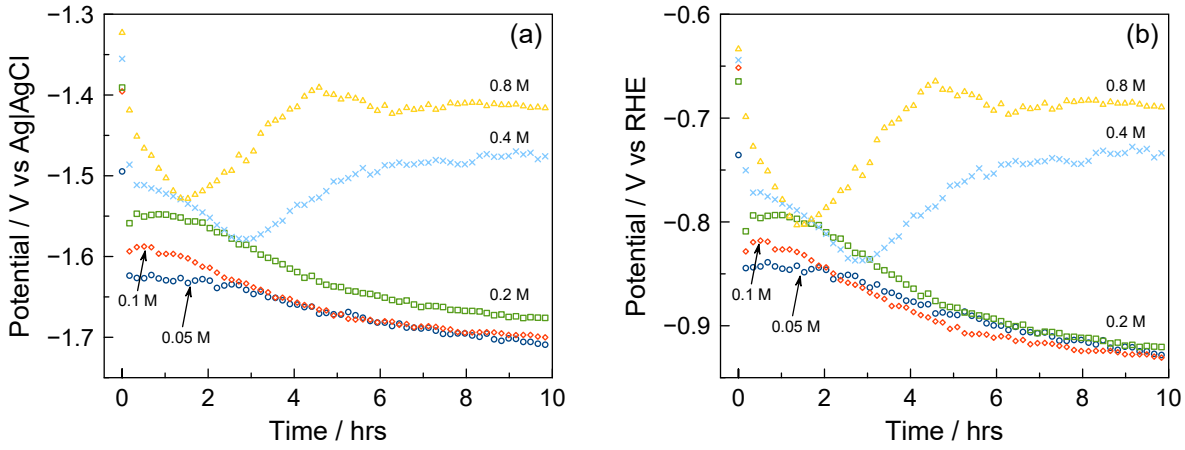

Figure 5.8: Electrode potential (a) vs Ag|AgCl KCl sat. and (b) vs RHE with time during galvanostatic CO_2 reduction on a polished Cu RCE (50 rpm) at −5 mA cm^{-2} in various concentrations of $KHCO_3$. The potential vs RHE was calculated using the calculated interfacial pH presented in Figure 5.10a.

With increasing electrolyte concentration, the electrode potential required to maintain the specified current of −5 mA cm^{-2} becomes generally less negative (or overpotential decreases) as portrayed in Figure 5.8a. This trend with increasing electrolyte concentration is consistent with the observation of other workers who studied CO_2 reduction in various concentrations [67, 74, 104] (also refer to Table 2.2), and was explained by the lower interfacial pH achieved at the electrode surface, which promoted the HER (due to the larger availability of H^+/H_{ads}) and hence the overall electrochemical activity of the electrode. For constant current electrolysis similar to our work, the improved electrochemical activity is manifested by a reduction in the overpotential required to maintain the specified current density. Consistently, in other works that performed CO_2 reduction at constant

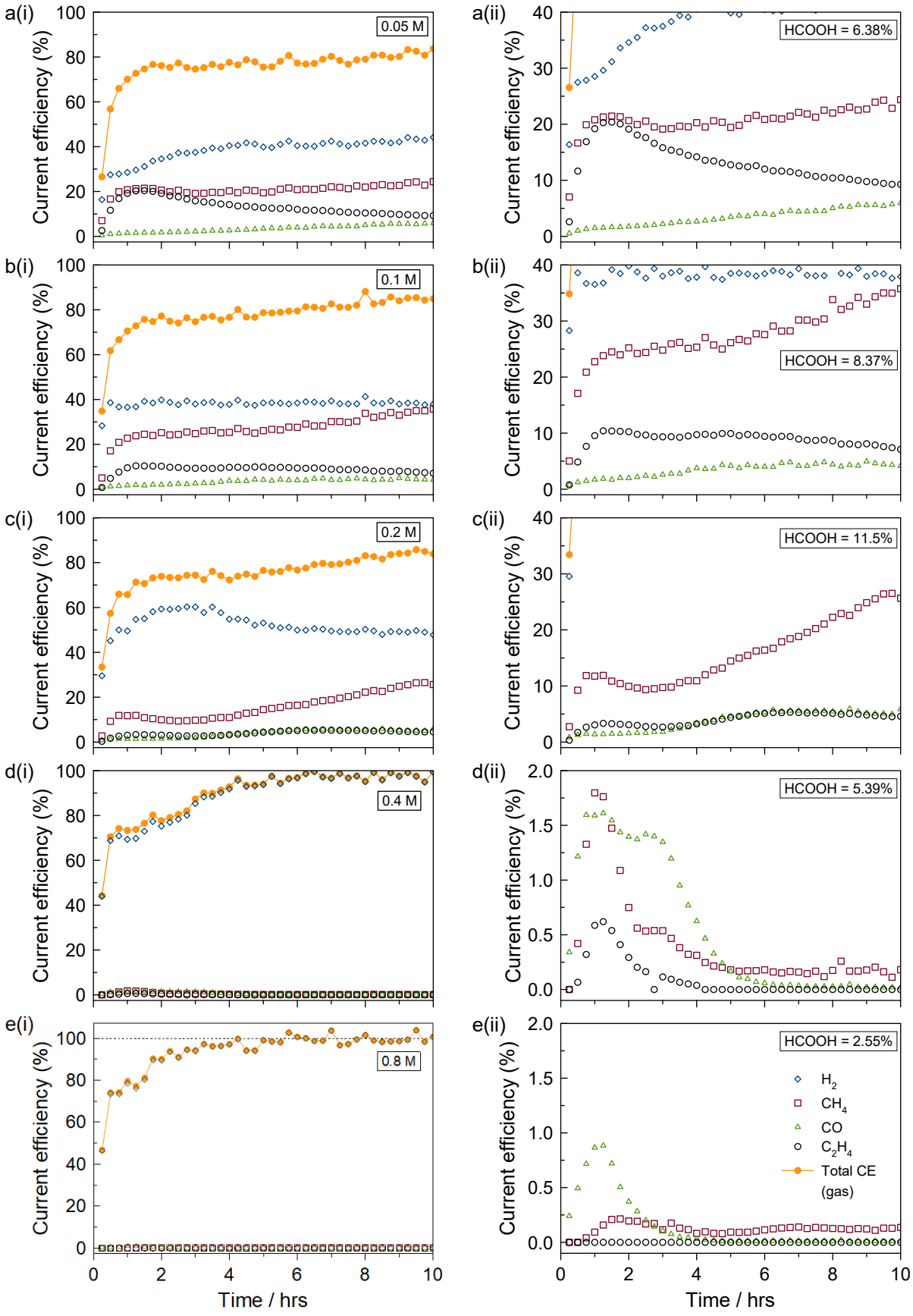

Figure 5.9: Current efficiencies with time for galvanostatic CO_2 reduction on a polished Cu RCE (50 rpm) at −5 mA cm^{-2} in various concentrations of $KHCO_3$. Figures on the right side column (ii) are enlargements of the figures on the left side column (i).

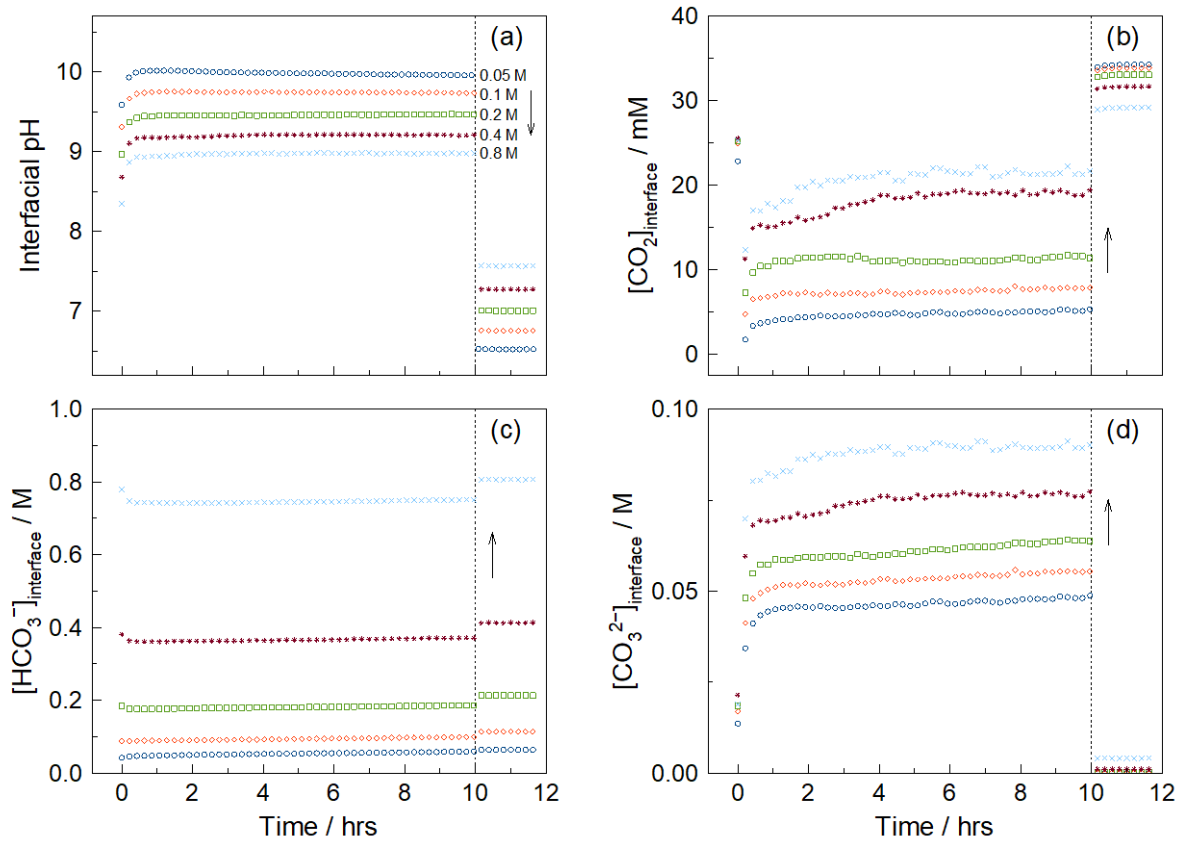

Figure 5.10: Estimated interfacial (a) pH and concentrations of (b) CO_2, (c) HCO_3^- and (d) CO_3^{2-} with time for galvanostatic CO_2 reduction on a polished Cu RCE (50 rpm) and −5 mA cm^{-2} in various concentrations of $KHCO_3$. The model simulation continues for an additional 2 hours after the end of electrolysis, where the interfacial pH and concentrations tend back to the bulk values. The inset arrow indicates increasing $KHCO_3$ concentration in the order annotated in (a).

potentials, the improvement is manifested by an increase of the electrolysis current at the specified potential.

Because the electrode potential is not comparable between experiments (with the exception of 0.05 and 0.1 M) and also varies with time (Figure 5.8), the resulting variations in current efficiencies with time and between experiments (Figure 5.9) is arguably a consequence of the variation in electrode potential, in line with the dependence of the CO_2 reduction reactions on potential (see section 2.3.1). This is supported by the observation that the total current efficiency toward CO_2 reduction products decreases with increasing $KHCO_3$ concentration while that toward the HER increases (Figure 5.11), consistent with the decrease in overpotential achieved with increasing concentration. However, the potential dependence of the reaction selectivity cannot explain the increased preference toward C_2H_4 (at the expense of CH_4) observed in the 0.05 M case when compared to the 0.1 M case since their potentials with time are remarkably similar especially from 2 hours onward. Instead, this is more consistent with the widely reported enhancement in selectivity toward C_2H_4 and alcohols in high pH environments, which can be brought about at the electrode interface when buffered electrolytes of low concentrations are used (see section 2.3.2). In general, the enhanced selectivity toward C_2H_4 and alcohols in high pH environments is tentatively explained by the existence of a pH-independent pathway for C_2H_4 (and possible other C_{2+} products) that occurs exclusively on (100) surfaces; hence, when the pH increases, pH-dependent pathways such as that for the production of H_2 and CH_4 become inhibited, allowing C_2H_4 and alcohols to be more selective (see section 2.3.7). Interestingly, the total

unaccounted current efficiency for concentrations 0.2 M and below is unusually high for our experimental method. Normally, for most of our work, HCOOH is the major liquid product and the total unaccounted current efficiency is usually <5%. Since ethanol (not measured by our method) is another commonly reported CO_2 reduction product on Cu electrodes, we suspect that the unaccounted charge likely pertains to the enhanced production of ethanol and other oxygenates at low electrolyte concentration, consistent with their reportedly improved selectivity in high pH environments.

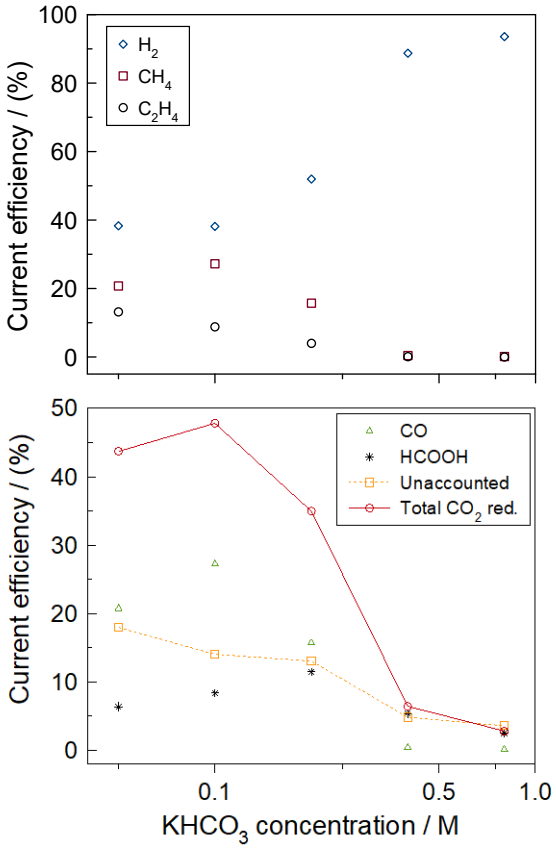

Figure 5.11: Total current efficiency for reduction products (H_2, CH_4, C_2H_4, CO and HCOOH) with $KHCO_3$ electrolyte concentration over 10 hours of galvanostatic CO_2 reduction on a polished Cu RCE (50 rpm) at −5 mA cm^{-2}. The total current efficiency toward CO_2 reduction includes CH_4, C_2H_4, CO and HCOOH only. The trends shown in this figure are comparable with those found in Hori's work [67].

Another interesting observation is the occurrence of a potential minimum at approximately 3 and 1.5 hours into electrolysis for the 0.4 and 0.8 M case respectively, after which the potential gradually decreases until a plateau at about −1.48 and −1.41 V respectively is reached (Figure 5.8). This minimum in electrode potential does not occur for concentrations 0.2 M and below. As the potential decreases past the minimum point, the corresponding current efficiencies toward all CO_2 reduction products decreases while that for the HER increases. Collectively, these observations suggest a poisoning mechanism of the Cu electrode toward CO_2 reduction in favour of the HER, where the extent of the poisoning increases with electrolyte concentration. As we have discussed previously in section 5.3.1 (see also section 2.3.5), the most commonly proposed causes for the poisoning/deactivation is the accumulation of CO_2 reduction products and intermediates (especially graphitic carbon) and the electrodeposition of trace metallic impurities present in the electrolyte solution. Although we have suggested previously (in section 5.3.1) that the deactivation is likely caused by the accumulation of CO_2 reduction products or intermediates, given the observation of thin carbon deposits on our Cu electrodes after electrolysis (Figure 5.2), the fact that the deactivation is

more severe at higher electrolyte concentrations under similar hydrodynamic conditions (50 rpm for all experiments) also strongly points toward deactivation by electrodeposition of metallic impurities. This is possible since an electrolyte solution prepared at higher concentrations will clearly have a higher concentration of metallic impurities; hence, the limiting current densities of their electrodeposition on the electrode surface will also be larger. Nevertheless, we do emphasise that the poisoning/deactivation of the Cu electrode for CO_2 reduction can very well occur through a variety of ways, and that the dominant poisoning mechanism in one system may not always be similar to that in another system.

5.4 Conclusions

In summary, the general behaviour of the electrode potential and CO_2 reduction activity over long periods of galvanostatic electrolysis at polycrystalline Cu was discussed. The effects of current density and electrolyte concentration on the long-term galvanostatic electrolysis were also investigated.

During galvanostatic CO_2 reduction, it was shown that the Cu electrode is initially more active toward the HER, which gradually deactivates due to the slow accumulation of CO_2 reduction products, most likely graphite or amorphous carbon, which decreases active sites on the surface of the electrode. The inhibition of the HER causes the overpotential of the electrode to increase, hence increasing the selectivity toward CO, CH_4 and C_2H_4 at the expense of H_2 as the electrode potential traverses through and beyond the onset potentials of the CO_2 reduction reactions. However, as the accumulation of the poisoning carbon continues, active sites capable of hydrogenating (via H_{ads}) adsorbed CO to CH_4 and C_2H_4 decreases; hence, the selectivity toward CH_4 and C_2H_4 decreases, while that of H_2 increases. Nevertheless, the remaining Cu sites and possibly those blocked by carbon continue to reduce CO_2 to CO, explaining the continuous increase in CO production with time throughout the whole electrolysis duration. This behaviour generally applies across all current densities studied, although with increasing current densities, the deactivation of CO_2 reduction activity occurs more rapidly, presumably due to a faster formation or deposition rate of poisoning species. In our work, CH_4 is found to be the dominant CO_2 reduction product on polycrystalline Cu, consistent with the majority of work in the literature. However, by decreasing the $KHCO_3$ electrolyte concentration, the selectivity toward C_2H_4 can be significantly increased. This is consistent with the widely reported enhancement in selectivity toward C_2H_4 and alcohols in high pH environments, which can be brought about at the electrode interface when buffered electrolytes such as $KHCO_3$ of low concentrations are used. The enhanced selectivity toward C_2H_4 and alcohols in high pH environments is tentatively explained by the existence of a pH-independent pathway for C_2H_4 (and possible other C_{2+} products) that occurs exclusively on (100) surfaces; hence, when the pH increases, pH-dependent pathways such as that for the production of H_2 and CH_4 become inhibited, allowing C_2H_4 and alcohols to be more selective. Indeed, by increasing the $KHCO_3$ concentration (which lowers the interfacial pH), the electrode becomes more active toward the HER, the improved electrochemical activity of which is manifested by a reduction in the overpotential required to maintain the specified current density.

6 Periodic Cyclic Voltammetry and Potentiostatic Steps

The contents of this chapter have been published in Electrochimica Acta under the title *"Altering the selectivity of galvanostatic CO_2 reduction on Cu cathodes by periodic cyclic voltammetry and potentiostatic steps"*, which is reference [147] in this thesis. Because the publication is presented here in its entirety and original journal structure, the reader may encounter some material within this chapter that have already been covered elsewhere in the thesis. Section 6.5 presents additional material related to the work but was not included in the original publication.

DOI: https://doi.org/10.1016/j.electacta.2016.10.185; for copyright license, see Appendix 14.

Abstract: Analysis of the product selectivity and potential of Cu cathodes during galvanostatic CO_2 reduction is reported. Initially, it is found that clean Cu cathodes are more selective for hydrogen evolution, but as the Cu is slowly poisoned by CO_2 reduction products (most likely carbon) the cathode potential becomes more negative, which in turn drives the formation of CH_4, C_2H_4 and CO. As the accumulation of surface poisons continues, the selectivity towards CH_4 and C_2H_4 begins to decrease due to the loss in neighbouring reaction sites that support the hydrogenation of CO_{ads} by H_{ads}. In an attempt to avoid these changes in product selectivity, periodic cyclic voltammetry and potentiostatic steps were used throughout extended periods of galvanostatic CO_2 reduction. Contrary to previous literature, it is demonstrated that temporarily interrupting galvanostatic CO_2 reduction with short periods at potentials between −0.5 and −0.1 V vs Ag|AgCl suppresses the formation of CH_4, CO and C_2H_4. It is proposed that this is due to the partial removal or oxidation of adsorbed CO_2 reduction intermediates and that this "clean" cathode surface is more active for the hydrogen evolution reaction. However, when brief potentiostatic steps (84 and 200 s) were conducted at more negative potentials (−1.2 V vs Ag|AgCl), the CO_2 reduction selectivity could be switched from CH_4 to CO, and maintained for at least 2 hours. This change in selectivity is proposed to be caused by an increase in the surface coverage of CO_{ads} (at the expense of H_{ads}) during the brief −1.2 V steps, which then enables the Cu cathode to switch between multiple steady-state surface coverages when the cathodic current is re-applied.

6.1 Introduction

The electrochemical reduction of CO_2 offers a potential method of producing carbon-based fuels from renewable energy so as to achieve a carbon-neutral energy cycle [1]. Cu is widely studied for this process as it is known to produce high amounts of hydrocarbons compared to other metals [41, 47, 48, 51]. Normally in aqueous electrolytes, Cu cathodes produce high levels of CH_4 and C_2H_4, while CO is only found as a minor product, usually corresponding to current efficiencies of less than 10% [23, 42, 67, 146], or sometimes not even detected [151, 152, 160, 164]. Experimental studies and theoretical simulations of the reaction mechanism however, strongly point towards adsorbed CO (CO_{ads}) as a major intermediate [24, 64, 81]. More support of this stems from electrochemical CO reduction, which has been shown to give the same product distribution as CO_2 reduction [67, 77, 115].

It is clear from current literature that the product distribution of CO_2 reduction is a complex function of many parameters: surface structure, oxides, crystal orientation, interfacial pH and operating conditions (e.g. potential, temperature, pressure). Hence, much work has been done on manipulating these parameters in an effort to tune the selectivity of CO_2 reduction. One method of controlling the selectivity of CO_2 reduction has been to incorporate brief anodic treatments throughout the normally continuous cathodic process [164-167]. In the case of Cu cathodes, either short anodic pulses or

potential sweeps into anodic conditions (i.e. cyclic voltammetry) have been successfully used to maintain or reactivate CO_2 reduction activity [149, 151, 153, 155, 160, 163] by removing poisoning species such as graphitic carbon or electrodeposited metallic impurities. In addition to reactivating the electrode, it has also been shown that the product selectivity favours C_2H_4 at the expense of CH_4 if the potential of the anodic pulses is increased from 0 to 0.50 V vs SCE [164]. In a similar way, the product selectivity on Ag cathodes can be switched from CH_4, C_2H_4 and ethanol to CO and HCOOH when the potential of these anodic pulses is greater than −0.4 V vs Ag|AgCl [167]. In general, it is suggested that these short anodic treatments alter the product selectivity by changing the surface structure of the cathode, e.g. forming oxides or changing the surface coverages of adsorbed species such as H_{ads}.

In this work, the influence of periodic cyclic voltammetry (between −1.2 V and −0.1 V vs Ag|AgCl) and periodic potentiostatic steps at −0.25, −0.5 or −1.2 V vs Ag|AgCl, on the behaviour of CO_2 reduction at Cu cathodes has been investigated. Importantly, we have selected potentials to specifically avoid substantial oxide formation and show that the periodic potentiostatic steps at relatively mild cathodic conditions can have a major impact on the product selectivity of CO_2 reduction on Cu. In this case, instead of changing the selectivity between CH_4 and C_2H_4, we show that the product selectivity on Cu electrodes can be changed from CH_4 to CO. We propose that these changes in product selectively can only be attributed to the changes in the surface coverages of adsorbed H_{ads} and CO_{ads}, possibly suggesting the presence of multiple steady-state surface coverages during CO_2 reduction.

6.2 Experimental

A polycrystalline 99.99% Cu disc (Advent Research Materials Ltd) with an exposed geometrical area of 3.14 cm^2 was used as the working electrode. The electrode was mechanically polished to a mirror finish using silicon carbide paper and alumina slurries (down to 0.05 μm). After polishing, the electrode was rinsed and ultra-sonicated with isopropanol and 18 MΩ cm deionised water.

A conventional two compartment H-type cell separated by a Nafion 115 cation exchange membrane was used along with a Ag|AgCl (sat. KCl) reference electrode and a Pt foil counter electrode. All potentials in this work are reported against the Ag|AgCl reference electrode unless specifically stated. In all cases, 30 ml of 0.2 M $KHCO_3$ (99.7% ACS reagent, Sigma Aldrich) saturated with high purity 99.995% CO_2 (pH = 7.0) was used as the electrolyte. This electrolyte was pre-electrolysed for 48 hours prior to CO_2 reduction experiments to remove any trace metallic impurities which may poison the Cu cathode [149].

During the CO_2 reduction experiments, the catholyte was continuously bubbled with the high purity CO_2 at 10 ml min^{-1} (Alicat mass flow controller). The outlet gas from the electrochemical cell was fed into a gas chromatograph (SRI Instruments, methanizer FID and TCD detectors, haysep-D column) to quantify the H_2, CO, CH_4, C_2H_4 and C_2H_6 produced from the CO_2 reduction process. The liquid reduction products (formic acid, acetic acid and methanol) were measured post-electrolysis using HPLC equipped with a SUPELCOGEL^{TM} C-610H column.

All electrochemical experiments were performed at room temperature and pressure, and controlled using a GAMRY Reference 3000 potentiostat. Throughout each experiment, the solution resistance was measured every 15 minutes using electrochemical impedance spectroscopy (EIS) at −5 mA cm^{-2} (with 5 mV rms amplitude, 100 kHz to 10 Hz) and all potential measurements were corrected post experiment. It is critical to regularly measure the solution resistance as during long-term CO_2 reduction, the transport of K^+ through the Nafion membrane (from anode to cathode) alters the

solution resistance over time. Note that we also prefer galvanostatic over potentiostatic CO_2 reduction due to these changes in solution resistance, and effects of interfacial pH [44] which are much more challenging to control during potentiostatic CO_2 reduction.

6.3 Results and discussion

6.3.1 The reduction of Cu oxides

Prior to CO_2 reduction, cyclic voltammetry between −0.1 V and −1.2 V at 100 mV s^{-1} was performed to confirm the complete reduction of the surface oxides which formed on the Cu cathode after mechanical polishing. Typically, during the first cycle from −0.1 to −1.2 V, two reduction peaks at −0.55 V and −0.75 V corresponding to reduction of Cu(II) to Cu(I), and Cu(I) to Cu(0) respectively are observed (Figure 6.1). During the subsequent cycles these reduction peaks are absent which indicates that the oxide layer formed after polishing is easily reduced, and thus it is unlikely that during CO_2 reduction (which typically occurs at −1.5 to −1.8 V in our experiments) any oxide will be present.

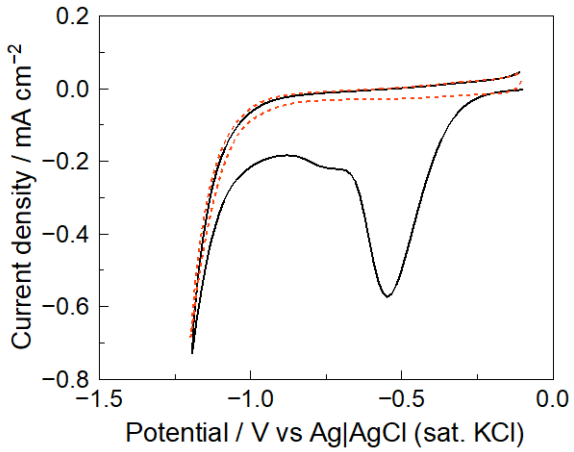

Figure 6.1: Cyclic voltammograms (100 mV s^{-1}) of a freshly polished Cu cathode in 0.2 M $KHCO_3$ which show the successful reduction of Cu oxides. (——), first cycle; (– –), subsequent cycles.

In the majority of the work that utilizes periodic anodic treatments during electrochemical CO_2 reduction, the potentials applied during these short treatment steps are very likely to form oxides on the Cu cathodes. In this work we have specifically avoided potentials where significant oxide formation will occur to rule out the contribution of these oxides altering the product selectivity on Cu, by keeping the potential more negative than −0.1 V. While Cu oxide does not form substantially at −0.1 V at pH = 7 (Figure 6.1), as the interfacial pH during CO_2 reduction can be significantly higher than the bulk pH [44], when performing the cyclic voltammetry measurements between periods of galvanostatic CO_2 reduction, the potential was held at −1.2 V for 20 s prior to the start of the cyclic voltammetry to allow the surface conditions to equilibrate with the bulk electrolyte. For experiments with periodic potentiostatic steps, the most positive potential applied was −0.25 V, and the average current measured during these steps was still cathodic, implying that Cu oxidation should be very minimal.

While our initial voltammetry results indicate that the Cu oxides which form following mechanical polishing are very easily reduced, Frese [45, 180] has suggested that a small amount of Cu_2O can be sufficiently stable during electrochemical CO_2 reduction, although in this case the observation is more relevant to Cu electrodes that were intentionally oxidised to promote CH_3OH production. Jermann

and Augustynski [160] and more recently Kim et al. [69] also suggested the persistence of copper oxide despite the strongly reducing conditions used for CO_2 reduction. However, given that our Cu cathodes were mechanically polished and that the formation of Cu oxides is minimal and easily reduced, we are confident that the effect of Cu oxides in our experiments is negligible.

6.3.2 Continuous galvanostatic CO_2 reduction

Galvanostatic CO_2 reduction (at −5 mA cm^{-2}) at these Cu cathodes reveals that significant changes in the current efficiency for various CO_2 reduction products occur over a 10 hour period (Figure 6.2). This data comes from 17 independent experiments. It is interesting to note that the CO_2 reduction activity lasted throughout the 10 hours, which is in contrast to many works that reported significant deactivation within 1 to 2 hours in $KHCO_3$ electrolytes [64, 66, 146, 149, 153, 160]. As found by others, the major gas products formed were H_2, CH_4, CO and C_2H_4, with only trace amounts of C_2H_6 detected. The major liquid product formed was formic acid and typically corresponded to a current efficiency of <10%, with only trace amounts of acetic acid detected and no methanol. By performing an overall charge balance, the total unaccounted charge was normally <5%.

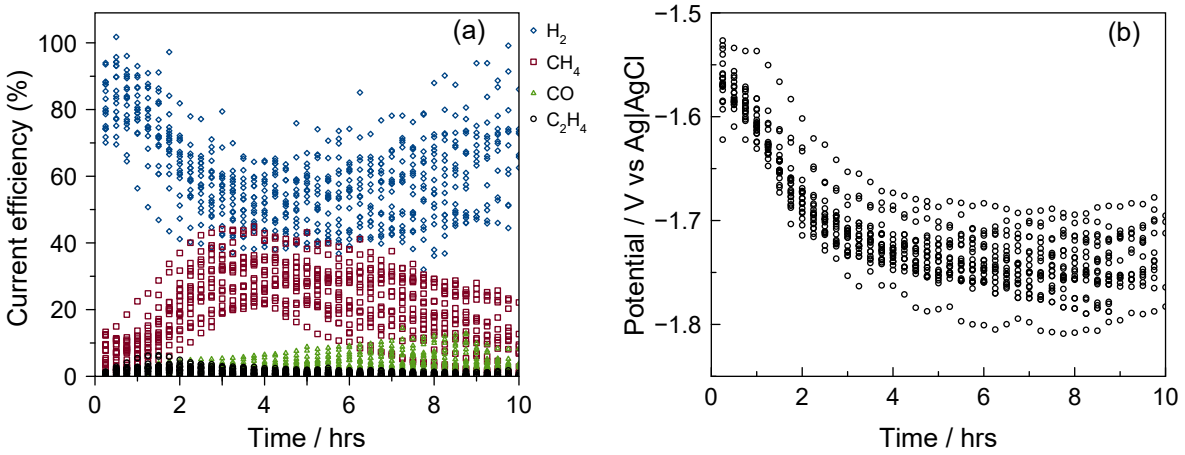

Figure 6.2: (a) Current efficiencies and (b) potential with time for galvanostatic CO_2 reduction on polished Cu in 0.2 M $KHCO_3$ at −5 mA cm^{-2}. Data from seventeen separate experiments are shown. H_2 (diamonds), CH_4 (squares), CO (triangles), C_2H_4 (circles).

The activation and then deactivation of the CO_2 reduction reaction on our Cu cathodes (Figure 6.2) is explained as follows. At the start of the CO_2 reduction period, the clean Cu cathode favours the H_2 evolution reaction (HER) over CO_2 reduction. During the first 3 hours, poisoning of the HER occurs by the slow accumulation of CO_2 reduction products, which decreases the available sites for HER and thus the potential becomes more negative to maintain the specified current. We believe this poison is most likely graphite or amorphous carbon which can form through the reduction of adsorbed CO_2 reduction intermediates [66, 104, 152, 153, 160, 165, 166, 228]. As the potential decreases, it traverses through the onset potential for CH_4 and C_2H_4 production, which many have reported to be in the vicinity of −1.5 to −1.7 V [23, 45, 66, 67, 160] for process conditions comparable to ours, and thus the current efficiency for CH_4, CO and C_2H_4 increases at the expense of H_2. As the accumulation of the poisoning carbon continues, the availability of clean Cu sites capable of hydrogenating adsorbed CO to CH_4 and C_2H_4 decrease and thus the selectivity towards CH_4 and C_2H_4 decreases. This results in the current efficiency for CH_4 and C_2H_4 reaching a maximum at 3-5 hours and 1-2 hours respectively. After this, the current efficiency for both CH_4 and C_2H_4 continue to decrease and the current efficiency for CO and H_2 both increase. The fact that the maximum current efficiency for C_2H_4 occurs at a different time to CH_4 is not surprising given that C_2H_4 formation follows a different

pathway to CH_4 formation [104], but still relies on the hydrogenation of adsorbed CO. While the slow poisoning of the Cu sites by carbon continues to occur, the remaining Cu sites (and possibly the carbon sites [127]) continue to reduce CO_2 to CO and thus the current efficiency for CO production increases with time throughout the whole electrolysis duration (essentially at the expense of CH_4 and C_2H_4). In these constant current electrolysis experiments the maximum current efficiency for CO formation is normally below 10%. Based on the preceding explanation of the activation and subsequent deactivation of the Cu cathode for CH_4 and C_2H_4 formation, we suggest that the hydrogenation of adsorbed CO must follow a Langmuir-Hinshelwood mechanism (i.e. hydrogenation via H_{ads}). In other words, the formation of CH_4 and C_2H_4 decreases because the availability of neighbouring reaction sites which support adjacent CO_{ads} and H_{ads} decrease, whereas if the mechanism followed a Eley-Rideal mechanism, one would expect no increase in CO evolution as any adsorbed CO could be still hydrogenated via H^+.

While the initial activation period for CO_2 reduction is not normally observed in the literature, Cu cathodes are always found to deactivate during continuous CO_2 reduction [64, 66, 104, 146, 149, 151, 153, 155, 160]. The majority of reports suggest that this deactivation is caused by the poisoning by some intermediates or products (especially graphitic carbon) formed during CO_2 reduction [66, 104, 152, 153, 160, 165, 166, 228]. In our work, examination of our Cu cathodes after long-periods of CO_2 reduction by SEM revealed the formation of thin carbon deposits (EDS analysis only detected Cu, C and O). Others have proposed that the deactivation of Cu cathodes is caused by the electrodeposition of trace metallic impurities (Fe^{2+} and Zn^{2+}) present in the electrolyte [149, 159], and hence advocate that pre-electrolysis of electrolyte solution is of paramount importance [149]. While this mechanism provides a simple explanation, others have tested this hypothesis and found no metallic impurities using surface sensitive techniques [153, 160] and in the work reported here we have used pre-electrolysis to avoid such issues. Terunuma et al. [163] has argued that this deactivation is not consistent with poisoning and instead suggested that the gradual reduction of Cu_2O to metallic Cu, which reduces adjacent Cu_2O and Cu sites, is the reason for the observed increase in current efficiency for CO and H_2 production and decrease in current efficiency for CH_4 and C_2H_4. We suggest that this mechanism seems unlikely in our work as the Cu_2O is shown to be easily reduced in the cyclic voltammetry measurements conducted prior to the galvanostatic CO_2 reduction (Figure 6.1).

As many have shown that morphology can influence the selectivity of CO_2 reduction [107, 194, 195, 227], the fact that polycrystalline Cu cathodes can undergo crystal re-orientation under strong cathodic conditions [140] could be an alternative explanation for both the activation and subsequent deactivation of Cu for CO_2 reduction. However in our case we found no evidence (by SEM) that the Cu itself changes morphology as a result of CO_2 reduction. We also note that while it is reported that polycrystalline Cu grains are first transformed to Cu(111) then Cu(100) [140], prior literature suggests that CH_4 is favoured on Cu(111), while C_2H_4 is favoured on Cu(100). Thus if our Cu cathode first transformed into Cu(111) then Cu(100) we would expect to see an increase in C_2H_4 formation with time as the Cu(100) develops. But in our experiments we find that the current efficiency for C_2H_4 reaches a maximum before the maximum in current efficiency for CH_4 and thus an explanation based on crystal re-orientation reported by [140] seems unlikely.

Despite the reproducibility of the trends explained above, a large spread, e.g. about ±25% for H_2 and CH_4, in the current efficiency of the products is observed (Figure 6.2a). While we have been unable to identify the underlying cause for these variations, it does highlight the apparent sensitivity of the electrochemical CO_2 reduction reaction. The large spread in current efficiency is mirrored by the large spread in potential of the electrode (Figure 6.2b), i.e. the current efficiency for CO_2 reduction is lower when the potential is less negative.

6.3.3 *Periodic cyclic voltammetry during galvanostatic CO_2 reduction*

In an attempt to avoid the deactivation of CO_2 reduction, a series of electrolysis experiments were conducted wherein the galvanostatic CO_2 reduction was periodically interrupted with cyclic voltammetry measurements. These cyclic voltammetry interruptions were applied every 15 minutes, 1, 2 and 5 hours, throughout the galvanostatic CO_2 reduction at −5 mA cm^{-2} for 10 hours (Figures 6.3 and 6.4).

Instead of preventing the loss in selectivity towards CH_4 and C_2H_4 as described elsewhere [149, 160], the overall CO_2 reduction activity became more suppressed as the frequency of the cyclic voltammograms (interrupting the galvanostatic CO_2 reduction) increased (Figure 6.3). For the case where a single set of voltammograms were recorded after 5 hours of CO_2 reduction at −5 mA cm^{-2}, before continuing the CO_2 reduction, the current efficiency with time behaviour is very similar to the case where CO_2 reduction was performed without any cyclic voltammetry treatments (Figure 6.3d vs Figure 6.2a). Importantly, it is observed that immediately after performing the cyclic voltammetry, the overall CO_2 reduction activity (notably shown by CH_4 production) is significantly suppressed while the HER is enhanced (Figure 6.3). This is followed by a gradual increase in the CH_4 current efficiency until the next set of voltammograms. Similarly, the current efficiency towards CO production also decreases after a set of voltammograms, whereas the current efficiency for C_2H_4 increases. We also find that the potential immediately following a cyclic voltammogram is much more positive (than just prior to the voltammograms) and slowly becomes more negative during continuous galvanostatic CO_2 until the next set of voltammetry measurements (Figure 6.4). To explain these observations, we propose that the use of cyclic voltammetry after a period of CO_2 reduction partially removes CO_2 reduction intermediates/products which in the previous section were suggested to be responsible for inhibiting the HER and promoting the CO_2 reduction reaction. This has the effect of resetting the cathode behaviour back to an earlier state where the HER is favoured. The fact that the current efficiency for C_2H_4 production also increases after these voltammograms is also consistent with the electrode being reverted back to an earlier state as the Cu electrode showed the highest C_2H_4 activity in the first 2 hours of electrolysis (Figure 6.2). Following this reactivation of the cathode for the HER, the CO_2 reduction intermediates begin to re-accumulate on the Cu cathode, poisoning the surface towards the HER and thus causing the potential to decrease to a point where the kinetics of CO_2 reduction begin to dominate over the HER.

The proposal that the cyclic voltammograms strip off CO_2 reduction intermediates is supported by the features present on these voltammograms. A large anodic peak centred about −0.8 V to −0.9 V (peak A1) and another peak at about −0.35 V (peak A2) become more pronounced as the period of galvanostatic CO_2 reduction increases prior to the voltammograms (Figure 6.5). Peak A1 appears to be coupled with a cathodic peak (C1) in the same potential range during the cathodic sweep, which is consistent with adsorbed species, most likely adsorbed CO_2 reduction intermediates, accumulated on the electrode surface during electrolysis. Peak A2 however does not show a cathodic counterpart and most likely is due to the oxidation of a CO_2 reduction product/intermediate on the surface. Cathodic peak C2 (about −0.5 V) is attributed to reduction of Cu oxide as can be inferred from Figure 6.1 and also from the literature [215, 216]. It is interesting to note that the anodic current measured at −0.1 V on these voltammograms is much greater than on the initial voltammograms measured when the cathode is first exposed to the electrolyte (Figure 6.1), suggesting that the Cu cathode is more easily oxidised after the cathode has been used for CO_2 reduction. It has been suggested that this can occur due to the differences between surface and bulk pH resulting from the cathodic current during the CO_2 reduction just prior to the voltammograms [44]. However, as we allow the interfacial pH to equilibrate with the bulk (at −1.2 V) before measuring these voltammograms, it seems unlikely that the additional

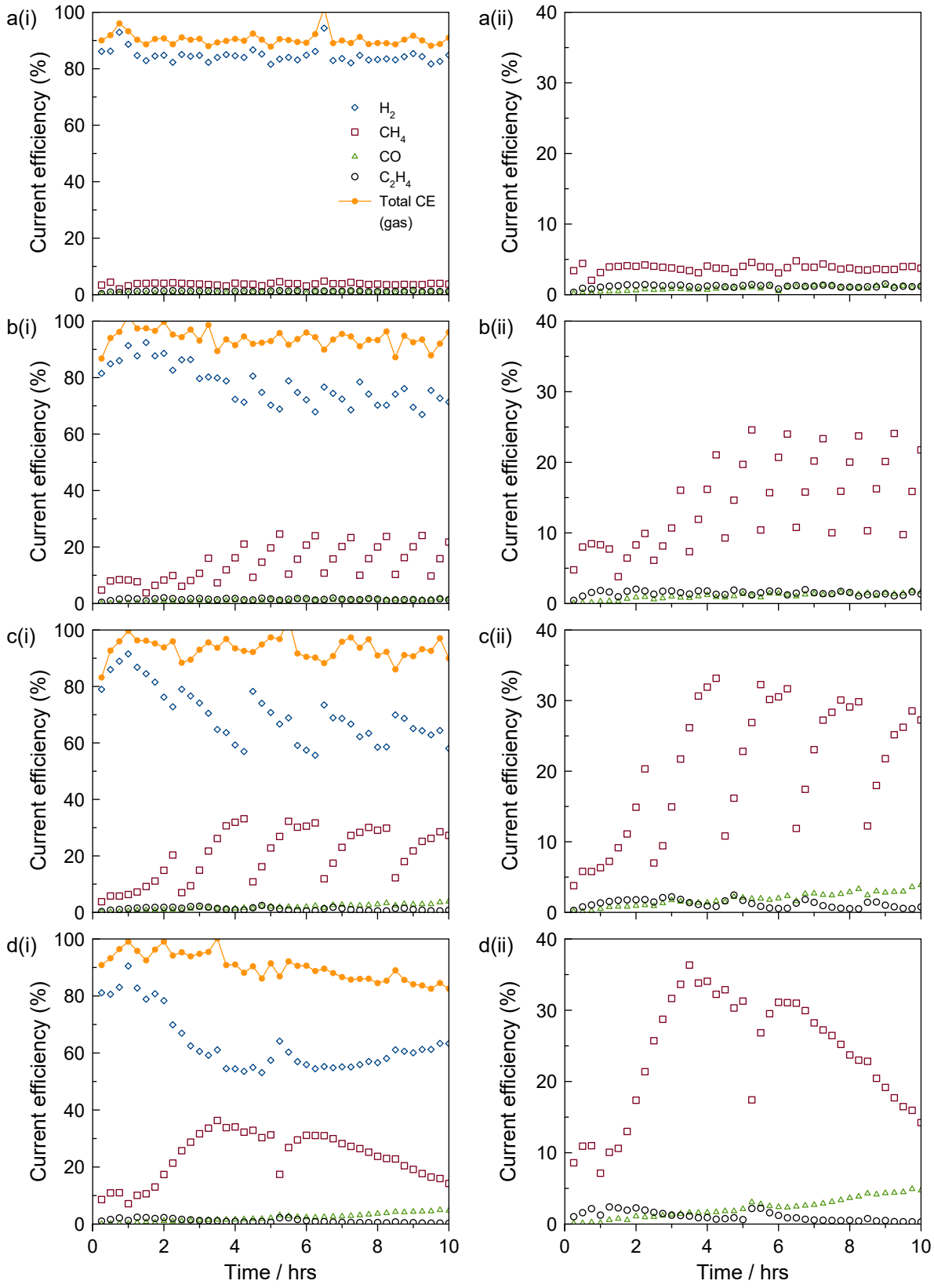

Figure 6.3: Current efficiencies during galvanostatic CO_2 reduction at −5 mA cm^{-2} in 0.2 M $KHCO_3$ on polished Cu with periodic cyclic voltammetry. The periodic cyclic voltammetry was performed every (a) 15 minutes, (b) 1 hour, (c) 2 hours and (d) 5 hours. The figures on the right side column (ii) are enlargements of the figures on the left side column (i). H_2 (diamonds), CH_4 (squares), CO (triangles), C_2H_4 (circles), total gas (circles with connecting line).

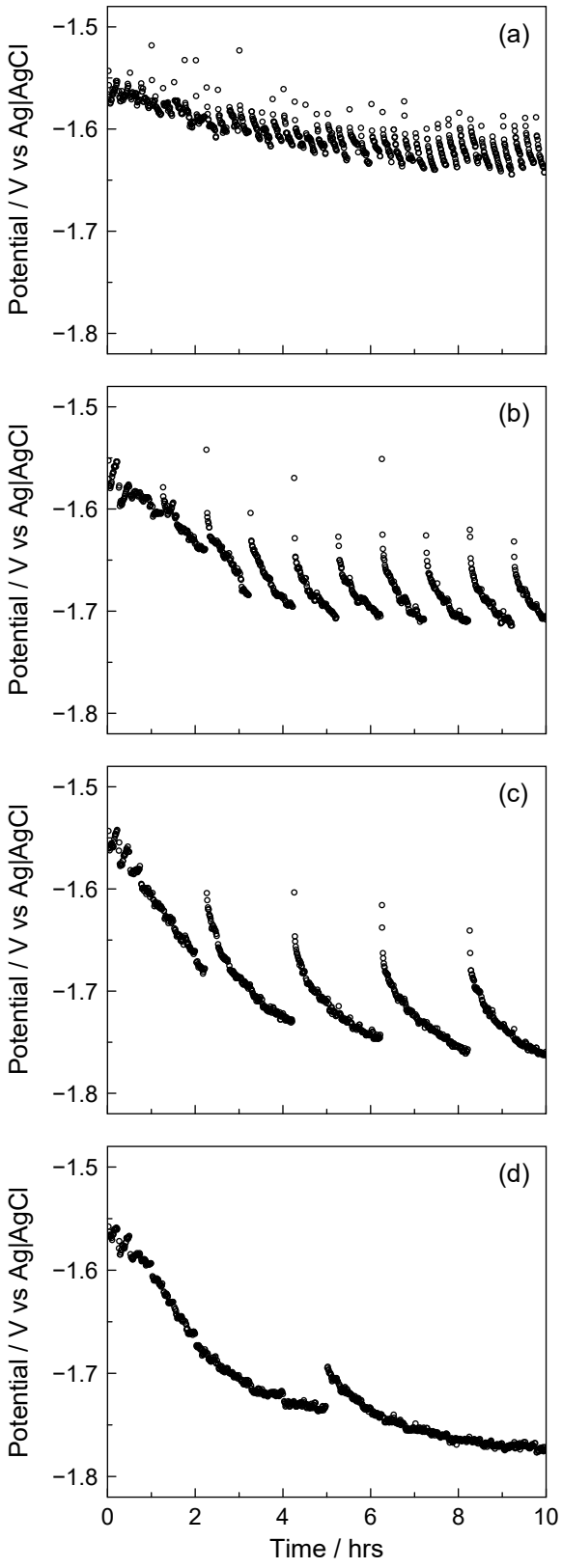

Figure 6.4: Potential during galvanostatic CO_2 reduction at −5 mA cm^{-2} in 0.2 M $KHCO_3$ on polished Cu with periodic cyclic voltammetry. The periodic cyclic voltammetry was performed every (a) 15 minutes, (b) 1 hour, (c) 2 hours and (d) 5 hours.

anodic current at −0.1 V is due to interfacial pH effects. Nevertheless, the Cu oxide formed during the cyclic voltammetry would be easily reduced upon re-application of the cathodic current for CO_2 reduction. More importantly, both the second and third cycles of the voltammograms show similar features (albeit with smaller peak sizes), which clearly indicates that the voltammetry does not completely remove the species responsible for the features found on the Cu cyclic voltammograms after a period of CO_2 reduction, although we note that the charge associated with peak A1 is always significantly larger than peak C1, suggesting that there is a net loss of surface bound species.

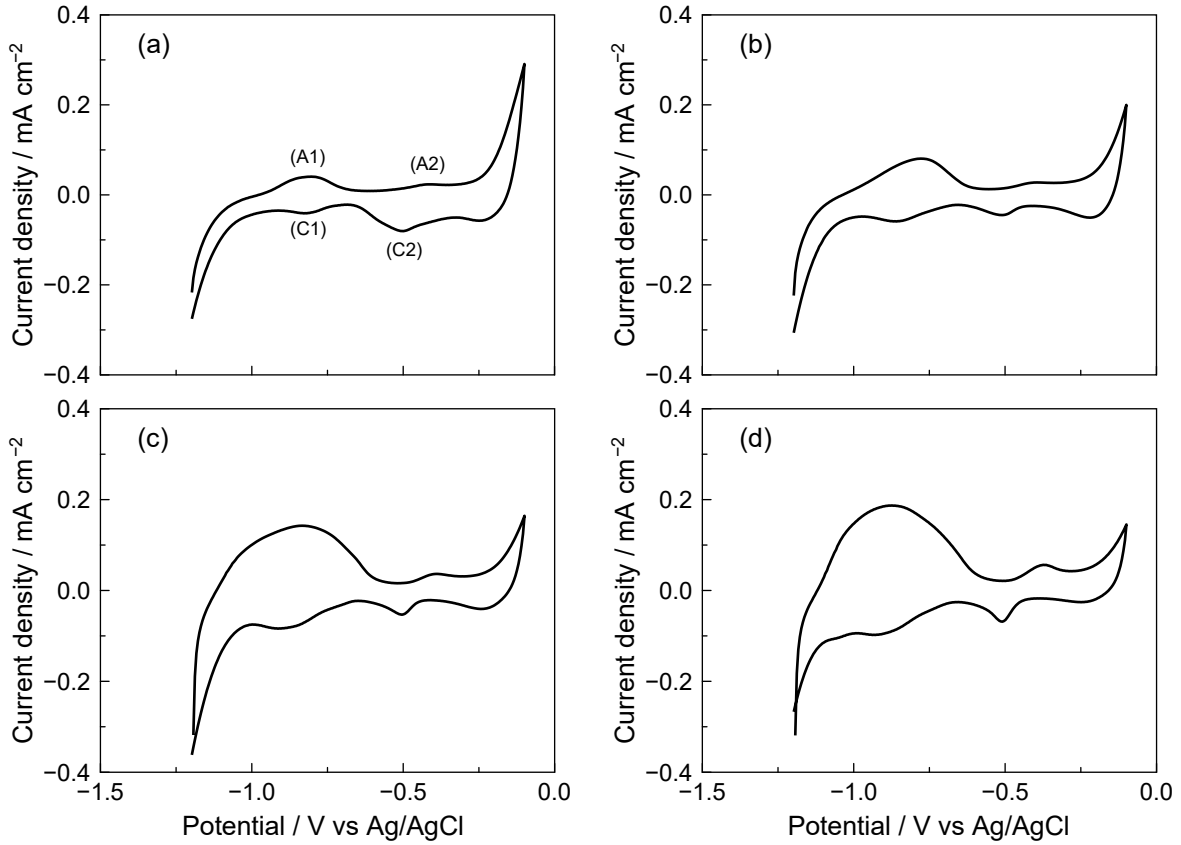

Figure 6.5: Cyclic voltammograms (first cycle) measured in between galvanostatic CO_2 reduction periods on polished Cu. The voltammograms measured from −1.2 V to −0.1 V and back to −1.2 V at 100 mV s^{-1} for 3 cycles were performed every (a) 15 minutes, (b) 1 hour, (c) 2 hours and (d) 5 hours.

The proposal that these voltammograms can strip off poisons from the Cu cathodes has been suggested elsewhere [149, 160], but generally is linked with an immediate enhancement in CO_2 reduction, whereas we find that this "clean" Cu surface is actually more active for HER. For example, the voltammograms obtained here are comparable with results described by Hori et. al. [149], who utilised anodic stripping cyclic voltammetry for the purpose of reactivating the Cu electrode. However, in their analysis, peaks A1 and A2 were attributed to stripping of Zn and Fe respectively, which were believed to be electrodeposited onto the Cu surface from the trace impurities in the electrolyte solution. To investigate this, we performed pre-electrolysis on our solution to remove these impurities, after which their concentrations were measured via ICP-MS. We found no trace of Zn and only approximately 10 ppb of Fe^{2+} in 0.2 M $KHCO_3$, which is 10 times below the manufacturer's specifications. The fact that Zn was not present at all in our solution confirms that peak A1 cannot be due to stripping of electrodeposited Zn from the electrode surface. Moreover, the observation that peaks A1 and A2 increased in size as the CH_4 formation rate increased is inconsistent with poisoning by impurities from the solution, since increased poisoning by Zn or Fe should promote the HER over

CO_2 reduction. In other words, if peaks A1 and A2 are due to the anodic stripping of electrodeposited metallic impurities, the reversed case would be expected, i.e. the experiment with the least overall CO_2 reduction activity should produce voltammograms with the largest A1 and A2 peaks, because the electrode would have been severely poisoned by the electrodeposited impurities which promote the HER. Thus we suggest that the features observed on the voltammograms are more consistent with the accumulation of adsorbed CO_2 reduction intermediates or products (such as carbon) which can be partially removed/oxidised.

6.3.4 Periodic potentiostatic steps during galvanostatic CO_2 reduction

As it is clear that temporarily interrupting galvanostatic CO_2 reduction with short periods at potentials between −1.2 V and −0.1 V has a large effect on the CO_2 reduction, we also investigated the effect of short (84 s) potentiostatic steps (at −0.25, −0.5 and −1.2 V) every 2 hours during galvanostatic CO_2 reduction. The potential of these short interruptions were chosen based on the positions of the anodic peaks in the voltammograms (Figure 6.5), i.e. more positive than A2, between A1 and A2, and more negative than A1.

It can be seen that performing short potentiostatic steps at −0.25 V or −0.5 V every 2 hours produced results that are similar to performing cyclic voltammograms every 2 hours, both in the current efficiency and potential with time behaviour (compare Figures 6.6a and 6.6b to Figure 6.3c). This supports our hypothesis that the CO_2 reduction intermediates or products adsorbed on the Cu surface can be removed/oxidised at potentials above −0.5 V, thereby restoring the Cu surface back to an earlier state. This is supported by previous infrared spectroscopy studies which showed that adsorption of CO only begins at potentials less than −0.8 V on the Cu surface [81, 122, 229], thus potentials of −0.5 V or higher are more than sufficient to remove CO_{ads}. We also note that the Pourbaix diagrams for carbon suggest that any carbon deposits can be oxidised above −0.4 V. The minor differences in results between −0.25 V and −0.5 V steps can be explained by the fact that peak A2 is much smaller than peak A1, hence the majority of adsorbed intermediates would have already been removed at −0.5 V.

Table 6.1: Averaged current during the −0.25, −0.5 and −1.2 V potentiostatic steps.

Step number	Average current, μA			
	−0.25 V (84 s)	−0.50 V (84 s)	−1.20 V (84 s)	−1.20 V (200 s)
First	−13.0	−12.6	−576	−562
Second	−3.5	−11.4	−450	−251
Third	−3.5	−12.4	−296	−192
Fourth	−4.1	−12.9	−252	−185

For the experiment with potentiostatic steps at −1.2 V for 84 s (Figure 6.6c), the current efficiency for CO production increased immediately after each potentiostatic step. In contrast, the current efficiency for CH_4 decreased, while that for H_2 was not significantly affected and continued to show a gradual decline over the whole electrolysis duration. While the current efficiencies for CH_4 and CO after each step gradually increased and decreased with time respectively until the next step was performed, it is clear that each −1.2 V step undoubtedly enhanced CO at the expense of CH_4. Unlike the potential during the 2 hours of CO_2 reduction after the short potentiostatic steps at −0.25 and −0.5 V, the potential during the galvanostatic CO_2 reduction after the −1.2 V steps is seen to remain stable (Figure 6.7). This suggests that while the changes in CO_2 reduction selectivity during the galvanostatic periods can be linked to the potential after the short potentiostatic steps at −0.25 and −0.5 V, the changes in selectivity after the −1.2 V potentiostatic steps cannot be due to changes in potential during CO_2 reduction.

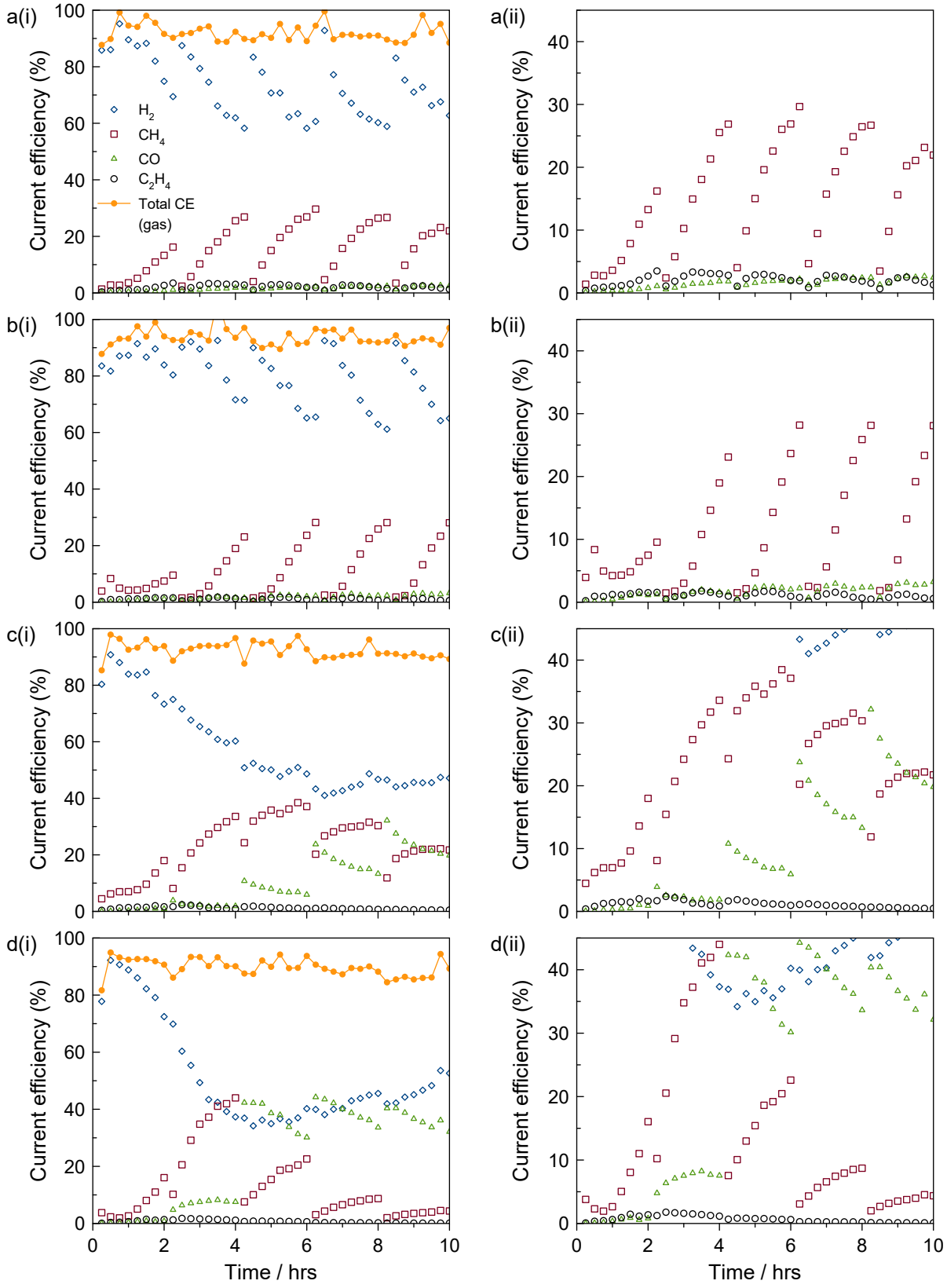

Figure 6.6: Current efficiencies during galvanostatic CO_2 reduction at −5 mA cm^{-2} in 0.2 M $KHCO_3$ on polished Cu interrupted with periodic potentiostatic steps. The periodic potentiostatic steps were performed every 2 hours at (a) −0.25, (b) −0.5 or (c) −1.2 V for 84 s, and at (d) −1.2 V for 200 s. The figures on the right side column (ii) are enlargements of the figures on the left side column (i). H_2 (diamonds), CH_4 (squares), CO (triangles), C_2H_4 (circles), total gas (circles with connecting line).

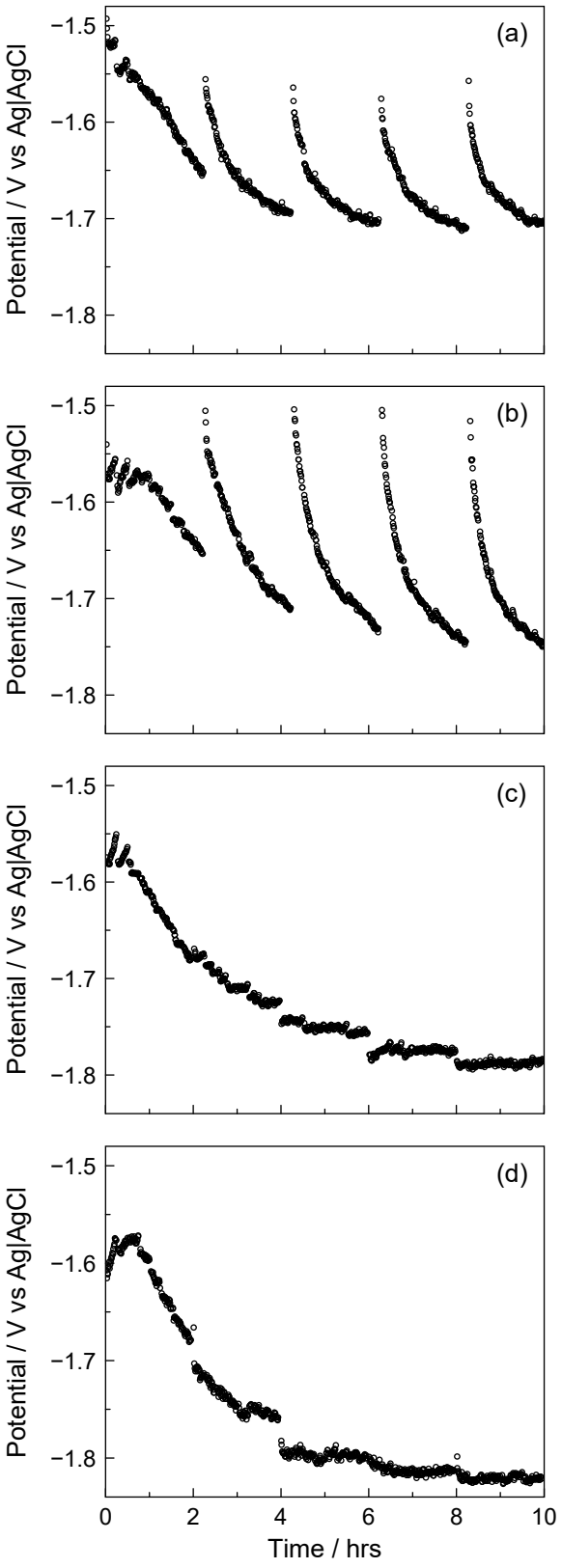

Figure 6.7: Potential during galvanostatic CO_2 reduction at −5 mA cm^{-2} in 0.2 M $KHCO_3$ on polished Cu interrupted with periodic potentiostatic steps. The periodic potentiostatic steps were performed every 2 hours at (a) −0.25, (b) −0.5 or (c) −1.2 V for 84 s, and at (d) −1.2 V for 200 s.

When the duration of these −1.2 V steps was increased 200 s (Figure 6.6d), the switch towards the higher CO production rate at the expense of CH_4 is even more noticeable, with the current efficiency for CO production increasing to 40%, while that of CH_4 dropped to 5% and H_2 to a minimum of 35%. It is completely unexpected and in contrast to prior work [67] that CO should form at the potentials (−1.75 to −1.8 V) found during the galvanostatic periods after these short steps at −1.2 V.

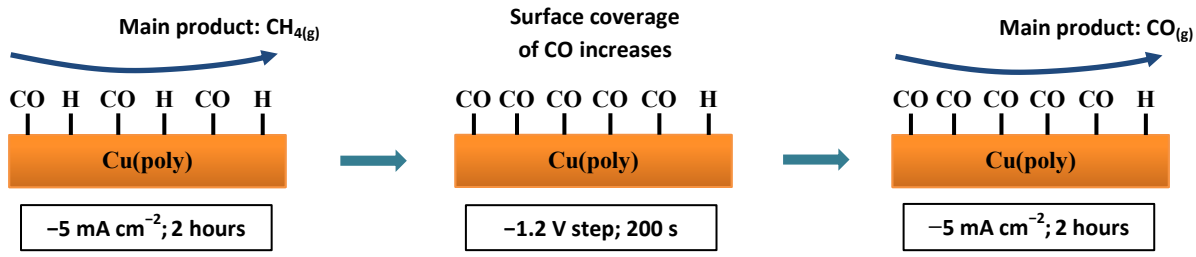

Figure 6.8: Illustration of multiple surface coverages of CO_{ads} and H_{ads} on polycrystalline Cu, brought about by a short potentiostatic −1.2 V step (200 s) in between two constant current (−5 mA cm^{-2}, 2 hours) electrochemical CO_2 reduction periods. $CO_{(g)}$ becomes the main CO_2 reduction product at the expense of $CH_{4(g)}$ when the surface coverages of CO_{ads} increased at the expense of H_{ads} during the short −1.2 V step.

In previous work, the formation of Cu oxides has been suggested to be the cause of the observed changes in CO_2 reduction product selectivity when brief periodic anodic treatments are used during CO_2 reduction [160, 164-166]. However, as the potentiostatic treatments at −1.2 V are much more negative than the potentials for Cu oxide formation and as the average current during these potentiostatic steps was found to be cathodic (Table 6.1), it seems extremely unlikely that the formation of Cu oxides are the cause of the observed selectivity change from CH_4 to CO. Others have proposed that pulsed CO_2 reduction influences product selectivity through changes in the surface coverage of H_{ads} [167]. While it is not surprising that changes to the surface coverage of adsorbed intermediates (e.g. CO_{ads} or H_{ads}) caused by brief anodic pulses would have a temporary effect on the CO_2 reduction behaviour, in our case the brief potentiostatic steps at −1.2 V (84 or 200s) alters the CO_2 reduction selectivity for at least 2 hours. Thus it seems unlikely that a temporary change in the surface coverages of H_{ads} or adsorbed CO_2 reduction intermediates such as CO_{ads} could play a significant role in our work. Instead we propose that the brief periods at −1.2 V enables the cathode to switch between multiple steady-state surface coverages (once the cathodic current is reapplied) rather than only causing a temporary change in surface coverages; a similar mechanism is seen in some electrochemical systems [230, 231] and heterogeneous catalysis [232-235]. In this work as the HER occurs in parallel with CO_2 reduction, and as the reaction between CO_{ads} and H_{ads} is the route to CH_4 production, we speculate that the competition for adsorption sites between CO_{ads} and H_{ads} is the underlying cause of the multiple steady-states found here. It is known that CO_{ads} is formed on the Cu surface below −0.8 V and its coverage continues to increase until the potential is negative enough (−1.5 V and below) for further reduction to hydrocarbons [81, 122, 229]. It is also known based on voltammetry that CO_{ads} significantly suppresses HER [80, 122]. Therefore, we propose that during the brief periods at −1.2 V, the surface coverage of CO_{ads} increases at the expense of H_{ads}, and then on the re-application of the cathodic current to drive CO_2 reduction, this new surface coverage is either maintained or enables the cathode to switch to a different steady-state surface coverage (with very low H_{ads}), wherein there is insufficient H_{ads} to further reduce CO to CH_4 and other hydrocarbons, and thus the cathode favours CO production (Figure 6.8). While we currently have no spectroscopic proof for this mechanism, we are currently investigating the possibility of tracking the CO surface coverage using in-situ FTIR spectroscopy in a similar fashion to that reported elsewhere [54, 81, 122, 229].

6.4 Conclusions

Periodic cyclic voltammetry and potentiostatic steps can be used to alter the electrochemical CO_2 reduction behaviour on Cu cathodes. During continuous galvanostatic CO_2 reduction, the CO_2 reduction selectivity towards CH_4 and C_2H_4 firstly increases before reaching a maximum and slowly decreases to a point where HER dominates. The increase in overall CO_2 reduction activity at the start is attributed to the inhibition of the HER by the slow accumulation of CO_2 reduction products such as carbon. This causes the potential to decrease, which in turn increases the driving force for CO_2 reduction to CH_4 and C_2H_4. Eventually the accumulation of poisons on the Cu reduces the availability of sites capable of hydrogenating the adsorbed CO to CH_4 and C_2H_4. By interrupting the galvanostatic CO_2 reduction with cyclic voltammetry between −1.2 V and −0.1 V, the overall CO_2 reduction activity is suppressed due to the partial removal or oxidation of the adsorbed CO_2 reduction intermediates or adsorbed poison, with this partially cleaned surface being more active towards the HER. Similarly, if the galvanostatic CO_2 reduction is interrupted with brief potentiostatic steps at −0.25 or −0.5 V, the cathode becomes more active for the HER, again because of the removal of accumulated CO_2 reduction products or intermediates which normally inhibit the HER. However, if the galvanostatic CO_2 reduction is briefly interrupted with a potentiostatic step at −1.2 V, upon re-application of the galvanostatic current, the product selectivity switches from CH_4 to CO. As the brief period at −1.2 V alters the CO_2 reduction selectivity for up to 2 hours, we propose that the brief potentiostatic step at −1.2 V enables the Cu cathode to switch between multiple steady-state surface coverages when the CO_2 reduction current is re-applied, rather than only bringing about a temporary change in surface coverages.

6.5 Additional material

From the current efficiency data of the continuous galvanostatic CO_2 reduction electrolysis (no periodic interruptions) presented in Figure 6.2a, where the electrode potential varied between −1.5 V to slightly less cathodic than −1.8 V (Figure 6.2b), the potential dependence of the current efficiencies of H_2, CH_4, CO and C_2H_4 can be extracted and plotted (Figure 6.9). From −1.5 to −1.7 V, as the potential becomes more cathodic, the current efficiency for H_2 decreases while that of the CO_2 reduction products increases. C_2H_4 reaches an optimum at approximately −1.65 V, while CH_4 and CO continue to increase with decreasing potentials up to −1.7 V and −1.8 V respectively. This trend is generally consistent with various reports on potential dependence of CO_2 reduction on Cu electrodes (see section 2.3.1). The observation that CH_4 and C_2H_4 do not share similar trends also suggests different reaction pathways for C_2H_4 and CH_4, which likely begins with adsorbed CO as the last common intermediate [83, 115, 118]. From −1.7 to −1.8 V however, H_2 and CH_4 deviate from the regularly observed trends, where a switch in their selectivity is observed. As highlighted in Figure 6.9, this generally occurred during the second half of the electrolysis (last 5 hours), and is likely due to gradual poisoning of the electrode, by graphitic carbon for example, that slowly changed the surface of the electrode to one that prefers the HER over CH_4 production.

In a similar manner, current efficiencies of H_2, CH_4, CO and C_2H_4 were plotted with potential using data from the experiments with periodic cyclic voltammetry and potentiostatic steps, along with additional data from experiments of similar fashion not shown here (Figure 6.10). The electrode potential for these experiments varied between −1.4 V to slightly more cathodic than −1.8 V. In this set of experiments, it is observed that the current efficiencies with potential follow the same trends as those in Figure 6.9 between −1.5 and −1.7 V. However, in between −1.7 and −1.8 V, instead of a switch in selectivity between H_2 and CH_4, the selectivity switches between CO and CH_4. The selectivity switch between CO and CH_4 continues and becomes more pronounced below −1.75V,

supposedly suggesting a direct influence of the electrode potential becoming more cathodic. However, we believe that a potential effect for this observation is unlikely since many works in the literature reported that current efficiency of CH_4 is much larger than CO at strong cathodic potentials (see section 2.3.1). Furthermore, the change in selectivity between CO and CH_4 is only observed for experiments with potentiostatic steps at −1.2 V as highlighted in Figure 6.10. Following the discussion in section 6.3.4, we suggest that the selectivity change between CO and CH_4 from −1.7 V and below is in fact due to the increased surface coverage of CO_{ads} at the expense of H_{ads} during the −1.2 V steps. When the cathodic current to drive CO_2 reduction is re-applied, this new surface coverage is either maintained or the electrode surface switches to a different steady-state surface coverage that has very low H_{ads}. Due to insufficient H_{ads} to reduce CO to CH_4 and other hydrocarbons, the cathode then favours CO production despite the electrode having a highly cathodic potential below −1.7 V.

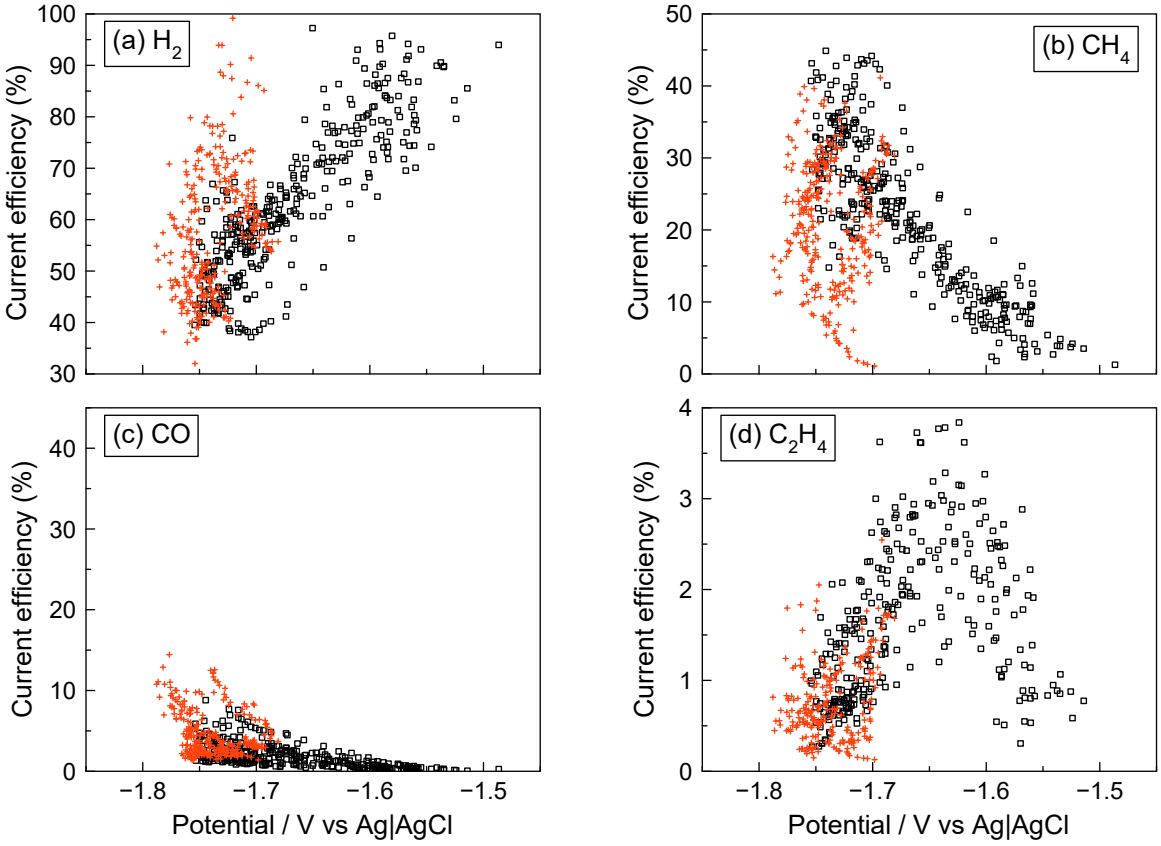

Figure 6.9: Current efficiency of (a) H_2, (b) CH_4, (c) CO and (d) C_2H_4 with potential for continuous galvanostatic CO_2 reduction on polished Cu with no periodic interruptions (data from Figure 6.2). (□) represents data within the first 5 hours of electrolysis, while (+) represent the last 5 hours.

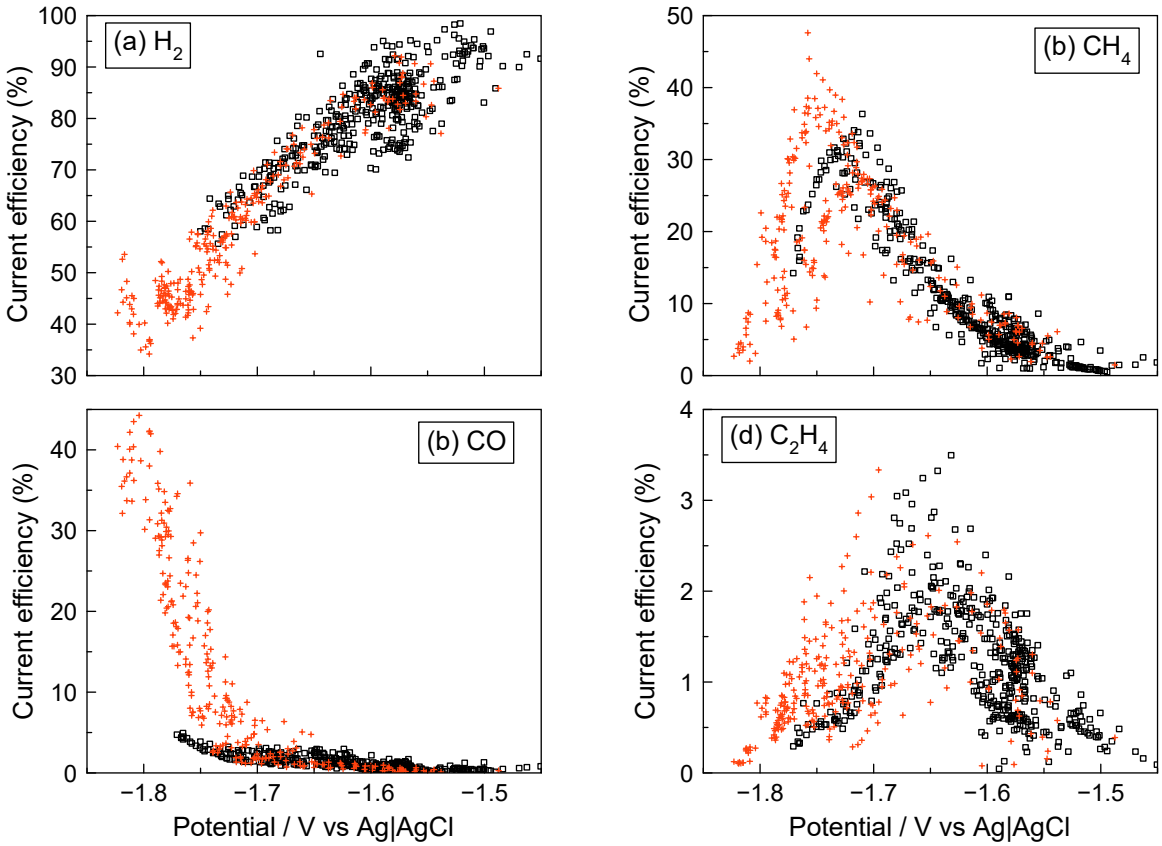

Figure 6.10: Current efficiency of (a) H_2, (b) CH_4, (c) CO and (d) C_2H_4 with potential for galvanostatic CO_2 reduction on polished Cu with periodic cyclic voltammetry and potentiostatic steps (data from Figures 6.3, 6.6 and additional data not shown). (□) represents data with periodic cyclic voltammetry and potentiostatic steps at −0.25 and −0.50 V, while (+) represents data with periodic potentiostatic steps at −1.2 V only.

7 The Effects of Mass Transfer on CO_2 Reduction

The contents of this chapter have been published in Electrochimica Acta under the title *"Effects of mass transfer on the electrocatalytic CO_2 reduction on Cu"*, which is reference [236] in this thesis. Because the publication is presented here in its entirety and original journal structure, the reader may encounter some material within this chapter that have already been covered elsewhere in the thesis. Section 7.5 presents additional material related to the work but was not included in the original publication.

DOI: https://doi.org/10.1016/j.electacta.2017.04.017; for copyright license, see Appendix 14.

Abstract: The effects of mass transfer on the electrocatalytic reduction of CO_2 on a polycrystalline Cu rotating cylinder electrode were investigated. When the rotation rate was increased, the current efficiency toward CO_2 reduction products decreased while that for the hydrogen evolution reaction increased. Furthermore, the product selectivity switched from CH_4 to CO as the rotation rate was increased. This observation is generally inconsistent with the widely reported dependence of the electrocatalytic CO_2 reduction on interfacial pH and CO_2 concentration. As increasing the rotation rate improves mass transfer of species to and from the electrode surface, the interfacial pH becomes closer to the bulk pH while the interfacial concentration of CO_2 at the electrode surface increases. However, increasing the rotation rate significantly decreased the CO_2 reduction activity for constant current electrochemical CO_2 reduction despite the increased availability of CO_2 at the electrode surface. As the changes in interfacial pH and CO_2 concentration with rotation rate cannot adequately explain the results, it is instead suggested that the enhanced mass transfer of dissolved CO away from the electrode surface at high rotation rates is the main reason behind the observed effects. We propose that this enhanced mass transfer of CO away from the electrode surface decreases the surface coverage of CO_{ads} (due to the equilibrium between CO_{ads} and dissolved CO at the electrode-electrolyte interface) and limits the further reduction of CO_{ads} to hydrocarbons.

7.1 Introduction

The electrochemical reduction of CO_2 has been intensively studied due to its potential to alleviate CO_2 emissions and store intermittent renewable energy in the form of carbon-based fuels [4]. Amongst the different metals studied in aqueous systems, Cu has a unique ability to reduce CO_2 to a wide range of hydrocarbons, although the reaction selectivity has been shown to be generally poor [32]. Hence many have focussed on optimising the activity and selectivity of CO_2 reduction on Cu cathodes by investigating the effects of surface oxides [69, 180, 182], crystal facets [118, 129, 133], and by using Cu nanoparticles [194-196, 202] etc.

However, an increasing number of investigations have also highlighted the sensitivity of the reaction selectivity to process conditions such as temperature [42, 51, 120, 121], CO_2 pressure [104, 121, 124, 128], and electrolyte buffer concentration [67, 74, 104]. Selectivity differences were also observed on porous electrodes where confinement of reactive species and diffusional limitations were determined to be the cause [107, 227]. And thus it has been emphasized that differences in reaction selectivity cannot always be exclusively attributed to differences in intrinsic catalytic behaviour [49, 104, 107]. Instead, the interfacial pH and CO_2 concentration at the electrode surface, which may both be significantly higher and lower respectively than in the bulk electrolyte during electrolysis [44, 105], were suggested to be the reason for the observed selectivity changes.

In addition to the above-mentioned factors, another interesting observation is that the selectivity can also change by simply agitating the electrolyte [23, 124, 168]. Clearly, stirring or agitating the electrolyte improves mass transfer to and from the electrode surface due to a decrease in the diffusion layer thickness. Hence, in relation to the local pH and CO_2 concentration, a higher stirring rate shifts the interfacial pH closer to that in the bulk, and increases the flux of dissolved CO_2 to the electrode [44]. Due to the sensitivity of CO_2 reduction on pH [74, 103, 104, 237, 238] and CO_2 concentration [51, 104, 120, 124], it is not surprising that mass transfer effects can greatly influence the reaction selectivity. Indeed, it has been observed that an increased selectivity for CO production is usually seen when the electrolyte is stirred, compared to one that is stagnant [23, 124].

It is well known that adsorbed CO is a major intermediate for CO_2 reduction [24, 54, 64, 81], and uniquely for Cu electrodes, CO is adsorbed with moderate strength [53, 54, 76] which in accordance to the Sabatier principle, facilitates its further reduction to hydrocarbons. The fact that CO binds neither too strongly nor too weakly on Cu suggests that the surface coverage of CO exists in equilibrium with dissolved CO in the diffusion layer [54]. This explains the observation of early potentiometric [80] and voltammetry [67] experiments, where CO was suggested to desorb easily when the electrolyte was stirred or purged with an inert gas to remove dissolved CO. Hence, in addition to local pH and CO_2 concentration, a significant change in CO surface coverage can also be caused by stirring the electrolyte due to mass transfer of dissolved CO away from the vicinity of the electrode surface. With decreased CO surface coverage, hydrocarbon production will decrease, explaining the observed enhanced selectivity towards CO for stirred electrolytes.

The sensitivity of the reaction selectivity on electrolyte stirring poses a challenge in comparing results in the literature as the hydrodynamics will undoubtedly vary between different cell configurations and research groups. Therefore, it was suggested that the level of stirring be quantified [44] so that the effects mass transfer on CO_2 reduction can be determined. To investigate this, we have performed constant current CO_2 reduction on a polycrystalline Cu rotating cylinder electrode (RCE), for which fundamental hydrodynamics allowing the prediction of mass transfer have been previously developed [222, 224, 225, 239]. The RCE was chosen over the more established rotating disk electrode due to the higher surface area available on the RCE which enables easier product analysis because of the higher reduction rates. By incorporating the RCE hydrodynamics and adapting the mathematical model developed by Gupta et al. [44] the interfacial concentrations (pH, CO_2 and carbonate species) at the electrode surface can be calculated and used to discuss the effects of mass transfer on the electrochemical reduction of CO_2 on Cu electrodes.

7.2 Experimental

A 15 mm diameter (geometric area = 3 cm^2) polycrystalline Cu rotating cylinder electrode (99.99%, Advent Research Materials Ltd) was used as the working electrode. The electrode was prepared by mechanical polishing with silicon carbide paper and alumina slurries until a mirror finish was obtained, which was followed by ultra-sonication and rinsing with isopropanol and 18 MΩ cm deionised water. After preparation, the electrode was exposed to air for approximately 15 minutes during which some surface oxide forms. This thin oxide layer was shown in our previous work to be easily reduced by performing cyclic voltammetry prior to CO_2 reduction [147]. In this work, we also performed a similar initial cyclic voltammetry prior to CO_2 reduction to ensure the reduction of this surface oxide.

Electrolysis was conducted in a conventional two compartment H-type cell separated by a Nafion 115 cation exchange membrane. A Ag|AgCl (sat. KCl) electrode and a Pt foil were used as the reference

and counter electrodes respectively. All potentials are reported against the Ag|AgCl reference unless stated otherwise. The electrode was mounted on a rotator shaft and placed in the centre of the catholyte chamber. The electrolyte was 400 ml of 0.2 M $KHCO_3$ (99.7% ACS reagent, Sigma Aldrich) saturated with high purity 99.9995% CO_2, giving a solution with pH 7. This electrolyte was pre-electrolysed for 48 hours beforehand to remove any trace metallic impurities that may poison the Cu electrode [149].

Throughout the CO_2 reduction experiments, the electrolyte was bubbled with the high purity CO_2 at 20 ml min^{-1} (Alicat mass flow controller) at a fixed distance of approximately 5 cm away from the electrode surface. The gas outlet of the cell was led to a gas chromatograph (SRI Instruments) equipped with a haysep-D column, methanizer FID and TCD detectors to quantify H_2, CO, CH_4, C_2H_4 and C_2H_6 every 15 minutes. From the gas chromatography measurements, the current efficiency (percentage of the total current going towards the formation of a certain product) as a function of time of the gaseous products can be calculated. Liquid products in the catholyte (formic acid, acetic acid and methanol) were measured post experiment using HPLC equipped with a SUPELCOGEL™ C-610H column. Because liquid products were only measured post experiment, only the total current efficiency (the current efficiency over the whole duration of electrolysis) for these products was calculated.

All electrochemical experiments were controlled using a GAMRY Reference 3000 potentiostat and performed at ambient temperature and pressure. The rotation rate of the cathode was controlled by a MSR rotator (Pine Research Instrumentation). Experiments were conducted at a constant current density of −5 mA cm^{-2} for 10 hours, with electrochemical impedance spectroscopy (EIS) measurements performed every 15 minutes to measure the solution resistance. To ensure that the constant current density CO_2 reduction was not interrupted during the solution resistance measurement, hybrid EIS was used with a 5 mV rms AC potential superimposed on top of an applied DC current density of −5 mA cm^{-2}, over the frequency range 100 kHz − 10 Hz.

All potential measurements were corrected by the measured solution resistance (R) post experiment using Ohm's law ($E_{\text{corrected}} = E_{\text{measured}} - i_{total}R_s$). The regular measurement of the solution resistance is important during long-term CO_2 reduction experiments because of the transport of K^+ ions through the Nafion membrane to the catholyte (from the anolyte), which decreases the solution resistance over time. Note that we prefer constant current over constant potential reduction as varying current densities during constant potential reduction will cause a variation in the interfacial pH [44]. For example, the estimated interfacial pH at −5 and −15 mA cm^{-2} is 9.6 and 10.4 respectively [44]. Hence, the interfacial pH can vary significantly throughout an experiment if the current density varies during a potentiostatic measurement. Indeed, in one long-term (10 hours) potentiostatic measurement, the current density varied between −2 to −13 mA cm^{-2}, which means that the interfacial pH also varied by approximately 1 unit. As this paper is focussed at the role of mass transfer rate on CO_2 reduction selectivity, operating galvanostatically ensures that any changes to the interfacial pH are only due to mass transfer effects.

7.3 Results and discussion

Constant current (−5 mA cm^{-2}) electrochemical CO_2 reduction on polycrystalline Cu RCE was carried out at 10, 50, 240, 500 and 1000 rpm for 10 hours at each rotation rates (Figures 7.1 and 7.2). By using RCE hydrodynamics and adapting the mathematical model developed by Gupta et al. [44], the interfacial pH and concentrations of CO_2, HCO_3^- and CO_3^{2-} with time were also estimated (Figure 7.3). The main difference between the model used here and that provided by Gupta et al. [44],

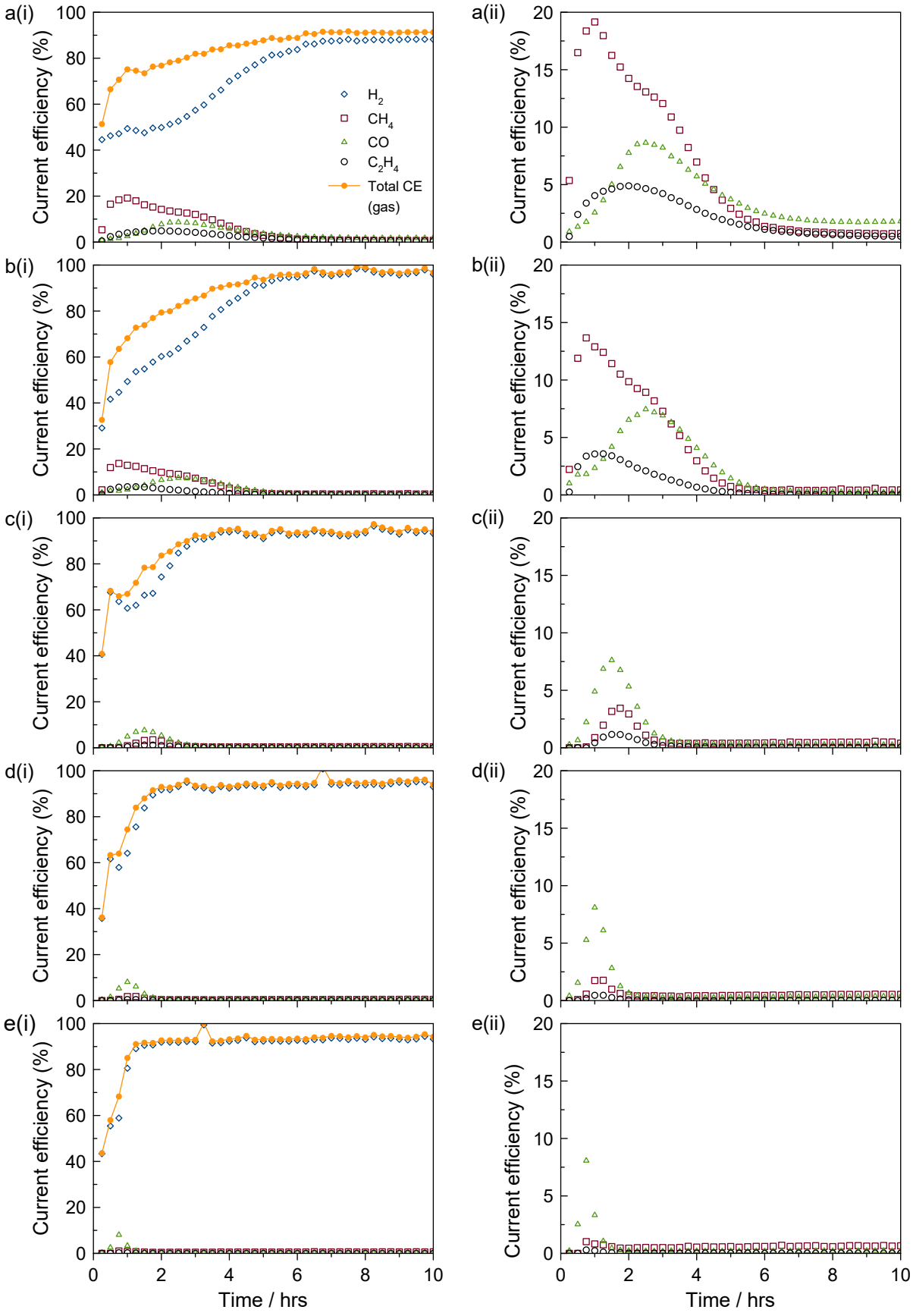

Figure 7.1: Current efficiencies of gaseous products with time for CO_2 reduction at −5 mA cm^{-2} in 0.2 M $KHCO_3$ using a Cu RCE at (a) 10, (b) 50, (c) 240, (d) 500 and (e) 1000 rpm. The figures on the right side column (ii) are enlargements of the figures on the left side column (i).

is the inclusion of differential equations to account for changes in the bulk electrolyte due to the electrode reactions and selective transfer of K^+ from the anolyte to the catholyte. Because changes in the bulk electrolyte will affect interfacial concentrations at the electrode surface, the simulated bulk concentrations with time were used as the boundary condition at the interface between the bulk electrolyte and the diffusion layer, instead of a fixed and constant boundary condition as used in [44]. Similarly, the current efficiency values which define the boundary condition at the electrode surface are also updated with time using values measured during the experiment. The model was also improved by including ionic strength and activity coefficients in the calculations using the Davies equation [75].

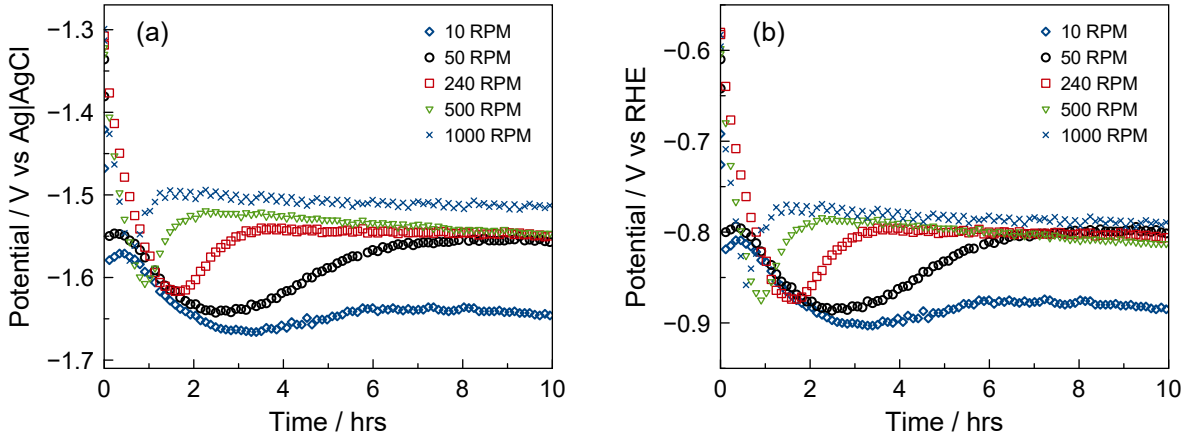

Figure 7.2: Electrode potential (a) vs Ag|AgCl KCl sat. and (b) vs RHE during the constant current CO_2 reduction on a Cu RCE at various rotation rates presented in Figure 7.1. The potential vs RHE was calculated using the calculated interfacial pH presented in Figure 7.3a.

The main gaseous products obtained during these long-term electrolysis experiments were H_2, CH_4, CO and C_2H_4 (Figure 7.1). The current efficiency for C_2H_6 production was very low (< 0.1%), and hence it is not reported. Formic acid was the main liquid product found in the electrolyte, along with traces of acetic acid. Methanol was not detected, consistent with existing reports for polycrystalline Cu [24, 47, 48, 66, 67, 83]. By performing an overall charge balance, along with the GC and HPLC measurements, we have found that that majority of current not going to gas products results in formic acid production. Thus in this work the current efficiency for formic acid production over the course of the electrolysis can be predicted with some confidence from the difference between the total applied current and that going to gas products. Over the 10 hours of electrolysis, the main CO_2 reduction product was found to be formic acid, followed by either CH_4 or CO depending on the rotation rate, and lastly C_2H_4. It is interesting that the current efficiency for formic acid is the highest, because it is more commonly reported that CH_4 and C_2H_4 are the major products of electrochemical CO_2 reduction on polycrystalline Cu [42, 48, 51, 63, 64, 66, 67, 74, 104, 120] at similar current densities. Previously we have also shown that CH_4 is the major product on Cu cathodes [147], and we believe that part of the reason for the increased formic acid production found here relates to differences in the electrode and cell geometry between the prior and present work, which alters the hydrodynamics of the electrolyte stirring induced by gas bubbles evolving off the surface of the cathode.

The current efficiency for gaseous CO_2 reduction products generally follows the same trends for all rotation rates, where a maximum is obtained between 0.5 and 2.5 hours into the experiment, depending on the rotation rate applied (Figure 7.1). Note that in the first 15 minutes of CO_2 reduction, the current efficiency for all gaseous products is always significantly lower due to the volume between the headspace of the electrochemical cell and the gas chromatograph which initially dilutes

the product gas. The time-dependent changes in total CO_2 reduction activity are observed to be correlated with the electrode potential (Figure 7.2), i.e., higher total CO_2 reduction activity is observed when the potential is more negative. To ensure that any changes in the overpotentials for pH dependent reactions are accounted for, the electrode potential was calculated against a "local" RHE by using the estimated interfacial pH shown in Figure 7.3a. For all rotation rates, the electrode potential generally follows the same trend with the potential initially becoming more negative through to a potential minimum before increasing back to almost a stable (but slightly decreasing) potential (Figure 7.2). As the rotation rate increases, the time to reach the minimum electrode potential decreases, and as a whole, the electrode potential (vs the Ag|AgCl reference electrode) becomes less negative. The differences in the minimum potential vs RHE due to the rotation rate are less than vs Ag|AgCl.

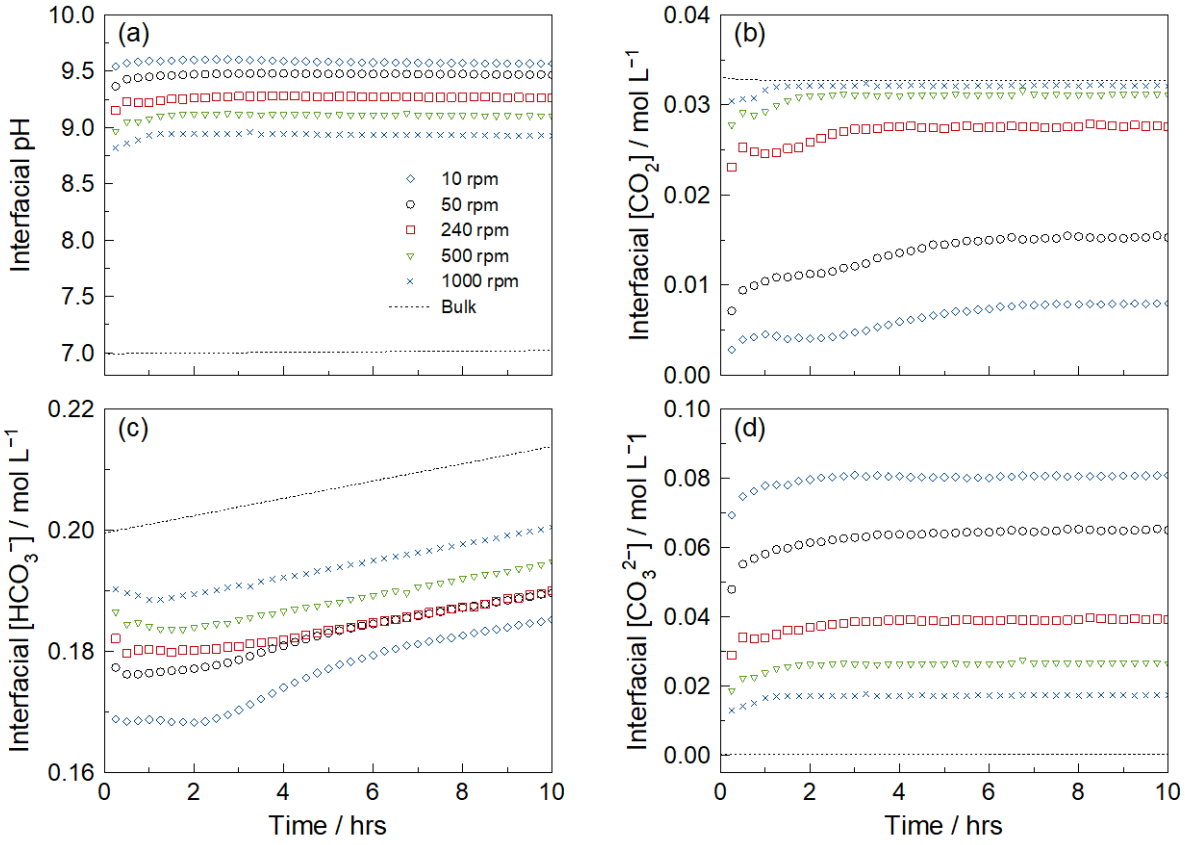

Figure 7.3: (a) Interfacial pH and concentrations of (b) CO_2, (c) HCO_3^- and (d) CO_3^{2-} during the constant current CO_2 reduction on a Cu RCE. The values were calculated by adapting the model developed by Gupta et al. [44], with the bulk electrolyte values given by the dashed line. At time = 0, all interfacial concentrations were equal to their bulk values.

The general behaviour of the electrode potential and CO_2 reduction activity over long periods of electrolysis at stationary Cu cathodes has been described elsewhere [147]. At the start of electrolysis, the electrode potential is in the vicinity of −1.3 to −1.5 V vs Ag|AgCl for all rotation rates, which is more positive than the −1.5 to −1.7 V vs Ag|AgCl normally required for observable hydrocarbon formation [23, 45, 66, 67, 160]. Normally between −1.3 to −1.5 V vs Ag|AgCl, the main CO_2 reduction products are formic acid and CO [32, 65, 67]. The dependence of the reaction selectivity of CO_2 reduction on potential is supported by a series of constant potential experiments (Figure 7.4), where it clearly shows that formic acid and CH_4 are favoured at more positive and negative potentials respectively. This is consistent with our data (Figure 7.1), where high formic acid production (as

inferred from the low total gaseous current efficiency) and low amounts of hydrocarbons were observed between −1.3 to −1.5 V vs Ag|AgCl at the start of electrolysis. As the electrolysis time increases, the electrode potential becomes more negative and the formation rate of formic acid decreases while that of H_2, CH_4, C_2H_4 and CO increases. This decrease in electrode potential with time can be explained by the blocking or poisoning of reaction sites by the slow accumulation of CO_2 reduction products or intermediates, such as CO_{ads} (or a more reduced form, e.g. COH_{ads} [104]). This decreases the available reaction sites, which means that a larger overpotential is required to maintain the specified current density, and hence, the electrode potential gradually becomes more negative, traversing through the onset potential for hydrocarbon formation.

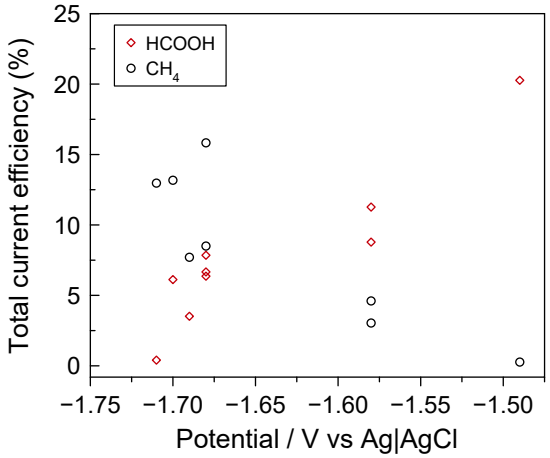

Figure 7.4: Total current efficiency of formic acid and CH_4 over 10 hours of constant potential CO_2 reduction on a polycrystalline Cu RCE at various potentials at 10 rpm.

After a certain time (30 min to 2.5 hour) the potential reaches the aforementioned minimum and then starts to become more positive (Figure 7.2). The time at which the potential minimum is reached is strongly dependent on rotation rate. This minimum in electrode potential corresponds to a maximum in the total CO_2 reduction selectivity, and as the potential becomes more positive the HER becomes more dominant. This can be explained by the widely reported poisoning of Cu electrodes in favour towards the HER, the reason of which still remains debatable. Most literature attributes the poisoning of CO_2 reduction on Cu electrodes to the formation of graphitic carbon (on the basis of XPS measurements) or some other product or intermediate species during CO_2 reduction [64, 152-154], although others suggest that the electrodeposition of metallic impurities (e.g. Fe^{2+} and Zn^{2+}) from the electrolyte is the main cause [149, 159]. However, based on stripping cyclic voltammetry measurements [147], and the absence or very low concentrations of these metallic impurities in this electrolyte as determined by ICP−MS, poisoning by metallic impurities seems unlikely in this work. The formation of carbon from CO_2 reduction on the other hand, has been supported by microscopic and spectroscopic evidence [63, 64, 147, 152-154]. In our previous work, we also observed thin carbon deposits on our Cu cathodes by SEM and EDS analysis after long-periods of CO_2 reduction [147]. In addition, carbon electrodes have been shown to be inactive for CO_2 reduction and give H_2 as the main product [51, 156-158]. Hence, the observed change in reaction selectivity from CO_2 reduction to the HER is consistent with the Cu surface being gradually covered by a layer of graphitic carbon, upon which the HER is more favourable.

The fact the deactivation of the Cu cathodes is faster as the rotation rate increases is consistent with the proposal that this increase in potential (and decrease in CO_2 reduction current efficiency) is related to carbon deposition:

$$CO + 2e^- + H_2O \rightleftharpoons C + 2OH^- \qquad E^0 = -0.310 \text{ vs SHE [217]} \qquad \text{R(7.1)}$$

At higher rotation rates, the mass transfer rate of OH^- away from the electrode is increased and therefore the interfacial pH is closer to the bulk solution compared to lower rotation rates (Figure 7.3a). Due to the lower interfacial pH, the carbon deposition reaction (reaction 7.1) is shifted more to the right, promoting carbon formation. This is supported by the reaction scheme suggested by Kas et al., where the formation of carbon is along the pH dependent pathway [104].

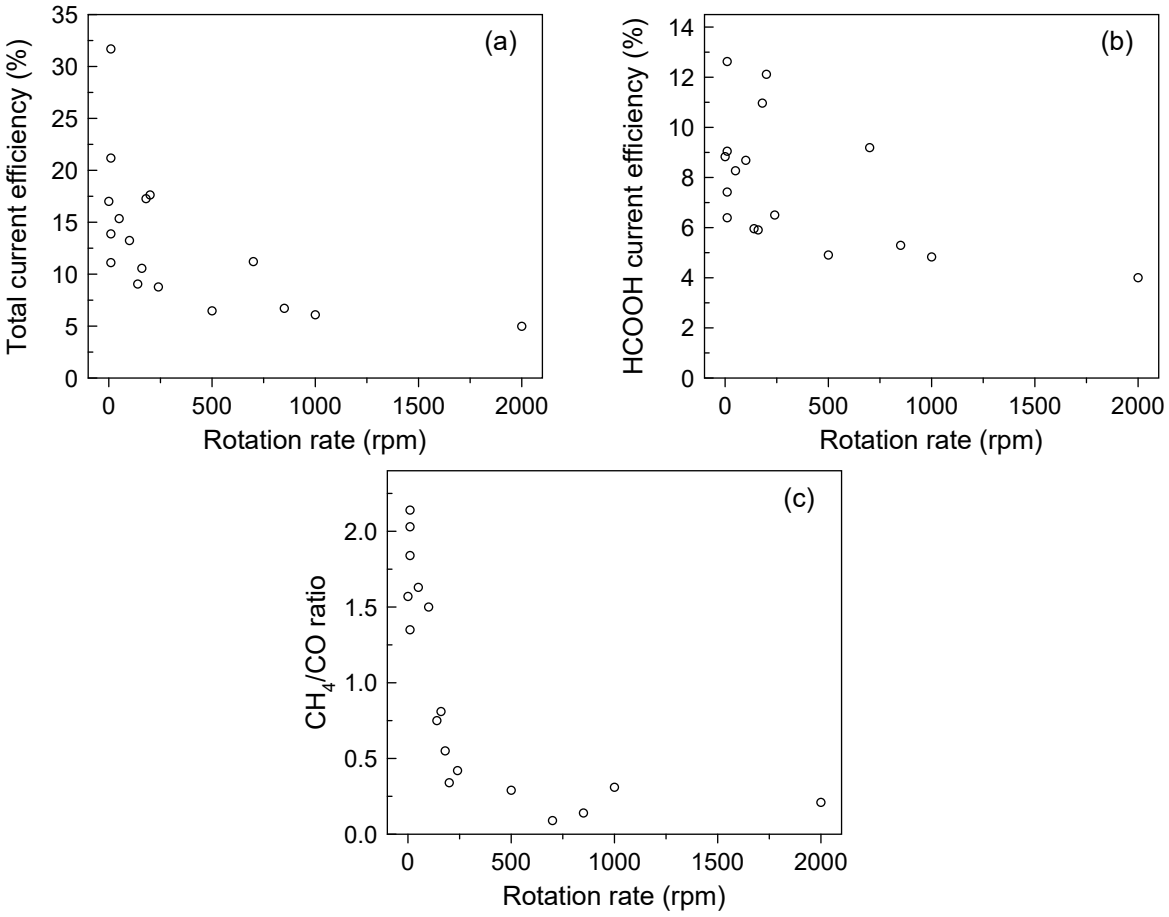

Figure 7.5: Total current efficiency of (a) all CO_2 reduction products (H_2 is excluded) and (b) formic acid over the entire electrolysis duration of 10 hours. (c) Total current efficiency ratio of CH_4 to CO. Rotation rate ranges from 10 to 2000 rpm.

The electrode potential continues to increase until it reaches an almost stable potential for the remainder of the electrolysis. Throughout this period, the HER is the dominant reaction with a current efficiency of about 90% and above. The very slow decrease in electrode potential after about 6 hours is likely due to changes in the bulk solution, notably the slow increase in the concentration of HCO_3^- (Figure 7.3c) due to the selective transport of K^+ from the anolyte through the Nafion membrane. As the concentration of HCO_3^- in the bulk solution increases, the interfacial concentration of HCO_3^- at the electrode surface will also increase, which may poison reaction sites and cause a gradual increase in overpotential. Other contributions could be the slow reduction of persistent Cu oxides [45, 69, 160, 180], or the restructuring of crystal orientations of the polycrystalline Cu under strong cathodic conditions [139, 140].

It is clear that altering the mass transfer (via electrode rotation rate) has a significant effect on the current efficiency and electrode potential during CO_2 reduction (Figures **7.1**, 7.2 and 7.5). To explain

these findings, we have considered the effects of rotation rate on the interfacial pH and CO_2 concentration at the electrode surface as well as the mass transfer of reduction products away from the electrode surface. The most obvious effect of rotation rate on product selectivity is that the current efficiencies for CH_4 and C_2H_4 decrease with increasing rotation rate whereas that for CO remains almost constant. Specifically, as the rotation rate increases, the maximum current efficiency for CH_4 decreases from about 19% at 10 rpm to 1% at 1000 rpm while that for CO remains about 8% for all rotation rates. Similarly, the maximum current efficiency for C_2H_4 also decreases from about 5% at 10 rpm to 0.5% at 1000 rpm. Given that CO is a common intermediate for both CH_4 and C_2H_4, it seems likely that the decrease in current efficiency for both CH_4 and C_2H_4 may be related to the transport of CO away from the electrode surface. As increasing the rotation rate will increase the transport rate of dissolved CO away from the electrode surface, the interfacial concentration of CO immediately adjacent to the cathode surface will decrease. Given that the surface coverage of CO_{ads} on Cu cathodes is in equilibrium with the dissolved CO at the electrode interface [54], it follows that increasing the rotation rate will decrease the surface coverage of CO_{ads}. Since CO_{ads}, or some reduced form of it, is known to inhibit the HER by blocking reaction sites and is well established to be a major intermediate towards hydrocarbon production, it is understandable why the potential becomes less negative and the overall current efficiency for CO_2 reduction decreases as the rotation rate is increased. Further support of this is given by the large difference in potential vs RHE between high and low rotation rates at times (> 6 hours) where the HER is dominant (Figure 7.2b). The fact that the potential vs RHE at 10 rpm is about 150 mV more negative than at 1000 rpm, but the HER is the prevalent reaction for both rotation rates, strongly suggests that the electrode at 10 rpm is more poisoned for HER than at 1000 rpm. Such changes are further highlighted by considering the ratio of the overall current efficiency for CH_4 to CO (Figure 7.5c). These observations are in agreement with some reports that show an increase in CO selectivity over hydrocarbons when the electrolyte solution is stirred, compared to one that is stagnant [23, 124].

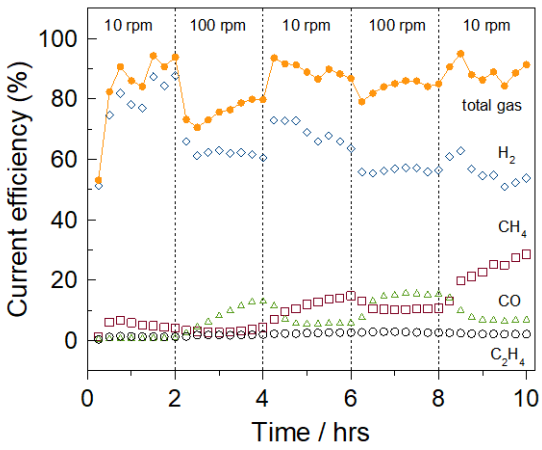

Figure 7.6: Current efficiencies with time for constant current CO_2 reduction at −5 mA cm^{-2} using a Cu RCE alternating between rotation rates of 10 and 100 rpm every 2 hours.

In addition to the surface coverage of CO_{ads}, the interfacial pH and CO_2 concentration at the electrode surface are also affected by the rotation rate (Figures 7.3a and 7.3b). Studies on the effect of pH on CO_2 reduction [74, 103, 104, 237, 238] have consistently shown that the CO_2 reduction selectivity favours H_2 and CH_4 at lower pH and C_2H_4 at higher pH [49, 83, 103, 118]. However, in our results, decreasing the interfacial pH by increasing the rotation rate, decreases the CH_4 production rate, suggesting that the changes in the surface coverage of CO when varying the hydrodynamics at the electrode surface are more important than the changes to the interfacial pH. Others have also shown

that increasing the concentration of dissolved CO_2 in the electrolyte (by using low temperatures or high CO_2 partial pressures) increases the overall current efficiency for CO_2 reduction [104, 121, 124, 128], presumably due to improved diffusion rates of CO_2 to the electrode surface. Similarly, the mass transfer rate of CO_2 to the electrode surface can be improved by increasing the rotation rate (Figure 7.3b). However, unlike the benefits obtained by increasing the interfacial CO_2 concentration at the electrode surface by increasing the bulk concentration of CO_2 in the electrolyte, increasing the interfacial CO_2 concentration at the electrode surface by enhancing mass transfer, decreases the overall CO_2 reduction efficiency.

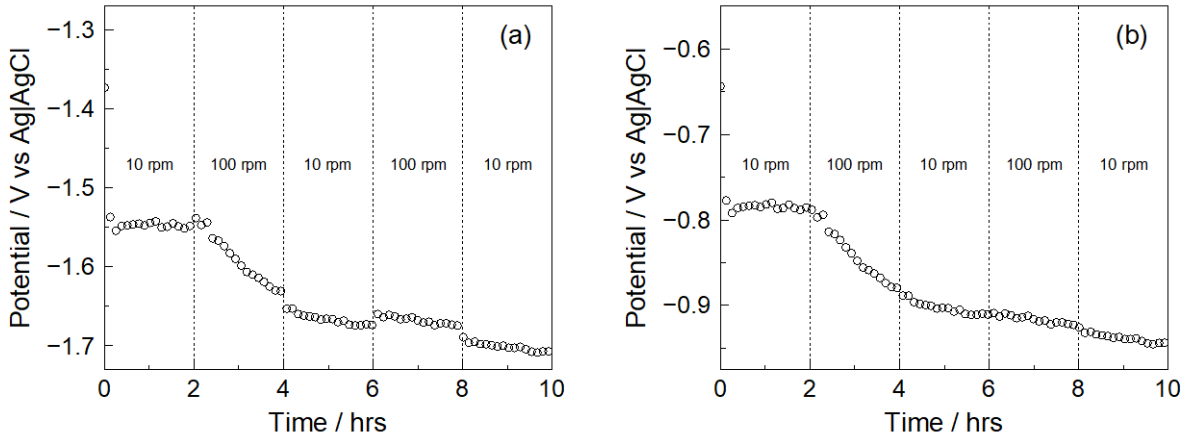

Figure 7.7: Electrode potential (a) vs Ag|AgCl KCl sat. and (b) vs RHE during the constant current CO_2 reduction on a Cu RCE alternating between rotation rates of 10 and 100 rpm every 2 hours.

To further show that the selectively between CH_4 and CO varies as a function of rotation rate, the rotation rate was alternated between 10 and 100 rpm every 2 hours within a single experiment (Figure 7.6). Whenever the rotation rate is increased from 10 to 100 rpm, the current efficiency for CO increases, while that for H_2 and CH_4 decreases. In addition, the total gaseous current efficiency also decreases, which implies an increase in formic acid production. This effect is reversed whenever the rotation rate is decreased from 100 to 10 rpm. As discussed above, such changes are not due to mass transport induced changes in the interfacial pH (the interfacial pH is 9.6 and 9.4 at 10 and 100 rpm respectively) but rather changes in the surface coverage of CO_{ads} on the electrode. Interestingly, alternating the rotation rate did not affect the current efficiency for C_2H_4, which remained at about 2.5% throughout. These results are consistent with those observed by Hara et al., where the current efficiency for CO and formic acid increased, while that for hydrocarbons and H_2 decreased when the electrolyte is stirred during electrochemical CO_2 reduction at 30 atm pressure on a Cu electrode [124]. As the electrode potentials with and without stirring of the electrolyte in their work were very similar (−1.56 V and -1.55 V vs Ag|AgCl with and without stirring respectively) the changes in product selectivity cannot be a result of changes in potential. Likewise, in this work, alternating between 10 and 100 rpm has no apparent effect on the electrode potential vs RHE (Figure 7.7b), confirming that the changes in CH_4 vs CO selectivity are not related to the electrode potential. Interestingly, unlike the 10 hour electrolysis experiments at fixed rotation rates (Figures **7.1** and 7.2), by alternating the rotation rate between 10 and 100 rpm every 2 hours, the increase in electrode potential and the loss in CO_2 reduction current efficiency was not observed. i.e., alternating between 10 and 100 rpm appears to prevent the HER from becoming the dominant reaction even after 10 hours of continuous electrolysis. Instead, a continuous decrease in the electrode potential over the entire 10 hour electrolysis period was found. This is an important observation as it may provide further insights into the normal deactivation mechanism or even methods to prevent deactivation of Cu cathodes. While

we have no clear explanation* for why alternating between 10 and 100 rpm appears to prevent the normal deactivation of the Cu cathode, we are attempting to use in-situ FTIR spectroscopy to investigate how hydrodynamics influences the intermediates adsorbed on the surface of Cu. Other experiments were also conducted to assess whether similar changes could be observed when alternating between 10 and 1000 rpm. While these experiments showed that the selectivity would switch between CH_4 and CO when the rotation rate was first changed from 10 to 1000 rpm, as the deactivation rate is very fast at 1000 rpm, practically all CO_2 reduction activity was lost after 2 hours at 1000 rpm, preventing further selectivity switching to be observed.

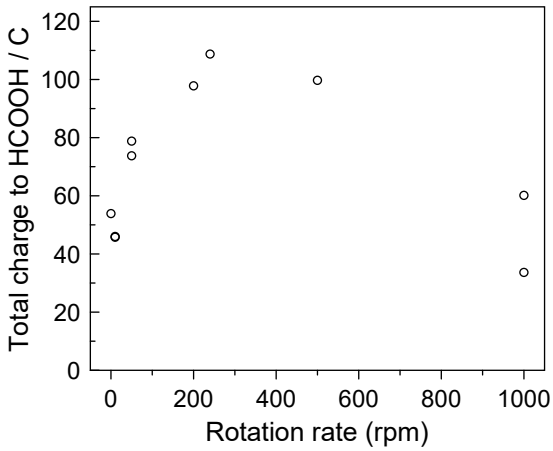

Figure 7.8: Total charge going towards the formation of formic acid over 10 hours of CO_2 reduction at −1.6 V vs Ag|AgCl on a polycrystalline Cu RCE at various rotation rates.

These alternating rotation rate experiments also provide some evidence that improved mass transfer can enhance formic acid formation, with the current efficiency for formic acid production increasing (based on the drop in total gas current efficiency) whenever the rotation rate is increased from 10 to 100 rpm (Figure 7.6). This effect can be explained by the increase in the interfacial concentration of CO_2 at the electrode surface (due to enhanced mass transfer), which is known to improve formic acid formation [124]. As the production of formic acid does not require the breaking of a C-O bond, and the final intermediate toward formic acid formation is likely an adsorbed CO_2^- species [26], we speculate that a higher interfacial CO_2 concentration at the electrode surface may increase the surface coverage of CO_2^-, which promotes the formation of formic acid. To further substantiate the increase in formic acid formation with enhanced mass transfer, a series of constant potential experiments at −1.6 V vs Ag|AgCl) at various rotation rates were performed (Figure 7.8). The results suggest a maximum in formic acid production at approximately 300 to 400 rpm. The decrease in formic acid production above 400 rpm is likely due to the overall deactivation of CO_2 reduction by formation of graphitic carbon as explained earlier. These results confirm that improved mass transfer rates enhance formic acid formation, most likely due to a higher availability of CO_2 at the electrode surface. However, this enhancement can be overridden by Cu electrode poisoning, the effect of which is greater at rotation rates above 300−400 rpm.

* It was later discovered (post-publication of the journal paper) that the likely reason for the absence of the deactivation of CO_2 reduction in this particular experiment (alternating between 10 and 100 rpm) is that a new batch of $KHCO_3$, possibly with much less impurities compared to the previous batch, was used. CO_2 reduction at −5 mA cm^{-2} and at a fixed rotation rate of 50 rpm for 10 hours in a 0.2 M $KHCO_3$ solution prepared using the new $KHCO_3$ batch (see Figure 5.9c in chapter 5) also did not show any loss in CO_2 reduction activity, and is in contrast to a similar experiment performed using the previous $KHCO_3$ batch (Figure 7.1b).

7.4 Conclusions

The hydrodynamics at cathode surfaces are expected to have a large influence on electrocatalytic CO_2 reduction due to the low concentration of dissolved CO_2 (at a CO_2 pressure of 1 bar) and the pH gradient which forms at the cathode surface in the electrolytes typically used for electrocatalytic CO_2 reduction. By using a polycrystalline Cu rotating cylinder electrode, the effects of the hydrodynamics or mass transfer rates on constant current electrochemical CO_2 reduction was investigated.

By increasing the mass transfer rates, the current efficiencies toward CO_2 reduction products decreased while that for the HER increased. The selectivity of CO_2 reduction was also observed to change, with CO becoming favoured over CH_4 as the mass transfer rates were increased. The effects of mass transfer on the interfacial pH and CO_2 concentration were calculated by a mathematical model and it was confirmed that as the mass transfer rates were increased, the interfacial pH and CO_2 concentration approaches the bulk values. However, the effects of mass transfer on the electrocatalytic CO_2 reduction were found to differ from the widely reported effects of interfacial pH and CO_2 concentration, where lower interfacial pH improves CH_4 production (over C_2H_4) and higher CO_2 concentration facilitates CO_2 reduction over the HER. Thus we conclude that changes in interfacial pH and CO_2 concentration brought about by mass transfer cannot fully explain the significant decrease in CO_2 reduction activity under high mass transfer conditions. Instead, the results are more consistent with the enhanced mass transfer of dissolved CO away from the electrode surface, which decreases the surface coverage of CO_{ads}, preventing the further reduction of CO_{ads} to hydrocarbons and changing the selectivity from CH_4 to CO.

These findings provide critical insights that must be considered for electrocatalytic CO_2 reduction. In almost all electrocatalytic CO_2 reduction literature to date, the hydrodynamics at the cathode surfaces are neither controlled nor quantified, which this work shows can have significant influence on the selectivity and activity of CO_2 reduction. This suggests that researchers need to consider these effects carefully, especially when comparing results between different experimental configurations or designing electrochemical cells and cathodes for industrial applications.

7.5 Additional material

To lend further support to the effects of the mass transfer of dissolved CO away from the electrode surface as described in the preceding sections, reduction electrolysis on the Cu RCE at various rotation rates were conducted in an Ar stripped 0.2 M $KHCO_3$ electrolyte under continuous Ar bubbling, where CO_2 reduction activity and hence dissolved CO and its mass transfer are largely absent in the system.

As expected for a system where CO_2 is not introduced, the current efficiency toward the HER is >95% for all rotation rates, although a very small amount of CH_4 (0.04%) and HCOOH (0.2%) were still produced due to the presence of a small amount of dissolved CO_2 from the carbonate equilibria despite continuous Ar bubbling[*]. Because a small amount of dissolved CO_2 is still present in the electrolyte, similar trends in the electrode potential with time (Figure 7.9) as with the CO_2 saturated case at various rotation rates are produced, although the potentials in the Ar stripped case are consistently more positive (by about 100 mV) than the CO_2 saturated case. This is explained by the fact that much less CO_{ads}, which is known to inhibit the HER, are present on the electrode surface; hence the electrode is more active for the HER and therefore requires relatively less overpotential.

[*] Theoretically, bubbling Ar through a $KHCO_3$ solution will eventually result in KOH as any dissolved CO_2 is gradually stripped away. However, due to sluggish kinetics of the liquid-to-gas transfer of dissolved CO_2 and the reverse CO_2 equilibria reactions (see Table 4.1), producing KOH simply by stripping $KHCO_3$ with Ar is practically impossible.

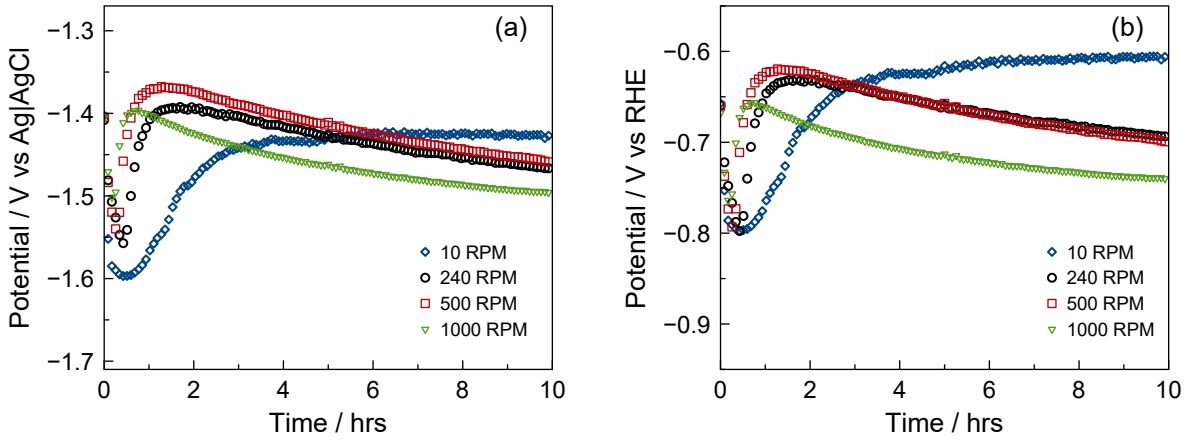

Figure 7.9: Electrode potential (a) vs Ag|AgCl KCl sat. and (b) vs RHE during constant current (−5 mA cm^{-2}) reduction on a Cu RCE in a 0.2 M $KHCO_3$ solution continuously bubbled with Ar at 20 ml min^{-1}at various rotation rates. The potential vs RHE was calculated using the calculated interfacial pH presented in Figure 7.10a.

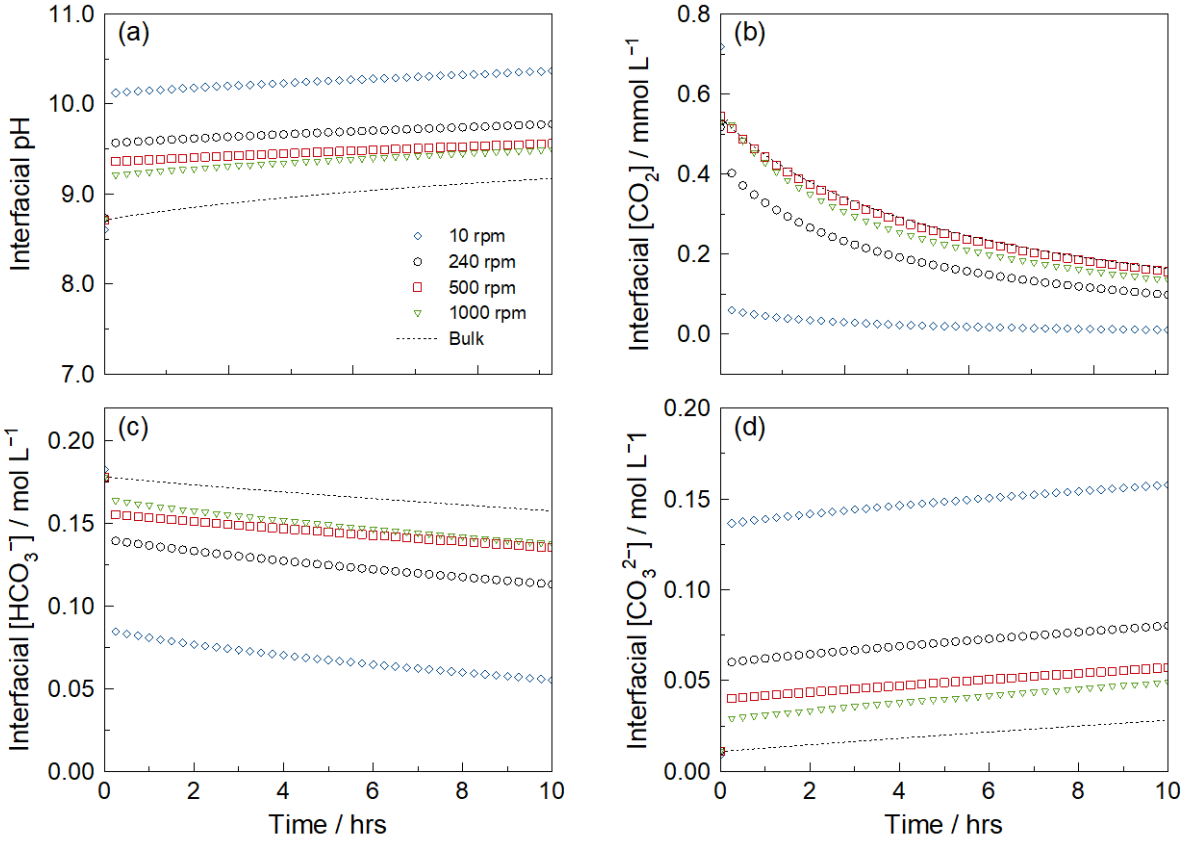

Figure 7.10: (a) Interfacial pH and concentrations of (b) CO_2, (c) HCO_3^- and (d) CO_3^{2-} during constant current (−5 mA cm^{-2}) reduction on a Cu RCE in a 0.2 M $KHCO_3$ solution continuously bubbled with Ar at 20 ml min^{-1}at various rotation rates. The values were calculated by adapting the model developed by Gupta et al. [44], with the bulk electrolyte values given by the dashed line.

Additionally, the potential minimum occurred much earlier with little spread in its magnitude and occurrence time, although generally retaining the sequential order in rotation rate. Similarly, this is explained by the fact that the amount of dissolved CO_2 is minimal in the Ar stripped case; hence the initial decrease in potential caused by the blocking and poisoning of reaction sites by the slow

accumulation of CO_2 reduction products or intermediates is lessened. The subsequent increase of the electrode potential past its minimum, i.e. decrease in HER overpotential, due to the formation of graphitic carbon from existing CO_{ads} is also observed, albeit over a much shorter time period. After this increase, as with the case for CO_2 reduction, the electrode potential gradually decreases for the remainder of the electrolysis but at a slightly faster rate, and is also thought to be caused by gradual changes in the bulk electrolyte with electrolysis time. For the Ar stripped case, the interfacial pH gradually increases with time (Figure 7.10a) due to the continuous stripping of dissolved CO_2 in the electrolyte as opposed to the CO_2 saturated case where the interfacial pH is relatively constant throughout. Hence, the faster rate at which the potential decreases is likely due to the additional inhibition of the HER by the gradual increase in interfacial pH. Interestingly, this is not observed for the slowest rotation rate (10 rpm). In fact, the overpotential seems to decrease slowly, suggesting an enhancement of the HER at much higher pH, as have been occasionally observed by others [103, 118]. Our attempts to measure the overpotential of the HER at various interfacial pH values by means of varying the rotation rate during a single continuous electrolysis experiment have also suggested that the HER is enhanced with increasing pH above pH = 9.8 (Figure 7.11). This is shown during stage 3 of the experiment (Figure 7.11), which represents the stage where the electrode potential gradually decreases with time after the occurrence of the minimum point during a fixed rotation rate experiment. As illustrated, the HER overpotential decreases with increasing interfacial pH for values above approximately pH = 9.8.

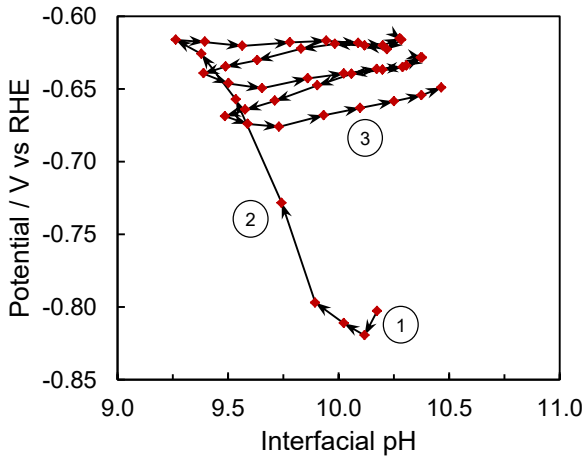

Figure 7.11: Electrode potential (vs RHE) with interfacial pH during constant current (−5 mA cm^{-2}) reduction on a Cu RCE in a 0.2 M $KHCO_3$ solution continuously bubbled with Ar at 20 ml min^{-1}. The interfacial pH is manipulated by means of doubling the rotation rate from 10 to 1280 rpm and subsequently halving from 1280 to 10 rpm in 15 minute intervals for each rotation rate for a total of 3 cycles. Stages 1 to 3 represent the initial decrease in electrode potential, the subsequent increase after the potential minimum, and the gradual decrease for the remainder of the electrolysis, respectively.

Another interesting observation is that the overpotential at 1000 rpm is about 50 mV higher than that at 240 and 500 rpm (during the gradual decrease in electrode potential). As the interfacial pH at 1000 rpm is lowest compared to the other rotation rates and is below 9.8, the apparent inhibition of the HER at 1000 rpm cannot be explained by differences in the interfacial pH. Instead, this might be due to the relatively higher interfacial concentration of HCO_3^- at 1000 rpm (Figure 7.10), which could poison reactions sites to a larger extent through adsorption compared to slower rotation rates.

8 CO_2 Reduction on Polycrystalline Cu Supported Au_9/TiO_2

8.1 Introduction

This chapter presents preliminary results of our work on galvanostatic CO_2 reduction on polycrystalline Cu supported Au_9/TiO_2 electrodes. The motivation of this work is in line with the current strategy of developing novel electrocatalysts with a level of surface heterogeneity that aims to harness the potential synergy between various catalytic materials in favour of improving the CO_2 reduction reaction. In essence, surface heterogeneity provides multiple adjacent active sites that facilitate the stabilisation and reaction between different adsorbed reaction intermediates. Commonly, this synergy can be achieved by depositing nanoparticles (which themselves exhibit high catalytic properties due to particle size effects) onto a catalytically active support, the interface between which is usually suggested to be the most active region of the electrocatalyst [203-206]. This has been observed for CO oxidation on oxide supported Au clusters, where theoretical simulations and spectroscopic analysis confirm that the interface between the Au clusters and an oxide phase enhances the adsorption and stabilisation of reaction intermediates [205, 240].

For this work, we have attempted to combine the uniqueness of Cu for the electro-reduction of CO_2 to hydrocarbons with the apparent improved selectivity of the reaction toward methanol in the presence of an oxide phase, e.g. Cu oxides [180-183] and Ru oxides [241, 242]. The enhanced selectivity toward methanol on oxides surfaces can partly be explained by recent theoretical simulations on Cu surfaces with oxygen-based species, e.g. surface oxidation state or presence of oxygen-containing spectator species [172], where the thermodynamically favoured product is predicted to shift from CH_4 to methanol due to a weakening of the oxygen binding strength of the methoxy intermediate to the Cu surface. In order to withstand the strong cathodic conditions encountered during CO_2 reduction, TiO_2 is chosen as the oxide phase to be investigated in our work as it is more thermodynamically stable in cathodic conditions [217]. Since the catalytic ability of Cu for CO_2 reduction in our system has already been determined previously (see chapter 5), the relevant behaviour of TiO_2 was ascertained in this work by performing constant current CO_2 reduction on polished Ti discs* at various current densities and surface treatments. To investigate the potential synergy between Cu and TiO_2, we have initially deposited TiO_2 nanoparticles onto polished polycrystalline Cu substrates through ion beam sputtering. However, the resulting TiO_2 coating was found to be mechanically unstable under typical electrolysis conditions where gas bubbles are continuously forming (see Appendix 11). Alternatively, a more robust coating was obtained by spin-coating commercially available TiO_2 (P25) nanoparticles onto the polished Cu substrates and subsequently annealing under an atmosphere of 2:8 ratio of air to Ar. By preparing TiO_2/Cu samples with various TiO_2 loadings, the effects of the presence of TiO_2 on the electrode potential and CO_2 reduction activity of long-term galvanostatic CO_2 reduction were investigated. Additionally, the level of heterogeneity of the TiO_2/Cu electrocatalyst is further increased by the addition of Au_9 clusters, which were initially immobilised on the TiO_2 nanoparticles before spin-coating onto the Cu substrates. The addition of Au presents another dimension of CO_2 electro-reduction since Au is known to be highly active for CO_2 reduction to CO at much lower overpotentials compared to Cu [59]. The effects of increasing the Au content in the TiO_2/Cu samples on CO_2 reduction were also investigated.

* Ti metal has a very high affinity for oxygen. Therefore after mechanical polishing, a thin layer of TiO_2 will form almost instantly on the surface.

8.2 Experimental

Three types of working electrodes were used in this work: a) polished Ti discs, b) polished Cu with spin-coated TiO_2 (P25) nanoparticles, and c) polished Cu with spin-coated Au_9/TiO_2 nanoparticles. The Ti discs (99.6%, Advent Research Materials Ltd) were prepared by mechanical polishing using silicon carbide paper down to the P2000 grit*, and subsequently rinsed and ultra-sonicated with isopropanol and 18.2 MΩ cm deionised water. Following the same procedure, all Cu substrates (polycrystalline 99.99%, Advent Research Materials Ltd) were mechanically polished, but unlike the Ti discs, a mirror finish was obtained using both silicon carbide paper and alumina slurries (down to 0.05 μm). Both the Ti discs and Cu substrates have an exposed geometrical area of 3.14 cm^2. TiO_2 suspensions were prepared by dispersing commercially available TiO_2 nanoparticles (P25, Degussa) in isopropanol. Two concentrations of TiO_2 suspension, 2 mg ml^{-1} and 20 mg ml^{-1}, were prepared and ultra-sonicated for at least 1 hour before spin-coating onto the Cu substrates. The Au_9/TiO_2 nanoparticles (Au weight content either 0.085% or 1.5%) were chemically synthesised elsewhere by Golovko's group according to the procedure outlined in their published works [243, 244]. As with the TiO_2 suspension, the Au_9/TiO_2 nanoparticles were also dispersed in isopropanol at 2 mg ml^{-1} and 20 mg ml^{-1} and ultra-sonicated for at least 1 hour before spin-coating. For spin-coating, 200 μl of suspension was first deposited onto the Cu substrate (static dispense method) to cover the entire surface, after which the substrate was spun at 2000 rpm for 30 s. After spin-coating, the samples were annealed in a tube furnace under an atmosphere of 2:8 ratio of air to Ar† at 250 °C. As the exact nanoparticle loading on the substrates could not be directly measured, we hereafter report the "loadings" based on the suspension concentrations, i.e. 2 mg ml^{-1} or 20 mg ml^{-1}.

A conventional two compartment H-type cell separated by a Nafion 115 cation exchange membrane was used along with a Ag|AgCl (sat. KCl) reference electrode and a Pt foil counter electrode. All potentials are reported against the Ag|AgCl reference electrode unless specifically stated. In all cases, 30 ml of 0.2 M $KHCO_3$ (99.7% ACS reagent, Sigma Aldrich) saturated with high purity 99.995% CO_2 (pH = 7.0) was used as the electrolyte. This electrolyte was pre-electrolysed for 48 hours prior to CO_2 reduction experiments to remove any trace metallic impurities which may poison the electrodes (see section 3.3). During CO_2 reduction, the catholyte was continuously bubbled with the high purity CO_2 at 10 ml min^{-1} (Alicat mass flow controller). The outlet gas from the electrochemical cell was fed into a gas chromatograph (SRI Instruments, methanizer FID and TCD detectors, haysep-D column) to quantify the H_2, CO, CH_4, C_2H_4 and C_2H_6 produced from the CO_2 reduction process. The liquid reduction products (formic acid, acetic acid and methanol) were measured post-electrolysis using HPLC equipped with a SUPELCOGEL™ C-610H column.

All electrochemical experiments were performed at room temperature and pressure, and controlled using a GAMRY Reference 3000 potentiostat. Throughout each experiment, the solution resistance was measured every 15 minutes using electrochemical impedance spectroscopy (EIS) at the specified current density (with 5 mV rms amplitude, 100 kHz to 10 Hz) and all potential measurements were corrected post experiment. It is critical to regularly measure the solution resistance as during long-term CO_2 reduction, the transport of K^+ through the Nafion membrane (from anode to cathode) alters the solution resistance over time. Note that we also prefer galvanostatic over potentiostatic CO_2

* Ti is a much harder metal than Cu; hence, polishing Ti to a mirror finish is significantly more difficult. Instead, the Ti discs were only polished down to the P2000 grit. Interestingly, it was discovered that the Ti discs become easier to polish to a smoother surface after undergoing CO_2 reduction electrolysis (see Appendix 12).

† Originally, the spin-coated samples were annealed in Ar at 250 °C. However, the coating did not fixate on the Cu substrate well enough and was physically unstable during electrolysis. The coating is strongly fixated if a portion of air was added into the Ar stream, and is most likely owing to the growth of a layer of Cu oxide, although we acknowledge that the presence of O_2 will probably sinter the Au_9 nanoparticles to some extent.

reduction due to these changes in solution resistance, and effects of interfacial pH which are much more challenging to control during potentiostatic CO_2 reduction (see section 3.6).

8.3 Results and discussion

The variation of the potential with time of the TiO_2/Cu electrodes over 10 hours of constant current electrolysis is presented in Figure 8.1, while the resulting overall current efficiencies over the whole duration of electrolysis are summarised in Table 8.1. The most prominent result of the TiO_2 additions on Cu is the significant shift of the electrode potentials to more positive values as the TiO_2 loading increases. This observation points to an increase in the electrochemical activity of the electrode, mostly toward the HER, where the total overpotential required to generate a specific current density becomes smaller with increasing TiO_2 content. As expected, due to the much lower overpotentials, the current efficiencies toward CO_2 reduction products decrease in favour toward the HER (Table 8.1), given that the CO_2 reduction reactions in general require larger overpotentials compared to H_2 evolution.

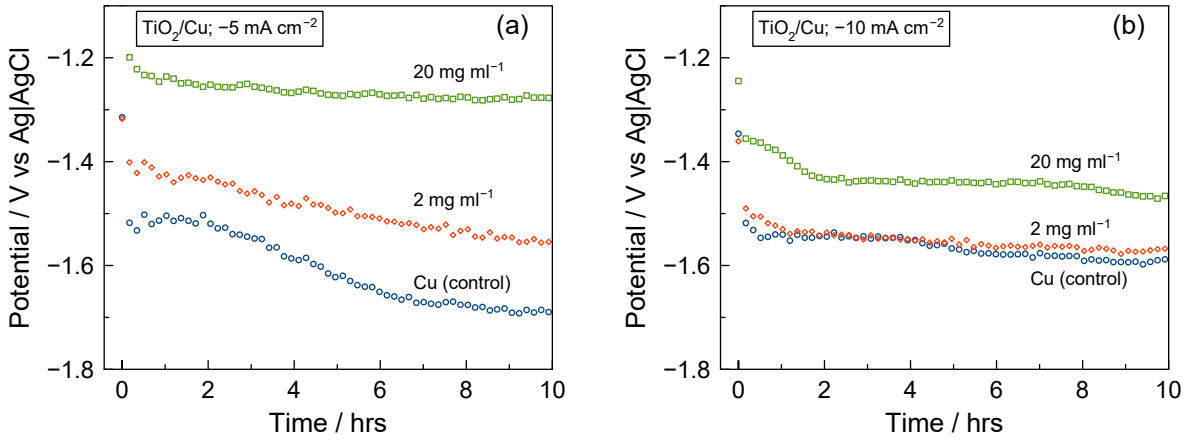

Figure 8.1: Potential with time for TiO_2/Cu samples of various TiO_2 (P25) loadings at (a) −5 mA cm^{-2} and (b) −10 mA cm^{-2} in 0.2 M $KHCO_3$. All samples (including the Cu control) were annealed at 250 °C under an atmosphere of 2:8 ratio of air to Ar.

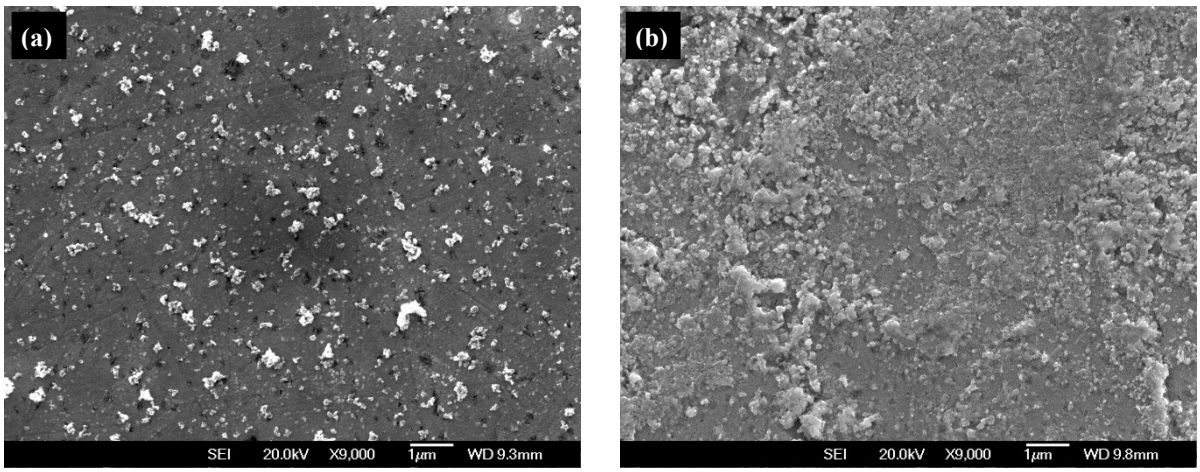

Figure 8.2: SEM images of TiO_2/Cu samples prepared via spin-coating of (a) 2 mg ml^{-1} and (b) 20 mg ml^{-1} TiO_2 (P25) suspension onto a polished Cu substrate. The nanoparticle loading is clearly increased when a more concentrated suspension was used.

In comparison to the Cu controls (Figure 8.1) and Ti electrodes (Figure 8.3) at similar current densities, the overpotentials exhibited by the TiO_2/Cu samples are significantly lower, especially for the 20 mg ml^{-1} spin-coated sample. This could suggest a possible synergy between the two materials, Cu and TiO_2, that enhances the HER activity to be more efficient than on either Cu or Ti itself. Interestingly, despite the low overpotentials, surprising amounts of CO are still produced on the TiO_2/Cu electrodes. The CO current efficiencies are generally comparable to that of the Cu controls and Ti electrodes at similar current densities but at much higher overpotentials (Tables 8.1 to 8.3). In agreement with results in the literature, H_2 is the main electrolysis product during CO_2 reduction experiments on all Ti electrodes, owing to the fact that CO is strongly adsorbed on Ti [47, 48]. This leads to the formation of a tightly adsorbed CO_{ads} monolayer on the electrode surface that prevents both the release of CO_{ads} as gaseous CO and the further reduction of CO_{ads} to hydrocarbons; hence, H_2 becomes the only principal product (see section 2.2). The blocking of active sites by CO_{ads} also explains the large overpotentials observed on the Ti electrodes. By adding TiO_2 nanoparticles onto the Cu surface, active sites at the TiO_2/Cu interface could have lowered the CO adsorption strength, allowing similar amounts of CO to be produced at much lower overpotentials. The introduction of Au_9 nanoparticles into the TiO_2/Cu electrocatalyst further reduced the overpotential (Figure 8.4), with the overpotential decreasing further with increasing Au_9 content. Similarly, even at these low overpotentials, CO production remains comparable with all other samples at similar current densities, i.e. −10 mA cm^{-2} (Table 8.3). The further reduction in overpotential and the continued production of CO with increasing Au_9 content is not surprising, since Au is known to be an active metal toward CO_2 reduction to CO at low overpotentials owing to its weak CO adsorption strength [47, 59].

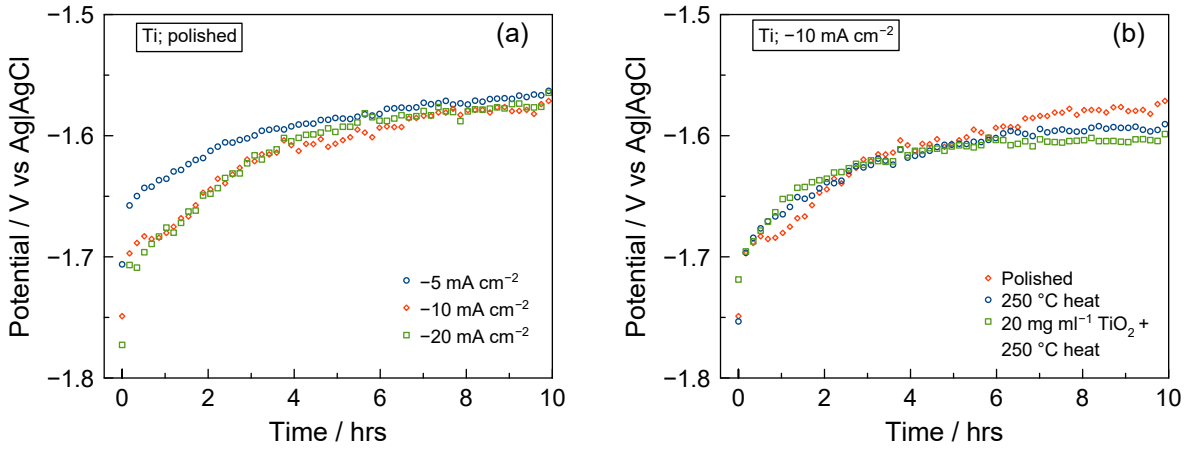

Figure 8.3: Potential with time for (a) polished Ti samples at various current densities and (b) polished Ti samples of different surface treatments at −10 mA cm^{-2}.

As much as the synergy between the various catalytic materials seems to be a plausible explanation for the observed improvements in catalytic activity, the decrease in overpotential could also be due to an increase in active surface area after the TiO_2 or Au_9/TiO_2 nanoparticles are deposited. This is consistent with the observation that the overpotential decreases with increasing nanoparticle loading. Comparing the Cu control and the TiO_2/Cu sample prepared using the 20 mg ml^{-1} TiO_2 suspension, the overpotential decreased by as much as 300 to 400 mV. In Kim et al.'s work [23], the HER on a Cu foil in N_2 saturated 0.5 M Na_2HPO_4 presents an apparent Tafel slope of 400 mV $decade^{-1}$ below −1.2 V vs SCE, which is seemingly large and reaching saturation current (possibly due to a change in the rate limiting step from water discharge to chemical combination of H_{ads}) but generally also in agreement with that observed in our work (refer to Figure 6.10a). Therefore, since H_2 is the main reduction product, assuming a Tafel slope of 400 mV $decade^{-1}$ would correspond to an increased

active surface area by a factor of 10 on the TiO_2/Cu sample with 20 mg ml^{-1} spin-coat compared to the Cu control. This is not implausible given the observed rougher surface of the TiO_2/Cu sample under SEM (Figure 8.2).

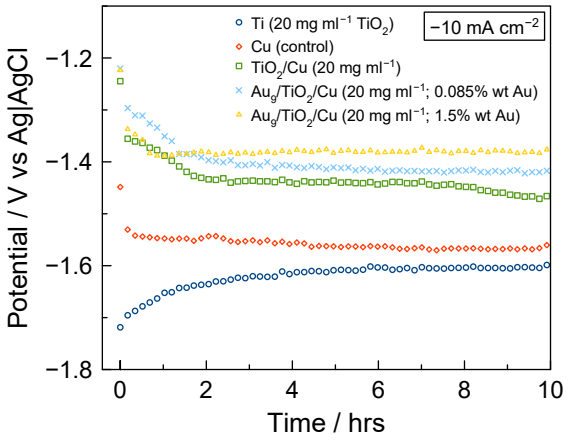

Figure 8.4: Potential with time for Au_9/TiO_2/Cu samples (0.085% and 1.5% wt Au) overlaid with that of other samples at −10 mA cm^{-2}. All samples (including the Cu control) were annealed at 250 °C under an atmosphere of 2:8 ratio of air to Ar.

The supposed effect of the increase in active surface area due to the nanoparticle coatings on the electrode potential may be contested by the electrode potential recorded on a polished Ti sample spin-coated with 20 mg ml^{-1} TiO_2 (Figure 8.3b). In this case, the electrode potential on the spin-coated Ti sample is found to be similar, even more negative at times, compared to the polished Ti sample at −10 mA cm^{-2}. However, it is also arguable that the Ti surface polished to the P2000 grit is initially rough to begin with; hence an addition of the TiO_2 layer would not have increased the active surface area by a significant proportion. A stronger contender against the effects of the increase in active surface area is the general comparability of the electrical double layer charging current between the various TiO_2/Cu and Au_9/TiO_2/Cu samples with the Cu controls observed within an initial cyclic voltammetry measurement before the start of electrolysis (not shown). This implies that the electrochemical active surface area is comparable for all samples prepared under similar conditions. Nevertheless, a more thorough estimate of the surface roughness should be performed, using cyclic voltammetry at various scan rates for example, to ascertain if the suggested improvements in catalytic activity is solely due to an effect of increased active surface area.

Table 8.1: Overall current efficiencies over 10 hours of electrolysis for TiO_2/Cu samples.

TiO_2/Cu electrode	Potential / V	Overall current efficiency (%)							
		H_2	CO	CH_4	C_2H_4	C_2H_6	HCOOH	CH_3COOH	Total
				−5 mA cm^{-2}					
Cu control	−1.61	81.9	1.59	4.39	0.92	0.02	8.60	0.07	97.5
2 mg ml^{-1}	−1.49	90.1	1.91	0.14	0.37	0.01	5.00	-	97.5
20 mg ml^{-1}	−1.26	95.5	0.30	-	0.01	0.01	3.00	-	98.9
				−10 mA cm^{-2}					
Cu control	−1.56	73.2	0.54	6.44	3.52	-	12.2	0.14	96.2
2 mg ml^{-1}	−1.55	74.8	0.40	4.50	4.13	0.01	10.6	0.11	94.6
20 mg ml^{-1}	−1.43	88.3	0.43	-	0.02	-	7.81	-	96.6

Table 8.2: Overall current efficiencies over 10 hours of electrolysis for Ti samples.

Ti disc electrode	Potential / V	Overall current efficiency (%)							
		H_2	CO	CH_4	C_2H_4	C_2H_6	HCOOH	CH_3COOH	Total
				−5 mA cm^{-2}					
Polished	−1.59	96.5	1.23	0.02	-	-	0.55	-	98.3
				−10 mA cm^{-2}					
Polished	−1.61	94.8	0.58	0.02	-	0.01	0.40	-	95.8
250 °C heat	−1.62	96.2	0.51	0.02	-	-	0.43	-	97.2
20 mg ml^{-1} TiO_2 + 250 °C heat	−1.62	96.9	0.54	0.03	-	-	0.80	-	98.3
				−20 mA cm^{-2}					
Polished	−1.61	99.0	0.18	0.02	-	-	0.26	-	99.5

Table 8.3: Overall current efficiencies over 10 hours of electrolysis at −10 mA cm^{-2} for Au_9/TiO_2/Cu samples.

Au_9/TiO_2/Cu electrode	Potential / V	Overall current efficiency (%)							
		H_2	CO	CH_4	C_2H_4	C_2H_6	HCOOH	CH_3COOH	Total
Cu control	−1.56	78.7	0.24	4.87	2.29	0.01	9.70	-	95.8
0.085% wt Au	−1.40	91.2	0.34	-	-	-	6.66	-	98.2
1.5% wt Au	−1.38	89.3	0.47	-	-	-	6.34	-	96.1

For the TiO_2/Cu samples, increasing the specified current density from −5 mA cm^{-2} to −10 mA cm^{-2} generally shifts the electrode potential to more negative values as expected, and is especially evident for the 20 mg ml^{-1} spin-coated sample. However, it is peculiar that a slightly lower overpotential is required at −10 mA cm^{-2} compared to −5 mA cm^{-2} for the Cu control sample. Again, this could be due to experimental variations in active surface area between the −5 and −10 mA cm^{-2} samples (which were prepared at different occasions) owing to a possible difference in the extent of oxide growth. Curiously, the electrode potentials for the polished Ti samples are also rather identical for all current densities studied, especially at −10 and −20 mA cm^{-2}, despite the active surface area being comparable between all three samples (they are mechanically polished to the same degree). Instead, this may be explained by a decrease in overpotential for H_2 formation as the interfacial pH becomes increasingly high at larger current densities[*]. The enhancement of the HER at very high pH has occasionally been observed on Cu electrodes [103, 118] , thus it is possible that a similar mechanism also applies for Ti electrodes.

Ideally, a comparison study of the electrochemical activity of electrodes should be conducted using constant potential rather than constant current analysis. However, as mentioned earlier, constant potential analysis in our case presents some experimental difficulties with regard to changes in the solution resistance, and also effects of interfacial pH which cannot be easily controlled. Nonetheless, the constant current analysis performed in this work did reveal some noteworthy results which warranted some discussion.

8.4 Conclusions

In this work, TiO_2/Cu and Au_9/TiO_2/Cu electrodes were prepared through spin-coating of commercial TiO_2 (P25) and chemically synthesised Au_9/TiO_2 nanoparticles onto polished Cu substrates in order to investigate the potential synergy between Au, TiO_2 and Cu during CO_2 reduction.

[*] For a fixed hydrodynamic condition, the interfacial pH at the electrode surface increases with current density due to the increasing consumption/formation rate of H^+/OH^-.

It was determined that as the TiO_2 loading increases, the electrode potential during constant current electrolysis tend to become more positive, i.e. overpotential decreases, pointing toward an enhancement in the electrochemical activity of the electrode. The increase in electrode potential is further observed when Au_9 nanoparticles are introduced into the TiO_2/Cu electrocatalyst. As the overpotential decreases, the current efficiencies toward CO_2 reduction products also decreases in favour of the HER since the CO_2 reduction reactions in general require a larger overpotential than H_2 evolution. This suggests that the enhancement in electrochemical activity is largely in favour toward the HER rather than CO_2 reduction. However, despite the very low overpotentials at the modified Cu electrodes, surprising amounts of CO are still produced with current efficiencies generally comparable to that of the Cu controls and Ti electrodes at similar current densities but at much higher overpotentials. Since Ti is known to produce only H_2 due to the strong adsorption of CO, it is possible that active sites at the Au_9/TiO_2/Cu interfaces lowered the CO adsorption strength, hence allowing similar amounts of CO to be produced at much lower overpotentials.

It is also possible that the observed improvements in catalytic activity on the modified Cu electrodes, especially the significant reduction in overpotential, are largely due to an increase in active surface area after the deposition of the nanoparticle coatings, although more supporting evidence and measurements of surface roughness, e.g. by cyclic voltammetry, is needed for verification. In addition, constant potential analysis should be performed since this work has a focus on comparing the electrochemical activity of various Cu modified electrodes, although one has to be aware of certain experimental challenges pertaining to changes in solution resistance (if cation exchange membranes are used) and the difficulty in controlling the effects of interfacial pH during electrolysis.

9 Conclusions and Recommendations

Herein, we summarise the main findings and conclusions of our work, and also provide some suggestions on the future direction of research on the electrochemical reduction of CO_2.

The experimental aspects of this work have revealed some important challenges that researchers need to be aware of. The main challenge pertains to the execution of potentiostatic electrolysis when cation exchange membranes are used. With cation exchange membranes, the major charge carrier across the membrane (from anolyte to catholyte during cathodic electrolysis) is the cation of the electrolyte, e.g. K^+ if $KHCO_3$ is the electrolyte; hence, during CO_2 reduction electrolysis, the solution resistance on the working electrode side (catholyte) decreases with time, the rate of which is dependent on the current density. This causes problems in positive feedback compensation since the current density, and hence the rate of decrease of the solution resistance, cannot be known in advance to prevent over-compensation, the occurrence of which can cause instrument instabilities. The majority of the work on aqueous electrochemical CO_2 reduction in the literature has opted for cation exchange membranes with the intention to prevent the migration of liquid products such as formate ($HCOO^-$) to the anode to be re-oxidised. In light of this challenge in potentiostatic control, researchers could opt to use anion exchange membranes instead and risk the loss of some liquid products, or ensure that the solution resistance and its decrease with electrolysis time are small to begin with. The latter can be achieved by increasing the electrolyte concentration, although one needs to be aware that the CO_2 reduction selectivity is a strong function of the electrolyte concentration, especially those with buffering abilities. Another option is to simply use a larger electrolyte volume, so that the effects of the transport of cations can be minimised, although a smaller electrolyte volume is sometimes desirable to increase the concentration of liquid products for ease of detection and analysis.

In addition to difficulties in potentiostatic control, the selective transport of the electrolyte cation into the catholyte also causes its buffer capacity to increase (if a buffering electrolyte is used). As mentioned earlier, the product selectivity is a strong function of the electrolyte buffer capacity due to the extent of buffering on the interfacial pH and CO_2 concentration. Furthermore, our measurements of the bulk electrolyte pH during electrolysis suggest that its species concentrations, and hence that at the electrode/electrolyte interface, are not in equilibrium. The fact that the bulk and interfacial concentrations are changing and are not in equilibrium during electrolysis had prompted us to adapt and improve an existing mathematical model by Gupta et al. [44] that numerically estimates the interfacial pH and $CO_2/HCO_3^-/CO_3^{2-}$ concentrations. By using the adapted model along with experimentally determined current efficiencies of CO_2 reduction, the bulk and interfacial concentrations throughout electrolysis were estimated and used to aid in the discussion of results when appropriate.

The reliability of our experimental method was demonstrated by performing a series of long-term constant current CO_2 reduction on polycrystalline Cu. The general behaviour of the electrode potential and CO_2 reduction activity over long periods of galvanostatic electrolysis has been discussed, along with the effects of current density and electrolyte concentration. Overall, our results are in good agreement with those found in the literature, and covers important observations such as the major reduction products on Cu electrodes, their pH and potential dependence, and the widely reported deactivation of CO_2 reduction. Regarding this deactivation, it has been shown in the literature that either short anodic pulses or potential sweeps into anodic conditions can be used to maintain or reactivate the CO_2 reduction activity through removal of poisoning species such as graphitic carbon or

electrodeposited metallic impurities. Hence, in an attempt to prolong the CO_2 reduction activity in our system, we have incorporated periodic cyclic voltammetry and potentiostatic steps throughout extended periods of galvanostatic CO_2 reduction. However, instead of prolonging the CO_2 reduction activity, it is demonstrated that temporarily interrupting galvanostatic CO_2 reduction with short periods at potentials between −0.5 and −0.1 V vs Ag|AgCl (either through cyclic voltammetry or potentiostatic steps) actually suppresses the formation of CH_4, CO and C_2H_4. We propose that this is due to the partial removal or oxidation of adsorbed CO_2 reduction intermediates and that this "clean" cathode surface is more active for the hydrogen evolution reaction. However, when brief potentiostatic steps were conducted at more negative potentials (−1.2 V vs Ag|AgCl), the CO_2 reduction selectivity could be switched from CH_4 to CO, and maintained for at least 2 hours. This change in selectivity is proposed to be caused by an increase in the surface coverage of CO_{ads} (at the expense of H_{ads}) during the brief −1.2 V steps, which then enables the Cu cathode to switch between multiple steady-state surface coverages when the cathodic current is re-applied.

An important experimental aspect of the electrochemical reduction of CO_2 that is quite often overlooked is the hydrodynamics close to the cathode surfaces. Due to the low solubility of CO_2 and the pH gradient which forms at the cathode surface during electrolysis, it is likely that the hydrodynamics at cathode surfaces have a large influence on electrocatalytic CO_2 reduction. Hence, we have investigated the effects of mass transfer on CO_2 reduction using a polycrystalline Cu rotating cylinder electrode. When the mass transfer rate increases (by increasing the rotation rate), the current efficiencies toward CO_2 reduction products decreased while that for the HER increased. Additionally, the selectivity of CO_2 reduction was observed to change, with CO becoming favoured over CH_4 with increasing mass transfer rates. By using the adapted mathematical model, it was shown that at high mass transfer rates, the interfacial pH and CO_2 concentration approaches the bulk values. However, the effects of mass transfer on the electrocatalytic CO_2 reduction were found to differ from the widely reported effects of interfacial pH and CO_2 concentration. Instead, the results are more consistent with the enhanced mass transfer of dissolved CO away from the electrode surface, which decreases the surface coverage of CO_{ads}, preventing the further reduction of CO_{ads} to hydrocarbons and changing the selectivity from CH_4 to CO. In almost all electrocatalytic CO_2 reduction literature to date, the hydrodynamics at the cathode surfaces are neither controlled nor quantified, which this work shows can have significant influence on the selectivity and activity of CO_2 reduction. This suggests that researchers need to consider these effects carefully, especially when comparing results between different experimental configurations or designing electrochemical cells and cathodes for industrial applications.

The ultimate research goal into the electrochemical reduction of CO_2 is the discovery of an electrocatalyst that is able to reduce CO_2 to high density fuels both efficiently and selectively. Currently, the mainstream approach by many researchers is to develop novel electrocatalysts with a degree of surface heterogeneity where multiple adjacent active sites are available to facilitate the stabilisation and reaction between different adsorbed reaction intermediates. This requirement can be achieved through supported metal nanoparticles, where the interface between metal nanoparticles and their support material synergistically serve as highly active sites. In our work, we have investigated the catalytic ability of TiO_2/Cu and Au_9/TiO_2/Cu electrodes prepared through spin-coating of commercial TiO_2 (P25) and chemically synthesised Au_9/TiO_2 nanoparticles onto polished Cu substrates. It was determined that as the TiO_2 loading increases, the electrode potential during constant current electrolysis tend to become more positive, i.e. overpotential decreases, pointing toward an enhancement in the electrochemical activity of the electrode. The increase in electrode potential is further observed when Au_9 nanoparticles are introduced into the TiO_2/Cu electrocatalyst.

However, we found that the enhancement in electrochemical activity is largely in favour toward the HER rather than CO_2 reduction. Nevertheless, despite the very low overpotentials at the modified Cu electrodes, surprising amounts of CO are still produced with current efficiencies generally comparable to that of the Cu controls and Ti electrodes at similar current densities but at much higher overpotentials. This suggests a form of synergy at the active sites of the $Au_9/TiO_2/Cu$ interfaces which may have lowered the CO adsorption strength, hence allowing similar amounts of CO to be produced at much lower overpotentials.

In light of the results of this work, we have the following recommendations for further work and the future direction of the electrochemical reduction of CO_2.

- Performing in-situ spectroscopy during electrochemical measurements can provide valuable real-time information regarding the electrode structure and reaction intermediates. In particular, IR-spectroscopy has been used during CO_2 reduction electrolysis to track reaction intermediates such as CO_{ads} [54, 79]. This method will prove useful to extend our work on periodic cyclic voltammetry and potentiostatic steps during constant current CO_2 reduction, where the suggested increase in the surface coverage of CO_{ads} (at the expense of H_{ads}) during certain potentiostatic steps can be proven.

- The effects of mass transfer on CO_2 reduction can be further studied using a rotating disc electrode (RDE). Unlike that of the rotating cylinder, the flow regime under the rotating disc is laminar across a wide range of rotation rates; hence, the hydrodynamics and mass transport relation of the rotating disc is very well established and numerical modelling of the transport of species is more accurate. This allows a better correlation between interfacial species concentrations, e.g. pH and CO_2 concentration, with the CO_2 reduction activity and selectivity. The disadvantages of using the RDE for CO_2 reduction studies is the difficulty in conventional product analysis, e.g. chromatography, due to the smaller electrode surface area (compared to the rotating cylinder) and the introduction of turbulence to the laminar regime due to gas evolution. These can be overcome by using the tip-based sampling technique of online electrochemical mass spectrometry (OLEMS) [83], where volatile reaction intermediates and products are detected online through mass spectrometry as they are being formed when the electrode potential is varied.

- In relation to the study of mass transfer, the mathematical model used in this work for estimating the interfacial concentrations can be further improved by incorporating water dissociation kinetics. This would also allow a more accurate estimation of the interfacial pH and species concentrations.

- Many aspects of the reaction mechanism of CO_2 reduction remain largely uncertain, although significant advances have been made recently on the discovery of several pH dependent/independent pathways and their occurrence on different crystal faces. Despite the complexity of the reaction, investigation into the mechanism of CO_2 reduction is an important area of research and must be further pursued in order to design more efficient and selective electrocatalysts for CO_2 reduction. Generally, it is the hope of many researchers to draw parallels between the mechanism of industrial gas-phase methanol production over $Cu/ZnO/AlO_3$ and that of electrochemical CO_2 reduction on Cu-based electrocatalysts, so that high density fuels such as methanol can also be produced electrochemically using renewable electricity.

- In the search for efficient and selective electrocatalysts for CO_2 reduction, we suggest further research into the development and characterisation of nanoparticles over metal oxide electrodes, since there are strong theoretical and experimental evidence that the interface between the materials is highly catalytic [203-206, 240]. Although continued research on Cu metal may proof beneficial on the fundamental level, the synergy between various catalytic materials may very well be the only way to achieve an electrocatalyst that is worthy of industrial applications.

Appendix 1: Calculations of thermodynamic potentials

The thermodynamic potentials for the various CO_2 reduction reactions given in Table 1.1 of chapter 1 are calculated using equations (A1.1) to (A1.3).

$$\Delta G^{\circ}_{f,rxn} = -nFE^{\circ} \qquad \text{E(A1.1)}$$

$$\Delta G^{\circ}_{f,rxn} = \sum \Delta G^{\circ}_{f,products} - \sum \Delta G^{\circ}_{f,reactants} \qquad \text{E(A1.2)}$$

$$E = E^{\circ} - \frac{RT}{nF} \ln \frac{a_{red}}{a_{ox}} \qquad \text{E(A1.3)}$$

where			
	ΔG°_f	Standard Gibbs energy of formation	kJ mol^{-1}
	E°	Standard half-cell reduction potential	V vs SHE
	E	Half-cell reduction potential	V vs SHE
	a_{red}	Chemical activity of species in reduced form	[-]
	a_{ox}	Chemical activity of species in oxidised form	[-]
	R	Ideal gas constant	8.314 J mol^{-1} K^{-1}
	T	Temperature	K
	n	Number of moles of e$^-$ transferred	mol e$^-$
	F	Faraday constant	96485 C per mol e$^-$

For example, the standard half-cell reduction potential for the formation of methanol from CO_2, reaction A1.1, is calculated as below:

$$\mathrm{Ox} + \mathrm{ne}^- \leftrightarrow \mathrm{red}$$

$$\mathrm{CO_{2(g)}} + 6\mathrm{H}^+ + 6\mathrm{e}^- \leftrightarrow \mathrm{CH_3OH_{(l)}} + \mathrm{H_2O_{(l)}} \qquad \text{R(A1.1)}$$

With the following standard Gibbs energy values from [102] and using equations (A1.1) and (A1.2):

$\Delta G^{\circ}_{f,CO_2} =$ −394.4 kJ mol^{-1} $\quad n =$ 6

$\Delta G^{\circ}_{f,CH_3OH} =$ −166.6 kJ mol^{-1} $\quad T =$ 298 K (standard state 25 °C)

$\Delta G^{\circ}_{f,H_2O} =$ −237.1 kJ mol^{-1}

$\Delta G^{\circ}_{f,rxn} =$ (−166.6 + (−237.1)) – (−394.4) = −9.3 kJ mol^{-1}

$E^{\circ} =$ (−9.3)(1000)/[−(6)(96485)] = 0.016 V vs SHE

To calculate the potential at pH 7, $a_{H^+}$is approximated as [H+] = 10^{-7} with a stoichiometric coefficient of 6, while the activity of all other species remain as 1. Hence, using equation (A1.3), i.e. the Nernst equation:

E° (pH 7) = 0.016 – 8.314(298)/[(6)(96485)]ln[1/(10^{-7})^6] = −0.398 V vs SHE

Appendix 2: Building a Ag|AgCl (sat. KCl) electrode

The Ag|AgCl reference electrode is a type of metal-ion secondary reference electrode. It is easily and cheaply prepared and maintained, stable with time and quite robust [245, 246]. The reference electrode (Figure A2.1) basically consists of a silver wire that is coated with silver chloride (AgCl), which in turn is in contact with a filling solution that contains the common ion (Cl^-). In our case, we use concentrated potassium chloride (KCl) solution as the filling solution. A Vycor porous glass frit held in place by heat shrink tubing seals the bottom of the reference electrode and serves as the ionically conducting pathway between the electrochemical cell and the reference electrode. At the top, epoxy glue is used as a permanent cap. The standard potential of the reference electrode is E^o = +0.222 V vs SHE, however because we use concentrated KCl as the filling solution, the potential of the electrode is actually E = +0.199 V vs SHE.

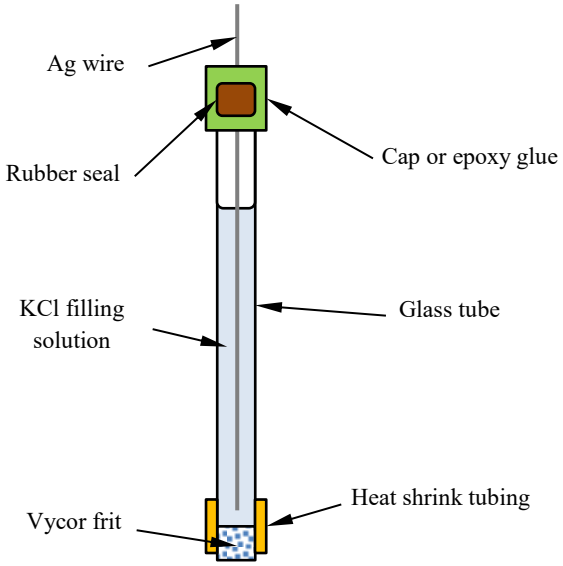

Figure A2.1: Illustration of a simple Ag|AgCl reference electrode. Adapted from [246].

There are many ways to build a Ag|AgCl electrode, but the key components are always the same. In general, the materials needed are:

a) Silver wire
b) Wire lead (e.g. copper wire) to attach to the silver wire outside the body of the electrode
c) Concentrated KCl solution
d) Concentrated nitric acid
e) Vycor frit with heat shrink tubing
f) A rubber seal
g) Epoxy glue
h) Suitable glass tube

General procedure to build the reference electrode:

1) Roughen the surface of the silver wire by dipping into concentrated nitric acid for about 10 seconds. Rinse with deionised water.

2) Place the silver wire into the glass tube and secure it in place using a rubber seal at the top of the glass tube (create a small opening through the centre of the rubber seal to allow a good length of wire to go through).
3) Seal the top of the glass tube with epoxy glue or heat shrink tubing. This prevents evaporation of the filling solution. Let the epoxy cure for a few hours.
4) Connect the silver wire above the rubber seal with a wire lead.
5) Fill the glass tube with concentrated KCl solution through the bottom opening using a syringe.
6) Secure a Vycor frit at the bottom of the glass tube using heat shrink tubing. It is advisable to expose some surface area of the frit at its sides to prevent bubbles from totally covering the frit when in use.
7) Once assembled, the silver wire needs to be coated by AgCl. This can be done by applying an anodic current of +20 μA for about 10 hours (or overnight) to the reference electrode assembled. Using a potentiostat, make the assembled reference electrode as the working electrode, and a Pt wire as the counter electrode. Connect the reference lead of the potentiostat to the counter leads. Place both working and counter electrodes in a solution of concentrated KCl.
8) After anodisation, the silver wire should have a white or grey coating. Leave the electrode in concentrated KCl solution for 1 day to allow the inner solution to equilibrate with the AgCl coating.
9) Check the potential of the newly made electrode with another working Ag|AgCl reference electrode (or any other reference electrodes with known potential) to ensure that the potential is correct.

Appendix 3: Calculation of time to reach steady-state for a CSTR

Due to the volume between the headspace of the electrochemical cell and the gas chromatograph (GC), the product gas is diluted for the first few GC measurements, leading to underestimated current efficiencies. To estimate the time needed for the concentrations of gaseous products in this volume to reach steady-state conditions, the volume is approximated as a continuous stirred tank reactor (CSTR) [247] as depicted in Figure A3.1.

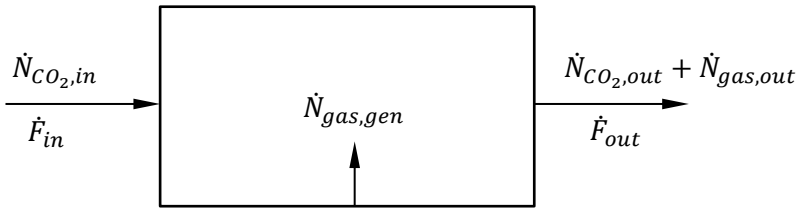

Figure A3.1: Approximation of the volume between the headspace of the electrochemical cell and the gas chromatograph as a continuous stirred tank reactor (CSTR). $\dot{N}$ are molar flow rates in mol s^{-1}, while $\dot{F}$ are volumetric flow rates in L s^{-1}. $\dot{N}_{gas,gen}$ represents the generation rate of a certain gaseous product during electrolysis that is released into the CSTR volume.

For a CSTR, ideal mixing is assumed; hence the composition in the reactor volume is uniform throughout the reactor and is identical to the composition of the reactor outflow. Isothermal conditions and therefore constant gas density is also assumed. In this example, we focus on the formation of one product gas, e.g. CH_4, from CO_2 reduction and model the change in concentration of CH_4 in the CSTR volume with time.

A mass balance on CH_4 in the CSTR volume:

$$\text{Accumulation} = \text{Flow in} - \text{Flow out} + \text{Generation} - \text{Consumption}$$

$$\frac{dN_{CH_4}}{dt} = 0 - \dot{N}_{CH_4,out} + \dot{N}_{CH_4,gen} - 0 \qquad \text{E(A3.1)}$$

Defining V [L] as the volume of the CSTR and C_{CH_4} [M] as the concentration of CH_4 in the CSTR volume and outlet flow, $\dot{F}_{out}$ [L s^{-1}] based on the assumption of ideal mixing, dividing equation (A3.1) by V gives:

$$\frac{dC_{CH_4}}{dt} = 0 - \frac{C_{CH_4}\dot{F}_{out}}{V} + \frac{\dot{N}_{CH_4,gen}}{V} \qquad \text{E(A3.2)}$$

Let $\tau = V/\dot{F}_{out}$, where τ [s] represents the residence time:

$$\frac{dC_{CH_4}}{dt} + \frac{C_{CH_4}}{\tau} = \frac{\dot{N}_{CH_4,gen}}{V} \qquad \text{E(A3.3)}$$

Equation (A3.3) is in the form of equation (A3.4), where an integrating factor, μ as given in equation (A3.5) is required to determine the solution for C_{CH_4} with respect to t:

$$\frac{dy}{dt} + py = q \quad \text{E(A3.4)}$$

$$\mu = e^{\int p dt} \quad \text{E(A3.5)}$$

With equation (A3.5), equations (A3.6) and (A3.7) are true:

$$\frac{d(\mu y)}{dt} = \mu q \quad \text{E(A3.6)}$$

$$y = \frac{1}{\mu}\int \mu q \, dt \quad \text{E(A3.7)}$$

With $y = C_{CH_4}$, $p = 1/\tau$ and $q = \dot{N}_{CH_4,gen}/V$:

$$\mu = e^{\int p dt} = e^{t/\tau + c_1} \quad \text{E(A3.8)}$$

$$C_{CH_4}(t) = \frac{1}{e^{t/\tau + c_1}}\int (e^{t/\tau + c_1})\left(\frac{\dot{N}_{CH_4,gen}}{V}\right) dt \quad \text{E(A3.9)}$$

$$= \frac{1}{e^{t/\tau} e^{C_1}}\left(\frac{\dot{N}_{CH_4,gen}}{V}\right)\int (e^{t/\tau} e^{C_1})\, dt \quad \text{E(A3.10)}$$

$$= \frac{e^{C_1}}{e^{t/\tau} e^{C_1}}\left(\frac{\dot{N}_{CH_4,gen}}{V}\right)\left[\tau e^{t/\tau} + C_2\right] \quad \text{E(A3.11)}$$

$$= \left(\frac{\dot{N}_{CH_4,gen}}{V}\right)\tau + \frac{C_2}{e^{t/\tau}} \quad \text{E(A3.12)}$$

Initial conditions: when $t = 0$, $C_{CH_4} = 0$ in the CSTR volume, so $C_2 = -(\dot{N}_{CH_4,gen}/V)\tau$. Hence,

$$C_{CH_4}(t) = \left(\frac{\dot{N}_{CH_4,gen}}{V}\right)\tau\left(1 - \frac{1}{e^{t/\tau}}\right) \quad \text{E(A3.13)}$$

To apply equation (A3.13) to a typical CO_2 reduction experiment in the rotating cylinder electrode set-up, the following example parameters are assumed: CSTR volume of 50 ml, outlet flowrate of 20 ml min^{-1}, and current efficiency of 30% for CH_4 at a total current of −15 mA. Hence, $\dot{N}_{CH_4,gen} = 7.77 \times 10^{-9}$ mol s^{-1} (8 mol e^- to produce 1 mol CH_4 and using 96485 C per mol e^-), $V = 0.05$ L, and $\tau = V/\dot{F}_{out} = 150$ s. The change in C_{CH_4} with time is shown in Figure A3.2a, and suggests that steady-state conditions can only be achieved after more than 15 minutes. Similarly, for a typical CO_2 reduction experiment in the planar disc electrode set-up, the following example parameters are assumed: CSTR volume of 10 ml, outlet flowrate of 10 ml min^{-1}, and current efficiency of 30% for CH_4 at a total current of −15 mA. Hence, $\dot{N}_{CH_4,gen} = 7.77 \times 10^{-9}$ mol s^{-1}, $V = 0.01$ L, and $\tau = V/\dot{F}_{out} = 60$ s. In this case, steady-state is achieved after more than 5 minutes (Figure A3.2b).

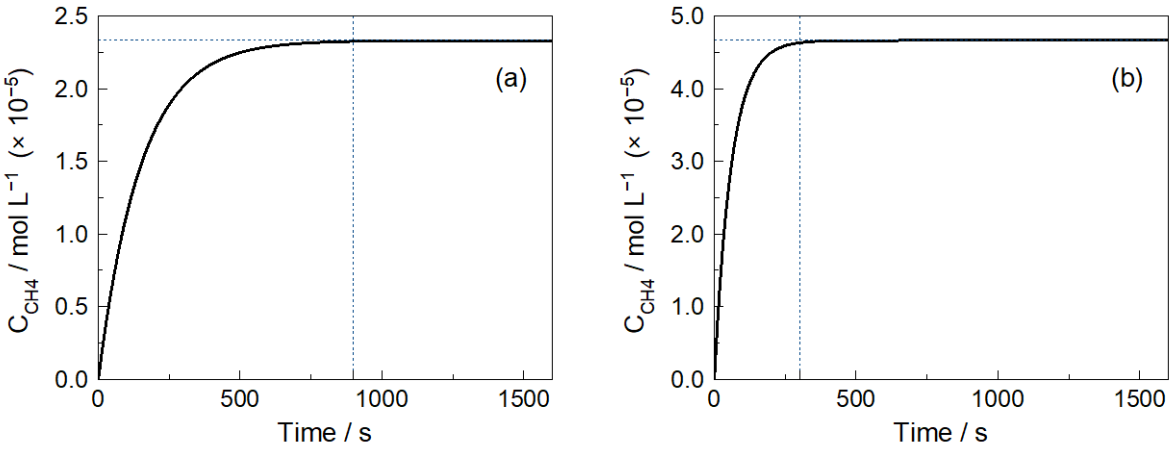

Figure A3.2: Calculation of time required to reach steady-state conditions in the volume between the headspace and gas chromatograph assuming a CSTR for (a) rotating cylinder electrode set-up where the volume is approximately 50 ml with a total flow rate of 20 ml min^{-1}, and (b) planar disc electrode set-up where the volume is approximately 10 ml with a total flow rate of 10 ml min^{-1}. For both set-ups, a CH_4 current efficiency of 30% at a total current of −15 mA was assumed.

Appendix 4: GC parameters, calibration and uncertainty analysis

The gas chromatograph (GC) used for this work is a SRI 8610C Gas Chromatograph (Multi-Gas #3 configuration) with TCD and FID detectors. The GC has two columns installed; a 6' molecular sieve 13x, and a 6' haysep-D. The GC is originally designed to use both columns for component separation, where the molecular sieve column would give a clear separation of "light" gases, i.e. H_2, air (N_2 + O_2), CO and CH_4, while the haysep-D column separates the "heavier" hydrocarbons, i.e. CO_2, C_2H_4 and C_2H_6. However, we found that using the haysep-D column by itself gives adequate separation for all gases, although the N_2 + O_2 peak may overlap slightly with the H_2 and CO peak if air contamination is severe enough. With minimal air contamination, the detection and quantification of H_2 through the TCD is not affected. Additionally, because H_2 and air do not appear in the FID, detection and quantification of CO by the FID is not affected. Using the haysep-D column by itself also gives better consistency in results and calibration than using both columns in tandem. Hence, we have opted to simplify and increase the reproducibility of our GC method by only utilising the haysep-D column. The parameters used for the GC analysis are summarised in Table A4.1.

Table A4.1: Summary of GC parameters used for analysis of product gas of CO_2 reduction

Parameter	Settings
Carrier gas (Ar)	EPC[a] 22 psi equivalent to 20 ml min^{-1} flow
H_2 gas (Instrument grade)	EPC 20 psi equivalent to 25 ml min^{-1} flow (for methaniser + FID)
Air	EPC 5 psi equivalent to 5 ml min^{-1} flow (for methaniser + FID)
Valve temperature	60 °C
TCD temperature and gain	150 °C, low gain
FID temperature and gain	300 °C, high gain
Methaniser temperature	300 °C
Column temperature	Initial: 40 °C hold for 2.3 min Ramp up: 30 °C min^{-1} to 90 °C and hold for 2.8 min Ramp down: −40 °C min^{-1} to 40 °C and hold for 6.9 min
	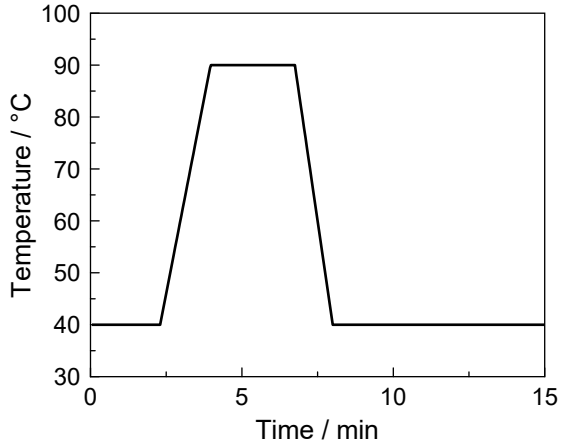
Valve event program	Time / min — Event 0.0 — ZERO signal 0.1 — G valve ON (inject position of sample loop) 0.3 — G valve OFF (load position of sample loop)
Sample loop size	1 ml

[a]Electronic Pressure Controller

The GC is calibrated using a custom calibration gas mixture (BOC Ltd) with composition as given in Table A4.2. A range of concentrations (in volume %) for calibration is then obtained by dilution of the calibration gas mixture with either Ar (99.999% purity, Zero Grade) or CO_2 (99.995% purity, Laser Grade) gas. For both GC calibration and measurements, the sample loop is used, and because its size is fixed at 1 ml, an external calibration is sufficient. However, due to a possibility of variation in gas pressure with gas flow rates in the sample loop, which can inadvertently introduce less or more material into the sample loop, it is advisable to perform the calibration using the same total gas flow rate used for measurements to prevent an over- or under-estimation in measured gas concentrations. The retention times of the various components involved are given in Table A4.2, and the calibration charts are shown in Figure A4.1. A typical chromatogram obtained during GC calibration is shown in Figure A4.2.

Table A4.2: Composition of the custom calibration gas mixture and the retention times of the various components involved using the GC parameters given in Table A4.1.

Gas	Volume ratio (%)	Uncertainty (±%)	Retention time / min[a]
H_2	4.84	0.02	0.84
CO	5.01	0.03	1.16
CH_4	5.02	0.03	1.75
C_2H_4	5.02	0.03	5.21
C_2H_6	5.01	0.03	6.37
CO_2	*Balance* = 75.10	-	Approximately 2.79[b]

[a]As determined from the TCD detector

[b]The CO_2 peak is too broad and exceeds the detectors' limit due to its high concentration to provide a precise retention time.

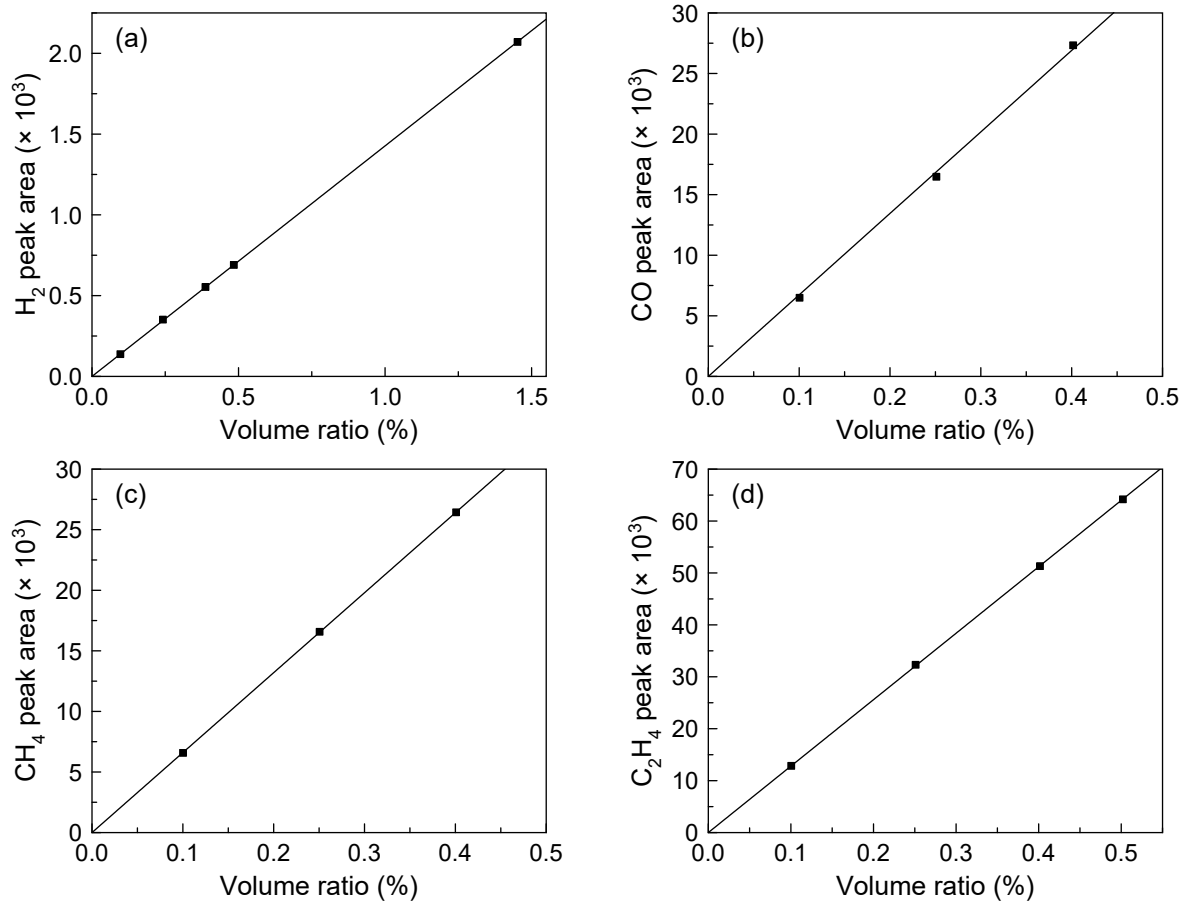

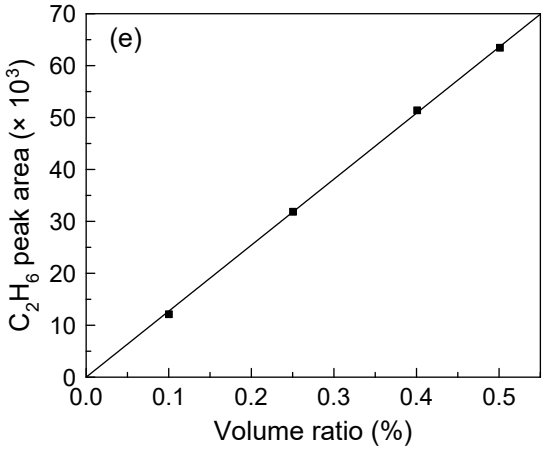

Figure A4.1: GC calibration charts for (a) H_2, (b) CO, (c) CH_4, (d) C_2H_4 and (e) C_2H_6. H_2 was measured from the TCD, while all other gases were measured from the FID. Line of best fit is forced through the origin.

The uncertainties of the gas concentrations calculated from the calibration data are estimated using equation (A4.1). By using the error propagation method, equation (A4.2), the uncertainties of the current efficiencies are estimated [248].

$$\Delta x = \frac{SE_{yx}}{m}\sqrt{\left[\frac{1}{k}+\frac{1}{n}+\frac{(y_0-\bar{y})^2}{m^2 s_x^2(n-1)}\right]} \qquad \text{E(A4.1)}$$

where Δx Estimated uncertainty of calculated value from a linear calibration

SE_{yx} Standard error of regression

m Slope of linear calibration

k Number of y-measurements

n Number of calibration data points

y_0 Mean of y-measurements

$\bar{y}$ Mean of y-values of calibration data points

s_x Sample variance of x-values of calibration data points

$$\Delta f = \sqrt{\frac{\partial f}{\partial u}(\Delta u)^2+\frac{\partial f}{\partial v}(\Delta v)^2+\frac{\partial f}{\partial w}(\Delta w)^2+\cdots} \qquad \text{E(A4.2)}$$

where Δf Estimated uncertainty of calculated variable from other variables

u, v, w ... Other variables with their respected uncertainties

$\Delta u, \Delta v, \Delta w$ ...

Table A4.3a summarises the statistical values of the calibration data required for use of equation (A4.1), while Table A4.4a summarises the calculations of current efficiencies and associated uncertainties for an example GC measurement.

Table A4.3a: Statistical values of calibration data given in Figure A4.1.

Gas	m	SE_{yx}[a]	n	s_x	$\bar{y}$
H_2	142671	3.15	5	2.86E-05	760
CO	6726739	350.54	3	2.27E-06	16767
CH_4	6599342	52.93	3	2.26E-06	16527
C_2H_4	12795799	135.49	4	3.09E-06	40169
C_2H_6	12711011	459.25	4	3.07E-06	39702

[a]Calculated using Excel function STEYX

Table A4.4a: Calculations of current efficiencies (CE) and associated uncertainties for an example GC measurement during CO_2 reduction. Total current −15.71 mA and total gas flow rate 20.7 ± 0.2 ml min^{-1}.

Gas	Peak area[a]	V_{ratio} (%)[b]	ΔV_{ratio} (±%)[c]	i_{gas} / mA[d]	Δi_{gas} / ±mA[e]	CE (%)[f]	ΔCE (±%)[g]
H_2	362	0.253	0.0025	6.886	0.095	43.8	0.6
CO	607	0.009	0.0084	0.245	0.229	1.6	1.5
CH_4	3445	0.052	0.0012	5.675	0.141	36.1	0.9
C_2H_4	90	0.0007	0.0016	0.115	0.262	0.7	1.7
C_2H_6	6	0.00005	0.0055	0.009	1.044	0.1	6.6

[a]Only one GC measurement was made per measurement period, hence k = 1.

[b]Calculated using the calibration data. Take CH_4 for example:

$$V_{ratio} = \frac{Peak\ Area}{Slope} = \frac{3445}{6599342} = 0.052\%$$

[c]Calculated using equation (A4.1). For CH_4:

$$\Delta x = \frac{SE_{yx}}{m}\sqrt{\left[\frac{1}{k}+\frac{1}{n}+\frac{(y_0-\bar{y})^2}{m^2 s_x^2(n-1)}\right]} = \frac{52.93}{6599342}\times\sqrt{\frac{1}{1}+\frac{1}{3}+\frac{(3445-16527)^2}{6599342^2(2.26\times10^{-6})(3-1)}} = \pm 0.0012\%$$

[d]Calculated assuming ideal gas law ($PV = nRT$) and Faraday constant (96485 C per mol e$^-$) to convert from volume to molar basis, and from molar basis to coulombs respectively. Experiments were conducted at ambient conditions (1 atm and 298.15 K). Total flow rate is 20.7 ml min^{-1}. For example, one mole of CH_4 requires z_{CH4} = 8 mole e$^-$, hence:

$$i_{CH4} = \frac{PV}{RT}(z_{CH4})(F) = \left[\left(\frac{101325(20.7\times0.00052)}{8.314\times298.15}\right)\left(\frac{1}{60\times10^6}\right)\right](8)(96485)(1000) = 5.7\ mA$$

[e]Calculated using equation (A4.2), where the contributing uncertainties are from the gas concentration (V_{ratio}) and total gas flow rate (V_{total}). The uncertainty of the total gas flow rate is based on the uncertainty values specified by the manufacturer of the mass flow controllers (ALICAT), which in this example is ±0.2 ml min^{-1}. For CH_4:

$$\Delta i_{CH4} = i_{CH4}\times\sqrt{\left(\frac{\Delta V_{ratio}}{V_{ratio}}\right)^2+\left(\frac{\Delta V_{total}}{V_{total}}\right)^2} = 5.675\times\sqrt{\left(\frac{0.0012}{0.052}\right)^2+\left(\frac{0.2}{20.7}\right)^2} = \pm 0.14\ mA$$

[f]Percentage of the total current going towards the formation of a certain product. For CH_4:

$$CE_{CH4} = \frac{i_{CH4}}{i_{total}} = \frac{5.68}{15.71} = 36.1\%$$

[g]Calculated using equation (A4.2), where the only contributing uncertainty is the partial current. For CH_4:

$$\Delta CE_{CH4} = \frac{\Delta i_{CH4}}{i_{total}} = \frac{0.141}{15.71} = \pm 0.9\%$$

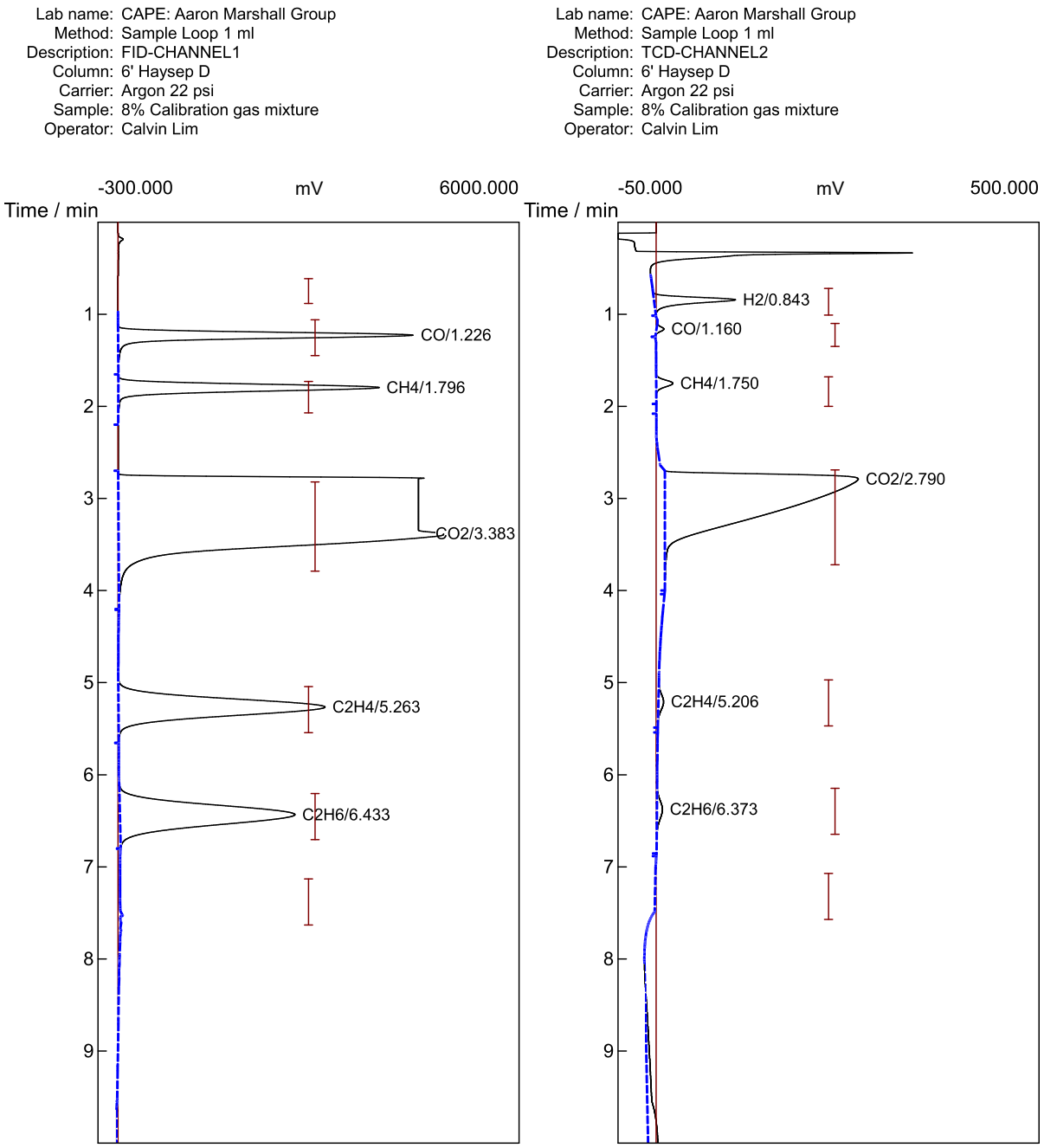

Figure A4.2: Typical chromatogram showing the separation of gases from the calibration gas mixture using the GC parameters given in Table A4.1. Note that the retention times on the TCD are slightly earlier compared to the FID because the TCD is placed, in series, before the FID since detection by FID irreversibly destroys the sample. At typical noise levels (±0.5 mV), the detection limits are approximately 100 ppm for H_2 and 10 ppm for CO_2 reduction products

Appendix 5: HPLC parameters and calibration

The HPLC used for liquid products analysis is a HP 1100 series HPLC equipped with a SUPELCOGEL^{TM} C-610H column with a diode array (UV/Vis) and a refractive index (RI) detector. The HPLC is calibrated to detect and quantify formic acid, acetic acid and methanol. The parameters used for the HPLC analysis are summarised in Table A5.1.

Table A5.1: Summary of HPLC parameters used for analysis of liquid products of CO_2 reduction.

Parameter	Settings
Mobile phase	0.1% H_3PO_4 (made from 85% H_3PO_4 HPLC grade)
Flow rate	0.5 ml min^{-1}
Injection volume	10 µL
Operating pressure	Approximately 46 bar pressure at 0.5 ml min^{-1}
Operating temperature	30 °C
UV/Vis detector wavelength	210 nm
Analysis time	30 mins per run

In general, the UV/Vis detector is more sensitive and less noisy compared to the RI detector. However, methanol is only visible on the RI detector. Hence, formic acid and acetic acid are primarily measured using the UV/Vis detector, while methanol is measured using the RI detector. The HPLC is calibrated using standards of formic acid, acetic acid and methanol made using DI water at various concentrations. Because a fix injection volume of 10 µL is used for both calibration and measurements, an external calibration is sufficient. Table A5.2 summarises the calibration data and the components' retention time using the parameters given in Table A5.1. Figure A5.1 presents the calibration data in graphical form. A typical HPLC chromatogram obtained during calibration for formic acid is shown in Figure A5.2.

Table A5.2: HPLC calibration data and retention times of components.

Component	Retention time / min	Slope / peak area M^{-1}
Formic acid[a]	19.3	47581
Acetic acid[a]	21.1	36702
Methanol[b]	24.7	3424

[a]Using the UV/Vis detector.
[b]Using the RI detector.

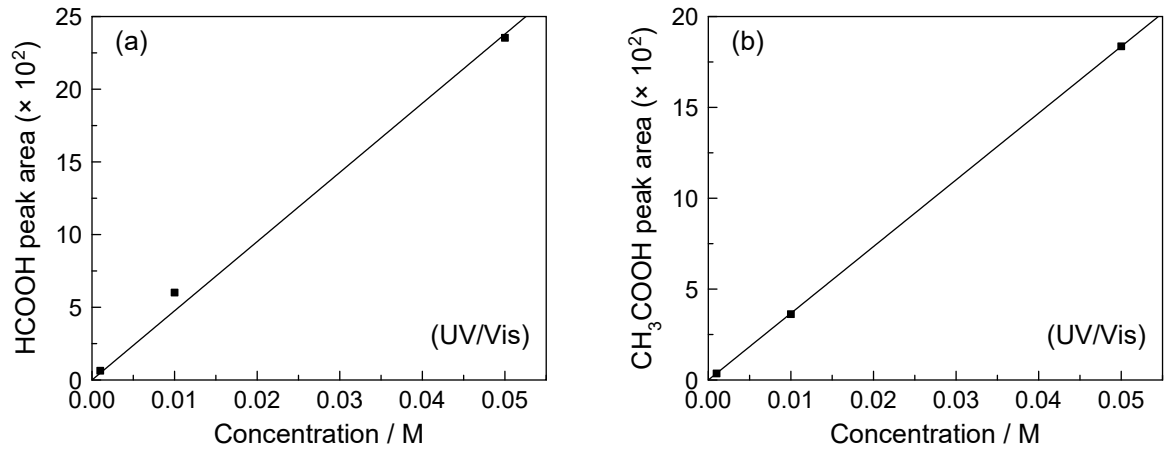

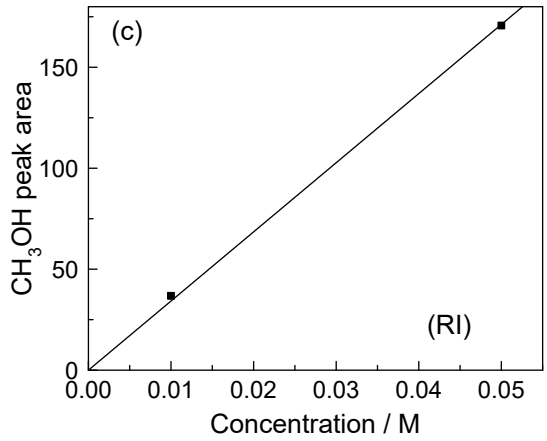

Figure A5.1: HPLC calibration charts for (a) formic acid, (b) acetic acid and (c) methanol. Line of best fit is forced through the origin.

Liquid products are only analysed post-electrolysis; therefore from the HPLC measurements, the total current efficiency over the whole electrolysis period is calculated. For example, after 10 hours of CO_2 reduction at −15.71 mA in 35 ml of 0.2 M $KHCO_3$, HPLC has detected formic acid with a concentration of 0.00673 ± 0.0023 M. 1 mol of formic acid requires 2 moles of e^-, hence the total charge going towards the formation of formic acid is:

$$\frac{35}{1000} L \times 0.00673 \frac{mol_{HCOOH}}{L} \times 2 \frac{mol_{e^-}}{mol_{HCOOH}} \times 96485 \frac{C}{mol_{e^-}} = 45.5\ C$$

The total current efficiency of formic acid is then calculated as the ratio between the total charge going towards the formation of formic acid and the total charge passed over 10 hours at −15.71 mA:

$$\frac{45.5\ C}{\frac{15.71}{1000}\frac{C}{s} \times (10 \times 3600) s} = 8.0 \pm 2.8\%$$

The uncertainties were calculated using the same uncertainty analysis method used on the gas chromatograph's calibration and measurements, i.e. equations (A4.1) and (A4.2); therefore the calculations are not repeated here.

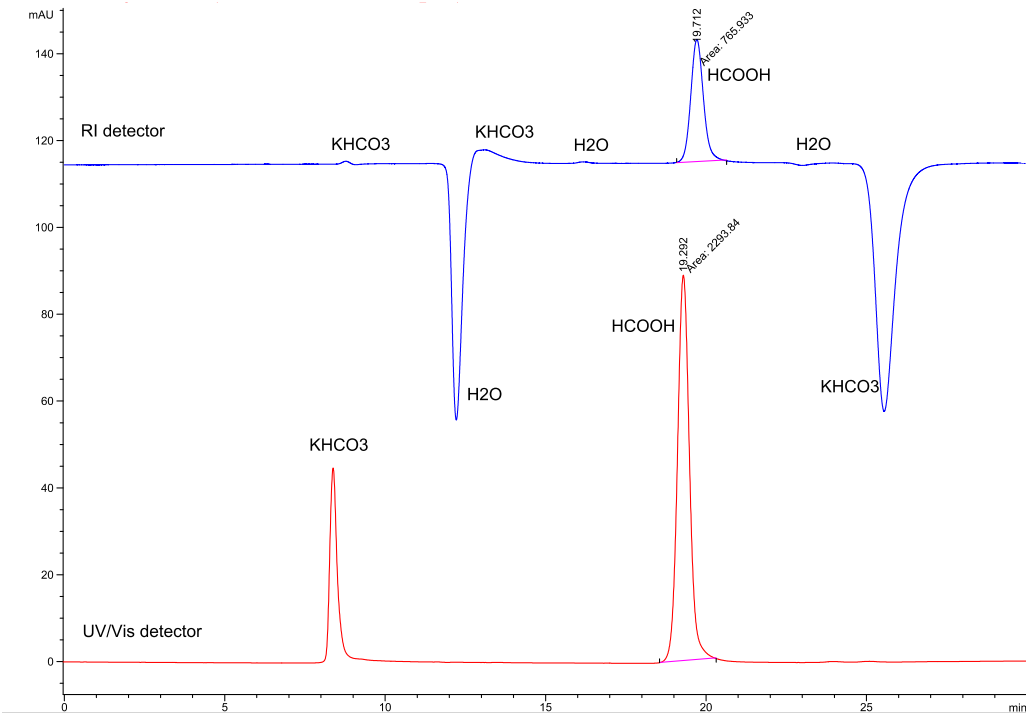

Figure A5.2: Typical chromatogram showing the detection of 0.05 M formic acid prepared in 0.5 M $KHCO_3$ using the HPLC parameters given in Table A5.1. Note that the retention times on the UV/Vis detector are slightly earlier compared to the RI detector because the UV/Vis detector is placed, in series, before the RI detector. Various peaks due to the elution of H_2O and the $KHCO_3$ solvent are annotated. At typical noise levels (±0.01 mAU on the UV/Vis detector), the detection limit of formic acid is approximately 0.1 mM.

Appendix 6: Equilibrium composition of a solution with CO_2 equilibria

An aqueous solution saturated with CO_2 will contain $CO_2/HCO_3^-/CO_3^{2-}$ species that are in equilibrium with each other due to the ionisation of carbonic acid (H_2CO_3), which is a relatively weak diprotic acid. Herein, a mathematical method to calculate the equilibrium composition of a CO_2 saturated $KHCO_3$ solution under a constant partial pressure of CO_2 (Figure A6.1) is presented. A recommended resource on CO_2 equilibria is a textbook by J.N. Butler [75], within which a thorough treatment on solving equilibrium compositions is given in chapters 1 and 2.

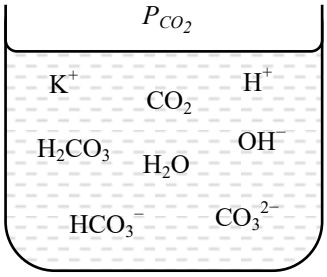

Figure A6.1: Illustration of a $KHCO_3$ solution in equilibrium under a CO_2 partial pressure of P_{CO_2}.

In a CO_2 saturated $KHCO_3$ solution, the various species involved are H_2O, K^+, H^+, CO_2, OH^-, HCO_3^- and CO_3^{2-}. The concentration of K^+ is similar to the concentration of the $KHCO_3$ solution itself, which we denote as C_{KHCO_3}, while for dilute solutions, we can assume the concentration of water to be nearly constant at $[H_2O]$ = 55.4 M at ambient conditions (1 atm, 25 °C). The concentration of dissolved CO_2 depends largely on the partial pressure of CO_2 and is normally expressed by Henry's Law, equation (A6.1).

$$K_H P_{CO_2} = [CO_2]\gamma_{CO_2} \qquad \text{E(A6.1)}$$

where	K_H	Henry's constant at zero ionic strength	M atm^{-1}
	P_{CO_2}	Partial pressure of CO_2	atm
	$[CO_2]$	Concentration of dissolved CO_2	M
	γ_{CO_2}	Activity coefficient of dissolved CO_2	[-]

The solubility of CO_2, hence K_H, depends greatly on temperature, i.e. the solubility decreases with increasing temperatures. At 25 °C, K_H is normally about 0.035 M atm^{-1}, which can also be calculated using the empirical equation by Carroll et al. [249] (several unit conversion steps are required). The activity coefficient γ_{CO_2} accounts for the modest decrease in CO_2 solubility due to the salt content or ionic strength of the solution, i.e. the "salting-out" effect [220, 221], and can be calculated using the empirical equation (A6.2) by Wigley and Plummer [219]. At 25 °C and ionic strength of 0.2 M, γ_{CO_2} is 1.05.

$$\log_{10}\gamma_{CO_2} = \frac{(33.5 - 0.109T + 0.0014T^2)I - (1.5 + 0.015T + 0.004T^2)I^2}{T + 273} \qquad \text{E(A6.2)}$$

where	T	Temperature	°C
	I	Ionic strength of solution	M

K_H can be combined with γ_{CO_2} to give the concentration equilibrium constant K_H* as shown in equation (A6.3).

$$\frac{K_H P_{CO_2}}{\gamma_{CO_2}} = [CO_2] = K_H^* P_{CO_2} \qquad \text{E(A6.3)}$$

As for the remaining species, i.e. H^+, OH^-, HCO_3^- and CO_3^{2-}, their relative concentrations are dictated by equilibrium reactions that are present in the solution, i.e. carbonic acid dissociation, reactions (A6.1) and (A6.2), and water ionisation, reaction (A6.3). The equilibrium constants (K_{a1}, K_{a2}, K_w) and their values at 25 °C are given as equations (A6.4) to (A6.6) [75, 102]. In equations (A6.4) and (A6.6), the activity of water (a_{H_2O}) is assumed to be very nearly equal to 1, which is acceptable for dilute solutions [250]. When CO_2 dissolves in water, carbonic acid (H_2CO_3) is first formed, after which it ionises to HCO_3^- and H^+; however, because the hydration of CO_2 to H_2CO_3 is quite slow compared to the subsequent ionisation of H_2CO_3, the concentration of H_2CO_3 at equilibrium is 3 orders of magnitudes lower than that of CO_2 [75]. Since H_2CO_3 is uncharged and has no particular significance in the acid-base equilibria, it is usually grouped with the relatively more concentrated dissolved CO_2 as $[CO_2]_{total} = [H_2CO_3] + [CO_2]$. For simplicity, we will just use $[CO_2]$ to refer to $[H_2CO_3] + [CO_2]$.

$$CO_2 + H_2O \leftrightarrow H_2CO_3 \leftrightarrow H^+ + HCO_3^- \qquad \text{R(A6.1)}$$

$$HCO_3^- \leftrightarrow H^+ + CO_3^{2-} \qquad \text{R(A6.2)}$$

$$H_2O \leftrightarrow H^+ + OH^- \qquad \text{R(A6.3)}$$

$$K_{a1} = \frac{a_{H^+} a_{HCO_3^-}}{a_{CO_2} a_{H_2O}} = \frac{\gamma_{H^+}\gamma_{HCO_3^-}}{\gamma_{CO_2}} \times \frac{[H^+][HCO_3^-]}{[CO_2]} = 10^{-6.35} \qquad \text{E(A6.4)}$$

$$K_{a2} = \frac{a_{H^+} a_{CO_3^{2-}}}{a_{HCO_3^-}} = \frac{\gamma_{H^+}\gamma_{CO_3^{2-}}}{\gamma_{HCO_3^-}} \times \frac{[H^+][CO_3^{2-}]}{[HCO_3^-]} = 10^{-10.33} \qquad \text{E(A6.5)}$$

$$K_w = \frac{a_{H^+} a_{OH^-}}{a_{H_2O}} = \gamma_{H^+}\gamma_{OH^-}[H^+][OH^-] = 10^{-14} \qquad \text{E(A6.6)}$$

where	K	Equilibrium constant in terms of activities	[-]
	a_j	Activity of species j	[-]
	γ_j	Activity coefficient of species j	[-]

In a similar way to that shown in equation (A6.3), the equilibrium constants K_{a1}, K_{a2} and K_w and their associated activity coefficients can be grouped to give the concentration equilibrium constants K_{a1}^*, K_{a2}^* and K_w^* (equations (A6.7) to (A6.9)).

$$\frac{K_{a1}\gamma_{CO_2}}{\gamma_{H^+}\gamma_{HCO_3^-}} = \frac{[H^+][HCO_3^-]}{[CO_2]} = K_{a1}^* \quad \text{E(A6.7)}$$

$$\frac{K_{a2}\gamma_{HCO_3^-}}{\gamma_{H^+}\gamma_{CO_3^{2-}}} = \frac{[H^+][CO_3^{2-}]}{[HCO_3^-]} = K_{a2}^* \quad \text{E(A6.8)}$$

$$\frac{K_w}{\gamma_{H^+}\gamma_{OH^-}} = [H^+][OH^-] = K_w^* \quad \text{E(A6.9)}$$

For dilute solutions generally with ionic strength below 0.5 M, the activity coefficients of the charged species can be adequately estimated using the Davies equation, given in equation (A6.10).

$$\log_{10}\gamma_j = -0.5{z_j}^2\left(\frac{\sqrt{I}}{1+\sqrt{I}} - 0.2I\right)\left(\frac{298}{T+273}\right)^{2/3} \quad \text{E(A6.10)}$$

where z_j Number of charge of ion j [-]

The ionic strength of the solution (I) is calculated using equation (A6.11) which is derived from the Debye-Hückel Theory.

$$I = \frac{1}{2}\sum_j C_j z_j^2 \quad \text{E(A6.11)}$$

where C_j Concentration of ion j M

Notice that the ionic strength of the solution depends on the individual concentration of the ions, which at present is unknown. Therefore, the equilibrium concentrations need to be solved iteratively, which will be explained below.

Since there are 4 unknowns that we desire to solve for, i.e. the concentrations of H^+, OH^-, HCO_3^- and CO_3^{2-}, and the equilibrium constants K_{a1}, K_{a2} and K_w (or K_{a1}^*, K_{a2}^* and K_w^*) provide three independent equations, an additional independent relation between species concentrations is required to provide a unique solution. This is satisfied by the charge balance between charged species as shown in equation (A6.12). Note that CO_3^{2-} carries two charges, hence the coefficient of 2 in the charge balance.

$$[K^+] + [H^+] = [HCO_3^-] + 2[CO_3^{2-}] + [OH^-] \quad \text{E(A6.12)}$$

By substituting C_{KHCO_3} for $[K^+]$, and expressing each term on the right hand side in terms of $[H^+]$, P_{CO_2} and the concentration equilibrium constants K_H*, K_{a1}^*, K_{a2}^* and K_w^* using equations (A6.3) and (A6.7) to (A6.9), a polynomial in terms of $[H^+]$ is obtained (equation (A6.13)).

$$f = [H^+]^3 + C_{KHCO_3}[H^+]^2 + \left(-K_{a1}^*K_H^*P_{CO_2} - K_w^*\right)[H^+] - 2K_{a1}^*K_{a2}^*K_H^*P_{CO_2} = 0 \quad \text{E(A6.13)}$$

As mentioned above, this polynomial needs to be solved iteratively due to the dependence of the ionic strength on the concentrations of charged species. To do this, the ionic strength is first set to zero, which sets all activity coefficients to be 1; hence the values of all concentration equilibrium constants will just be equal to their values at zero ionic strength. The polynomial can then be solved for $[H^+]$

using a numerical method such as Newton's method (see equation (A6.14), where *f'* is the first derivative of *f*), which is easily implemented in EXCEL or MATLAB (see Appendix 7).

$$[H^+]_{k+1} = [H^+]_k - \frac{f}{f'} \qquad \text{E(A6.14)}$$

With $[H^+]$ determined, the concentrations of all other species can be calculated. Once the concentrations of all charged species are solved for the case of $I = 0$, the calculations are re-iterated but with the ionic strength now set to the value determined by the calculated concentrations. This is repeated until numerical convergence is achieved to a satisfactory tolerance level. To shorten the number of iterations, instead of zero, the ionic strength can initially be estimated as $I = C_{KHCO_3}$ which is already fair approximation to the actual value of I at equilibrium. From $[H^+]$, the pH can be calculated using equation (A6.15).

$$pH = -\log_{10} a_{H^+} = -\log_{10}[H^+]\gamma_{H^+} \qquad \text{E(A6.15)}$$

Figure A6.2 compares the equilibrium pH values calculated using the equations presented above with those measured experimentally.

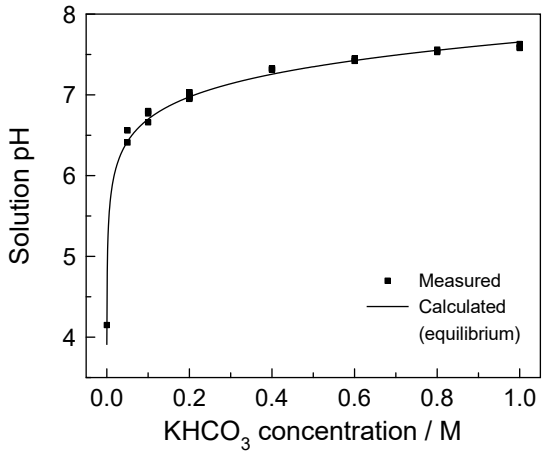

Figure A6.2: Equilibrium pH values of CO_2 saturated $KHCO_3$ solution at various concentrations calculated from equilibrium constants with ionic strength corrections using the Davies equation, compared with values that were experimentally measured.

Appendix 7: MATLAB script for CO_2 equilibria

The following is a MATLAB script written to calculate the equilibrium concentrations of CO_2 equilibria using the method presented in Appendix 6.

```
%=========================================================================
%CO2 EQUILIBRIA MODEL
%AUTHOR: CALVIN LIM
%LAST MODIFIED: 04/MARCH/2017
%
%Input parameters:  a = %CO2 in 1 atm total pressure, %, e.g. 100%
%                   b = Concentration of KHCO3 solution in M, e.g. 0.2 M
%
%Returns a vector y containing concentrations in M and the pH
%                   y = [CO2_conc; HCO3_conc; CO3_conc; OH_conc]
%=========================================================================

function y = CO2_equib(a,b)

%Additional user inputs within function:

T = 25;                             %Temperature, degrees C
CO2_perc = a;                       %Percent CO2 of total pressure,%
P_total = 1;                        %Total pressure, atm
P_CO2 = P_total*CO2_perc/100;       %CO2 partial pressure, atm
C_KHCO3 = b;                        %Concentration of KHCO3, M

%Constants:

Mw_H2O = 1.00797*2 + 15.9994;       %Molecular weight of water, g/mol
Dens_H2O = 997.1; %Density of water at 25 C, g/L
pKa1 = 6.35;      %H2CO3 dissociation constant at 25C, zero ionic strength
pKa2 = 10.33;     %HCO3- dissociation constant at 25C, zero ionic strength
pKw = 13.996;     %Water ion-product constant at 25C

Ka1 = 10^-pKa1;
Ka2 = 10^-pKa2;
Kw = 10^-pKw;

%Henry's constant using empircal equation by Carroll et al.:

ln_H = -6.8346 + 1.2817*10^4/(T+273) - 3.7668*10^6/(T+273)^2 +
2.997*10^8/(T+273)^3;

%Henry's constant, H in MPa
%(x_CO2)*H = P_total*P_CO2*f_CO2, where f_CO2 = 1 at zero ionic strength

H = exp(ln_H);
x_CO2 = P_CO2*101325/(H*10^6);                  %mol fraction CO2 in water
C_CO2 = (x_CO2*Dens_H2O/Mw_H2O)*(1/(1-x_CO2));  %[CO2], M
Kh = C_CO2/P_CO2; %Henry's constant in M/atm at zero ionic strength

%Number of charge of each ion:

z_H = 1;
z_OH = -1;
```

```
z_HCO3 = -1;
z_CO3_2 = -2;

%Ionic strength calculation:

for J = 1:100

    %First iteration IonS = 0

    if J == 1

        IonS = 0;

    else

        %Subsequent iterations, IonS based on previous concentrations

        IonS = 0.5*(C_KHCO3 + H_conc + OH_conc + HCO3_conc + CO3_conc*4);

        %Convergence criteria

        if abs(IonS - IonS_old) < 10^-6

            return

        end

    end

%Activity coefficient of single ions based on Davies equation:

a_H = 10^(-0.5*(z_H)^2*(sqrt(IonS)/(1+sqrt(IonS))-0.2*IonS));
a_OH = 10^(-0.5*(z_OH)^2*(sqrt(IonS)/(1+sqrt(IonS))-0.2*IonS));
a_HCO3 = 10^(-0.5*(z_HCO3)^2*(sqrt(IonS)/(1+sqrt(IonS))-0.2*IonS));
a_CO3_2 = 10^(-0.5*(z_CO3_2)^2*(sqrt(IonS)/(1+sqrt(IonS))-0.2*IonS));

%Activity coefficient of dissolved CO2 based on salting-out model using
%Empirical equation by Wigley and Plummer:

a_CO2 = 10^(((33.5 - 0.109*T + 0.0014*T^2)*IonS - (1.5 + 0.015*T +
0.004*T^2)*IonS^2)/(T + 273));

%Concentration of CO2 in solution based on Henry's Law:

CO2_conc = Kh*P_CO2/a_CO2;

%Concentration equilibrium constants:

Ka1_conc = Ka1*a_CO2/(a_HCO3*a_H);
Ka2_conc = Ka2*a_HCO3/(a_CO3_2*a_H);
Kw_conc = Kw/(a_H*a_OH);

%Newton's method to solve for H_conc from polynomial for [H+] derived using
the charge balance:

H_conc = 1;        %Initial value for [H+]
Iter_results(1,:) = [0, H_conc];    %Iteration results
```

```
109
110   for I = 1:500
111
112       f = H_conc^3 + C_KHCO3*H_conc^2 + (-Ka1_conc*CO2_conc - Kw_conc)*H_conc
113   - 2*Ka1_conc*Ka2_conc*CO2_conc;
114
115       %First derivation of f
116       df = 3*H_conc^2 + 2*C_KHCO3*H_conc + (-Ka1_conc*CO2_conc - Kw_conc);
117
118       H_conc = H_conc - f/df;    %Newton's method
119
120       Iter_results(I+1,:) = [I, H_conc];
121
122       if abs(-f/df) < 1e-10      %Convergence criteria for Newton's method
123
124           break;
125
126       end
127
128   end
129
130   %Calculate concentrations of all species with determined [H+]
131
132   OH_conc = Kw_conc/H_conc;
133   HCO3_conc = Ka1_conc*CO2_conc/H_conc;
134   CO3_conc = Ka1_conc*Ka2_conc*CO2_conc/H_conc^2;
135   pH = -log10(a_H*H_conc);
136
137   IonS_old = IonS;               %Store current Ionic strength value
138
139   %Output vector
140   y = [CO2_conc; HCO3_conc; CO3_conc; OH_conc];
141
142   end
143
144   end
```

Appendix 8: Two-film theory for gas-liquid transfer

In our work, CO_2 gas is introduced into the catholyte solution through gas bubbling. To model the mass transfer of CO_2 from the gas bubbles into the catholyte solution, the two-film theory by Lewis and Whitman [251] is applied. Basically, the two-film theory states that the resistance to gas-liquid transfer is encountered at the gas and liquid thin films close to the gas-liquid interface as depicted in Figure A8.1. At the gas-liquid interface, the model assumes that the interfacial concentrations are always in equilibrium; hence the interface itself offers zero resistance. The thin films adjacent to the interface are assumed to be stagnant; hence, mass transfer through the films is governed solely by molecular diffusion, which permits the concentration gradients to be approximated as linear at steady-state.

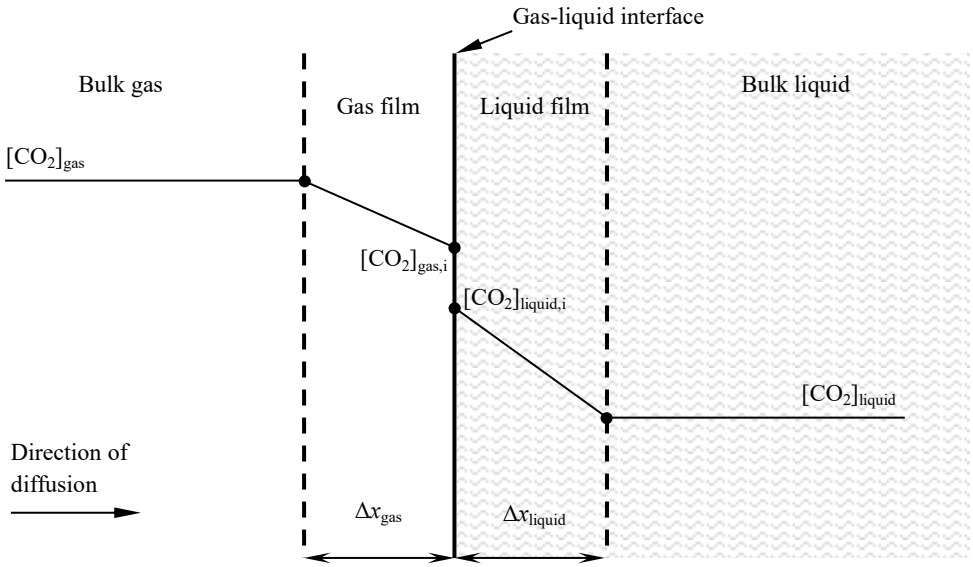

Figure A8.1: Schematic of the gas-liquid interface during CO_2 saturation by gas bubbling based on the two-film model.

By invoking Fick's first law, equation (A8.1), and approximating the concentration gradients as linear, the mass transfer or flux of CO_2 through the films can be written as equations (A8.2) and (A8.3) for the gas and liquid films respectively.

$$J_{CO_2} = -D_{CO_2}\frac{\partial[CO_2]}{\partial x} \qquad \text{E(A8.1)}$$

$$J_{CO_2} = \frac{D_{CO_2,gas}}{\Delta x_{gas}}\left([CO_2]_{gas} - [CO_2]_{gas,i}\right) = k_G\left([CO_2]_{gas} - [CO_2]_{gas,i}\right) \qquad \text{E(A8.2)}$$

$$J_{CO_2} = \frac{D_{CO_2,liquid}}{\Delta x_{liquid}}\left([CO_2]_{liquid,i} - [CO_2]_{liquid}\right) = k_L\left([CO_2]_{liquid,i} - [CO_2]_{liquid}\right) \qquad \text{E(A8.3)}$$

where			
	J	Molar mass flux	mol m^{-2} s^{-1}
	D	Diffusion coefficient	m^2 s^{-1}
	$[CO_2]$	CO_2 concentration	mol m^{-3}
	Δx	Film thickness	m

	k	Mass transfer coefficient	$m\ s^{-1}$

Experimentally, it is difficult to directly measure the interfacial concentrations; therefore, it would be more convenient if the flux can be expressed in terms of the bulk concentrations. Hence, equation (A8.4) is defined, where K_M is the overall mass transfer coefficient, and $[CO_2]_{eq}$ is the concentration of CO_2 in the liquid phase when in equilibrium with the bulk gas phase. The assumption that the interfacial concentrations are always in equilibrium allows them to be related through Henry's law, written as equation (A8.5). Similarly, $[CO_2]_{eq}$ is also related to $[CO_2]_{liquid}$ through Henry's law as shown in equation (A8.6).

$$J_{CO_2} = K_M\left([CO_2]_{eq} - [CO_2]_{liquid}\right) \quad \text{E(A8.4)}$$

$$[CO_2]_{gas,i} = H_c[CO_2]_{liquid,i} \quad \text{E(A8.5)}$$

$$[CO_2]_{gas} = H_c[CO_2]_{eq} \quad \text{E(A8.6)}$$

where	K_M	Overall mass transfer coefficient	$m\ s^{-1}$
	H_c	Henry's constant	[-] (molar ratio)

An expression for K_M can be obtained by substituting the interfacial concentrations in equation (A8.5) with relations from equations (A8.2) and (A8.3), as shown below:

From equations (A8.2) and (A8.3):

$$[CO_2]_{gas,i} = [CO_2]_{gas} - \frac{J_{CO_2}}{k_G} \quad \text{E(A8.7)}$$

$$[CO_2]_{liquid,i} = [CO_2]_{liquid} + \frac{J_{CO_2}}{k_L} \quad \text{E(A8.8)}$$

Substitute them into equation (A8.5) and rearranging:

$$[CO_2]_{gas} - \frac{J_{CO_2}}{k_G} = H_c\left([CO_2]_{liquid} + \frac{J_{CO_2}}{k_L}\right) \quad \text{E(A8.9)}$$

$$\frac{\frac{[CO_2]_{gas}}{H_c} - [CO_2]_{liquid}}{J_{CO_2}} = \frac{1}{k_L} + \frac{1}{H_c k_G} \quad \text{E(A8.10)}$$

Inserting equations (A8.4) and (A8.6) gives:

$$\frac{[CO_2]_{eq} - [CO_2]_{liquid}}{J_{CO_2}} = \frac{1}{k_L} + \frac{1}{H_c k_G} \quad \text{E(A8.11)}$$

$$\frac{1}{K_M} = \frac{1}{k_L} + \frac{1}{H_c k_G} \quad \text{E(A8.12)}$$

Hence, equation (A8.12) can be viewed as a resistance expression, where $1/K_M$ represents the total resistance to mass transfer, and is equal to the sum of the resistances in the liquid film ($1/k_L$) and the gas film ($1/k_G$). For gases with poor solubility, H_c is much larger than unity. In most cases, k_G is

typically larger than k_L since the diffusion coefficients are much greater in gases than in liquids. Additionally, the gas film thickness is usually smaller than the liquid films. These conditions suggest that the $1/(H_c k_G)$ term in equation (A8.12) is negligible in comparison to the $1/k_L$ term and hence permits the further simplification to equation (A8.13).

$$\frac{1}{K_M} = \frac{1}{k_L} \qquad \text{E(A8.13)}$$

This implies that for sparingly soluble gases, such as CO_2, the gas-liquid transfer is essentially controlled by the liquid-side film, as opposed to highly soluble gases such as ammonia.

Appendix 9: MATLAB script for bulk electrolyte model

The following is a MATLAB script written to simulate the changes in the concentrations of species in the bulk electrolyte during CO_2 reduction electrolysis as outlined in section 4.2.

```
%=========================================================================
%CO2 REDUCTION BULK ELECTROLYTE MODEL
%AUTHOR: CALVIN LIM
%LAST MODIFIED: 13/MAY/2017
%=========================================================================

clear all
clf
clc

load current_data; %Load current efficiency data

%A column vector within current_data should contain the following
%information
%current_data(1,:) = Current density in mA/cm2
%current_data(3:8,:) = Current efficiencies in % in order from CH4, CO,
%C2H4,C2H6 and HCOO-. Current efficiency of HCOO- is estimated as the
%balance current efficiency (100% - sum of current efficiency of other
%products)
%current_data(10,:) = Time per GC measurement in seconds. Typically 900 s.
%current_data(11,:) = %CO2 in inlet CO2 flow. Typically 100%.
%current_data(12,:) = RCE rotation rate in rpm

global K eq_conc_CO2 I K_conc_change CO2_consump OH_form

K = 3.25e-03;  %Fitted beta value, 1/s
N = 41;        %Number of simulation runs
K_conc = 200;  %Initial concentration of K+, mol/m3

Faraday = 96485;    %Faraday constant, C per mol_e
z_CH4 = 8;          %mol of electrons required per mol of product
z_CO = 2;
z_C2H4 = 12;
z_C2H6 = 14;
z_H2 = 2;
z_HCOO = 2;
cath_vol = 0.035;   %catholyte volume, L

%Loop to solve for bulk electrolyte concentrations using MATLAB's ode15s
%solver
for I = 1:N

%Obtain equilibrium concentrations of bulk KHCO3 electrolyte

eq_conc = CO2_equib(current_data(11,I), K_conc/1000);

%Equilibrium CO2 concentration of bulk KHCO3 electrolyte
eq_conc_CO2 = eq_conc(1)*1000;

%Electrochemical reactions, i.e. source terms
current = current_data(1,I)/1000;   %Current, A
```

```
52
53  current_eff = current_data(3:8,I);
54  eff_CH4 = current_eff(1);           %Current efficiencies, %
55  eff_CO = current_eff(2);
56  eff_C2H4 = current_eff(3);
57  eff_C2H6 = current_eff(4);
58  eff_H2 = current_eff(5);
59  eff_HCOO = current_eff(6);
60
61  %Source terms
62  CO2_consump = (abs(current)/Faraday)*(eff_HCOO/z_HCOO + eff_CO/z_CO +
63  eff_CH4/z_CH4 + 2*(eff_C2H4/z_C2H4) + 2*(eff_C2H6/z_C2H6))/(cath_vol/1000);
64  OH_form = (abs(current)/Faraday)*(eff_HCOO/z_HCOO + 2*(eff_CO/z_CO) +
65  8*(eff_CH4/z_CH4) + 12*(eff_C2H4/z_C2H4) + 14*(eff_C2H6/z_C2H6) +
66  2*(eff_H2/z_H2))/(cath_vol/1000);
67
68  %Change in [K+] due to transfer from anolyte to catholyte
69  K_conc_change = (abs(current)/Faraday)/(cath_vol/1000);
70
71  %Inital concentrations [CO2, HCO3, CO3, OH, K+], units in mol/m^3.
72  %Note that [OH] cannot be zero.
73
74  if I == 1
75      initial_cond = [eq_conc*1000; K_conc];
76  else
77      initial_cond = y(end,:)';
78  end
79
80  %ode15s solver
81  options = odeset('RelTol', 1e-10, 'AbsTol',1e-14,'InitialStep',1e-2);
82
83  %Simulation duration, s
84  tspan = current_data(10,I);
85
86  if I == 1
87  [time,y] = ode15s(@CO2_bulk_ODEs, linspace(0,tspan,tspan+1) , initial_cond,
88  options);
89  else
90  [time2,y2] = ode15s(@CO2_bulk_ODEs, linspace(0,tspan,tspan+1) ,
91  initial_cond, options);
92
93  %Storing results as vector time and y
94  time(size(time)+1 : size(time)+size(time2(2:end))) = time(end) +
95  time2(2:end);
96  y(size(y,1)+1 : size(y,1)+size(y2(2:end,:,:),1) ,:,:) = y2(2:end,:,:);
97
98  end
99
100 %Updating K_conc value
101 K_conc = y(end,5);
102
103 end
104
105 %Estimating pH using water ionization equilibrium with ionic strength
106 %correction.
107
108 H_conc = 10^-14./(y(:,4)/1000); %Concentration of H+, mol/L
109
```

```
%Iterative loop to calculate H_conc
for J = 1:100

%Ionic Strength, mol/L
Ionic = 0.5*(y(:,5) + H_conc*1000 + y(:,2) + 2^2*y(:,3)+ y(:,4))/1000;

%Activity coefficient of OH. Similar to f_H since both have charge z = 1;
f_OH = 10.^(-0.5*1^2*((sqrt(Ionic)./(1+sqrt(Ionic))-0.2*Ionic)));
H_conc = 10^-14./(f_OH.^2.*y(:,4)/1000);

end

%Calculating pH
pH = 14 + log10(f_OH) + log10(y(:,4)/1000);

%PLOTTING=========================================================================

subplot(2,2,1)
plot(time/3600, pH,'k-')
xlim([0 14])
xlabel('Time [hours]')
ylabel('pH')
legend('pH - model','Location','East')

subplot(2,2,2)
plot(time/3600, y(:,1)/1000,'-')
xlim([0 14])
xlabel('Time [hours]')
ylabel('Conc [mol/L]')
legend('CO2','Location','East')

subplot(2,2,3)
plot(time/3600, log10(y(:,2)/1000),'b-', time/3600, log10(y(:,4)/1000),'r-
', time/3600, log10(y(:,3)/1000), 'g-')
xlim([0 14])
ylim([-10 0])
xlabel('Time [hours]')
ylabel('log(Conc)')
legend('HCO3', 'OH', 'CO3', 'Location', 'southeast')

subplot(2,2,4)
plot(time/3600, y(:,2)/1000,'b-', time/3600, y(:,4)/1000,'r-', time/3600,
y(:,3)/1000, 'g-')
xlim([0 14])
xlabel('Time [hours]')
ylabel('Conc [mol/L]')
legend('HCO3', 'OH', 'CO3','Location', 'east')

display(pH(end),'pH(end)')
```

The following is the MATLAB function `CO2_bulk_ODEs.m` that contains the ODEs.

```
function dydt = CO2_bulk_ODEs(x,y)

global  K eq_conc_CO2 I K_conc_change CO2_consump OH_form

%Rate constants for reactions
%k_1r and k_2r depends slightly on [K+] when made consistent with
%equilibrium constants.
%The polynomial fits are purely empirical and used %to aid in coding.
Z = y(5)/1000;
k_1f = 5.93;         %m3/(mol*s)
k_1r = (6.52149*10^-06)*Z^2 - 3.19874*10^-05*Z + 1.33903*10^-04; %1/s
k_2f = 1*10^5;       %m3/(mol*s)
k_2r = -31560*Z^5 + 105153*Z^4 - 138484*Z^3 + 93684*Z^2 - 33501*Z + 15531;
%1/s

%Estimating pH using water ionization equilibrium with ionic strength
%correction.
H_conc = 10^-14/(y(4)/1000);  %Concentration of H+, mol/L

%Iterative loop to calculate H_conc
for J = 1:100

%Ionic Strength, mol/L
Ionic = 0.5*(y(5) + H_conc*1000 + y(2) + 2^2*y(3) + y(4))/1000;

%Activity coefficient of OH. Similar to f_H since both have charge z = 1;
f_OH = 10.^(-0.5*1^2*((sqrt(Ionic)./(1+sqrt(Ionic))-0.2*Ionic)));
H_conc = 10^-14/(f_OH^2*y(4)/1000);
end

C_bal_OH = y(5) + H_conc*1000 - y(2) - 2*y(3);  %Charge balance

%ODEs
%y = [CO2, HCO3, CO3, OH, K+], concentration in mol/m3
r1 = K*(eq_conc_CO2 - y(1)) - y(1)*C_bal_OH*k_1f + y(2)*k_1r - CO2_consump;
r2 = y(1)*C_bal_OH*k_1f - y(2)*k_1r - y(2)*C_bal_OH*k_2f + y(3)*k_2r;
r3 = y(2)*C_bal_OH*k_2f - y(3)*k_2r;
r4 = -y(1)*y(4)*k_1f + y(2)*k_1r - y(2)*y(4)*k_2f + y(3)*k_2r + OH_form;
r5 = K_conc_change;

dydt = [r1;
        r2;
        r3;
        r4;
        r5];
end
```

Appendix 10: MATLAB script for finite difference model

The following is a MATLAB script written to estimate the interfacial concentrations at the electrode surface and their changes with CO_2 reduction electrolysis time as outlined in section Finite difference model4.3.

```
%=========================================================================
%CO2 REDUCTION FINITE DIFFERENCE MODEL
%AUTHOR: CALVIN LIM
%LAST MODIFIED: 19/MAY/2017
%=========================================================================

clear all
clc

load current_data;
load bulk_data;

%bulk_data is an array that contains the bulk electrolyte concentrations
%with time obtained from simulation using the bulk electrolyte model
%A row vector within bulk_data should contain the following information:
%bulk_data(:,1) = electrolysis time in seconds
%bulk_data(:,2) = concentration of CO2, mol/L
%bulk_data(:,3) = concentration of HCO3-, mol/L
%bulk_data(:,4) = concentration of CO3_2-, mol/L
%bulk_data(:,5) = concentration of OH-, mol/L
%bulk_data(:,6) = concentration of K+, mol/L

density = 1000;             %Water density, kg/m3
F = 96485;                  %Faraday constanbt, C per mol_e-
vis_water = 0.891;          %Water viscosity at 25 C, mPa.s
area = 3*10^-4;             %Electrode area, m2
vol_cath = 0.4;             %Volume of catholyte, L
d_cyl = 0.015;              %RCE outer diameter, m

N = 60;                         %Number of simulation runs
K_conc_ini = bulk_data(1,6);    %Initial concentration of K+, mol/L
x_points = 100;                 %Number of grids in x direction

master_sol = zeros(1,x_points,4);
K_conc = zeros(1,1);
time = zeros(1,1);

for I = 1:N

%Extracting bulk concentrations, i.e. boundary condition at x = 0
index = find(bulk_data(:,1)==time(end));

CO2_eq = bulk_data(index,2);
HCO3_eq = bulk_data(index,3);
CO3_eq = bulk_data(index,4);
OH_eq = bulk_data(index,5);
K_eq = bulk_data(index,6);

bulk_conc = 1000*[CO2_eq; HCO3_eq; CO3_eq; OH_eq];  %units mol/m3

```

```
%Diffusion coefficients
    %Viscosity of electrolyte. Purely empirical polynomial based on data
    %from Gupta
vis_elect = 0.01686*K_eq^2 + 0.12490*K_eq + 1.00195;
%Correcting diffusion coefficients based on Stokes-Eistein equation
D_CO2 = (1.91*10^-9)*vis_water/vis_elect;     %units  m2/s
D_HCO3 = (1.19*10^-9)*vis_water/vis_elect;
D_CO3 = (9.23*10^-10)*vis_water/vis_elect;
D_OH = (5.27*10^-9)*vis_water/vis_elect;

diff_coeff = [D_CO2; D_HCO3; D_CO3; D_OH];

%Boundary layer thickness, units m

%Overall mass transfer coefficienct using equation by Eisenberg
RPM = current_data(12,I);   %Rotation rate in rpm
Km_CO2 = 0.01*(d_cyl^0.4)*((vis_elect/1000)/density)^(-
0.344)*(D_CO2^0.644)*(RPM^0.7);
Km_HCO3 = 0.01*(d_cyl^0.4)*((vis_elect/1000)/density)^(-
0.344)*(D_HCO3^0.644)*(RPM^0.7);
Km_CO3 = 0.01*(d_cyl^0.4)*((vis_elect/1000)/density)^(-
0.344)*(D_CO3^0.644)*(RPM^0.7);
Km_OH = 0.01*(d_cyl^0.4)*((vis_elect/1000)/density)^(-
0.344)*(D_OH^0.644)*(RPM^0.7);

%Boundary layer thickness
b_CO2 = D_CO2/Km_CO2;          %units m
b_HCO3 = D_HCO3/Km_HCO3;
b_CO3 = D_CO3/Km_CO3;
b_OH = D_OH/Km_OH;

%Average boundary layer thickness, units m
b = mean([b_CO2,b_HCO3,b_CO3,b_OH]);

%Mesh parameters
t = current_data(10,I);          %Total time per run, units s
t_points = t+1;
tspan = linspace(0,t,t_points);
xmesh = linspace(0,b,x_points);
mesh_data = [b,x_points,t,t_points];

%Extracting current density and efficiencies
current_density = abs(current_data(1,I)/1000)/area;    %units A/m2
current_eff = current_data(3:8,I);

%Specifiying initial conditions

    if I == 1

        initial_cond = 1000*[CO2_eq; HCO3_eq; CO3_eq; OH_eq];
        J = size(master_sol,1) - 1;

    else

        clear initial_cond
        initial_cond(1,:) = sol(end,:,1);
        initial_cond(2,:) = sol(end,:,2);
        initial_cond(3,:) = sol(end,:,3);
        initial_cond(4,:) = sol(end,:,4);
```

```
110             J = size(master_sol,1);
111
112         end
113
114         sol = PDE_solver(bulk_conc, diff_coeff, initial_cond, current_density,
115     current_eff, mesh_data, I, K_eq);
116
117         if I == 1
118             master_sol(J+1:J+size(sol,1),:,:) = sol;
119             time(J+1:J+size(sol,1)) = tspan;
120             K_conc(J+1:J+size(sol,1)) = K_conc_ini +
121     t*(current_data(1,I)/1000)*(1/F)/vol_cath;
122
123         else
124             master_sol(J+1:J+size(sol,1)-1,:,:) = sol(2:end,:,:);
125             time(J+1:J+size(sol,1)-1) = tspan(2:end) + time(end);
126             K_conc(J+1:J+size(sol,1)-1) = K_conc(end) +
127     t*(current_data(1,I)/1000)*(1/F)/vol_cath;
128
129         end
130
131     end
132
133     %Extracting results from solution matrix master_sol
134     CO2_conc = master_sol(:,:,1)/1000;
135     HCO3_conc = master_sol(:,:,2)/1000;
136     CO3_conc = master_sol(:,:,3)/1000;
137     OH_conc = master_sol(:,:,4)/1000;
138
139     %Estimating pH using water ionization equilibrium with ionic strength
140     %correction.
141     H_conc = 10^-14./(OH_conc);
142
143     %Iterative loop to calculate H_conc
144     for J = 1:100
145
146     %Ionic Strength, mol/L
147     Ionic = bsxfun(@plus,0.5*(K_conc)',0.5*(H_conc + HCO3_conc + 2^2*CO3_conc +
148     OH_conc));
149
150     %Activity coefficient of OH. Similar to f_H since both have charge z = 1;
151     f_OH = 10.^(-0.5*1^2*((sqrt(Ionic)./(1+sqrt(Ionic))-0.2*Ionic)));
152     H_conc = 10^-14./(f_OH.^2.*OH_conc);
153
154     end
155
156     pH = 14 + log10(f_OH) + log10(OH_conc);
157
158     %Plotting
159     figure
160     surf(xmesh,time,pH)
161     title('pH')
162     xlabel('Distance, m')
163     ylabel('Time, s')
164
165     figure
166     surf(xmesh,time,CO2_conc)
167     title('CO2 conc')
```

```
xlabel('Distance, m')
ylabel('Time, s')

figure
surf(xmesh,time,HCO3_conc)
title('HCO3 conc')
xlabel('Distance, m')
ylabel('Time, s')

figure
surf(xmesh,time,CO3_conc)
title('CO3 conc')
xlabel('Distance, m')
ylabel('Time, s')
```

The following are MATLAB functions under the function file `PDE_solver.m` that contains the required functions for solving the PDEs using MATLAB's `pdefun` solver.

```
function  sol = PDE_solver(bulk_conc, diff_coeff, initial_cond,
current_density, current_eff, mesh_data, counter, K_eq)

global Diff_coeff k_1f k_1r k_2f k_2r Initial_cond CO2_consump OH_form
Counter Mesh_data Bulk_conc

Counter = counter;
Initial_cond = initial_cond;
Mesh_data = mesh_data;
Bulk_conc = bulk_conc;
Diff_coeff = diff_coeff;

%Rate constants for reactions
%k_1r and k_2r depends slightly on [K+] when made consistent with
%equilibrium constants.
%The polynomial fits are purely empirical and used %to aid in coding.

k_1f = 5.93;            %m3/(mol.s)
k_1r = (6.52149*10^-06)*K_eq^2 - 3.19874*10^-05*K_eq + 1.33903*10^-04; %1/s
k_2f = 1*10^5;          %m3/(mol.s)
k_2r = -31560*K_eq^5 + 105153*K_eq^4 - 138484*K_eq^3 + 93684*K_eq^2 -
33501*K_eq + 15531; %1/s

%Electrode surface source terms
J = current_density;    %Current, A/m2
F = 96485;              %Faraday constant [=] C/mol_e
z_CH4 = 8;              %Mol of electrons per mol of product
z_CO = 2;
z_C2H4 = 12;
z_C2H6 = 14;
z_H2 = 2;
z_HCOO = 2;

eff_CH4 = current_eff(1);   %Current efficiencies
eff_CO = current_eff(2);
eff_C2H4 = current_eff(3);
eff_C2H6 = current_eff(4);
eff_H2 = current_eff(5);
eff_HCOO = current_eff(6);

```

```
CO2_consump = (J/F)*(eff_HCOO/z_HCOO + eff_CO/z_CO + eff_CH4/z_CH4 +
2*(eff_C2H4/z_C2H4) + 2*(eff_C2H6/z_C2H6));
OH_form = (J/F)*(eff_HCOO/z_HCOO + 2*(eff_CO/z_CO) + 8*(eff_CH4/z_CH4) +
12*(eff_C2H4/z_C2H4) + 14*(eff_C2H6/z_C2H6) + 2*(eff_H2/z_H2));

m = 0;
xmesh = linspace(0,Mesh_data(1),Mesh_data(2));
tspan = linspace(0,Mesh_data(3),Mesh_data(4));

%Reader is advised to consult MATLAB's PDE solver method for use of the
pdepe
%solver
sol = pdepe(m,@pdefun,@icfun,@bcfun,xmesh,tspan);

end

function [c,f,s] = pdefun(x,t,u,DuDx)

global Diff_coeff k_1f k_1r k_2f k_2r Initial_cond CO2_consump OH_form
Counter Mesh_data Bulk_conc

c = ones(4,1);
f = Diff_coeff.*DuDx;
s_CO2 = -u(1)*u(4)*k_1f + u(2)*k_1r;
s_HCO3 = u(1)*u(4)*k_1f - u(2)*k_1r - u(2)*u(4)*k_2f + u(3)*k_2r;
s_CO3 = u(2)*u(4)*k_2f - u(3)*k_2r;
s_OH = -u(1)*u(4)*k_1f + u(2)*k_1r - u(2)*u(4)*k_2f + u(3)*k_2r;
s = [s_CO2; s_HCO3; s_CO3; s_OH];

end

function u0 = icfun(x)

global Diff_coeff k_1f k_1r k_2f k_2r Initial_cond CO2_consump OH_form
Counter Mesh_data Bulk_conc

if Counter == 1;
    u0 = Initial_cond;
else
    x_spacing = Mesh_data(1)/(Mesh_data(2)-1);
    index = int16(x/x_spacing) + 1;
    u0 = Initial_cond(:,index);
end
end

function [p_left,q_left,p_right,q_right] =
bcfun(x_left,u_left,x_right,u_right,t)

global Diff_coeff k_1f k_1r k_2f k_2r Initial_cond CO2_consump OH_form
Counter Mesh_data Bulk_conc

p_left = u_left - Bulk_conc;
q_left = zeros(4,1);
p_right = [CO2_consump; 0; 0; -OH_form];
q_right = ones(4,1);

end
```

Appendix 11: CO_2 reduction on polycrystalline Cu electrodes with sputter coated TiO_2 layers

The following summarises the experimental results of electrochemical CO_2 reduction on polycrystalline Cu electrodes with sputter coated TiO_2 layers.

The conversion of CO_2 to hydrocarbons such as CO and CH_4 can be achieved via electrochemical reduction on Cu electrodes, which amongst other metals studied, is shown to be unique in terms of its ability to reduce CO_2 at much higher efficiencies. In this work, the reduction process is carried out at constant current in an aqueous $KHCO_3$ solution saturated with CO_2. Continuous monitoring of the gaseous products is carried out using gas chromatography at regular intervals, while products in the liquid phase are measured post reaction using HPLC. The results are presented as current efficiencies with time, which is the fraction of the total current applied utilised to produce the various reduction products as the reaction progresses. As it is suspected that methanol, a high density hydrocarbon, could be produced at composite metal/oxide cathodes, the influence of thin TiO_2 coatings on copper on CO_2 reduction behaviour was examined.

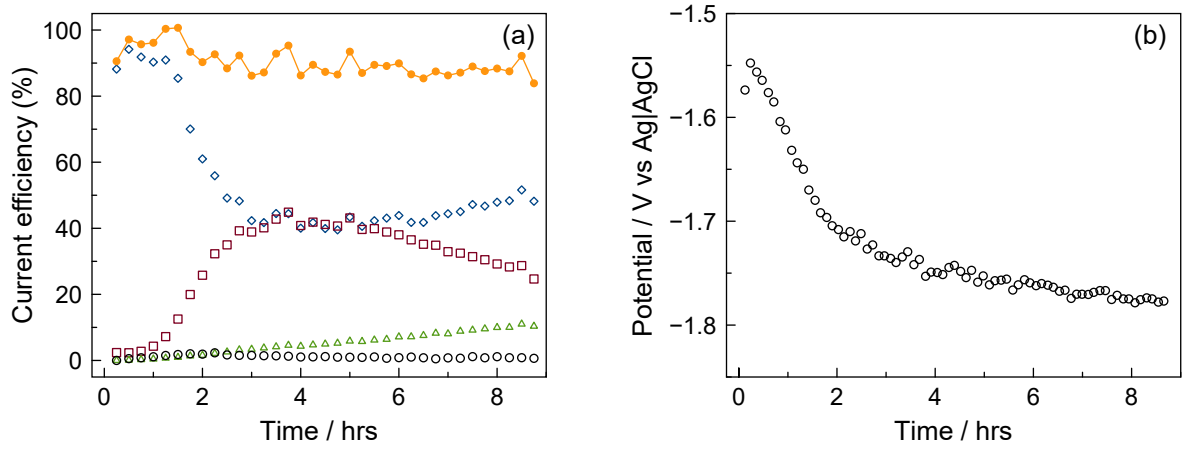

Figure A11.1: Typical (a) current efficiencies and (b) potential with time for electrochemical CO_2 reduction on polished polycrystalline Cu in 0.2 M $KHCO_3$ at −5 mA cm^{-2}. Legend for (a): H_2 (diamonds), CH_4 (squares), CO (triangles), C_2H_4 (circles), total gaseous current efficiency (filled circles with lines).

A representative result of current efficiencies with time of CO_2 reduction on a mirror polished polycrystalline Cu electrode is presented in Figure A11.1. High efficiency for H_2 evolution (about 90%) is usually achieved during the first hour of the experiment, after which its efficiency gradually decreases over the next two hours to give way for the increase of CH_4 from less than 10% to approximately 40%, and small increases for CO and C_2H_4. It is not unusual for the efficiency of CH_4 to remain at its maximum for one to two hours, after which H_2 evolution gradually regains preference over CH_4 production. Current efficiency for CO typically increases gradually throughout the entire experiment although seldom going above 10%, while C_2H_4 exhibits a similar response as CH_4 but attaining its maximum efficiency, usually less than 5%, approximately two hours before CH_4. Gaseous products make up 80 to 90% of the total current efficiency, while detectable liquid products, formate and acetate, make up about 5 to 10%, leaving the unaccounted current efficiency to be about 5% which can be attributed to measurement errors, undetected products or both. Generally, the time-dependent changes in the CO_2 reduction activity and selectivity can be correlated with the electrode potential with time (Figure A11.1b), in accordance to the potential dependence of the CO_2 reduction

reaction. Additionally, electrode poisoning for example by the electrodeposition of trace metallic impurities or the accumulation of CO_2 reduction products or intermediates is also a major contributor to the changes in product selectivity.

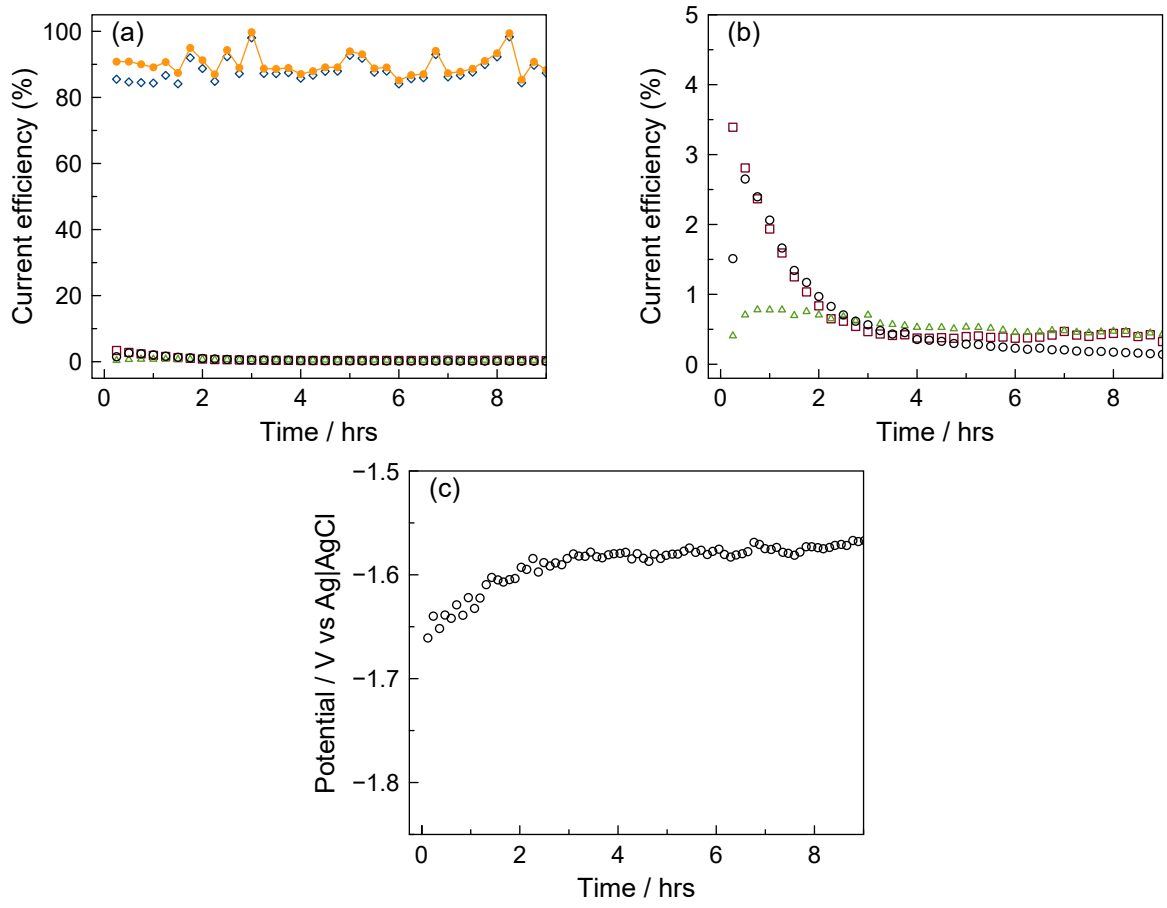

Figure A11.2: (a) current efficiencies and (c) potential with time for electrochemical CO_2 reduction on a polycrystalline Cu sputter coated with TiO_2 for 30 mins (corresponding to approximately 12 nm layer thickness) in 0.2 M $KHCO_3$ at −5 mA cm^{-2}. (b) is an enlargement of (a) to better display the current efficiency data for CH_4, CO and C_2H_4. Legend for (a): H_2 (diamonds), CH_4 (squares), CO (triangles), C_2H_4 (circles), total gaseous current efficiency (filled circles with lines).

Using the same experimental conditions, CO_2 reduction was performed on TiO_2 coated polycrystalline copper electrodes of various layer thicknesses (approximately 3, 6 and 12 nm, corresponding to 5, 20 and 30 mins of sputtering time) obtained using an ion beam sputtering system. All three electrodes delivered comparable results and is represented by that of the electrode with a 12 nm thick TiO_2 layer (Figure A11.2). H_2 evolution remained dominant at high current efficiencies of more than 80% throughout, while all other gaseous products achieved its maximum, suppressed to less than 4%, within the first hour, after which a gradual decay is seen. Formate makes up about 8% of the current efficiency, leaving the unaccounted efficiency to be about 2%. The electrode potential in this case is more positive than −1.6 V after 2 hours of electrolysis, and is approximately 150 mV less cathodic than that of the polished Cu without any TiO_2 coating. This shows that the addition of the TiO_2 coating greatly promotes the H_2 reaction at the expense of CO_2 reduction. Furthermore, given that the electrode potential is much more positive than the onset potentials for CO_2 reduction on Cu, the low current efficiencies toward CO_2 reduction are expected.

SEM micrographs of the electrodes tested (specifically the electrodes with the 6 nm and 12 nm TiO_2 layer) revealed that the sputtered TiO_2 layer may not be stable enough for electrolysis. This is suggested by a multitude of circular regions observed on the electrode surface exposed to electrolysis, where the TiO_2 layer seemed to be "pushed out" by bubbles formed during the experiment (Figure A11.3). These circular regions were not observed on the electrode surface not exposed to electrolysis (Figure A11.4). SEM imaging did not reveal much detail on the electrode with the thinnest layer of TiO_2 (3 nm).

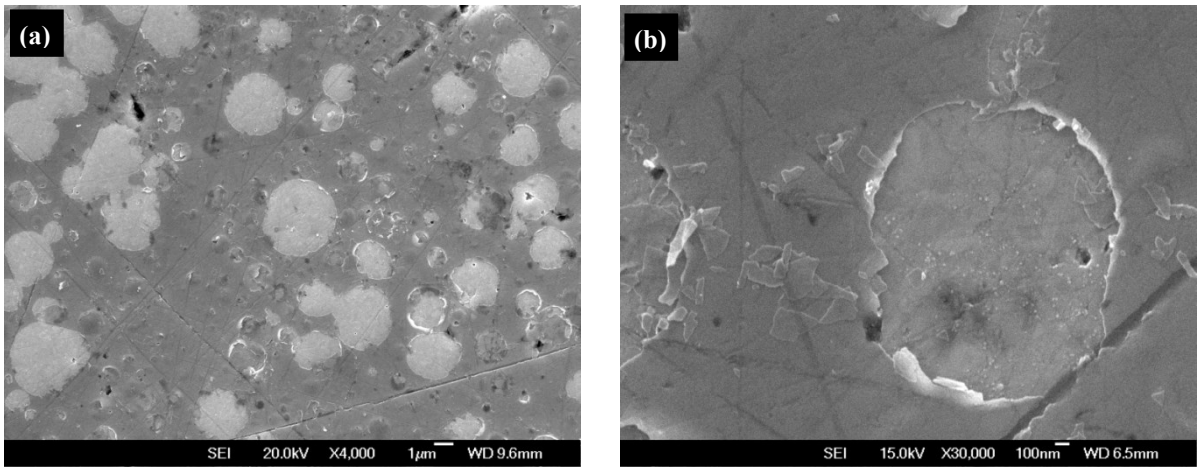

Figure A11.3: SEM images of the TiO_2 coated Cu electrode surface (30 mins sputtering time) after CO_2 reduction electrolysis. (a) ×4000 and (b) ×30,000 magnification.

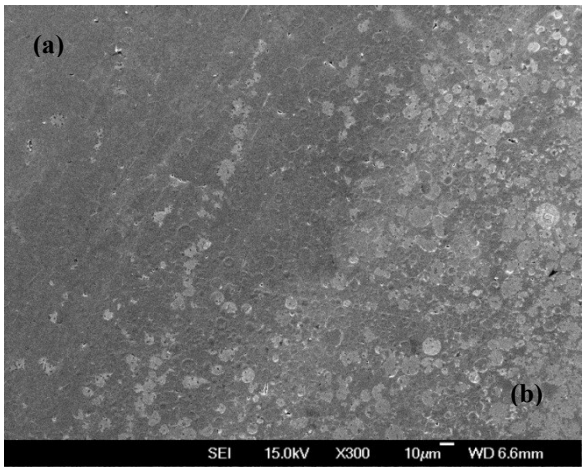

Figure A11.4: SEM image of the TiO_2 coated Cu electrode surface (30 mins sputtering time) after CO_2 reduction electrolysis comparing the surface topography where the electrode was (a) not exposed to electrolysis and (b) exposed to electrolysis.

From the experimental results obtained, it can be concluded that the TiO_2 coatings deposited on Cu electrodes by sputtering are mechanically unstable during electrolysis as highlighted by the SEM micrographs. It is also concluded that a TiO_2 layer thickness of as thin as 3 nm (5 mins sputtering time) can significantly inhibit the CO_2 reduction activity in favour of the H_2 evolution reaction, and increasing the layer thickness to 6 and 12 nm has no major effect in the inhibition already observed.

We thank and acknowledge Dr John Kennedy (GNS Science, New Zealand) for his generous assistance in preparing the sputtered TiO_2/Cu samples.

Appendix 12: Mechanical polishing of Ti discs

Ti is a much harder metal than Cu [252]. Hence, polishing Ti electrodes to a mirror finish is significantly more difficult and time consuming compared to Cu. Nevertheless, for all our experiments involving Ti discs, the discs were mechanically polished using SiC paper up to the P2000 grit (Figures A12.1a and A12.2a). However, an interesting observation was made when the Ti discs were re-polished after undergoing the typical cathodic conditions of CO_2 reduction electrolysis in our work. By solely using the SiC paper P2000 grit for re-polishing, it was observed that a much smoother surface than previously achieved can be obtained with relative ease (Figures A12.1b and A12.2b). This smoother surface is only seen on the electrode area that was exposed to electrolysis, suggesting an effect of the cathodic current on the surface structure of Ti, possibly relating to restructuring of crystal orientations similar to that observed for polycrystalline Cu under alkaline cathodic conditions [139, 140].

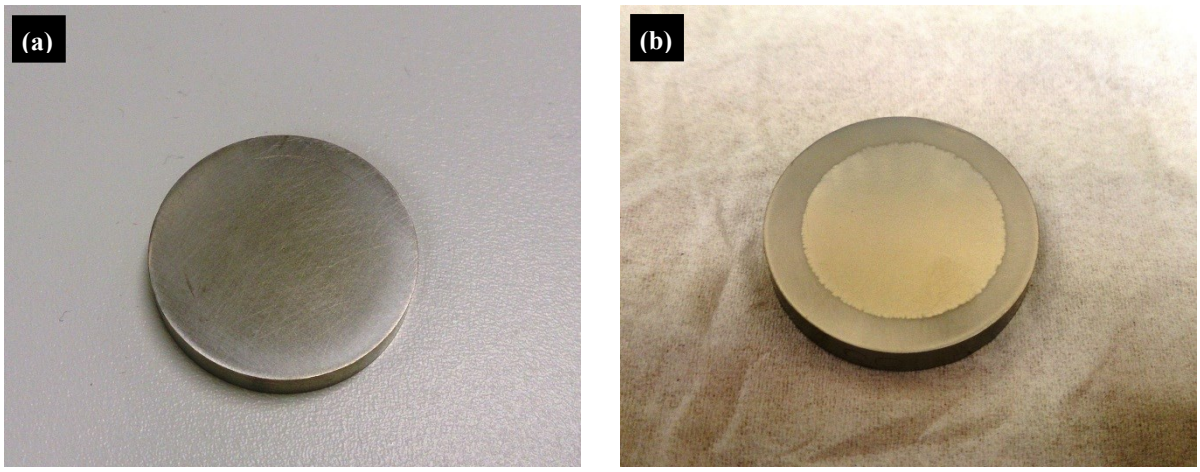

Figure A12.1: Ti disc surface as to the naked eye (a) after mechanical polishing with SiC paper up to the P2000 grit before undergoing CO_2 reduction electrolysis, and (b) after mechanical polishing solely with SiC paper P2000 grit after CO_2 reduction electrolysis. Note that for (b), a much smoother surface can be achieved on the area exposed to electrolysis.

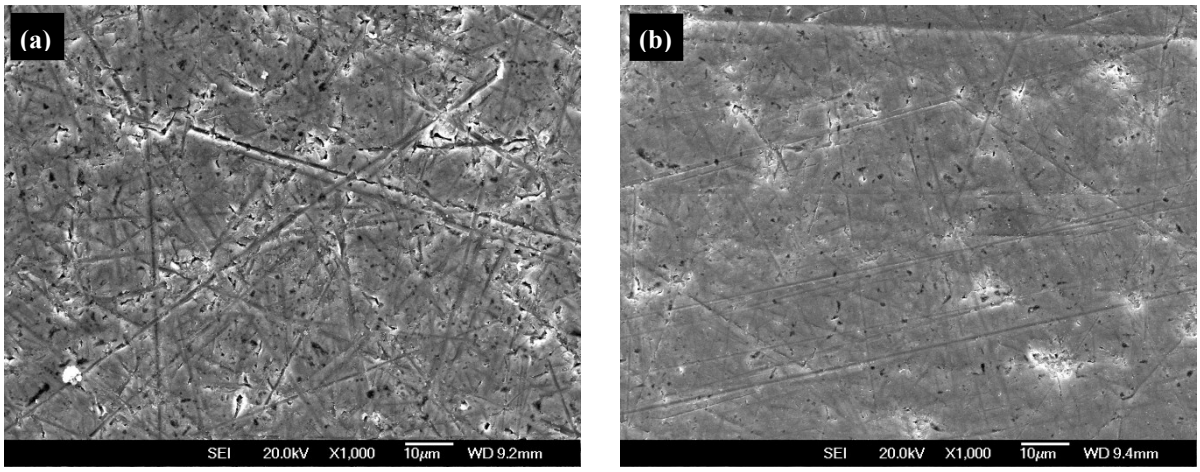

Figure A12.2: SEM images of the Ti disc surface (a) after mechanical polishing with SiC paper up to the P2000 grit before undergoing CO_2 reduction electrolysis, and (b) after mechanical polishing solely with SiC paper P2000 grit after CO_2 reduction electrolysis.

It is also observed that the Ti surface after mechanical polishing with SiC paper contains embedded SiC particles that have been inadvertently transferred during polishing (Figure A12.3), similar to the case for some of our polished Cu electrodes (see section 3.6). Our efforts to remove them by ultra-sonication have been unsuccessful. Based on our results on polished Cu electrodes, the influence of the embedded SiC particles on the electrocatalytic reduction of CO_2 is inconclusive.

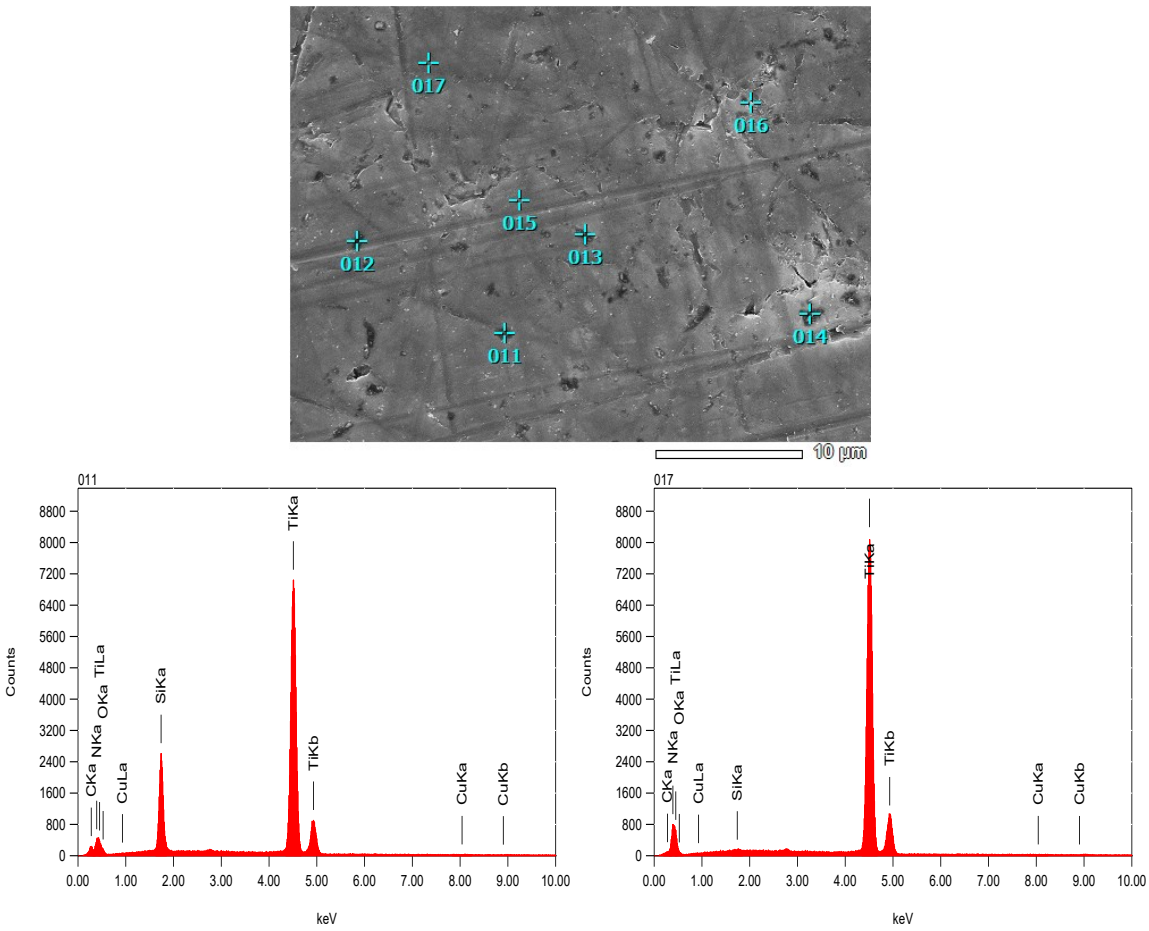

Figure A12.3: SEM and EDS analysis of the Ti surface after polishing with SiC paper. Points 011, 012, 013 and 014 show examples of the SiC particles, which is confirmed by EDS. EDS analysis on points 015, 016 and 017 do not show any SiC.

Appendix 13: High formate production on polycrystalline Cu

The following documents an unexpected but isolated result of a CO_2 reduction experiment on polished polycrystalline Cu where significantly high formate production rates (current efficiencies up to 34%) were observed.

The parameters and conditions for this particular experiment are identical to that of a typical constant current CO_2 reduction experiment on polished polycrystalline Cu, as detailed in section 5.2. Typically, the results conform to that given in Figure 5.1, however for this particular experiment, significant deviations were observed (Figure A13.1).

One major deviation is the more rapid deactivation of the CO_2 reduction reaction in favour toward H_2 evolution. Usually for our system, the deactivation process becomes evident after 4-5 hours of electrolysis, but in this case, CO_2 reduction activity began to deactivate rapidly after 1 hour. Interestingly, instead of maintaining dominant H_2 evolution activity, which usually occurs after the onset of deactivation, the H_2 current efficiency dramatically declined down to 50% at approximately 4-5 hours and remained so for the entire duration of electrolysis. As all CO_2 reduction products remained minimal after deactivation, the total gaseous current efficiency also dramatically declined, in step with H_2. This suggests that a large portion of the current is going toward the production of liquid products for time >4 hours. Indeed, liquid products analysis post-electrolysis revealed that the overall current efficiency toward formate production is unexpectedly high (34.4%), especially since for polycrystalline Cu, CH_4 and C_2H_4 are usually the dominant CO_2 reduction products (Table A13.1).

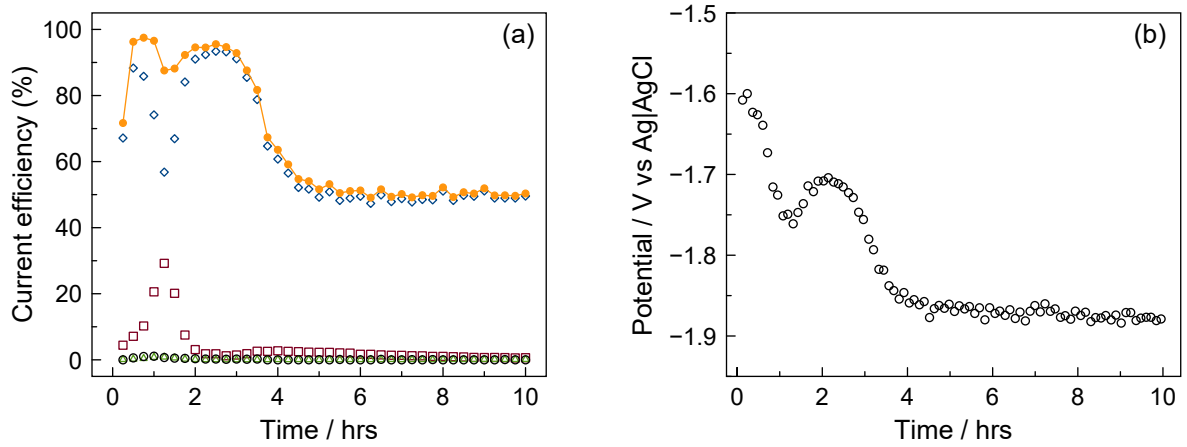

Figure A13.1: a) Current efficiencies of gaseous products and (b) electrode potential with time for a particular electrochemical CO_2 reduction experiment on polished polycrystalline Cu where the formate production rate is unusually high. Conditions: 0.2 M $KHCO_3$, −5 mA cm^{-2}. Legend for (a): H_2 (diamonds), CH_4 (squares), CO (triangles), C_2H_4 (circles), total gaseous current efficiency (filled circles with lines).

A possible explanation for this behaviour is the fact that the Cu electrode was heavily poisoned, likely by electrodeposition of heavy metal impurities like Pb, Fe or Zn. Pb is known to favour formate production, while Fe and Zn usually favours H_2 production (see section 2.2). However, there are occasional reports in the literature, like that of [41], where Zn was reported to produce formate with current efficiencies as high as 85% at −1.56 V vs SHE. Hence, it is quite possible that the Cu electrode for this particular experiment was heavily poisoned by Pb or Zn. As for the source of the

contamination, it remains a mystery, since ICP-MS analysis of our pre-electrolysed solutions usually confirms very low amounts of Pb (<1 ppb) and undetectable amounts of Zn (see Table 3.1).

Table A13.1: Overall current efficiencies of reduction products for long-term (10 hours) CO_2 reduction on polished polycrystalline Cu electrode. 0.2 M $KHCO_3$, −5 mA cm^{-2}, 10 ml min^{-1} CO_2 flow.

CO_2 reduction product	Current efficiency (%)	
	Typical results	Isolated results (Figure A13.1)
H_2	43.8	61.6
CO	1.6	0.1
CH_4	36.1	3.8
C_2H_4	0.7	0.2
C_2H_6	0.1	0.0
HCOOH	8.0	34.4
Total:	90.3	100.1

Appendix 14: Copyright permissions

Copyright license for Figure 2.5 and Figure 2.6:

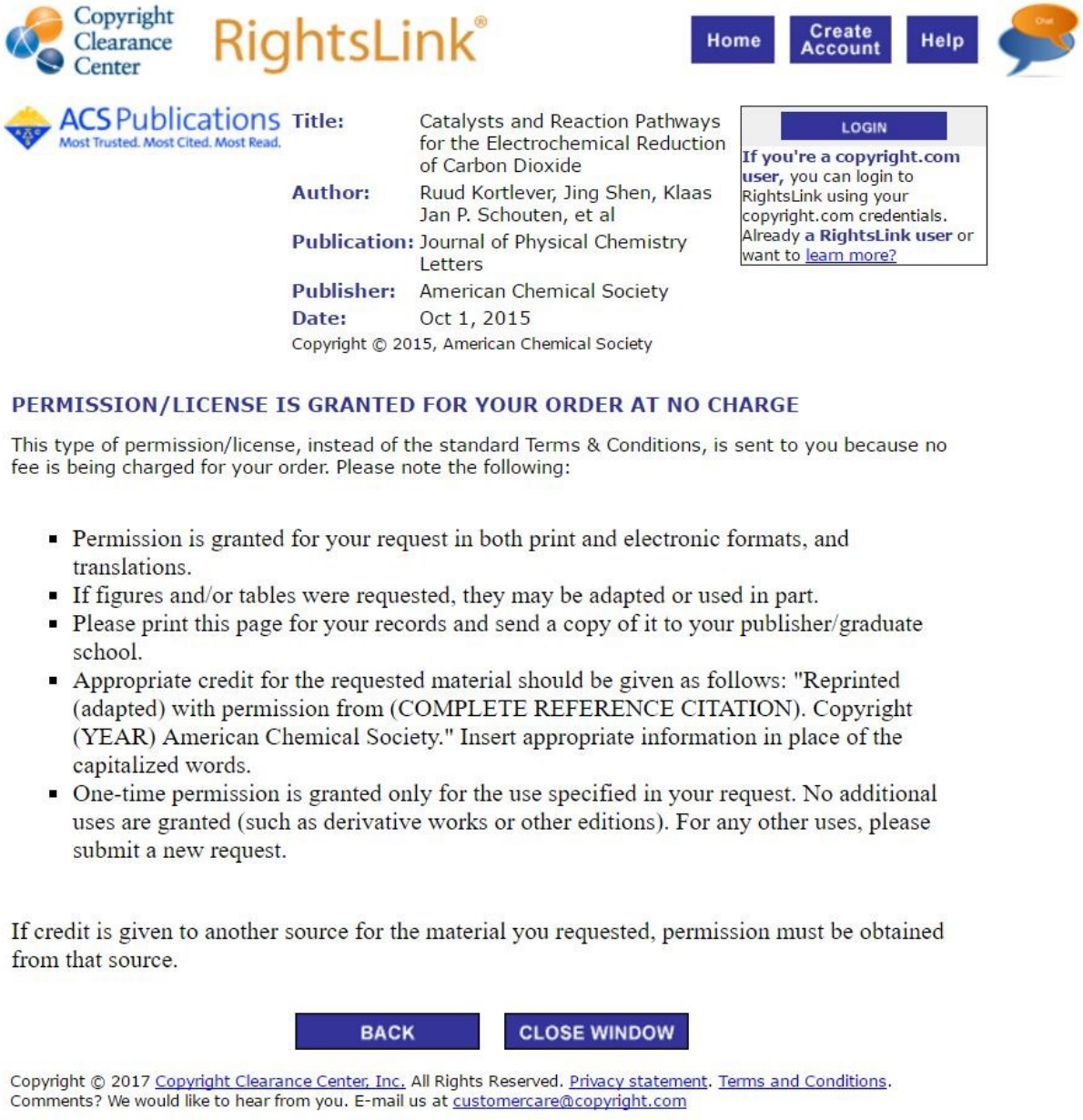

Copyright Clearance Center RightsLink®

Home | Create Account | Help

ACS Publications
Most Trusted. Most Cited. Most Read.

Title: Catalysts and Reaction Pathways for the Electrochemical Reduction of Carbon Dioxide
Author: Ruud Kortlever, Jing Shen, Klaas Jan P. Schouten, et al
Publication: Journal of Physical Chemistry Letters
Publisher: American Chemical Society
Date: Oct 1, 2015
Copyright © 2015, American Chemical Society

LOGIN
If you're a copyright.com user, you can login to RightsLink using your copyright.com credentials. Already **a RightsLink user** or want to learn more?

PERMISSION/LICENSE IS GRANTED FOR YOUR ORDER AT NO CHARGE

This type of permission/license, instead of the standard Terms & Conditions, is sent to you because no fee is being charged for your order. Please note the following:

- Permission is granted for your request in both print and electronic formats, and translations.
- If figures and/or tables were requested, they may be adapted or used in part.
- Please print this page for your records and send a copy of it to your publisher/graduate school.
- Appropriate credit for the requested material should be given as follows: "Reprinted (adapted) with permission from (COMPLETE REFERENCE CITATION). Copyright (YEAR) American Chemical Society." Insert appropriate information in place of the capitalized words.
- One-time permission is granted only for the use specified in your request. No additional uses are granted (such as derivative works or other editions). For any other uses, please submit a new request.

If credit is given to another source for the material you requested, permission must be obtained from that source.

BACK | CLOSE WINDOW

Copyright © 2017 Copyright Clearance Center, Inc. All Rights Reserved. Privacy statement. Terms and Conditions.
Comments? We would like to hear from you. E-mail us at customercare@copyright.com

Copyright license for chapter 6:

Title: Altering the selectivity of galvanostatic CO2 reduction on Cu cathodes by periodic cyclic voltammetry and potentiostatic steps

Author: C.F.C. Lim,D.A. Harrington,A.T. Marshall

Publication: Electrochimica Acta

Publisher: Elsevier

Date: 20 December 2016

Logged in as:
Calvin Fung Chye Lim
Account #:
3001176913

LOGOUT

Order Completed

Thank you for your order.

This Agreement between Mr. Calvin Fung Chye Lim ("You") and Elsevier ("Elsevier") consists of your license details and the terms and conditions provided by Elsevier and Copyright Clearance Center.

Your confirmation email will contain your order number for future reference.

Printable details.

License Number	4156421194089
License date	Jul 26, 2017
Licensed Content Publisher	Elsevier
Licensed Content Publication	Electrochimica Acta
Licensed Content Title	Altering the selectivity of galvanostatic CO2 reduction on Cu cathodes by periodic cyclic voltammetry and potentiostatic steps
Licensed Content Author	C.F.C. Lim,D.A. Harrington,A.T. Marshall
Licensed Content Date	Dec 20, 2016
Licensed Content Volume	222
Licensed Content Issue	n/a
Licensed Content Pages	8
Type of Use	reuse in a thesis/dissertation
Portion	full article
Format	both print and electronic
Are you the author of this Elsevier article?	Yes
Will you be translating?	No
Title of your thesis/dissertation	ELECTROCHEMICAL REDUCTION OF CARBON DIOXIDE ON COPPER ELECTRODES
Expected completion date	Aug 2017
Estimated size (number of pages)	180
Requestor Location	Mr. Calvin Fung Chye Lim 12 Winfield Drive Wigram Christchurch, Canterbury 8042 New Zealand Attn: Mr. Calvin Fung Chye Lim
Total	0.00 USD

ORDER MORE CLOSE WINDOW

Copyright license for chapter 7:

Title: Effects of mass transfer on the electrocatalytic CO2 reduction on Cu

Author: C.F.C. Lim,D.A. Harrington,A.T. Marshall

Publication: Electrochimica Acta

Publisher: Elsevier

Date: 1 June 2017

Logged in as:
Calvin Fung Chye Lim
Account #:
3001176913

LOGOUT

Order Completed

Thank you for your order.

This Agreement between Mr. Calvin Fung Chye Lim ("You") and Elsevier ("Elsevier") consists of your license details and the terms and conditions provided by Elsevier and Copyright Clearance Center.

Your confirmation email will contain your order number for future reference.

Printable details.

License Number	4156430167543
License date	Jul 26, 2017
Licensed Content Publisher	Elsevier
Licensed Content Publication	Electrochimica Acta
Licensed Content Title	Effects of mass transfer on the electrocatalytic CO2 reduction on Cu
Licensed Content Author	C.F.C. Lim,D.A. Harrington,A.T. Marshall
Licensed Content Date	Jun 1, 2017
Licensed Content Volume	238
Licensed Content Issue	n/a
Licensed Content Pages	8
Type of Use	reuse in a thesis/dissertation
Portion	full article
Format	both print and electronic
Are you the author of this Elsevier article?	Yes
Will you be translating?	No
Title of your thesis/dissertation	ELECTROCHEMICAL REDUCTION OF CARBON DIOXIDE ON COPPER ELECTRODES
Expected completion date	Aug 2017
Estimated size (number of pages)	180
Requestor Location	Mr. Calvin Fung Chye Lim 12 Winfield Drive Wigram Christchurch, Canterbury 8042 New Zealand Attn: Mr. Calvin Fung Chye Lim
Total	0.00 USD

ORDER MORE CLOSE WINDOW

Bibliography

[1] G.A. Olah, *et al.*, Chemical Recycling of Carbon Dioxide to Methanol and Dimethyl Ether: From Greenhouse Gas to Renewable, Environmentally Carbon Neutral Fuels and Synthetic Hydrocarbons, Journal of Organic Chemistry, 74 (2008) 487-498.

[2] N.S. Lewis, D.G. Nocera, Powering the planet: Chemical challenges in solar energy utilization, Proceedings of the National Academy of Sciences, 103 (2006) 15729-15735.

[3] G.A. Olah, Beyond Oil and Gas: The Methanol Economy, Angewandte Chemie International Edition, 44 (2005) 2636-2639.

[4] D.T. Whipple, P.J.A. Kenis, Prospects of CO_2 Utilization via Direct Heterogeneous Electrochemical Reduction, The Journal of Physical Chemistry Letters, 1 (2010) 3451-3458.

[5] G. Centi, S. Perathoner, Opportunities and prospects in the chemical recycling of carbon dioxide to fuels, Catalysis Today, 148 (2009) 191-205.

[6] A. Bandi, *et al.*, CO_2 recycling for hydrogen storage and transportation - Electrochemical CO_2 removal and fixation, Energy Conversion and Management, 36 (1995) 899-902.

[7] C. Song, Global challenges and strategies for control, conversion and utilization of CO_2 for sustainable development involving energy, catalysis, adsorption and chemical processing, Catalysis Today, 115 (2006) 2-32.

[8] M. Saito, R&D activities in Japan on methanol synthesis from CO_2 and H_2, Catalysis Surveys from Asia, 2 (1998) 175-184.

[9] M. Saito, *et al.*, Methanol synthesis from CO_2 and H_2 over a Cu/ZnO-based multicomponent catalyst, Energy Conversion and Management, 38, Supplement (1997) S403-S408.

[10] C.H. Bartholomew, R.J. Farrauto, Hydrogen Production and Synthesis Gas Reactions, Fundamentals of Industrial Catalytic Processes, John Wiley & Sons, Inc., 2005, pp. 339-486.

[11] M. Behrens, *et al.*, The Active Site of Methanol Synthesis over $Cu/ZnO/Al_2O_3$ Industrial Catalysts, Science, 336 (2012) 893-897.

[12] W.W. Russell, G.H. Miller, Catalytic Hydrogenation of Carbon Dioxide to Higher Hydrocarbons, Journal of the American Chemical Society, 72 (1950) 2446-2454.

[13] R.W. Dorner, *et al.*, Heterogeneous catalytic CO_2 conversion to value-added hydrocarbons, Energy & Environmental Science, 3 (2010) 884-890.

[14] B. Wang, *et al.*, CO_2 bio-mitigation using microalgae, Applied Microbiology and Biotechnology, 79 (2008) 707-718.

[15] J. Pawel, *et al.*, Carbon Dioxide Capture and Utilization using Biological Systems: Opportunities and Challenges, Journal of Bioprocessing & Biotechniques, 4 (2014).

[16] B. Kumar, *et al.*, Photochemical and Photoelectrochemical Reduction of CO_2, Annual Review of Physical Chemistry, 63 (2012) 541-569.

[17] A.J. Morris, *et al.*, Molecular Approaches to the Photocatalytic Reduction of Carbon Dioxide for Solar Fuels, Accounts of Chemical Research, 42 (2009) 1983-1994.

[18] K. Li, *et al.*, A critical review of CO_2 photoconversion: Catalysts and reactors, Catalysis Today, 224 (2014) 3-12.

[19] J.O.M. Bockris, J.C. Wass, The Photoelectrocatalytic Reduction of Carbon Dioxide, Journal of the Electrochemical Society, 136 (1989) 2521-2528.

[20] M. Gattrell, *et al.*, Electrochemical reduction of CO_2 to hydrocarbons to store renewable electrical energy and upgrade biogas, Energy Conversion and Management, 48 (2007) 1255-1265.

[21] L. Wenzhen, Electrocatalytic Reduction of CO_2 to Small Organic Molecule Fuels on Metal Catalysts, Advances in CO_2 Conversion and Utilization, American Chemical Society, 2010, pp. 55-76.

[22] Y. Hori, CO_2-reduction, catalyzed by metal electrodes, Handbook of Fuel Cells, John Wiley & Sons, Ltd, 2010.

[23] J.J. Kim, *et al.*, Reduction of CO_2 and CO to methane on Cu foil electrodes, Journal of Electroanalytical Chemistry, 245 (1988) 223-244.

[24] A.A. Peterson, *et al.*, How copper catalyzes the electroreduction of carbon dioxide into hydrocarbon fuels, Energy & Environmental Science, 3 (2010) 1311-1315.

[25] J.-P. Jones, *et al.*, Electrochemical CO_2 Reduction: Recent Advances and Current Trends, Israel Journal of Chemistry, 54 (2014) 1451-1466.

[26] R.P.S. Chaplin, A.A. Wragg, Effects of process conditions and electrode material on reaction pathways for carbon dioxide electroreduction with particular reference to formate formation, Journal of Applied Electrochemistry, 33 (2003) 1107-1123.

[27] J. Jordan, P.T. Smith, Free-radical Intermediate in the Electroreduction of Carbon Dioxide, Proceedings of the Chemical Society, (1960) 246-247.

[28] A.W.B. Aylmer-Kelly, *et al.*, Studies of electrochemically generated reaction intermediates using modulated specular reflectance spectroscopy, Faraday Discussions of the Chemical Society, 56 (1973) 96-107.

[29] E. Lamy, *et al.*, Standard potential and kinetic parameters of the electrochemical reduction of carbon dioxide in dimethylformamide, Journal of Electroanalytical Chemistry and Interfacial Electrochemistry, 78 (1977) 403-407.

[30] H.A. Schwarz, R.W. Dodson, Reduction potentials of CO_2^- and the alcohol radicals, The Journal of Physical Chemistry, 93 (1989) 409-414.

[31] P.S. Surdhar, *et al.*, Reduction potential of the carboxyl radical anion in aqueous solutions, The Journal of Physical Chemistry, 93 (1989) 3360-3363.

[32] K.P. Kuhl, *et al.*, New insights into the electrochemical reduction of carbon dioxide on metallic copper surfaces, Energy & Environmental Science, 5 (2012) 7050-7059.

[33] B.P. Sullivan, Electrochemical and Electrocatalytic Reactions of Carbon Dioxide, Elsevier, Amsterdam, 1993.

[34] C.M. Sánchez-Sánchez, *et al.*, Electrochemical approaches to alleviation of the problem of carbon dioxide accumulation, Pure and Applied Chemistry, 73 (2001) 1917.

[35] M. Jitaru, Electrochemical Carbon Dioxide Reduction - Fundamental and Applied Topics (review), Journal of the University of Chemical Technology and Metallurgy, 42 (2007) 333-344.

[36] R.J. Lim, *et al.*, A review on the electrochemical reduction of CO_2 in fuel cells, metal electrodes and molecular catalysts, Catalysis Today, 233 (2014) 169-180.

[37] J. Qiao, *et al.*, A review of catalysts for the electroreduction of carbon dioxide to produce low-carbon fuels, Chemical Society Reviews, 43 (2014) 631-675.

[38] E.E. Benson, *et al.*, Electrocatalytic and homogeneous approaches to conversion of CO_2 to liquid fuels, Chemical Society Reviews, 38 (2009) 89-99.

[39] M. Rakowski Dubois, D.L. Dubois, Development of Molecular Electrocatalysts for CO_2 Reduction and H_2 Production/Oxidation, Accounts of Chemical Research, 42 (2009) 1974-1982.

[40] C.D. Windle, E. Reisner, Heterogenised Molecular Catalysts for the Reduction of CO_2 to Fuels, CHIMIA International Journal for Chemistry, 69 (2015) 435-441.

[41] Y. Hori, *et al.*, Production of CO and CH_4 in Electrochemical Reduction of CO_2 at Metal Electrodes in Aqueous Hydrogencarbonate Solution, Chemistry Letters, 14 (1985) 1695-1698.

[42] Y. Hori, *et al.*, Production of Methane and Ethylene in Electrochemical Reduction of Carbon Dioxide at Copper Electrode in Aqueous Hydrogencarbonate Solution, Chemistry Letters, 15 (1986) 897-898.

[43] Y. Hori, *et al.*, Enhanced formation of ethylene and alcohols at ambient temperature and pressure in electrochemical reduction of carbon dioxide at a copper electrode, Journal of the Chemical Society, Chemical Communications, (1988) 17-19.

[44] N. Gupta, *et al.*, Calculation for the cathode surface concentrations in the electrochemical reduction of CO_2 in $KHCO_3$ solutions, Journal of Applied Electrochemistry, 36 (2006) 161-172.

[45] K.W. Frese Jr, Chapter 6 - Electrochemical Reduction of CO_2 at Solid Electrodes, in: B.P. Sullivan (Ed.) Electrochemical and Electrocatalytic Reactions of Carbon Dioxide, Elsevier, Amsterdam, 1993, pp. 145-216.

[46] M.A. Scibioh, B. Viswanathan, Electrochemical Reduction of Carbon Dioxide: A Status Report, Proceedings of the Indian National Science Academy, 70 (2004) 407-462.

[47] M. Gattrell, *et al.*, A review of the aqueous electrochemical reduction of CO_2 to hydrocarbons at copper, Journal of Electroanalytical Chemistry, 594 (2006) 1-19.

[48] Y. Hori, Electrochemical CO_2 Reduction on Metal Electrodes, in: C.G. Vayenas, *et al.* (Eds.) Modern Aspects of Electrochemistry, Springer New York, 2008, pp. 89-189.

[49] R. Kortlever, *et al.*, Catalysts and Reaction Pathways for the Electrochemical Reduction of Carbon Dioxide, The Journal of Physical Chemistry Letters, 6 (2015) 4073-4082.

[50] M. Azuma, *et al.*, Carbon dioxide reduction at low temperature on various metal electrodes, Journal of Electroanalytical Chemistry and Interfacial Electrochemistry, 260 (1989) 441-445.

[51] M. Azuma, *et al.*, Electrochemical Reduction of Carbon Dioxide on Various Metal Electrodes in Low-Temperature Aqueous $KHCO_3$ Media, Journal of the Electrochemical Society, 137 (1990) 1772-1778.

[52] P. Sabatier, Hydrogénations et déshydrogénations par catalyse, Berichte der deutschen chemischen Gesellschaft, 44 (1911) 1984-2001.

[53] A.A. Peterson, J.K. Nørskov, Activity Descriptors for CO_2 Electroreduction to Methane on Transition-Metal Catalysts, The Journal of Physical Chemistry Letters, 3 (2012) 251-258.

[54] A. Wuttig, *et al.*, Tracking a Common Surface-Bound Intermediate during CO_2-to-Fuels Catalysis, ACS Central Science, (2016).

[55] K.P. Kuhl, *et al.*, Electrocatalytic Conversion of Carbon Dioxide to Methane and Methanol on Transition Metal Surfaces, Journal of the American Chemical Society, 136 (2014) 14107-14113.

[56] Y. Hori, *et al.*, Electrocatalytic process of CO selectivity in electrochemical reduction of CO_2 at metal electrodes in aqueous media, Electrochimica Acta, 39 (1994) 1833-1839.

[57] J. Pacansky, *et al.*, SCF ab-initio ground state energy surfaces for CO_2 and CO_2^-, The Journal of Chemical Physics, 62 (1975) 2740-2744.

[58] S. Sakaki, An ab initio MO/SD-CI study of model complexes of intermediates in electrochemical reduction of CO_2 catalyzed by $NiCl_2$(cyclam), Journal of the American Chemical Society, 114 (1992) 2055-2062.

[59] Y. Chen, *et al.*, Aqueous CO_2 Reduction at Very Low Overpotential on Oxide-Derived Au Nanoparticles, Journal of the American Chemical Society, 134 (2012) 19969-19972.

[60] K. Hara, *et al.*, Electrochemical reduction of carbon dioxide under high pressure on various electrodes in an aqueous electrolyte, Journal of Electroanalytical Chemistry, 391 (1995) 141-147.

[61] R.L. Cook, *et al.*, Efficient High Rate Carbon Dioxide Reduction to Methane and Ethylene at in situ Electrodeposited Copper Electrode, Journal of the Electrochemical Society, 134 (1987) 2375-2376.

[62] R.L. Cook, *et al.*, Electrochemical Reduction of Carbon Dioxide to Methane at High Current Densities, Journal of the Electrochemical Society, 134 (1987) 1873-1874.

[63] R.L. Cook, *et al.*, On the Electrochemical Reduction of Carbon Dioxide at In Situ Electrodeposited Copper, Journal of the Electrochemical Society, 135 (1988) 1320-1326.

[64] D.W. DeWulf, *et al.*, Electrochemical and Surface Studies of Carbon Dioxide Reduction to Methane and Ethylene at Copper Electrodes in Aqueous Solutions, Journal of the Electrochemical Society, 136 (1989) 1686-1691.

[65] H. Noda, *et al.*, Potential Dependencies of the Products on Electrochemical Reduction of Carbon Dioxide at a Copper Electrode, Chemistry Letters, 18 (1989) 289-292.

[66] S. Wasmus, *et al.*, Reduction of Carbon Dioxide to Methane and Ethene - an On-line MS Study with Rotating Electrodes, Electrochimica Acta, 35 (1990) 771-775.

[67] Y. Hori, *et al.*, Formation of Hydrocarbons in the Electrochemical Reduction of Carbon Dioxide at a Copper Electrode in Aqueous Solution, Journal of the Chemical Society, Faraday Transactions 1: Physical Chemistry in Condensed Phases, 85 (1989) 2309-2326.

[68] C.S. Chen, *et al.*, Stable and selective electrochemical reduction of carbon dioxide to ethylene on copper mesocrystals, Catalysis Science & Technology, 5 (2015) 161-168.

[69] D. Kim, *et al.*, Insights into an autonomously formed oxygen-evacuated Cu_2O electrode for the selective production of C_2H_4 from CO_2, Physical Chemistry Chemical Physics, 17 (2015) 824-830.

[70] D. Ren, *et al.*, Selective Electrochemical Reduction of Carbon Dioxide to Ethylene and Ethanol on Copper(I) Oxide Catalysts, ACS Catalysis, 5 (2015) 2814-2821.

[71] B. Kumar, *et al.*, Controlling the Product Syngas H_2:CO Ratio through Pulsed-Bias Electrochemical Reduction of CO_2 on Copper, ACS Catalysis, 6 (2016) 4739-4745.

[72] Y. Kwon, *et al.*, CO_2 Electroreduction with Enhanced Ethylene and Ethanol Selectivity by Nanostructuring Polycrystalline Copper, ChemElectroChem, 3 (2016) 1012-1019.

[73] A.S. Varela, *et al.*, Tuning the Catalytic Activity and Selectivity of Cu for CO_2 Electroreduction in the Presence of Halides, ACS Catalysis, 6 (2016) 2136-2144.

[74] A.S. Varela, *et al.*, Controlling the selectivity of CO_2 electroreduction on copper: The effect of the electrolyte concentration and the importance of the local pH, Catalysis Today, 260 (2016) 8-13.

[75] J.N. Butler, Carbon Dioxide Equilibria and Their Applications, Taylor & Francis, 1991.

[76] Y. Hori, *et al.*, Electrochemical Reduction of Carbon Monoxide to Hydrocarbons at Various Metal Electrodes in Aqueous Solution, Chemistry Letters, 16 (1987) 1665-1668.

[77] Y. Hori, *et al.*, Electroreduction of CO to CH_4 and C_2H_4 at a Copper Electrode in Aqueous Solutions at Ambient Temperature and Pressure, Journal of the American Chemical Society, 109 (1987) 5022-5023.

[78] R.L. Cook, *et al.*, Evidence for Formaldehyde, Formic Acid, and Acetaldehyde as Possible Intermediates during Electrochemical Carbon Dioxide Reduction at Copper, Journal of the Electrochemical Society, 136 (1989) 1982-1984.

[79] J. Heyes, *et al.*, CO_2 Reduction on Cu at Low Overpotentials with Surface-Enhanced in Situ Spectroscopy, The Journal of Physical Chemistry C, 120 (2016) 17334-17341.

[80] Y. Hori, *et al.*, Adsorption of CO, intermediately formed in electrochemical reduction of CO_2, at a copper electrode, Journal of the Chemical Society, Faraday Transactions, 87 (1991) 125-128.

[81] Y. Hori, *et al.*, Infrared Spectroscopy of Adsorbed CO and Intermediate Species in Electrochemical Reduction of CO_2 to Hydrocarbons on a Cu Electrode, Electrochimica Acta, 40 (1995) 2617-2622.

[82] Y. Hori, *et al.*, Adsorption of CO accompanied with simultaneous charge transfer on copper single crystal electrodes related with electrochemical reduction of CO_2 to hydrocarbons, Surface Science, 335 (1995) 258-263.

[83] K.J.P. Schouten, *et al.*, A new mechanism for the selectivity to C_1 and C_2 species in the electrochemical reduction of carbon dioxide on copper electrodes, Chemical Science, 2 (2011) 1902-1909.

[84] A. Naitoh, *et al.*, Electrochemical reduction of carbon dioxide in methanol at low temperature, Electrochimica Acta, 38 (1993) 2177-2179.

[85] T. Saeki, *et al.*, Electrochemical Reduction of Liquid CO_2 : Drastic Enhancement of Current Density, Journal of the Electrochemical Society, 141 (1994) L130-L132.

[86] T. Saeki, *et al.*, Electrochemical Reduction of CO_2 with High Current Density in a CO_2-Methanol Medium, The Journal of Physical Chemistry, 99 (1995) 8440-8446.

[87] T. Saeki, *et al.*, Electrochemical reduction of CO_2 with high current density in a CO_2 + methanol medium at various metal electrodes, Journal of Electroanalytical Chemistry, 404 (1996) 299-302.

[88] S. Kaneco, *et al.*, Electrochemical reduction of carbon dioxide to ethylene at a copper electrode in methanol using potassium hydroxide and rubidium hydroxide supporting electrolytes, Electrochimica Acta, 51 (2006) 3316-3321.

[89] S. Kaneco, *et al.*, Electrochemical Reduction of CO_2 to Methane at the Cu Electrode in Methanol with Sodium Supporting Salts and Its Comparison with Other Alkaline Salts, Energy & Fuels, 20 (2006) 409-414.

[90] I. Shoichiro, *et al.*, Selective Formation of Formic Acid, Oxalic Acid, and Carbon Monoxide by Electrochemical Reduction of Carbon Dioxide, Bulletin of the Chemical Society of Japan, 60 (1987) 2517-2522.

[91] U. Kaiser, E. Heitz, Zum Mechanismus der elektrochemischen Dimerisierung von CO_2 zu Oxalsäure, Berichte der Bunsengesellschaft für physikalische Chemie, 77 (1973) 818-823.

[92] C. Amatore, J.M. Saveant, Mechanism and kinetic characteristics of the electrochemical reduction of carbon dioxide in media of low proton availability, Journal of the American Chemical Society, 103 (1981) 5021-5023.

[93] Y. Tomita, *et al.*, Electrochemical Reduction of Carbon Dioxide at a Platinum Electrode in Acetonitrile-Water Mixtures, Journal of the Electrochemical Society, 147 (2000) 4164-4167.

[94] B.A. Rosen, *et al.*, Ionic Liquid–Mediated Selective Conversion of CO_2 to CO at Low Overpotentials, Science, 334 (2011) 643-644.

[95] L.L. Snuffin, *et al.*, Catalytic Electrochemical Reduction of CO_2 in Ionic Liquid $EMIMBF_3Cl$, Journal of the Electrochemical Society, 158 (2011) F155-F158.

[96] S. Stucki, *et al.*, Coupled CO_2 recovery from the atmosphere and water electrolysis: Feasibility of a new process for hydrogen storage, International Journal of Hydrogen Energy, 20 (1995) 653-663.

[97] K.S. Lackner, Capture of carbon dioxide from ambient air, The European Physical Journal Special Topics, 176 (2009) 93-106.

[98] K. Ogura, M. Salazar-Villalpando, CO_2 electrochemical reduction via adsorbed halide anions, JOM Journal of the Minerals Metals and Materials Society, 63 (2011) 35-38.

[99] K. Ogura, Electrochemical reduction of carbon dioxide to ethylene: Mechanistic approach, Journal of CO2 Utilization, 1 (2013) 43-49.

[100] K. Hara, *et al.*, Change in the product selectivity for the electrochemical CO_2 reduction by adsorption of sulfide ion on metal electrodes, Journal of Electroanalytical Chemistry, 434 (1997) 239-243.

[101] P. Dubé, G.M. Brisard, Influence of adsorption processes on the CO_2 electroreduction: An electrochemical mass spectrometry study, Journal of Electroanalytical Chemistry, 582 (2005) 230-240.

[102] CRC Handbook of Chemistry and Physics, 90th Edition (Internet Version 2010), CRC Press/Taylor and Francis, Boca Raton, FL, 2010.

[103] K.J.P. Schouten, *et al.*, The influence of pH on the reduction of CO and to hydrocarbons on copper electrodes, Journal of Electroanalytical Chemistry, 716 (2014) 53-57.

[104] R. Kas, *et al.*, Manipulating the Hydrocarbon Selectivity of Copper Nanoparticles in CO_2 Electroreduction by Process Conditions, ChemElectroChem, 2 (2015) 354-358.

[105] I. Katsounaros, *et al.*, The effective surface pH during reactions at the solid–liquid interface, Electrochemistry Communications, 13 (2011) 634-637.

[106] M.R. Singh, *et al.*, Effects of electrolyte, catalyst, and membrane composition and operating conditions on the performance of solar-driven electrochemical reduction of carbon dioxide, Physical Chemistry Chemical Physics, 17 (2015) 18924-18936.

[107] A.S. Hall, *et al.*, Mesostructure-Induced Selectivity in CO_2 Reduction Catalysis, Journal of the American Chemical Society, 137 (2015) 14834-14837.

[108] M. Akira, H. Yoshio, Product Selectivity Affected by Cationic Species in Electrochemical Reduction of CO_2 and CO at a Cu Electrode, Bulletin of the Chemical Society of Japan, 64 (1991) 123-127.

[109] G.Z. Kyriacou, A.K. Anagnostopoulos, Influence CO_2 partial pressure and the supporting electrolyte cation on the product distribution in CO_2 electroreduction, Journal of Applied Electrochemistry, 23 (1993) 483-486.

[110] M.E. Essington, Soil and Water Chemistry: An Integrative Approach, CRC Press, 2004.

[111] A.N. Frumkin, Influence of cation adsorption on the kinetics of electrode processes, Transactions of the Faraday Society, 55 (1959) 156-167.

[112] M.R. Thorson, *et al.*, Effect of Cations on the Electrochemical Conversion of CO_2 to CO, Journal of the Electrochemical Society, 160 (2013) F69-F74.

[113] W. Paik, *et al.*, Kinetic studies of the electrolytic reduction of carbon dioxide on the mercury electrode, Electrochimica Acta, 14 (1969) 1217-1232.

[114] Y. Hori, S. Suzuki, Electrolytic Reduction of Carbon Dioxide at Mercury Electrode in Aqueous Solution, Bulletin of the Chemical Society of Japan, 55 (1982) 660-665.

[115] Y. Hori, *et al.*, Electrochemical Reduction of CO at a Copper Electrode, Journal of Physical Chemistry B, 101 (1997) 7075-7081.

[116] A.H. Wonders, *et al.*, On-line mass spectrometry system for measurements at single-crystal electrodes in hanging meniscus configuration, Journal of Applied Electrochemistry, 36 (2006) 1215-1221.

[117] R. Sander, Compilation of Henry's law constants, version 3.99, Atmospheric Chemistry and Physics Discussions, 14 (2014) 29615-30521.

[118] K.J.P. Schouten, *et al.*, Two Pathways for the Formation of Ethylene in CO Reduction on Single-Crystal Copper Electrodes, Journal of the American Chemical Society, 134 (2012) 9864-9867.

[119] J.O.M. Bockris, N. Pentland, The mechanism of hydrogen evolution at copper cathodes in aqueous solutions, Transactions of the Faraday Society, 48 (1952) 833-839.

[120] S. Kaneco, *et al.*, High-efficiency electrochemical CO_2-to-methane reduction method using aqueous $KHCO_3$ media at less than 273 K, Journal of Solid State Electrochemistry, 7 (2003) 152-156.

[121] A. Kudo, *et al.*, Electrochemical Reduction of High Pressure CO_2 on Ni Electrodes, Journal of the Electrochemical Society, 140 (1993) 1541-1545.

[122] Y. Hori, *et al.*, Adsorption of Carbon Monoxide at a Copper Electrode Accompanied by Electron Transfer Observed by Voltammetry and IR Spectroscopy, Electrochimica Acta, 39 (1994) 2495-2500.

[123] Y.-J. Zhang, *et al.*, Competition between CO_2 Reduction and H_2 Evolution on Transition-Metal Electrocatalysts, ACS Catalysis, 4 (2014) 3742-3748.

[124] K. Hara, *et al.*, Electrochemical Reduction of CO_2 on a Cu Electrode under High Pressure: Factors that Determine the Product Selectivity, Journal of the Electrochemical Society, 141 (1994) 2097-2103.

[125] K. Hara, T. Sakata, Large Current Density CO_2 Reduction under High Pressure Using Gas Diffusion Electrodes, Bulletin of the Chemical Society of Japan, 70 (1997) 571-576.

[126] M. Todoroki, *et al.*, Electrochemical reduction of high pressure CO_2 at Pb, Hg and In electrodes in an aqueous $KHCO_3$ solution, Journal of Electroanalytical Chemistry, 394 (1995) 199-203.

[127] K. Hara, *et al.*, Electrochemical CO_2 reduction on a glassy carbon electrode under high pressure, Journal of Electroanalytical Chemistry, 421 (1997) 1-4.

[128] S. Nakagawa, *et al.*, Effect of pressure on the electrochemical reduction of CO_2 on Group VIII metal electrodes, Journal of Electroanalytical Chemistry and Interfacial Electrochemistry, 308 (1991) 339-343.

[129] Y. Hori, *et al.*, Selective Formation of C_2 Compounds from Electrochemical Reduction of CO_2 at a Series of Copper Single Crystal Electrodes, The Journal of Physical Chemistry B, 106 (2002) 15-17.

[130] Y. Hori, *et al.*, Electrochemical reduction of carbon dioxide at various series of copper single crystal electrodes, Journal of Molecular Catalysis A: Chemical, 199 (2003) 39-47.

[131] I. Takahashi, *et al.*, Electrochemical reduction of CO_2 at copper single crystal Cu(S)-[n(111)×(111)] and Cu(S)-[n(110)×(100)] electrodes, Journal of Electroanalytical Chemistry, 533 (2002) 135-143.

[132] J. Christophe, *et al.*, Electroreduction of Carbon Dioxide on Copper-Based Electrodes: Activity of Copper Single Crystals and Copper–Gold Alloys, Electrocatalysis, 3 (2012) 139-146.

[133] K.J.P. Schouten, *et al.*, Structure Sensitivity of the Electrochemical Reduction of Carbon Monoxide on Copper Single Crystals, ACS Catalysis, 3 (2013) 1292-1295.

[134] F.S. Roberts, *et al.*, Electroreduction of Carbon Monoxide Over a Copper Nanocube Catalyst: Surface Structure and pH Dependence on Selectivity, ChemCatChem, 8 (2016) 1119-1124.

[135] F. Calle-Vallejo, M.T.M. Koper, Theoretical Considerations on the Electroreduction of CO to C_2 Species on Cu(100) Electrodes, Angewandte Chemie, 125 (2013) 7423-7426.

[136] J.H. Montoya, *et al.*, Insights into C-C Coupling in CO_2 Electroreduction on Copper Electrodes, ChemCatChem, 5 (2013) 737-742.

[137] J.H. Montoya, *et al.*, Theoretical Insights into a CO Dimerization Mechanism in CO_2 Electroreduction, The Journal of Physical Chemistry Letters, 6 (2015) 2032-2037.

[138] W. Luo, *et al.*, Facet Dependence of CO_2 Reduction Paths on Cu Electrodes, ACS Catalysis, 6 (2016) 219-229.

[139] Y.-G. Kim, M.P. Soriaga, Cathodic regeneration of a clean and ordered Cu(100)-(1×1) surface from an air-oxidized and disordered electrode: An operando STM study, Journal of Electroanalytical Chemistry, 734 (2014) 7-9.

[140] Y.-G. Kim, *et al.*, The Evolution of the Polycrystalline Copper Surface, First to Cu(111) and Then to Cu(100), at a Fixed CO_2RR Potential: A Study by Operando EC-STM, Langmuir, (2014).

[141] Y.-G. Kim, *et al.*, Regulating the Product Distribution of CO Reduction by the Atomic-Level Structural Modification of the Cu Electrode Surface, Electrocatalysis, 7 (2016) 391-399.

[142] H. Matsushima, *et al.*, Reconstruction of Cu(100) Electrode Surfaces during Hydrogen Evolution, Journal of the American Chemical Society, 131 (2009) 10362-10363.

[143] P. Kedzierzawski, J. Augustynski, Poisoning and Activation of the Gold Cathode during Electroreduction of CO_2, Journal of the Electrochemical Society, 141 (1994) L58-L60.

[144] R. Kostecki, J. Augustynski, Electrochemical reduction of CO_2 at an activated silver electrode, Berichte der Bunsengesellschaft für physikalische Chemie, 98 (1994) 1510-1515.

[145] H. Yano, *et al.*, Electrochemical reduction of CO_2 at three-phase (gas|liquid|solid) and two-phase (liquid|solid) interfaces on Ag electrodes, Journal of Electroanalytical Chemistry, 533 (2002) 113-118.

[146] G. Kyriacou, A. Anagnostopoulos, Electroreduction of CO_2 on differently prepared copper electrodes: The influence of electrode treatment on the current efficiences, Journal of Electroanalytical Chemistry, 322 (1992) 233-246.

[147] C.F.C. Lim, *et al.*, Altering the selectivity of galvanostatic CO_2 reduction on Cu cathodes by periodic cyclic voltammetry and potentiostatic steps, Electrochimica Acta, 222 (2016) 133-140.

[148] G. Brisard, *et al.*, Oxygen reduction and hydrogen evolution–oxidation reactions on Cu(hkl) surfaces, Journal of Electroanalytical Chemistry, 480 (2000) 219-224.

[149] Y. Hori, *et al.*, "Deactivation of copper electrode" in electrochemical reduction of CO_2, Electrochimica Acta, 50 (2005) 5354-5369.

[150] B.D. Smith, *et al.*, A Surface Enhanced Raman Scattering Study of the Intermediate and Poisoning Species Formed during the Electrochemical Reduction of CO_2 on Copper, Journal of the Electrochemical Society, 144 (1997) 4288-4296.

[151] R. Shiratsuchi, *et al.*, Pulsed Electroreduction of CO_2 on Copper Electrodes, Journal of the Electrochemical Society, 140 (1993) 3479-3482.

[152] J.-F. Xie, *et al.*, Efficient electrochemical CO_2 reduction on a unique chrysanthemum-like Cu nanoflower electrode and direct observation of carbon deposite, Electrochimica Acta, 139 (2014) 137-144.

[153] J. Lee, Y. Tak, Electrocatalytic activity of Cu electrode in electroreduction of CO_2, Electrochimica Acta, 46 (2001) 3015-3022.

[154] H. Yano, *et al.*, Efficient electrochemical conversion of CO_2 to CO, C_2H_4 and CH_4 at a three-phase interface on a Cu net electrode in acidic solution, Journal of Electroanalytical Chemistry, 519 (2002) 93-100.

[155] P. Friebe, *et al.*, A Real-Time Mass Spectroscopy Study of the (Electro)chemical Factors Affecting CO_2 Reduction at Copper, Journal of Catalysis, 168 (1997) 374-385.

[156] J. Wu, *et al.*, Achieving Highly Efficient, Selective, and Stable CO_2 Reduction on Nitrogen-Doped Carbon Nanotubes, ACS Nano, 9 (2015) 5364-5371.

[157] N. Yang, *et al.*, Electrochemistry of Carbon Dioxide on Carbon Electrodes, ACS Applied Materials & Interfaces, (2015).

[158] S. Zhang, *et al.*, Polyethylenimine-Enhanced Electrocatalytic Reduction of CO_2 to Formate at Nitrogen-Doped Carbon Nanomaterials, Journal of the American Chemical Society, 136 (2014) 7845-7848.

[159] A. Wuttig, Y. Surendranath, Impurity Ion Complexation Enhances Carbon Dioxide Reduction Catalysis, ACS Catalysis, 5 (2015) 4479-4484.

[160] B. Jermann, J. Augustynski, Long-term activation of the copper cathode in the course of CO_2 reduction, Electrochimica Acta, 39 (1994) 1891-1896.

[161] E.A. Batista, M.L.A. Temperini, Spectroscopic evidences of the presence of hydrogenated species on the surface of copper during CO_2 electroreduction at low cathodic potentials, Journal of Electroanalytical Chemistry, 629 (2009) 158-163.

[162] Q. Lu, *et al.*, A selective and efficient electrocatalyst for carbon dioxide reduction, Nature Communications, 5 (2014) 3242.

[163] Y. Terunuma, *et al.*, Relationship between hydrocarbon production in the electrochemical reduction of CO_2 and the characteristics of the Cu electrode, Journal of Electroanalytical Chemistry, 434 (1997) 69-75.

[164] G. Nogami, *et al.*, Pulsed Electroreduction of CO_2 on Copper Electrodes - II, Journal of the Electrochemical Society, 141 (1994) 1138-1142.

[165] J. Yano, S. Yamasaki, Pulse-mode electrochemical reduction of carbon dioxide using copper and copper oxide electrodes for selective ethylene formation, Journal of Applied Electrochemistry, 38 (2008) 1721-1726.

[166] J. Yano, *et al.*, Selective ethylene formation by pulse-mode electrochemical reduction of carbon dioxide using copper and copper-oxide electrodes, Journal of Solid State Electrochemistry, 11 (2007) 554-557.

[167] R. Shiratsuchi, G. Nogami, Pulsed Electroreduction of CO_2 on Silver Electrodes, Journal of the Electrochemical Society, 143 (1996) 582-586.

[168] D.P. Summers, K.W. Frese, Electrochemical reduction of carbon dioxide. Characterization of the formation of methane at ruthenium electrodes in carbon dioxide saturated aqueous solution, Langmuir, 4 (1988) 51-57.

[169] X. Nie, *et al.*, Selectivity of CO_2 Reduction on Copper Electrodes: The Role of the Kinetics of Elementary Steps, Angewandte Chemie International Edition, 52 (2013) 2459-2462.

[170] X. Nie, *et al.*, Reaction mechanisms of CO_2 electrochemical reduction on Cu(111) determined with density functional theory, Journal of Catalysis, 312 (2014) 108-122.

[171] J.B. Hansen, P.E. Højlund Nielsen, Methanol Synthesis, Handbook of Heterogeneous Catalysis, Wiley-VCH Verlag GmbH & Co. KGaA, 2008.

[172] Y.-J. Zhang, A.A. Peterson, Oxygen-induced changes to selectivity-determining steps in electrocatalytic CO_2 reduction, Physical Chemistry Chemical Physics, 17 (2015) 4505-4515.

[173] P. Hirunsit, *et al.*, CO_2 Electrochemical Reduction to Methane and Methanol on Copper-Based Alloys: Theoretical Insight, The Journal of Physical Chemistry C, 119 (2015) 8238-8249.

[174] P. Hirunsit, Electroreduction of Carbon Dioxide to Methane on Copper, Copper–Silver, and Copper–Gold Catalysts: A DFT Study, The Journal of Physical Chemistry C, 117 (2013) 8262-8268.

[175] M. Watanabe, *et al.*, Design of alloy electrocatalysts for CO_2 reduction, Journal of Electroanalytical Chemistry and Interfacial Electrochemistry, 305 (1991) 319-328.

[176] M. Watanabe, *et al.*, Design of Alloy Electrocatalysts for CO_2 Reduction, Journal of the Electrochemical Society, 138 (1991) 3382.

[177] F. Jia, *et al.*, Enhanced selectivity for the electrochemical reduction of CO_2 to alcohols in aqueous solution with nanostructured Cu–Au alloy as catalyst, Journal of Power Sources, 252 (2014) 85-89.

[178] D. Kim, *et al.*, Synergistic geometric and electronic effects for electrochemical reduction of carbon dioxide using gold–copper bimetallic nanoparticles, Nature Communications, 5 (2014) 4948.

[179] M. Karamad, *et al.*, Intermetallic Alloys as CO Electroreduction Catalysts - Role of Isolated Active Sites, ACS Catalysis, 4 (2014) 2268-2273.

[180] K.W. Frese, Electrochemical Reduction of CO_2 at Intentionally Oxidized Copper Electrodes, Journal of the Electrochemical Society, 138 (1991) 3338-3344.

[181] T.-Y. Chang, *et al.*, Electrochemical reduction of CO_2 by Cu_2O-catalyzed carbon clothes, Materials Letters, 63 (2009) 1001-1003.

[182] M. Le, *et al.*, Electrochemical Reduction of CO_2 to CH_3OH at Copper Oxide Surfaces, Journal of the Electrochemical Society, 158 (2011) E45-E49.

[183] M. Ren, *et al.*, Regenerative Methanol Fuel Cells: Reduction of CO_2 to Methanol on Oxidized Cu Electrodes, ECS Transactions, 33 (2011) 253-259.

[184] L.D. Burke, J.A. Collins, Role of surface defects in the electrocatalytic behaviour of copper in base, Journal of Applied Electrochemistry, 29 (1999) 1427-1438.

[185] S. Lee, *et al.*, Electrocatalytic Production of C_3-C_4 Compounds by Conversion of CO_2 on a Chloride-Induced Bi-Phasic Cu_2O-Cu Catalyst, Angewandte Chemie, 127 (2015) 14914-14918.

[186] C.W. Li, M.W. Kanan, CO_2 Reduction at Low Overpotential on Cu Electrodes Resulting from the Reduction of Thick Cu_2O Films, Journal of the American Chemical Society, 134 (2012) 7231-7234.

[187] C.W. Li, *et al.*, Electroreduction of carbon monoxide to liquid fuel on oxide-derived nanocrystalline copper, Nature, 508 (2014) 504-507.

[188] J. Qiao, *et al.*, Formation of Cu nanostructured electrode surfaces by an annealing–electroreduction procedure to achieve high-efficiency CO_2 electroreduction, Electrochemistry Communications, 38 (2014) 8-11.

[189] D. Raciti, *et al.*, Highly Dense Cu Nanowires for Low-Overpotential CO_2 Reduction, Nano Letters, 15 (2015) 6829-6835.

[190] A. Verdaguer-Casadevall, *et al.*, Probing the Active Surface Sites for CO Reduction on Oxide-Derived Copper Electrocatalysts, Journal of the American Chemical Society, 137 (2015) 9808-9811.

[191] J. Bugayong, G.L. Griffin, Electrochemical Reduction of CO_2 Using Supported Cu_2O Nanoparticles, ECS Transactions, 58 (2013) 81-89.

[192] D. Chi, *et al.*, Morphology-controlled CuO nanoparticles for electroreduction of CO_2 to ethanol, RSC Advances, 4 (2014) 37329-37332.

[193] M. Ma, *et al.*, Selective electrochemical reduction of CO_2 to CO on CuO-derived Cu nanowires, Physical Chemistry Chemical Physics, 17 (2015) 20861-20867.

[194] R. Kas, *et al.*, Electrochemical CO_2 reduction on Cu_2O-derived copper nanoparticles: controlling the catalytic selectivity of hydrocarbons, Physical Chemistry Chemical Physics, 16 (2014) 12194-12201.

[195] W. Tang, *et al.*, The importance of surface morphology in controlling the selectivity of polycrystalline copper for CO_2 electroreduction, Physical Chemistry Chemical Physics, 14 (2012) 76-81.

[196] F.S. Roberts, *et al.*, High Selectivity for Ethylene from Carbon Dioxide Reduction over Copper Nanocube Electrocatalysts, Angewandte Chemie International Edition, 54 (2015) 5179-5182.

[197] K. Ogura, *et al.*, Catalytic Reduction of CO_2 to Ethylene by Electrolysis at a Three-Phase Interface, Journal of the Electrochemical Society, 150 (2003) D163-D168.

[198] K. Ogura, *et al.*, Selective formation of ethylene from CO_2 by catalytic electrolysis at a three-phase interface, Catalysis Today, 98 (2004) 515-521.

[199] H. Yano, *et al.*, Selective electrochemical reduction of CO_2 to ethylene at a three-phase interface on copper(I) halide-confined Cu-mesh electrodes in acidic solutions of potassium halides, Journal of Electroanalytical Chemistry, 565 (2004) 287-293.

[200] A. Eilert, *et al.*, Formation of Copper Catalysts for CO_2 Reduction with High Ethylene/Methane Product Ratio Investigated with In Situ X-ray Absorption Spectroscopy, The Journal of Physical Chemistry Letters, 7 (2016) 1466-1470.

[201] O.A. Baturina, *et al.*, CO_2 Electroreduction to Hydrocarbons on Carbon-Supported Cu Nanoparticles, ACS Catalysis, 4 (2014) 3682-3695.

[202] R. Reske, *et al.*, Particle Size Effects in the Catalytic Electroreduction of CO_2 on Cu Nanoparticles, Journal of the American Chemical Society, 136 (2014) 6978-6986.

[203] Y. Yamada, *et al.*, Nanocrystal bilayer for tandem catalysis, Nature Chemistry, 3 (2011) 372-376.

[204] D.R. Rolison, *et al.*, Role of Hydrous Ruthenium Oxide in Pt−Ru Direct Methanol Fuel Cell Anode Electrocatalysts: The Importance of Mixed Electron/Proton Conductivity, Langmuir, 15 (1999) 774-779.

[205] I.X. Green, *et al.*, Spectroscopic Observation of Dual Catalytic Sites During Oxidation of CO on a Au/TiO_2 Catalyst, Science, 333 (2011) 736-739.

[206] P. Diao, *et al.*, Electrocatalytic activity of supported gold nanoparticles toward CO oxidation: The perimeter effect of gold–support interface, Electrochemistry Communications, 12 (2010) 1622-1625.

[207] E. Andrews, *et al.*, Electrochemical Reduction of CO_2 at Cu Nanocluster / $(10\bar{1}0)$ ZnO Electrodes, Journal of the Electrochemical Society, 160 (2013) H841-H846.

[208] Y. Song, *et al.*, High-Selectivity Electrochemical Conversion of CO_2 to Ethanol using a Copper Nanoparticle/N-Doped Graphene Electrode, ChemistrySelect, 1 (2016) 6055–6061.

[209] H. De Jesús-Cardona, *et al.*, Voltammetric study of CO_2 reduction at Cu electrodes under different $KHCO_3$ concentrations, temperatures and CO_2 pressures, Journal of Electroanalytical Chemistry, 513 (2001) 45-51.

[210] R. Kortlever, *et al.*, Electrochemical carbon dioxide and bicarbonate reduction on copper in weakly alkaline media, Journal of Solid State Electrochemistry, 17 (2013) 1843-1849.

[211] E.A. Ticianelli, *et al.*, Methods to Advance Technology of Proton Exchange Membrane Fuel Cells, Journal of the Electrochemical Society, 135 (1988) 2209-2214.

[212] Z. Lu, *et al.*, State of Water in Perfluorosulfonic Ionomer (Nafion 117) Proton Exchange Membranes, Journal of the Electrochemical Society, 155 (2008) B163-B171.

[213] M. Amjadi, *et al.*, Preparation, characterization and cell performance of durable nafion/SiO_2 hybrid membrane for high-temperature polymeric fuel cells, Journal of Power Sources, 210 (2012) 350-357.

[214] P.T. Kissinger, W.R. Heineman, Cyclic voltammetry, Journal of Chemical Education, 60 (1983) 702.

[215] S.B. Ribotta, M.E. Folquer, The effects of temperature and pH on the dissolution and passivation processes of copper in carbonate-bicarbonate solutions, Journal of the Brazilian Chemical Society, 8 (1997) 159-163.

[216] M.P. Sánchez, *et al.*, Electrochemical Behaviour of Copper in Aqueous Moderate Alkaline Media, Containing Sodium Carbonate and Bicarbonate, and Sodium Perchlorate, Electrochimica Acta, 35 (1990) 1337-1343.

[217] M. Pourbaix, Atlas of electrochemical equilibria in aqueous solutions, Pergamon Press, Oxford; New York, 1966.

[218] A. Bard, L. Faulkner, Electrochemical Methods: Fundamentals and Applications, John Wiley & Sons, Inc, 2001.

[219] T.M.L. Wigley, L.N. Plummer, Mixing of carbonate waters, Geochimica et Cosmochimica Acta, 40 (1976) 989-995.

[220] S. Weisenberger, A. Schumpe, Estimation of gas solubilities in salt solutions at temperatures from 273 K to 363 K, AIChE Journal, 42 (1996) 298-300.

[221] A. Schumpe, The estimation of gas solubilities in salt solutions, Chemical Engineering Science, 48 (1993) 153-158.

[222] D.R. Gabe, D.J. Robinson, Mass transfer in a rotating cylinder cell - II. turbulent flow, Electrochimica Acta, 17 (1972) 1129-1137.

[223] D.R. Gabe, The rotating cylinder electrode, Journal of Applied Electrochemistry, 4 (1974) 91-108.

[224] D.R. Gabe, D.J. Robinson, Mass transfer in a rotating cylinder cell - I. Laminar flow, Electrochimica Acta, 17 (1972) 1121-1127.

[225] M. Eisenberg, *et al.*, Ionic Mass Transfer and Concentration Polarization at Rotating Electrodes, Journal of the Electrochemical Society, 101 (1954) 306-320.

[226] C.H. Hamann, *et al.*, Electrochemistry, 2nd ed., Wiley-VCH, 2007.

[227] S. Sen, *et al.*, Electrochemical Reduction of CO_2 at Copper Nanofoams, ACS Catalysis, 4 (2014) 3091-3095.

[228] G. Kyriacou, A. Anagnostopoulos, Electrochemical reduction of CO_2 at Cu + Au electrodes, Journal of Electroanalytical Chemistry, 328 (1992) 233-243.

[229] Y. Hori, *et al.*, FTIR measurements of charge displacement adsorption of CO on poly- and single crystal (100) of Cu electrodes, Electrochimica Acta, 44 (1998) 1389-1395.

[230] M.T.M. Koper, *et al.*, Potential Oscillations and S-Shaped Polarization Curve in the Continuous Electro-oxidation of CO on Platinum Single-crystal Electrodes, The Journal of Physical Chemistry B, 105 (2001) 8381-8386.

[231] G.P. Sakellaropoulos, B.G. Volintine, 50 Multiple steady states in electrochemical reactors, Chemical Engineering Science, 35 (1980) 396-404.

[232] C.G. Takoudis, L.D. Schmidt, Multiple steady states in reaction controlled surface catalysed reactions, Chemical Engineering Science, 36 (1981) 377-386.

[233] C.G. Takoudis, *et al.*, Isothermal sustained oscillations in a very simple surface reaction, Surface Science, 105 (1981) 325-333.

[234] C.G. Takoudis, *et al.*, Steady state multiplicity in surface reactions with coverage dependent parameters, Chemical Engineering Science, 36 (1981) 1795-1802.

[235] R.A. Saymeh, R.D. Gonzalez, Catalytic oxidation of carbon monoxide over iridium/silica. An in situ infrared and kinetic study, The Journal of Physical Chemistry, 90 (1986) 622-628.

[236] C.F.C. Lim, *et al.*, Effects of mass transfer on the electrocatalytic CO_2 reduction on Cu, Electrochimica Acta, 238 (2017) 56-63.

[237] P. Bumroongsakulsawat, G.H. Kelsall, Effect of solution pH on CO: formate formation rates during electrochemical reduction of aqueous CO_2 at Sn cathodes, Electrochimica Acta, 141 (2014) 216-225.

[238] D. Gao, *et al.*, pH effect on electrocatalytic reduction of CO_2 over Pd and Pt nanoparticles, Electrochemistry Communications, 55 (2015) 1-5.

[239] C.T.J. Low, *et al.*, The Rotating Cylinder Electrode (RCE) and its Application to the Electrodeposition of Metals, Australian Journal of Chemistry, 58 (2005) 246-262.

[240] L.M. Molina, B. Hammer, Theoretical study of CO oxidation on Au nanoparticles supported by MgO(100), Physical Review B, 69 (2004) 155424.

[241] A. Bandi, Electrochemical Reduction of Carbon Dioxide on Conductive Metallic Oxides, Journal of the Electrochemical Society, 137 (1990) 2157-2160.

[242] J.P. Popić, *et al.*, Reduction of carbon dioxide on ruthenium oxide and modified ruthenium oxide electrodes in 0.5 M $NaHCO_3$, Journal of Electroanalytical Chemistry, 421 (1997) 105-110.

[243] D.P. Anderson, *et al.*, Chemically synthesised atomically precise gold clusters deposited and activated on titania. Part II, Physical Chemistry Chemical Physics, 15 (2013) 14806-14813.

[244] D.P. Anderson*, et al.*, Chemically-synthesised, atomically-precise gold clusters deposited and activated on titania, Physical Chemistry Chemical Physics, 15 (2013) 3917-3929.

[245] D.T. Sawyer*, et al.*, Electrochemistry for Chemists, Wiley, New York, 1995.

[246] The Ag/AgCl Reference Electrode, Research Solutions and Resources LCC, http://www.consultrsr.net/resources/ref/agcl.htm, accessed on 13 April 2017.

[247] H.S. Fogler, Elements of chemical reaction engineering, Prentice Hall, 2006.

[248] G. Currell, A. Dowman, Essential Mathematics and Statistics for Science, 2nd ed., Wiley-Blackwell, 2009.

[249] J.J. Carroll*, et al.*, The Solubility of Carbon Dioxide in Water at Low Pressure, Journal of Physical and Chemical Reference Data, 20 (1991) 1201-1209.

[250] D. Keeports, Equilibrium Constants and Water Activity, Journal of Chemical Education, 82 (2005) 999.

[251] W.K. Lewis, W.G. Whitman, Principles of Gas Absorption, Industrial & Engineering Chemistry, 16 (1924) 1215-1220.

[252] G.V. Samsonov, Mechanical Properties of the Elements, in: G.V. Samsonov (Ed.) Handbook of the Physicochemical Properties of the Elements, Springer US, Boston, MA, 1968, pp. 387-446.